VILNIUS UNIVERSITY

INSTITUTE OF PHYSICS OF CENTER FOR PHYSICAL SCIENCES AND TECHNOLOGY

ŠARŪNAS BAGDZEVIČIUS

PROCESSING, STRUCTURAL AND BROADBAND DIELECTRIC CHARACTERIZATION OF STRONTIUM TITANATE AND RELATED PEROVSKITE CERAMICS AND THIN FILMS

Doctoral dissertation

Physical sciences, Physics (02P)

Vilnius

2014

The thesis was prepared at Vilnius University (Vilnius, Lithuania) in 2009 – 2011 and École Polytechnique Fédérale de Lausanne (Lausanne, Switzerland) in 2012-2014.

Academic supervisor:

Prof. habil. dr. Jūras Banys (Vilnius University, physical sciences, physics - 02P).

Scientific advisors:

Dr. Robertas Grigalaitis (Vilnius University, physical sciences, physics - 02P);

Prof. dr. Nava Setter (École Polytechnique Fédérale de Lausanne, engineering sciences, solid state engineering - 08T).

3

Content

Abbreviations used in this thesis

AFD: AntiFerroDistortive. Non ferrodistortive structural phase transition, which is not associated with ferroelectric, ferroelastic or ferromagnetic ordering in low temperature phase.

AFM: Atomic Force Microscopy. Microscopical technique creating topological profiles at nm length scales.

APB: AntiPhase Boundaries. Domain boundaries in antiferrodistortive materials like $SrTiO_3$ or antiferroelectric materials like $PbZrO_3$ below structural phase transition temperatures.

BET: Brunauer–Emmett–Teller (BET) theory and specific surface area measurement technique.

BF: Bright Field. One of TEM microscopy operating modes. Image is constructed from non-diffracted (transmitted) electrons.

BHF: buffered HF acid. Also known as BOE − buffered oxide etchant used to etch oxides and silicon.

CVD: chemical vapour phase deposition.

DF: Dark Field. One of TEM microscopy operating modes. Image is constructed from Bragg diffracted electrons.

HAADF: High Angle Annular Dark Field. One of TEM microscopy operating modes. Image is constructed from inelastically scattered to high angles electrons, also known as Z-contrast.

KNN-Sb_x: Sodium potassium niobate doped with antimony - $(K_{0.5}Na_{0.5})(Nb_{1-x}Sb_x)O_3$. Ferroelectric material investigated in this thesis.

LAO: Lanthanum aluminate - $LaAlO_3$. A substrate material used in this thesis.

LSAT: Lanthanum-Strontium Aluminate-Tantalate $(LaAlO_3)_{0.3}$-$(Sr_2AlTaO_6)_{0.7}$. A substrate material used in this study with a small but important lattice mismatch with $SrTiO_3$.

LSMO: Lanthanum strontium manganite - $La_{0.8}Sr_{0.2}MnO_3$. Lattice matched to $SrTiO_3$ electrode material used in thin film heterostructures.

MBE: molecular beam epitaxy. One of physical deposition methods usually used to grow superb quality thin films of semiconductors.

NBT-ST-PT: $0.4Na_{0.5}Bi_{0.5}TiO_3–(0.6-x)SrTiO_3-xPbTiO_3$ ceramic. Interesting ternary solid state solution with variable phase transition temperature depending on lead titanate content.

NMR: Nuclear Magnetic Resonance. A spectroscopical technique allowing probing local chemical environment of material.

PFM: Piezoelectric Force Microscopy. Microscopical technique creating profiles of local piezoelectric response of material at nm length scales.

PLD: Pulsed Laser Deposition. One of physical deposition techniques used for deposition of compositionally complex materials like high K superconductors and stoichiometric oxides in scientific environment.

PNR: Polar Nano Region. Polar regions inside nonpolar matrix in macroscopically paraelectric phase. Their dynamic strongly influences dielectric and other material responses below Burns temperature.

PT: Lead titanate - $PbTiO_3$. Ferroelectric material with superb electromechanical properties, still allowed using in some electromechanical applications.

PZT: Lead zirconium titanate – $Pb(Zr_xTi_{1-x})O_3$. Lead containing ferroelectric material with superb electromechanical properties, still allowed using in some electromechanical applications.

RBRF: Random Bond-Random Field model. Mean field model describing properties of ferroelectric relaxor materials.

RHEED: Reflection High Energy Electron Diffraction. An electron diffraction based technique allowing probing material surface in situ.

RSM: XRD Reciprocal Space Map. Diffraction technique allowing mapping crystallographic planes in reciprocal space.

RTD: Resistance Temperature Detector. One of the temperature measurement methods.

SAED: Selected Area Electron Diffraction. Electron diffraction technique for local structural analysis.

SBT: Strontium titanate doped with bismuth - $(Sr_{x-1}Bi_x)TiO_3$. Doped incipient ferroelectric material investigated in this thesis.

SPM: Scanning Probe Microscopy. Microscopical technique creating topological profiles at nm length scales, due to various surface sensitive interactions like electron tunnelling, piezoelectric effect, conductivity etc.

SRO: Strontium ruthenate - $SrRuO_3$. Lattice matched to $SrTiO_3$ electrode material used in thin film heterostructures.

STO or ST: Strontium Titanate - $SrTiO_3$. An incipient ferroelectric and one of the materials studied in this thesis.

TEM/SEM: Transmission/Scanning Electron Microscopy. Analytical technique allowing imaging at sub nanometre length scale.

XRD: X-Ray Diffraction. Diffraction technique for structural analysis.

YSZ: Yttrium Stabilized Zirconia – solid solution of ZrO_2 and Y_2O_3. Hard and chemical inert material used as a grinding media in powder processing.

1.Introduction

This thesis describes an experimental investigation of incipient ferroelectric strontium titanate and related solid state systems done during Ph. D. programme at Vilnius University (Vilnius, Lithuania) and EPFL (École Polytechnique Fédérale de Lausanne, Lausanne, Switzerland).

It consists of two main parts – processing and characterization of ferroic materials (ferroelectric, incipient ferroelectric and disordered materials). This research studies $(Sr_{1-1.5x}Bi_x)TiO_3$ [SBT] ceramic, $(K_{0.5}Na_{0.5})(Nb_{1-x}Sb_x)O_3$ [KNN-Sb$_x$] ceramic and $0.4Na_{0.5}Bi_{0.5}TiO_3–(0.6-x)SrTiO_3-xPbTiO_3$ [NBT-ST-PT] ceramic, also $SrTiO_3$ thin films grown epitaxially on lattice matched and mismatched substrates (strained thin films). Ceramic and thin film processing conditions, structural and dielectric properties in wide temperature and frequency ranges were investigated during this study.

One of the biggest functionally active material class is ternary metal oxides with perovskite or distorted perovskite structures. Nonmagnetic perovskites can undergo few phase transitions – ferroelectric (often related to displacement of B-site ion) and structural ones (related to rotation of oxygen octahedra), when soft mode condensates at different points of Brillouin Zone [I1]. Which one will dominate depends on so called "tolerance factor" t [I2, I3] which describes the relative filling of space by the compound forming ions.

Incipient ferroelectric $SrTiO_3$ (STO) is a model system for investigation of ferroelectric and structural phase transition because $t \approx 1$ [I1] this means both instabilities are competing in sufficiently close temperature ranges and both are rather sensitive to chemical and misfit strain.

Chemical strain can be induced by different homovalent and heterovalent ion substitution. Heterovalent Bi doped $SrTiO_3$ was used in this work, bismuth with oxidation state 3+ changes strontium with oxidation state 2+ in the perovskite A-site and to maintain overall charge neutrality there is introduced

Sr vacancies. Chemical strain in $SrTiO_3$ induces polar and antiferrodistortive nanoregion formation [I4] below Burns temperature [I5] and causes a complex dielectric relaxational dynamics below the phonon frequency range, which was investigated using broadband dielectric spectroscopy in Vilnius University.

Misfit strain was introduced to the system by depositing epitaxial $SrTiO_3$ thin films on the lattice mismatched substrates. Misfit strain effects on $SrTiO_3$ phase diagram were experimentally investigated, induced misfit strain enhances ferroelectric and antiferrodistortive phase transitions temperatures [I6, I7], making both transitions more accessible for characterization and more important for technologies and applications - ferroelectric phase transition enhanced above liquid nitrogen temperature and antiferrodistortive one above the room temperature. Pulsed laser deposition and structural characterization of thin films were done in EPFL.

To compare doped $SrTiO_3$ ceramic dielectric properties two similar disordered solid state systems was chosen − $(K_{0.5}Na_{0.5})(Nb_{1-x}Sb_x)O_3$ lead free ferroelectric material and $0.4Na_{0.5}Bi_{0.5}TiO_3$-$(0.6-x)SrTiO_3$-$xPtTiO_3$ disordered solid solution with tunable ferroelectric phase transition temperature by $SrTiO_3$ and $PtTiO_3$ quantities. Broadband dielectric spectroscopy and data analysis were done in Vilnius University.

The aim and tasks of the work

The aim of this thesis is investigation of chemical and misfit strain influences on phase transition temperatures and dielectric properties of $SrTiO_3$ and related perovskite ceramics and thin films.

The tasks of the dissertation are:

1. Investigate deposition conditions and deposit strain free and strained $SrTiO_3$ thin films with suitable electrodes on various substrates by pulsed laser deposition technique.

2.	Experimentally investigate misfit strain effects on $SrTiO_3$ phase diagram, structural and dielectric properties and observe ferroelectricity in antiferrodistortive domain boundaries by scanning probe microscopical techniques.

3.	Investigate chemical strain effects on dielectric properties in bismuth doped $SrTiO_3$ ceramics, antimony doped $(K_{0.5}Na_{0.5})NbO_3$ ceramics and $0.4Na_{0.5}Bi_{0.5}TiO_3$-$(0.6$-$x)SrTiO_3$-$xPtTiO_3$ solid solution by mean of broadband dielectric spectroscopy.

Scientific novelty

1.	Antiferrodistortive phase transition in epitaxially strained $SrTiO_3$ thin films was investigated for the first time above the room temperature by scanning probe microscopy. Ferroelectricity in the antiferrodistortive phase boundaries of strained $SrTiO_3$ thin films was not experimentally observed by piezoelectric force microscopy in 150 K – 370 K temperature range.

2.	For the first time dielectric properties of $(Sr_{1-1.5x}Bi_x)TiO_3$ $(x > 0.17)$, $(K_{0.5}Na_{0.5})(Nb_{x-1}Sb_x)O_3$ $(0.02 \leq x \leq 0.1)$ and $0.4Na_{0.5}Bi_{0.5}TiO_3$-$(0.6$-$x)SrTiO_3$-$xPtTiO_3$ $(0 \leq x \leq 0.25)$ ceramics were investigated in the wide frequency (10 mHz – 50 GHz) and temperature (25 K – 1000 K) ranges. Dielectric spectra were analysed and phase diagrams (where applicable) of these materials were depicted.

Statements presented for defence

1.	The strain induced in $SrTiO_3$ due epitaxial clamping by substrate or chemical doping leads to a fine tuning of polar and antiferrodistortive properties and changes of the phase transition temperature.

2.	Antiferrodistortive phase transition in compressively strained STO thin films occurs at higher temperatures than predicted by theoretical

calculations. Ferroelectricity is not observed in antiferrodistortive phase boundaries.

3. Variation of tolerance factor strongly influences antiferrodistortive and polar anomalies and phase transition temperatures of $A^{2+}B^{4+}O_3$ and $A^+B^{5+}O_3$ perovskite ceramics.

1.1. Articles published in the topic of dissertation.

1. **Grigalaitis R., Banys J., Bagdzevičius Š., Sternberg A., Bormanis K.** „Dielectric investigation of lead-free perovskite strontium titanate with 25% bismuth ceramics", Physica status solidi C : Current topics in solid state physics, 2009, vol. 6, iss. 12, p. 2743-2745, ISSN 1610-1634.

2. **Bagdzevičius Š., Banys J., Grigalaitis R., Bormanis K., Sternberg A.** „Dipolar glass-like perovskite $Sr_{0.8}Bi_{0.2}TiO_3$ ceramic", Ferroelectrics, 2010, vol. 400, p. 434-440, DOI: 10.1080/00150193.2010.506082.

3. **Bagdzevičius Š., Banys J., Grigalaitis R., Sternberg A, Bormanis K.** „Broadband dielectric investigation of sodium potassium niobate ceramic doped 8% of antimony", Ferroelectrics, 2012, vol. 428, p. 14–19, DOI: 10.1080/00150193.2012.675261.

4. **Svirskas Š., Ivanov M., Bagdzevičius Š., Dunce M., Antonova M., Birks E., Sternberg A., Brilingas A., Banys J.** „Dynamics of Phase Transition in 0.4NBT-0.4ST-0.2PT Solid Solution", Integrated Ferroelectrics, 2012, vol. 134, p. 81–87, DOI: 10.1080/10584587.2012.665300.

5. **Bagdzevičius Š., Grigalaitis R., Banys J., Sternberg A., Bormanis K.** „Dielectric investigation of sodium potassium niobate ceramic doped 7% of antimony", Solid State Ionics, 2012, vol. 225, p. 667–671, DOI: 10.1016/j.ssi.2012.03.024.

6. **Svirskas Š., Ivanov M., Bagdzevicius Š., Macutkevič J., Brilingas A., Banys J., Dec J., Miga S., Dunce M., Birks E., Antonova M., Sternberg A.** "Dielectric properties of $0.4Na_{0.5}Bi_{0.5}TiO_3$-(0.6-x)$SrTiO_3$-x$PbTiO_3$ solid solution", Acta Materialia, 2014, vol. 64, p. 123-132, DOI: 10.1016/j.actamat.2013.11.040.

Other publications

7. **Banys J., Bagdzevicius S., Kinka M., Samulionis V., Grigalaitis R., Castel E., Josse M., Maglione M.** „Dielectric Studies Of $Ba_2Pr_xNd_{1-x}FeNb_4O_{15}$ Ceramics", 2011 International Symposium on Applications of Ferroelectrics (ISAF/PFM) and 2011 International Symposium on Piezoresponse Force Microscopy and Nanoscale Phenomena in Polar Materials Proceedings, 2011, DOI: 10.1109/ISAF.2011.6013985.

8. **Kinka, M., Josse M., Castel E., Bagdzevicius S., Samulionis V., Grigalaitis R., Banys J., Maglione M.** „Coexistence of Ferroelectric and Relaxor States in $Ba_2Pr_xNd_{1-x}FeNb_4O_{15}$ Ceramics", IEEE TUFFC, 2012, vol. 59, issue 9, p. 1879-1882, DOI: 10.1109/TUFFC.2012.2400.

1.2.   Contributions to conferences.

1. Bagdzevičius Š., Grigalaitis R., Banys J., Bormanis K., Sternberg A. „Bešvinių $(1-x)SrTiO_3$-$(x)BiTiO_3$ keramikų elektriniai tyrimai", 38-oji Lietuvos nacionalinė fizikos konferencija: programa ir pranešimų tezės, Vilnius, Lithuania, p. 80, 8-10 of June (2009).

2. Grigalaitis R., Banys J., Bagdzevičius Š., Bormanis K., Sternberg A. „Dielectric investigation of lead-free perovskite strontium titanate with 25% bismuth ceramics", 15th semiconducting and insulating materials conference, Vilnius, Lithuania: programme and abstracts, p. 112, 15-19 of June (2009).

3. Banys J., Bagdzevičius Š., Grigalaitis R., Sternberg A., Bormanis K. „Dipolar glass-like dispersion of perovskite $0.8SrTiO_3$-$0.2BiTiO_3$ ceramics", 2nd seminar: Properties of ferroelectric and superionic systems = 2-й семінар : Властивості сегнетоелектричних і

суперіонних систем, Uzhhorod, Ukraine, p. 26, 19-20 of October (2009).

4. Banys J., Bagdzevičius Š., Grigalaitis R., Sternberg A., Bormanis K. „Broadband dielectric studies of perovskite (1-x)SrTiO$_3$-(X)BiTiO$_3$ ceramics", COST 539 action - ELENA : final workshop "Electroceramics from nanopowders produced by innovative methods": programme and book of extended abstracts, Aveiro, Portugal, p. 144-145, 28-30 of October (2009).

5. Banys J., Bagdzevičius Š., Grigalaitis R., Sternberg A., Bormanis K. „Broadband dielectric studies of perovskite 0.8SrTiO$_3$-0.2BiTiO$_3$ ceramics", ICE 2009 : international conference on electroceramics: abstracts, Delhi, India, p. 121-122, 13-17 of December (2009).

6. Bagdzevičius Š., Grigalaitis R., Banys J., Sternberg A., Bormanis K. „Broadband dielectric investigation of sodium potassium niobate with 10% antimony substitution", Functional materials and nanotechnologies (FM&NT-2010) : international conference: book of abstracts, Riga, Latvia, p. 107, 16-19 of March (2010).

7. Banys J., Bagdzevičius Š., Grigalaitis R., Sternberg A., Bormanis K. „Broadband dielectric studies of dipolar glass-like perovskite 0.75SrTiO$_3$-0.25BiTiO$_3$ ceramic", Electroceramics: the 12th international conference: abstracts book, Trondheim, Norway, p. 1, 13-16 of June (2010).

8. Bagdzevičius Š., Grigalaitis R., Banys J., Sternberg A., Bormanis K. „Broadband dielectric investigation of sodium potassium niobate ceramics with 8% antimony substitution", I Lithuanian-Ukrainian-Polish Meeting on Ferroelectrics Physics: Programme & Abstracts, Vilnius, Lietuva, p. 99, 12-16 of September (2010).

9. Bagdzevičius Š., Banys J., Grigalaitis R., Sternberg A., Bormanis K. „Broadband dielectric studies of dipolar glass-like bismuth doped SrTiO$_3$ ceramic", 3nd seminar: Properties of ferroelectric and

superionic systems = 3-й семінар : Властивості сегнетоелектричних і суперіонних систем, Uzhgorod, Ukraine, p. 14, 26-27 of November (2010).

10. Bagdzevičius Š., Grigalaitis R., Banys J., Sternberg A., Bormanis K. „Stibiu legiruotos natrio kalio niobato keramikos dielektriniai tyrimai", LMA jaunųjų mokslininkų konferencija - Fizinių ir Technologijos mokslų tarpdalykiniai tyrimai, Vilnius, Lietuva, p. 4, 8 of February (2011).

11. Bagdzevičius Š., Grigalaitis R., Banys J., Sternberg A., Bormanis K., Zauls V. „Dielectric Spectroscopy of 7 % Sb Doped $(K_{0.5}Na_{0.5})NbO_3$ Ceramic", Functional materials and nanotechnologies (FM&NT-2011): international conference: book of abstracts, Riga, Latvia, p. 212, 5-8 of April (2011).

12. Svirskas Š., Ivanov M., Bagdzevičius Š., Banys J., Dunce M., Antonova M., Birks E., Sternberg A., Zauls V. „Dielectric Properties of $0.4Na_{1/2}Bi_{1/2}TiO_3–(0.6-x)SrTiO_3–xPbTiO_3$ Solid Solutions", Functional materials and nanotechnologies (FM&NT-2011): international conference: book of abstracts, Riga, Latvia, p. 210, 5-8 of April (2011).

13. Bagdzevičius Š., Grigalaitis R., Banys J., Sternberg A., Bormanis K. „Broadband dielectric investigation of sodium potassium niobate ceramic doped 8% of antimony", 12th European Meeting on Ferroelectricity (EMF 2011): book of abstracts, Bordeaux, France, Program P3-14, 26 of June–1 of July (2011).

14. Svirskas Š., Ivanov M., Bagdzevičius Š., Banys J., Dunce M., Antonova M., Birks E., Sternberg A. „Broadband Dielectric Spectroscopy of $0.4Na_{1/2}Bi_{1/2}TiO_3–(0.6-x)SrTiO_3–xPbTiO_3$ Solid Solutions", 12th European Meeting on Ferroelectricity (EMF 2011): book of abstracts, Bordeaux, France, Program P3-26, 26 of June–1 of July (2011).

15. Bagdzevičius Š., Grigalaitis R., Banys J., Sternberg A., Bormanis K. „Dielectric investigation of sodium potassium niobate ceramic doped 7% of antimony", International Conference on Solid State Ionics (SSI-18th): Program of Poster Session II, Warszawa, Poland, p. 16 (P422), 3-8 of July (2011).

16. Grigalaitis R., Bdikin I., Kholkin A. L., Bagdzevicius S., Banys J., Tornau E. E., Sternberg A. and Bormanis K. "Local piezoelectricity in $SrTiO_3$-$BiTiO_3$ ceramics", The 20th IEEE International Symposium on Applications of Ferroelectrics and International Symposium on Piezoresponse Force Microscopy & Nanoscale Phenomena in Polar Materials (ISAF-2011-PFM): Program, Vancouver, Canada, p. 120, 24-27 of July (2011).

17. Svirskas Š., Ivanov M., Bagdzevičius Š., Banys J., Dunce M., Antonova M., Birks E., Sternberg A. „Investigation of $0.4Na_{1/2}Bi_{1/2}TiO_3$-$(0.6-x)SrTiO_3$-$xPbTiO_3$ solid solutions", International Symposium on Integrated Functionalities (ISIF 2011): Programme, Cambridge, England, p. 109, 31 of July – 4 of August (2011).

18. Bagdzevičius Š., Grigalaitis R., Banys J., Sternberg A., Bormanis K. „Dielektriniai stibiu legiruotos Natrio kalio niobato keramikos tyrimai", 39-oji Lietuvos nacionalinė fizikos konferencija (LNFK-39): Program, Vilnius, Lithuania, p. VI, 6-8 of October (2011).

19. Bagdzevičius Š., Kranauskaitė I., Grigalaitis R., Banys J., Sternberg A., Bormanis K. „Dielektriniai bismutu legiruotos Stroncio titanato keramikos tyrimai",39-oji Lietuvos nacionalinė fizikos konferencija (LNFK-39): Program, Vilnius, Lithuania, p. VI, 6-8 of October (2011).

20. Svirskas Š., Ivanov M., Bagdzevičius Š., Banys J., Dunce M., Antonova M., Birks E., Sternberg A. „Kietojo tirpalo $0.4Na_{1/2}Bi_{1/2}TiO_3$–$(0.6-x)SrTiO_3$-$xPbTiO_3$ plačiajuostė dielektrinė

spektroskopija",39-oji Lietuvos nacionalinė fizikos konferencija (LNFK-39): Program, Vilnius, Lithuania, p. VII, 6-8 of October (2011).

21. Bagdzevičius Š., Grigalaitis R., Banys J., Sternberg A., Bormanis K. „Broadband dielectric investigation of sodium potassium niobate ceramics with 8% antimony substitution", 10th international conference of Lithuanian chemists (CHEMISTRY 2011): book of abstract, Vilnius, Lithuania, p. 25, 14-15 of October (2011).

22. Bagdzevičius Š., Grigalaitis R., Banys J., Sternberg A., Bormanis K. „Dipolar glass-like perovskite $0.8SrTiO_3$-$0.2BiTiO_3$ ceramics",10th international conference of Lithuanian chemists (CHEMISTRY 2011): book of abstract, Vilnius, Lithuania, p. 26, 14-15 of October (2011).

23. Svirskas Š., Ivanov M., Bagdzevičius Š., Banys J., Dunce M., Antonova M., Birks E., Sternberg A., Zauls V. „Dielectric properties of $0.4Na_{1/2}Bi_{1/2}TiO_3$–$(0.6–x)SrTiO_3$-$xPbTiO_3$ solid solutions",10th international conference of Lithuanian chemists (CHEMISTRY 2011): book of abstract, Vilnius, Lithuania, p. 108, 14-15 of October (2011).

24. Bagdzevičius Š., Grigalaitis R., Banys J., Sternberg A., Bormanis K. „Broadband dielectric investigation of bismuth modified lead-free strontium titanate ceramic", 9th Students' Meeting and 2nd ESR COST MP0904 Workshop": book of abstracts, Novi Sad, Serbia, p. 133, 16-18 of November (2011).

25. Banys J., Bagdzevičius Š., Grigalaitis R., Sternberg A., Bormanis K. „Dielectric Investigation of Lead-Free $(K_{0.5}Na_{0.5})NbO_3$ Ceramic Doped 7% Sb", ICE2011 International Conference on Electroceramics: Abstract book, Sydney, Australia, 12-16 of December (2011).

26. Svirskas Š., Ivanov M., Bagdzevičius Š., Banys J., Dunce M., Antonova M., Birks E., Sternberg A. „Dynamics of phase transition in $0.4Na_{0.5}Bi_{0.5}TiO_3$-$(0.6-x)SrTiO_3$-$xPbTiO_3$ solid solutions", Open

Readings 2012 (55th Scientific Conference for Young Students of Physics and Natural Sciences):book of abstracts, Vilnius, Lithuania, p 102, 28-31 of March (2012).

27. Kranauskaitė I., Bagdzevičius Š., Grigalaitis R., Banys J., Stenbergs A., Bormanis K. „Dielectric studies of bismuth doped strontium titanate", Open Readings 2012 (55th Scientific Conference for Young Students of Physics and Natural Sciences):book of abstracts, Vilnius, Lithuania, p 143, 28-31 of March (2012).

28. Svirskas Š., Ivanov M., Bagdzevičius Š., Banys J., Dunce M., Antonova M., Birks E., Sternberg A. „Dynamics of Phase Transition in $0.4Na_{0.5}Bi_{0.5}TiO_3$-$(0.6-x)SrTiO_3$-$xPbTiO_3$ Solid Solutions", FM&NT 2012 (Functional materials and nanotechnologies): book of abstracts, Riga, Latvia, p. 140, 17-20 of April (2012).

29. Bagdzevičius Š., Grigalaitis R., Banys J., Sternberg A., Bormanis K. „Dielectric investigation of sodium potassium niobate ceramic doped 7% of antimony", The Third COST MP0904 WG Workshop „Advanced characterization and functional properties of ferroelectrics and multiferroics", Vilnius, Lietuva, P11, 23 of April (2012).

30. Svirskas Š., Ivanov M., Bagdzevičius Š., Banys J., Dunce M., Antonova M., Birks E., Sternberg A. „Dynamics of phase transition in $0.4Na_{0.5}Bi_{0.5}TiO_3$-$(0.6-x)SrTiO_3$-$xPbTiO_3$", The Third COST MP0904 WG Workshop „Advanced characterization and functional properties of ferroelectrics and multiferroics", Vilnius, Lietuva, P13, 23 of April (2012).

31. Svirskas Š., Ivanov M., Bagdzevičius Š., Banys J., Dunce M., Antonova M., Birks E., Sternberg A. "Dynamics of phase transition in $0.4Na_{0.5}Bi_{0.5}TiO_3$-$(0.6-x)SrTiO_3$-$xPbTiO_3$", XX Polish-Czech Seminar „Structural and ferroelectric phase transitions", Ustroń, Poland, 21-25 of May (2012).

32. Svirskas Š., Ivanov M., Bagdzevičius Š., Banys J., Dunce M., Antonova M., Birks E., Sternberg A. „Dielectric Dispersion and Phase Diagram of $0.4Na_{0.5}Bi_{0.5}TiO_3$-$(0.6-x)SrTiO_3$-$xPbTiO_3$ Ceramics", 11th ISFD and 11th RCBJSF Symposium (11th International Symposium on Ferroic Domains and Micro-to Nanoscopic Structures and 11th Russia/CIS/Baltic/Japan Symposium on Ferroelectricity): Abstract book, Ekaterinburg, Russia, p. 47, 20-24 of August (2012).

33. Svirskas Š., Ivanov M., Bagdzevičius Š., Banys J., Dunce M., Antonova M., Birks E., Sternberg A. „Distribution of relaxation times in $0.4Na_{0.5}Bi_{0.5}TiO_3$-$(0.6-x)SrTiO_3$-$xPbTiO_3$ solid solutions", 2nd Ukrainian–Polish–Lithuanian Meeting on Ferroelectrics Physics (UPL MFP-2), Lviv, Ukraine, 9-13 of September (2012).

34. Banys J., Bagdzevičius Š., Kranauskaitė I., Grigalaitis R., Sternberg A., Bormanis K. „Broadband dielectric studies of Bi doped in $SrTiO_3$ ceramics", 2nd Ukrainian–Polish–Lithuanian Meeting on Ferroelectrics Physics (UPL MFP-2), Lviv, Ukraine, 9-13 of September (2012).

35. Bagdzevičius Š., Banys J., Setter N. „PLD deposition and characterization of homoepitaxial $SrTiO_3$ thin films", COST MPO904 Action „SIMUFER" & IEEE-ROMSC 2012: Abstract book, Iasi, Romania, p. 76, 24-26 of September (2012).

36. Bagdzevičius Š., Banys J., Setter N. "PLD Deposition and Characterization of Heteroepitaxial $SrTiO_3$ Thin films", COST MPO904 Action "SIMUFER" Recent advances in ferro/piezoelectric and multiferroic-based composites: book of abstracts, Faenza, Italy, 22-23 of April (2013).

37. Kranauskaitė I., Ivanov M., Bagdzevičius Š., Bormanis K., Banys J. "Broadband dielectric investigation of $(Sr_{1-1.5x}Bi_x)TiO_3$ (x=0.15, 0.1, 0.05)", FM&NT 2013 (Functional materials and nanotechnologies): book of abstracts, Tartu, Estonia, 21-27 of April (2013).

21

38. Bagdzevičius Š., Banys J., Setter N. "SrTiO$_3$ heteroepitaksinių plonųjų sluoksnių impulsinis lazerinis nusodinimas ir charakterizavimas", 40-oji Lietuvos nacionalinė fizikos konferencija: book of abstract, Vilnius, Lithuania, 10-12 of June (2013).

39. Kranauskaitė I., Ivanov M., Bagdzevičius Š., Bormanis K., Banys J. "Plačiajuosčiai dielektriniai (Sr$_{1-1.5x}$Bi$_x$)TiO$_3$ (x=0.15, 0.1, 0.05) keramikų tyrimai", 40-oji Lietuvos nacionalinė fizikos konferencija: book of abstracts, Vilnius, Lithuania, 10-12 of June (2013).

40. Bagdzevičius Š., Banys J., Setter N. "PLD Deposition and Characterization of Compressively-Strained Heteroepitaxial SrTiO$_3$ Thin films", The Third ESR Workshop, COST MP0904: book of abstracts, Novi Sad, Serbia, p. 136, 6-9 of November (2013).

41. Š. Bagdzevičius, J. Banys, N. Setter "Pulsed laser deposition and characterization of compressively-strained SrTiO$_3$ thin films", European Conference on Application of Polar Dielectrics 2014: abstract book, Vilnius, Lithuania, p. 171, 7-11 of July (2014).

References

I1 Tagantsev A. K., Courtens E., Arzel L. *Phys. Rev. B*, 64, 224107 (2001).

I2 Goldschmidt, V. M. *Die Naturwissenschaften*, 21, 477 (1926).

I3 Parkin S., Kronmller H., Johnsson M., Lemmens P. "Handbook of magnetism and advanced magnetic materials", John Wiley & Sons, Hoboken, NJ, USA (2007).

I4 Porokhonskyy V., Pashkin A., Bovtun V., Petzelt J., Savinov M., Samoukhina P., Ostapchuk T., Pokorny J., Avdeev M., Kholkin A. and Vilarinho P., *Phys. Rev. B*, 69, 144104 (2004).

I5 Burns G., Dacol, F. H. *Solid State Commun.*, 48, 853 (1983).

I6 Pertsev N. A., Tagantsev A. K., Setter N. *Phys. Rev. B, Rapid Comm.*, 61, 825 (2000).

I7 Yamada T., Kiguchi T., Tagantsev A. K., Morioka H., Iijima T., Ohsumi H., Kimura S., Osada M., Setter N., Funakubo H. *Integrated Ferroelectrics*, 115, 57 (2010).

2. Literature review - state of the art.

2.1. Ferroic phase transitions.

In this chapter I will provide the state of the art information about ferroic phase transitions and ferroic materials studied in this thesis. Main concern is given to non-magnetic ferroic phase transitions and materials, particularly ferroelectrics, incipient ferroelectrics, ferroelastics and disordered solid state systems like ferroelectric relaxors or dipolar glasses. All materials studied are crystalline or polycrystalline - ceramics, so in the text I will speak about crystalline materials if not explicitly stated otherwise.

Speaking about structural phase transition we compare two phases with different crystal structures and symmetry relations between them. These relations and transformation of them sets how the phase transition progresses and what properties material can exhibit above and below phase transformation. At the lowest level there are two essentially different phase transitions – distortive and reconstructive transitions [A2].
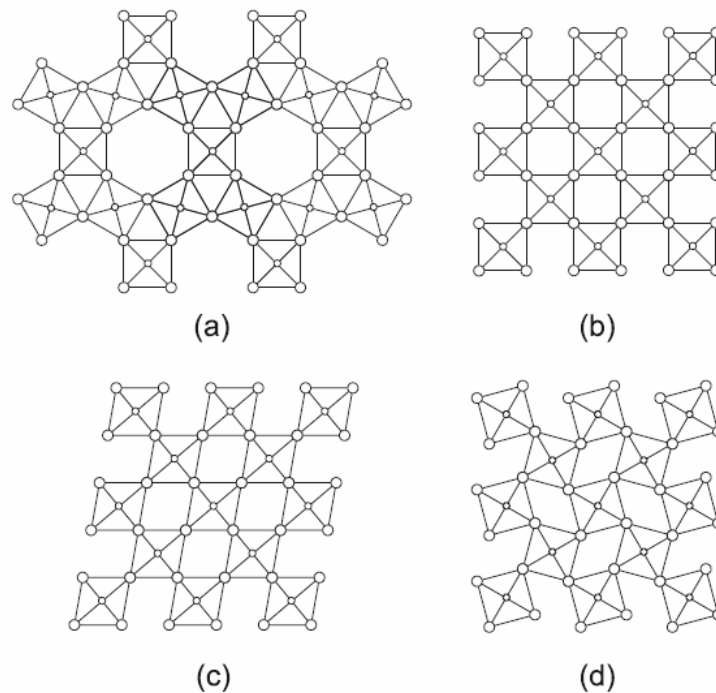

Fig. 2.1.1. Possible distortions of crystal structure, adapted from [A1].

Two phases has nothing in common except chemical composition if material exhibits reconstructive transition. It requires complete reconstruction of crystalline lattice – at least part of the chemical bonds is broken and rebuild after. Reconstructive transitions involve formation of dislocations and drastic changes at the transition temperature with large latent heat and thermal hysteresis; also in general have first-order character [A3]. Crystal structure distortions are schematically depicted in Fig. 2.1.1, transition from phase a) to any other one shown in b), c) or d) would illustrate reconstructive transition. Group–subgroup relation is not conserved between the symmetry of the phases during these transitions.

On the other hand there is distortive transition – chemical bonds are not broken and reconstructed. High symmetry structure S_G is systematically distorted until eventually goes into the lower symmetry structure S_F; this can be understood by looking at Fig. 2.1.1 c) and d), both structures can be obtained by slight changes of structure b). At the transition point crystal symmetry changes from point symmetry group G (one of 32 point groups) to the symmetry group F. For distortive phase transitions the group-subgroup relation holds, it means F should be a subgroup of G:

$$G \subset F. \hspace{3cm} 2.1$$

Speaking about the symmetry of the crystal we are always considering average ions positions, if the ions at the transition temperature perform small harmonic (strictly defining – quasiharmonic) oscillation around their average positions – transitions is classified as displacive. Lowering of the symmetry at transition point is caused by displacement of potential well bottoms, where ions oscillate. If ions perform thermally activated jumps between two equilibrium positions – transitions is called order-disorder type. In real materials both types of transitions and mixed behaviour is encountered. Any transition fulfilling 2.1 relation is called ferroic transition and lower symmetry phase is called ferroic phase.
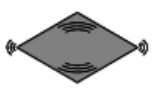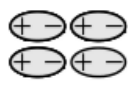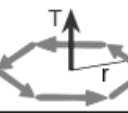
space / time	invariant	change
invariant	ferroelastic	ferroelectric
change	ferromagnetic	ferrotoroidic

Fig. 2.1.2. Time and space parity of primary ferroics, adapted from [A5].

There are four primary types of ferroic materials (Fig. 2.1.2): ferromagnetics – order parameter is spontaneous magnetization, ferroelectrics – spontaneous polarization, ferroelastics – spontaneous strain and maybe ferrotoroidics, which is not wide accepted phenomena, because it is hard to experimentally distinguish between ferrotoroidic and antiferromagnetic materials, both have no net magnetisation and order parameter temporal symmetry is the same (both are time variants).
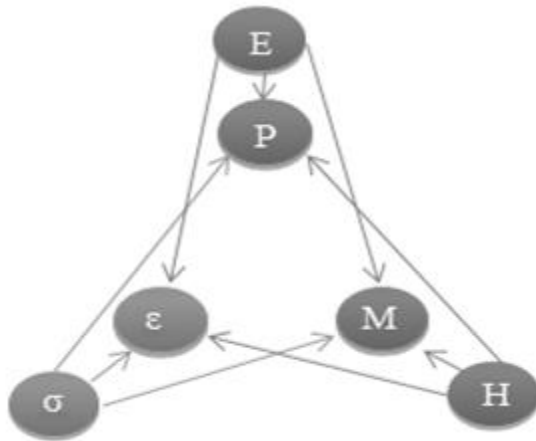
Fig. 2.1.3. Schematic illustration of ferroic and multiferoic interactions. The electric field E, magnetic field H, and stress σ control the electric polarization P, magnetization M, and strain ε, respectively. In a ferroic material, P, M, or ε is spontaneously formed. In a multiferroics, the coexistence of at least two ferroic forms of ordering leads to additional interactions.

Ferrotoroidics comes into account from thermodynamics considerations [A4], time and space symmetry properties of primary ferroics can be seen in Fig. 2.1.2. Widely accepted practice is to analyse just three of theoretically four ferroic materials as depicted in Fig. 2.1.3.

The most interesting materials for applications are those where two or more ferroic order is exhibited at the same temperatures, those materials are called multiferroics. In magnetolelectric phenomena

26

magnetisation can be changed by electric field and polarisation can be switched by magnetic stimulus. Similar phenomenon holds for the piezoelectrics – applied stress produce surface charges (changing polarisation) and applied electrical field induces deformations of the crystal, similar phenomena is observable in magnetoelastic materials also.

The first ferroic group discovered and the most widely investigated and found in applications is ferromagnetism [A6]. As ferromagnetic materials temperature is raised, it will finally reach the temperature at which thermal energy is sufficiently large to randomise magnetic dipoles direction and destroy net magnetisation, this is illustrated in Fig. 2.1.4.
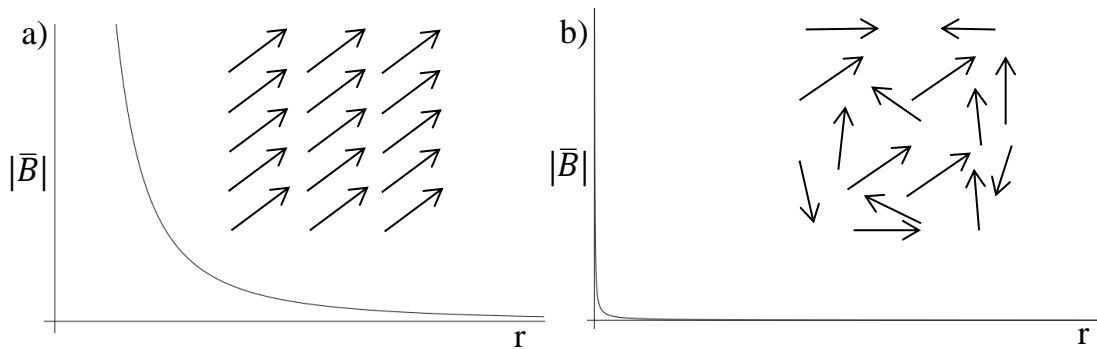
Fig. 2.1.4. Ordered array of magnetic dipoles a) and randomly aligned magnetic dipoles b).

This effect is called a phase transition and the temperature point at which it happens is called Curie temperature T_C. There are few necessary properties which ferromagnetic materials should exhibit: the ability to have magnetic moment in the absence of magnetic field, the possibility to form ordered arrays of magnetic dipoles – magnetic axe or axes and possibility to switch the direction or rotate these magnetic dipoles in response to external magnetic field.

Thermal destruction of ordered structures may occur also in ferroelectric and ferroelastic materials, the temperature is likewise called the ferroelectric Curie temperature and transition – ferroelectric phase transition (temperature of structural phase transitions in ferroelastics case). While magnetic moment is

27

a property that a single particle (for instance an electron) can have, the dielectric dipole (or multipole) requires at least two differently charged particles, therefore ferroelectricity is more complex phenomenon.

2.2. Ferroelectrics and incipient ferroelectrics.

2.2.1. Crystallographic considerations and basic definitions.

According to Neumann's principle [A7], any physical property of the crystal should possess the symmetry of the point symmetry group of the medium. It means that symmetry of the physical property should be at least as high as the symmetry of material. Thus if physical parameter is subjected to a symmetry operation of the crystal, the value of this parameter should remain the same as before, other way such property is absent in the material.

There are 32 point groups (Fig. 2.2.1) in 7 crystal systems, 11 of them possess center of symmetry, from the left 21 all except one are non-centrosymetric and exhibit linear electromechanical effect – piezoelectricity. Applied mechanical stress or electrical field may polarize piezoelectric material. Crystals belonging to the ten of the twenty non centrosymmetric crystal classes have a unique polar axis and are polar – possess spontaneous polarization.
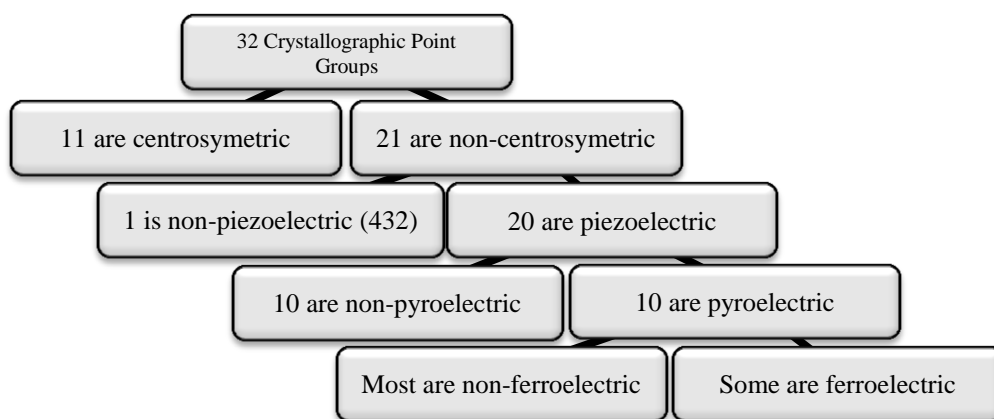
Fig. 2.2.1. Hierarchical classification of crystalline materials according to crystallographic point groups.

28

In general polarization is temperature dependent property – temperature changes will induce polarization, charges will be accumulated on the surfaces and effect could be observed by flowing charges – pyroelectric current. This effect is called pyroelectricity and crystals – pyroelectrics. Several materials in pyroelectric crystal class possess electric field reorientable polarization – these materials are called ferroelectrics.

The macroscopic polarization for any finite size system is straightforwardly defined as the dipole moment per unit volume of the system of charges in the material:

$$P = \frac{1}{v_{uc}} \sum_i e_i r_i; \qquad\qquad 2.2$$

P – polarization as in *Maxwell* equations, v_{ac} – unite cell volume, e_i – charge and r_i – radius vector. Summation is over all charges in the elementary unite cell of the crystal.

For any infinite structure (as it is always considered in phenomenological theories) it is possible to calculate the average dipole moment density, but the result will depend on the way in which the part was chosen (see Fig. 2.2.2), it means the result will not represent a bulk property of the material.
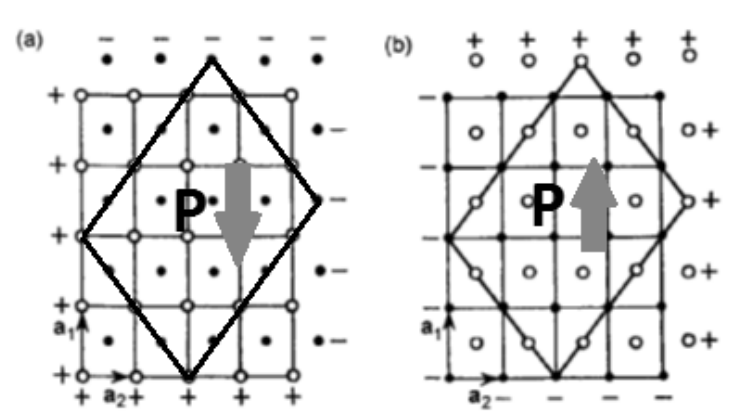
Fig. 2.2.2. Disambiguousness in choosing electroneutral element of the crystal lattices for polarization description, adapted from [A8].

To overcome this disambiguate one should use variation of the dipole moment density resulting from small change of the charge positions in the

29

lattice. Consequently any strict definition of the ferroelectric phase transition should deal with the change of polarization and not with polarization itself. For instance one could use a pyroelectric effect to define spontaneous polarization:

$$p_i = \left(\frac{\partial P_i}{\partial T}\right)_{E=0}; \qquad 2.3$$

pyroelectric coefficient p is a polar vector defined as the derivative of the polarization with respect to temperature at zero electric field. A phase transition is called ferroelectric if it results in a lower symmetry phase in which the vector of pyroelectric coefficient acquires new components which were zero, by the symmetry, in the high-symmetry phase [A1]. And spontaneous polarization in this case could be defined as:

$$P_s(T_f) = \int_{T_p}^{T_f} p(T)dt . \qquad 2.4$$

It means at given temperature in the ferroelectric phase we define spontaneous polarization as the change of polarization during cooling from a temperature in the paraelectric phase. The most "modern theory of polarization" is to define it as an integrated current through a transformation from one structural variant above phase transition to another, the result being expressed as a Berry phase [A8].
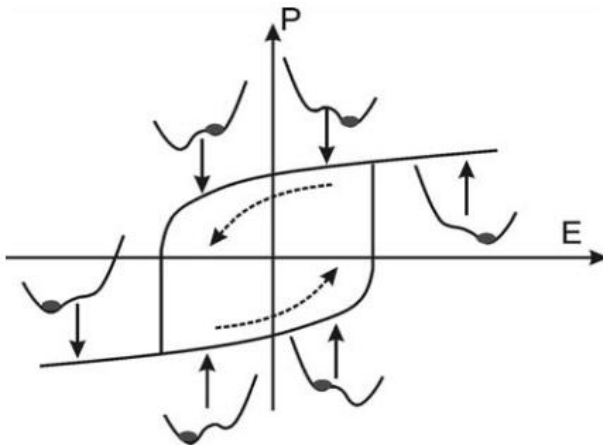
Fig. 2.2.3. Ferroelectric hysteresis loop in an idealized ferroelectric [A8, A9].

A ferroelectric material exhibits dipolar moment even in the absence of external electric fields. Ferroelectrics exhibits nonlinear, electric field depending polarization which shows hysteretic behavior as presented in Fig. 2.2.3, ordinary, non-leaky linear dielectric does not show significant hysteresis.

In the ferroelectrics below T_c there are at least two free energy minimums corresponding to two spatially differently oriented spontaneous polarizations. Changing electric field will eventually switch the polarization from one minima to another. The key properties found from hysteresis loop measurements are the remnant polarization P_R at zero applied field, and the coercive field E_C necessary to induce switching (reversal of polarization).

The ferroelectricity (spontaneous polarization) usually appears at certain temperature, called the Curie temperature. Phase above this temperature is called paraelectric, there is no spontaneous polarization in paraelectric state, and few ferroelectric materials don't have Curie temperature, because they melt before reaching this temperature. Another extrema is incipient ferroelectrics, where extrapolated phase transition temperature becomes lower than absolute zero due to the ferroelectric soft mode interaction with quantum fluctuations at very low temperatures. Ferroelectric phase transitions (and ferroelectric materials) as ferroic transitions can also be classified into two types – displacive and order-disorder. In displacive ferroelectrics spontaneous polarization below T_c appears in relation with spontaneous polar displacements of ions in one or more sublattices. In order-disorder case spontaneous polarization appears as a consequence of orientation of dipoles in one polar direction.

2.2.2. Soft mode in ferroic crystals.

Phase transition itself and its character can be defined in terms of soft modes – the dynamic of the lowest frequency optical phonon mode. If the soft mode can propagate in the material at the transition – transition is called displacive, and if the soft mode is strongly diffusive (doesn't propagate) – transition is called order-disorder [A10]. In this case there is no phonon at all, only large amplitude ion hopping motion between two or more potential wells.

Above absolute zero temperature atoms in crystals vibrate around their equilibrium positions. In the crystalline materials these collective motions can be approximated by quasi particles - phonons - lattice waves propagating in crystals with certain wavelengths and frequencies. In the lattice with one atom per primitive basis there are three phonon modes with different frequencies – one longitudinal and two transverse branches. In those crystals only acoustic phonons are possible and they have elastic nature. In the long wavelength limit the sound velocity gives the wavelength of the phonons, no coupling with electromagnetic waves is possible, because $v_{sound} \ll c$; $q_{acoustic} \gg q_{light}$.

The phonon dispersion relation shows new features in crystals with more than one atom per primitive basis. Two phonon branches develops – acoustic longitudinal LA, transverse TA and optical longitudinal LO, transverse TO. Ions moving in opposite directions in TO modes create dipolar moments which couples to electromagnetic radiation [A11]. The softening of the TO mode is caused by interplay of the lack of restoring force (elastic, short range force) at the transition temperature and long range electric fields. At the transition crystal structure becomes unstable in comparison to one of these phonon modes and freezes at the new equilibrium position. If the soft mode frequency completely vanishes (during second order phase transition) at Brillouin zone center – ferroelectric phase transition takes place with development of spontaneous polarization. If this softening happens at the corner of Brillouin zone – we will face antiferrodistortive phase transition as in bulk $SrTiO_3$ at 105 K transition [A12]. Antiferrodistortive soft mode in $SrTiO_3$ could be an example of complete mode softening and splitting below phase transition (unite cell doubling) at Brillouin zone boundary, as shown in Fig. 2.2.4.

There is linear relation between squared mode frequency and temperature called Cochran law:

$$\omega_{TO}^2 = \gamma |T - T_C| . \qquad\qquad 2.5$$

This law relates mode frequency to the phase transition temperature [A13].
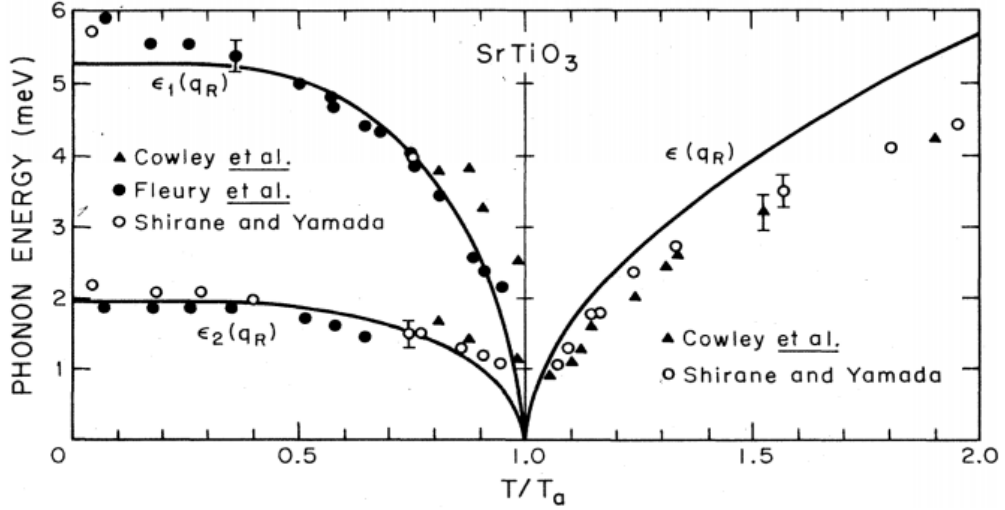
Fig. 2.2.4. Experimental data showing the lowering of soft antiferrodistortive mode in $SrTiO_3$ [A12].

Lyddane-Sachs-Teller model relates higher frequency modes to low frequency dielectric permittivity [A14] i.e. soft mode impact to static dielectric permittivity:

$$\frac{\varepsilon_0}{\varepsilon_\infty} = \prod_{j=1}^{n} \frac{\omega_{LOj}^2}{\omega_{TOj}^2} \quad . \qquad\qquad 2.6$$

At phase transition temperature mode frequency decreases to zero, consequently static dielectric permittivity increases to infinity (in the second order phase transitions).

2.2.3. Incipient ferroelectrics.

There is a subgroup of ferroelectrics, where softening of polar phonon mode is also observable, but there is no ferroelectric phase transition. Such materials (like $CaTiO_3$, $KTaO_3$ and $SrTiO_3$) are called incipient ferroelectrics.

The soft mode frequency at high temperatures follows the Cochran law like in usual ferroelectric in the paraelectric phase (Fig. 2.2.5), but ferroelectric phase is never reached, because the ferroelectric phase transition temperature is either virtually below 0 K (as in $CaTiO_3$ and $KTaO_3$) or quantum fluctuations prevents the appearance of the FE order (as in $SrTiO_3$).

SrTiO$_3$ should be called quantum paraelectric [A15], a subset of incipient ferroelectrics. In such materials quantum fluctuations prevents complete mode softening, dielectric susceptibility starts to deviate from Curie-Weiss law.

Dielectric susceptibility saturates at low temperatures in agreement with Barrett model [A15, A16] which models the lattice dynamics of the incipient ferroelectric with a system of identical oscillators:

$$\varepsilon = \frac{A_B}{\frac{1}{2}T_B\left[\coth\left(\frac{T_B}{2T}\right)-\frac{2T_0}{T_B}\right]} , 2.7$$

T_B is a crossover temperature below which the quantum fluctuations starts to play significant role, above this temperature classical approximation and a Curie-Weiss law are suitable. T_0 marks extrapolated (in some case hypothetical) temperature from Curie-Weiss law. Barrett's model is one of the few theoretical models constructed to explain soft mode behavior in incipient ferroelectrics [A17-19], for example another one is Vendic model described in [A20]. This model describes the lattice dynamics of the incipient ferroelectric with a system of spatially coupled oscillators and permittivity is expressed as:

$$\varepsilon = \frac{A_V}{T_V\left[\sqrt{\frac{1}{16}+\left(\frac{T}{T_V}\right)^2}-\frac{T_0}{T_V}\right]} , \qquad 2.8$$

T_V is a temperature at which the quantum fluctuations start to play significant role as in Barrett model.

Fig. 2.2.5. Incomplete phonon mode softening in quantum paraelectric Adapted from [A15].

Incipient ferroelectrics exhibit very high (tens of thousands) and temperature independent dielectric permittivity at low temperatures and in general has low microwave losses (no microwave dielectric dispersion [A21]) (Fig. 2.2.6) depending on the quality of materials and electric field strength and frequencies [A21].

Incipient ferroelectric is low loss material because its symmetry (centrosymetric materials) allows only three- and four-quantum mechanism contribution to dielectric losses [A22]. Imaginary part of dielectric permittivity can be described by power laws:

$$\varepsilon'' \propto \omega^n T^m, \qquad 2.9$$

where n=1-5 and m=1-9 [A22].

Lack of center of symmetry can be induced by electric field (very important in tunable materials) or other symmetry braking stimulus like uniaxial stress or chemical doping. In such cases one will deal also with field-induced quasi-Debye loss mechanism:

Fig. 2.2.6. Temperature dependence of the loss tangent in SrTiO$_3$ crystal. Dots – experimental data [A23], curve - prediction of the phonon theory $tan\delta \propto \omega T^2 \varepsilon^{1.5}$ [A24].

$$tan\delta_{QD}(E_0) = A\omega I(E_0)n_r, \qquad 2.10$$

where the function I (E_0) → 1 in the limit of small relative tunability, it means $n_r = \frac{\varepsilon(0)-\varepsilon(E_0)}{\varepsilon(0)} \ll 1$. Quasi-Debye dielectric losses can be higher by few orders of magnitude in comparison with three- and four-quantum mechanisms [A25]. There are also extrinsic contribution to losses like loss owing to charged defects generating acoustic waves at the frequencies of the applied field [A26],

impact of local polar regions like grain boundaries induced polar phase in $SrTiO_3$ ceramic [A27].

2.3. Relaxors, dipolar glasses and disordered materials.

2.3.1. Relaxor ferroelectrics.

Relaxor ferroelectrics (FR for short) are crystalline (or polycrystalline) materials having extraordinary properties like very broad dielectric relaxational dispersion (thereof title "relaxors"), very high dielectric permittivity, high piezoelectric properties comparable even to PZT [A28].

At high temperatures FR are in non-polar paraelectric phase (PE), which is indistinguishable from ordinary ferroelectric PE (valid Curie-Weiss law). During cooling they transform to ergodic relaxor (ER) state in which appears nanometric size polar regions (PNRs) with randomly distributed directions of the dipole moments. This transformation occurs at the Burns temperature T_B [I5]. Though this transformation is not structural, because there is no change of crystal structure (symmetry) at the macroscopic and mesoscopic scales, still PNRs drastically affect crystal properties and for this reason the state below T_B is considered as a new one, different from PE. In the vicinity of T_B the PNRs are mobile (can be reoriented) therefore the state is called ergodic [A29]. On cooling down further their dynamics slows down and at low temperatures T_F (usually few hundred K below T_B) PNR becomes frozen or at least their dynamic critically slows down. FR enters nonergodic (NR) state but macroscopic average structure remains centrosymetric cubic. Similar behavior is encountered in another disordered phase called dipole glass or spin glass phase. The transition to NR phase is manifested in the dielectric constant with characteristic very broad dispersion. Permittivity maximum (at temperature T_m) is the same order of magnitude as in the ordinary ferroelectric perovskites (displacive transition), but in contrast to FE, its maximum is diffused and shifts

to higher temperatures on measurement frequency increase as depicted in Fig. 2.3.1 a).

The nonergodic phase can be transformed to FE phase by strong enough external electric field. This feature distinguished FR from dipolar glasses. In many relaxors transformation to FE phase occurs spontaneously at T_C, hence nonergodic phase doesn't exist at all (Fig. 2.3.1 b), c) and d)).
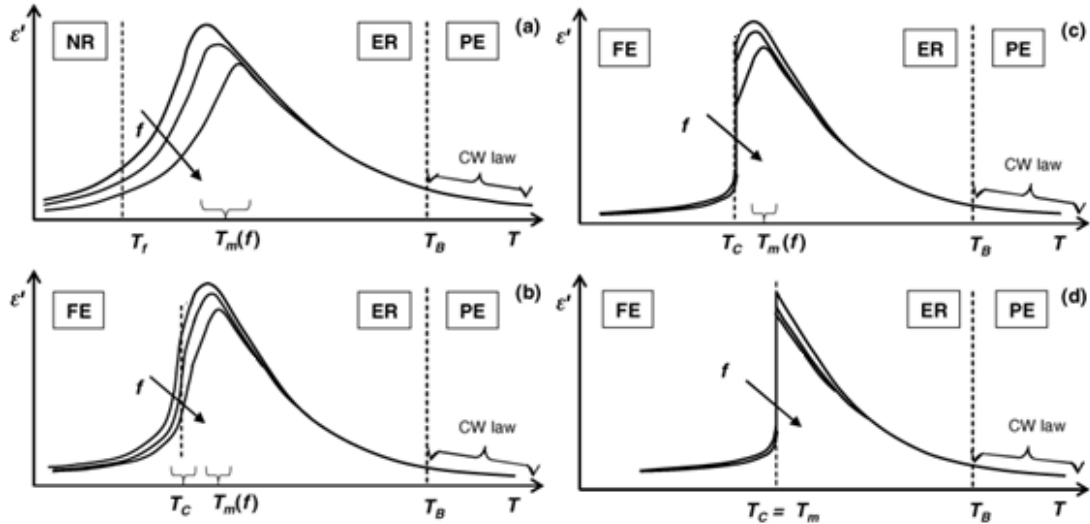
Fig. 2.3.1. Different possibilities for the temperature evolution of structure and dielectric properties in compositionally disordered ferroelectric relaxors, adapted from [A29].

Compositional disorder is a common feature of FR. The phenomenon was first observed in slightly distorted perovskites, where chemical or charge (nonstoichiometric materials) disorder exists. Canonical FR is considered lead based perovskite materials like $Pb(Mg_{1/3}Nb_{2/3})O_3$ (PMN) [A30], $Pb(Sc_{1/2}Ta_{1/2})O_3$ (PST) [A31], $Pb(Sc_{1/2}Nb_{1/2})O_3$ (PSN), $Pb(Zn_{1/3}Nb_{2/3})O_3$ (PZN) or their solid solution with lead titanate - PMN-PT, PZN-PT. Energetically most favorable ground state should be compositionally ordered e.g. in the $A(B'_{1/2}B''_{1/2})O_3$ each type of B-site ions should be located in its own sublatice, crystal should exhibit superstructure with complete translational symmetry [A29].

Thermal motion is capable to destroy such ordering at certain pretty high temperatures (for example ~1500 K for perovskite PST and PSN [A32]) – material is transformed into compositionally disordered state similar to the long ago observed one in many metallic alloys. Quick cooling – quenching – from such disordered state to room temperatures (in general below T_B) preserves metastable state with compositional disorder; heat treatment below T_B cannot vary chemical order in reasonable time scale. The degree of compositional disorder can greatly influence the FE properties. For example, the disordered $Pb(In_{1/2}Nb_{1/2})O_3$ (PIN) crystals are relaxor ferroelectrics, but in the ordered state, they are antiferroelectrics with a sharp phase transition [A33, A34], confirming the general rule that the relaxor behaviour can only be observed in disordered crystals [A29]. Nowadays there are a lot of experimental, indirect (Fig. 2.3.2) and direct (Fig. 2.3.3), evidence of PNR existence.

One of the first experimental indirect evidences came from the temperature dependences of the optic index of refraction (n) which appear to be linear at $T > T_B$ (shown in Fig. 2.3.2). At lower temperatures a deviation from linearity was observed which was attributed to the variation of n induced (via quadratic electrooptic effect) by local spontaneous polarization inside the PNRs [I5]. Later existence of PNRs was confirmed by X-ray and elastic diffuse neutron scattering

Fig 2.3.2. Schematical typical temperature dependences of the refractive index (n), unit cell volume (V), reciprocal dielectric permittivity ($1/\varepsilon$) and birefringence (Δn) in the canonical relaxor [A29].

38

experiments [A36-39]. Diffuse scattering found in synchrotron X-Ray experiments [A39] below T_B reassembles scattering caused by FE critical fluctuations, but at the same time have significant differences, which allows concluding that PNRs are more compact and have better defined borders than FE critical fluctuations [A39]. Subsequently with improvements in scanning probe microscopy techniques, especially piezoelectric force microscopy, PNRs were directly imaged in relaxor ferroelectrics (shown in 2.3.3 b), c) and d)).
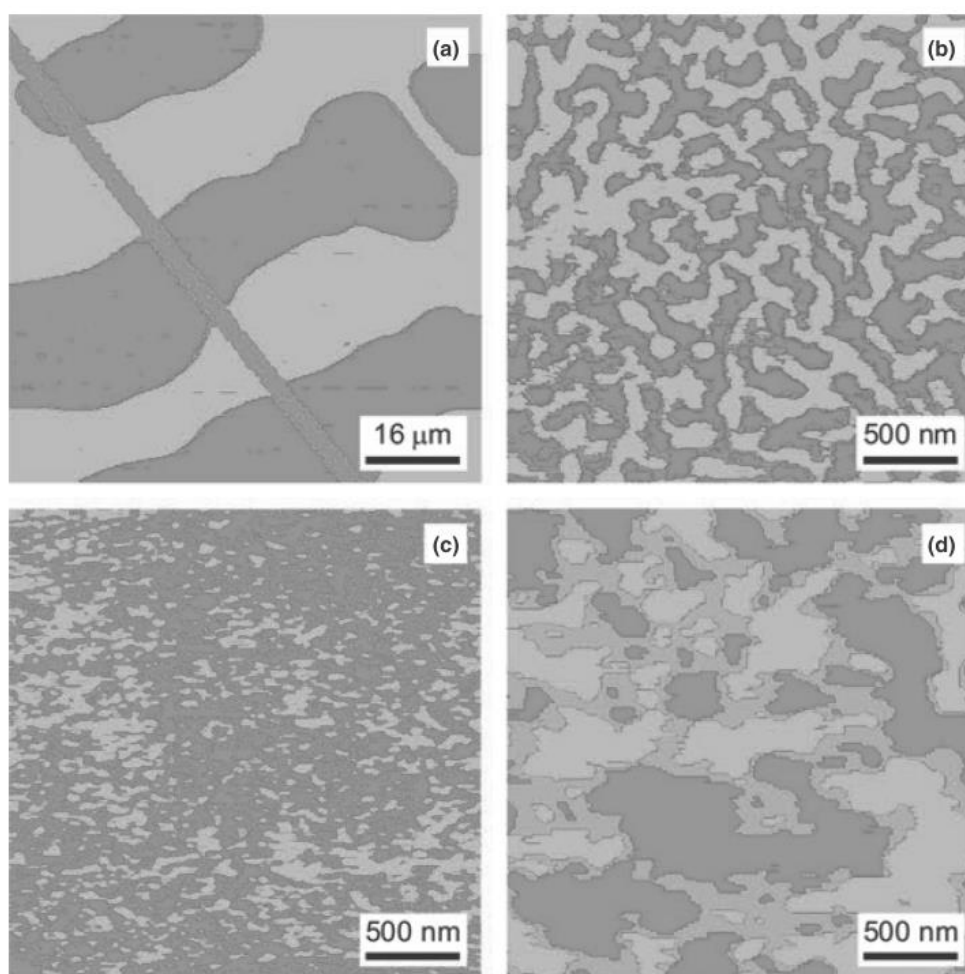
Fig. 2.3.3. 180° and 90° domains in a ferroelectric PbTiO$_3$ single crystal at RT a); polar structures in a relaxor PLZT ceramic below the transition temperature b); polar nanoregions in a relaxor SBN single crystal above the transition temperature c) polar nanoregions in a BaTi$_{0.85}$Sn$_{0.15}$O$_3$ ceramic above the transition temperature d). Polar structures were observed by PFM. Light and dark grey colors correspond to polarization oriented up and down, respectively. [A35].

From the lattice dynamic point of view FR in the PE phase is analogous to displacive ferroelectrics. For example in PMN far above T_B the dispersion of the transverse acoustic (TA) and lowest energy TO phonons were found to be very similar to that existing in the PE phase of classical displacive ferroelectric $PbTiO_3$ [A37]. On cooling down to $T \approx T_B$, the optic branch softens in the same manner as in displacive ferroelectrics, i.e., the frequency of the mode at wave vector $q = 0$ follows the Cochran law. In the temperature range between T_f and T_B, the lattice dynamics is different from one observable in the ferroelectrics. The propagating TO modes are observed here only for the wave vectors larger than q_{wf}. For $q<q_{wf}$, the modes are over damped. The TO phonon branch drops sharply into the TA branch at q_{wf} [A40], resembling a waterfall - the phenomenon is called "waterfall". Some authors [A41, A42] explain such behaviour in relation with PNRs size. Large damping of TO modes is due to the presence of PNRs which prevent the propagation of phonons with wavelength larger than the size of PNR. Another group [A43] proved that q_{wf} depends on the choice of the Brillouin zone and the damping related to PNR size is incorrect concept. In their opinion the waterfall effect was explained by the interactions of acoustic and optic branches, additionally similar effect can be observed in usual ferroelectrics [A43].

Dielectric response to small, harmonic signal has been studied in almost all FR materials, but lots investigations swept narrow frequency from Hz to few MHz range. Nowadays it is evident that dielectric dispersion in RF exists in the whole accessible frequency spectrum from the phonon frequencies to the lowest measurable frequencies (10^{-5} Hz). Polarization in RF can be divided to several parts:

$$\varepsilon = 1 + \chi_e + \chi_{Ph} + \chi_{CR} + \chi_{UR} + \chi_{LF}, \qquad 2.11$$

χ_e is determined by optical polarization mechanism, observable in all materials due to electronic polarization at very high frequencies (optical frequencies). Electronic contribution in FR persists at all temperatures, but its contribution to

40

static susceptibility at T_m (as shown in Fig. 2.1.14 region 1) is negligible small $\chi'_e = (n^2 - 1) \sim 10$ in comparison with maximum value (usually up to 10^4 at T_m).

Polar soft mode behaviour in PE phase is modified and maximum contribution to static permittivity is observed not at Tc (as in usual ferroelectrics respectively to LST relationship [A14]) but at T_B (shown in Fig. 2.3.4 region 2), where PNR starts to emerge. Below T_B Curie-Weiss law is no more valid and modified version is necessary to describe dielectric permittivity [A45]. At T_m soft mode – phonon - contribution χ_{Ph} is no more dominant as in usual ferroelectrics.
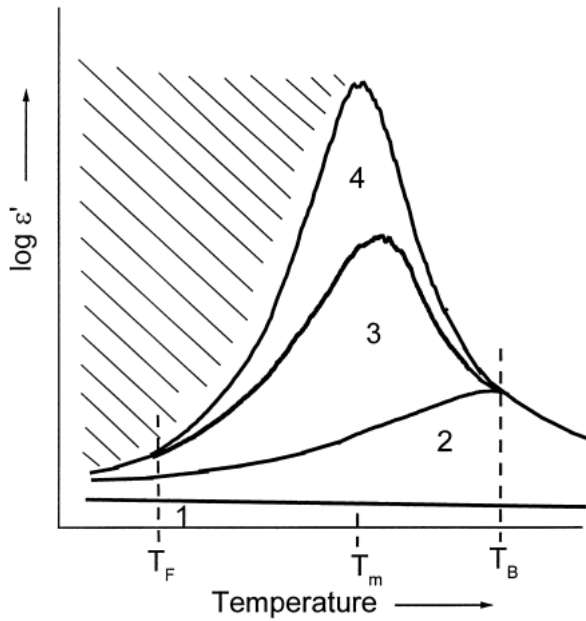
Fig. 2.3.4. Structure of the dielectric permittivity spectrum of relaxor ferroelectric, adapted from [A44].

Contributions due to dipole reversal and change of polar cluster size - "breathing" – are observed in wide temperature range below T_B. χ_{UR} ("universal relaxation" [A29]) is more prominent at temperatures between T_B and T_m, both real and imaginary parts of χ_{UR} continuously decrease according to the power law [A29] (depicted in Fig. 2.3.1 a)):

$$\chi'_{UR} = \tan(\frac{n\pi}{2})\chi''_{UR} \propto f^{n-1} \qquad 2.12$$

n is close but smaller than 1. This dispersion might be linked to MW dispersion discerned in [A44] due to fluctuations of the PNR boundaries (Fig. 2.1.14 region 3), this mechanism gives the contribution above and below T_F. In contrast another dispersion (χ_{CR} contribution, "conventional relaxation" [A29])

41

is absent below T_F and is assumed due to flipping (reversal) of polar clusters (Fig. 2.3.4 region 4).

The last term χ_{LF} (low frequency term) in 2.11 equation (also depicted as shaded area in Fig. 2.1.14) represents all possible not related to relaxor ferroelectricity contributions like hopping charge carriers, Maxwell-Wagner relaxation, ionic and electronic conductivity at high temperatures etc. This term gives impact only at ultra-low frequencies (10^{-2} Hz and lower) or high temperatures.

The dynamics of PNRs generally provides two additional polarization mechanisms and also modifies phonon contribution to dielectric relaxation spectra, which can be described by modified Curie-Weiss law [A45], with additional (diffusive) exponent γ, ranging from 1 (normal ferroelectric) to 2 (ideal FR):

$$\frac{1}{\varepsilon} - \frac{1}{\varepsilon_m} = \frac{(T-T_m)^\gamma}{C}, \qquad 2.13$$

ε_m dielectric permittivity maximum value. Another modification described in [A46] relates order parameter $q(T)$ with PNR fraction effectively frozen (noncontributing to dispersion) at particular time t and temperature T:

$$\varepsilon(T) = \frac{C(1-q(T))}{T-T_{CW}(1-q(T))}. \qquad 2.14$$

When $T>T_B$, $q(T) \rightarrow 0$ and formula 2.14 become equivalent to classical Curie-Weiss formulation.

Another difference from usual ferroelectrics is validity of Vogel-Fulcher relation (instead of Arrhenius relationship) for the characteristic relaxation time τ of the corresponding relaxation process:

$$\tau = \tau_0 exp\left(\frac{E_a}{k_B(T-T_{VF})}\right), \qquad 2.15$$

where τ_0 represents attempt relaxation time, E_a - activation energy and T_{VF} – freezing temperature. Although there is another conclusions [A47] that Vogel-Fulcher-type relationship can be obtained without implying freezing in the system at T_{VF} temperature. Tagantsev in [A47] showed that VF relation in FR can be direct consequence of gradual broadening (on the logarithmic scale) of the spectrum with decreasing temperature.

Most apparent differences between ferroelectric relaxors and usual ferroelectric materials can be summarizes as follows:

Ferroelectric hysteresis loop is almost square shaped (schematically depicted in Fig. 2.3.5 a)), possess large remnant polarization (P_R) due to switching of macroscopic polarization domains. In relaxor ferroelectrics hysteresis loops are slim (Fig. 2.3.5 b)) and develops only way below T_m temperatures. Such behaviour indicates that long range ordering of polar entities needs much higher fields, while in low field regime polarization strongly decays, due to natural thermal randomization of dipoles, this manifests in small remnant polarization.

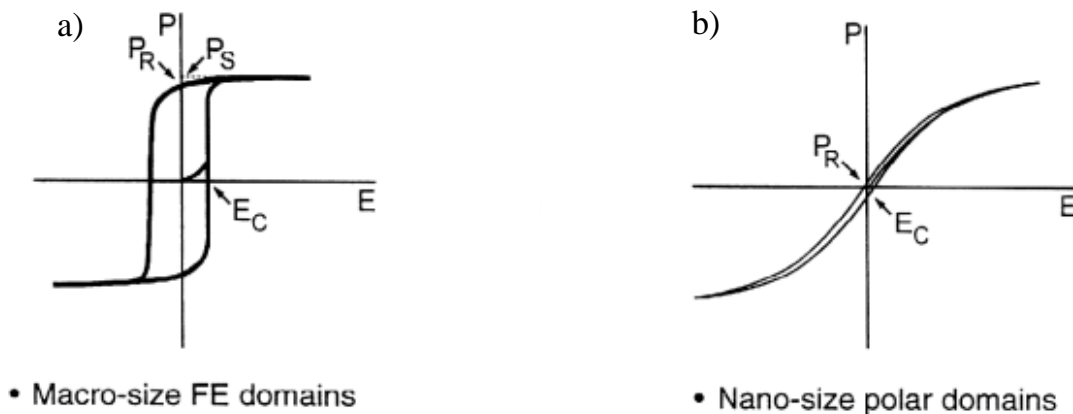• Macro-size FE domains   • Nano-size polar domains

Fig. 2.3.5. Usual ferroelectric a) and relaxor ferroelectric material b) hysteresis loops, adapted from [G4].

Polarization of ferroelectrics decrease and vanish at phase transition temperature T_C (schematically depicted in Fig. 2.3.6 a)), there is no polarization

43

above T_C. In the FR case (depicted in Fig. 2.3.6 b)), there is no abrupt change of polarization neither at T_m or T_F temperatures.
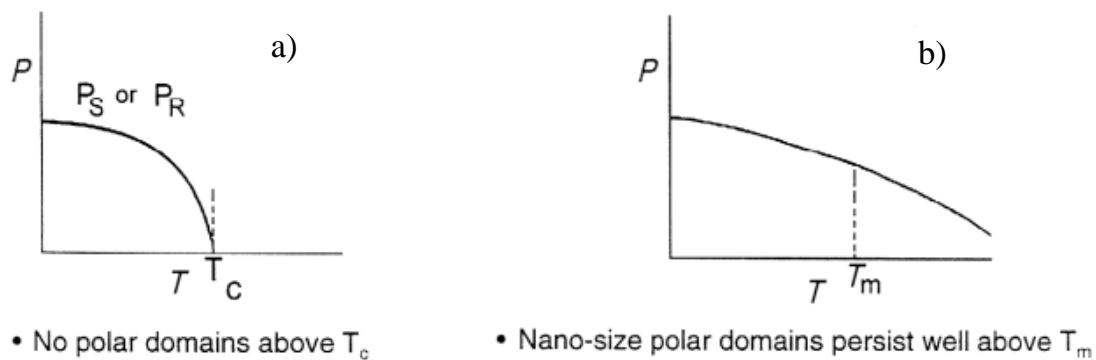

Fig. 2.3.6. Spontaneous polarization in normal ferroelectrics and RF.
Adapted from [G4].

Static dielectric permittivity at the ferroelectric phase transitions T_C demonstrate sharp and narrow peak. In contrast FR exhibits very broad and temperature depending ε peak maximum with strong frequency dispersion (Fig. 2.3.1). Dielectric permittivity in FE obeys Curie-Weiss law above and below phase transition temperature, while in FR strongly deviates from Curie-Weiss behaviour and coincides just above T_B.

2.3.2. Dipolar glasses.

Dipolar (quadrupole, octupole – orientational glasses in general) glasses are crystalline materials with built in random fields due to randomly substituted impurity ions that carry dipolar moment and are located in random (irregular) lattice sites (random bonds). In analogy to magnetic spin glasses [A48], due to local fields and bonds spread at various crystal sites, dipole moments gets frozen (cannot be reoriented by electric fields at reasonable time scale) into random orientations without long range FE order. On cooling down crystals are transformed into low-temperature glassy state (according to dielectric, elastic properties), but stays crystalline from crystallographic point of view – there is no macroscopic structural phase transition. Freezing in the system is manifested by diverging dipolar relaxation time at T_{VF} according to

Vogel-Fulcher equation. In dipole glasses the interactions among the dipoles are the cause for such kind of freezing, they are frustrated (i.e. can be either ferroelectric or antiferroelectric, but cannot be both at the same time) and thus favor the configurations with random directions of dipoles, in contrast to the ferroelectrics and antiferroelectrics in which the dipole directions are parallel and antiparallel, respectively [A29].
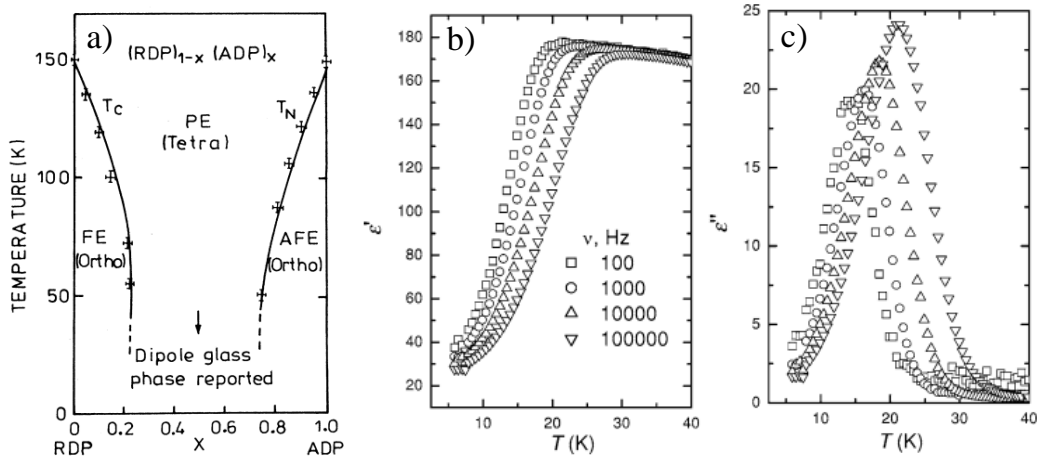
Fig. 2.3.7. Phase diagram of $RDP_{1-x}ADP_x$ a) [A50] and characteristic dipolar glass dielectric dispersion at low temperatures of $BP_{1-x}BPI_x$ b) and c) [A52].

Established examples are the mixture of ferroelectric and antiferroelectric materials – $RDP_{1-x}ADP_x$ [A49-50] (rubidium dihydrogen phosphate with ammonium dihydrogen phosphate) and $BP_{1-x}BPI_x$ (betaine phosphate with betaine phosphite) [A51-52]. Depending on the ratio of constituents these materials show interesting phase diagram with phase transitions to ferroelastics, ferroelectric, antiferroelectric and dipolar glass states (shown in Fig. 2.3.7 a)) and characteristic dielectric dispersion (shown in 2.3.7 b) and c)) in dipolar glass phase.

Frustrated ground state (glassy state) in RADP occurs due to competing electric interaction and in $BP_{1-x}BPI_x$ incomplete proton ordering (due to competing ferroelectric and antiferroelectric ordering) in the hydrogen bond system cause glassy behaviour. $BP_{1-x}BPI_x$ is also known as a proton glass system.

2.3.3. Disordered materials.

Spin and dipolar glasses, relaxor ferroelectrics and doped incipient ferroelectric have couple common properties – in all of them there is built in chemical, topological, charge or other (spin, dipole moment frustration etc.) disorder, these materials in general can be called disordered materials.

Dipolar glasses can be described by molecular mean field model - RBRF (random bond random field model). Model and its application in NMR experiments are depicted in [A53]. The same group of authors recently modified it to quantitatively describe relaxor ferroelectrics (compressible spherical dipolar glass model of relaxor ferroelectrics [A54]). The RBRF model was adapted in [A51-52] to describe dielectric properties of glassy state in $BP_{1-x}BPI_x$ at low temperatures and was called dipolar glass model. Results of both models applied in NMR and dielectric experiments coincide very well.
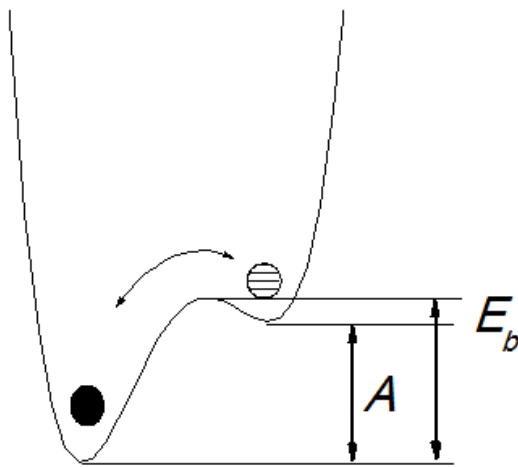
Fig. 2.3.8 Two well asymmetric potential, experienced by proton in dipolar glass model.

In dipolar glass model applied for $BP_{1-x}BPI_x$ it is considered a proton (or deuteron) moving in the double well (asymmetric) potential (Fig. 2.3.8).

Kinetic energy consist of fast ion motion in one minima and occasional thermally activated jumps between the wells (in [A52] quantum tunneling is neglected). The probability for proton to overcome potential barrier is controlled by Boltzmann distribution [A52]. Hydrogen bond dipoles have relaxational dielectric response at lower frequencies and in [A55] it was shown that relaxation time of the dipole is given by following formula:

$$\tau = \tau_0 \frac{exp[E_b/k_B(T-T_0)]}{2\cosh[A/2k_BT]},$$ 2.16

τ_0 represents attempt relaxation time, T_0 – Vogel-Fulcher (freezing) temperature, A – describes local potential asymmetry due to the mean molecular fields of other dipoles and E_b – potential height. Local polarization as the time-averaged dipole moment of an individual O-H··O bond is given by the asymmetry parameter A as follows:

$$p = \tanh[A/2k_BT].$$ 2.17

Further consideration is also applied that A and E_b parameters of the local potential are both randomly distributed around their average values A_0 and E_{b0} according to Gaussian distribution:

$$w(E_b) = \frac{1}{\sqrt{2\pi}\sigma_{Eb}} exp\left[\frac{(E_b-E_{b0})^2}{2\sigma_{Eb}^2}\right]$$ 2.18

and $$w(A) = \frac{1}{\sqrt{2\pi}\sigma_A} exp\left[\frac{(A-A_0)^2}{2\sigma_A^2}\right],$$ 2.19

where σ_{Eb} and σ_A are standard deviation of E_b and A, respectively, from their mean values. Distribution function of the relaxation times is given:

$$w(\ln \tau) = \int_{-\infty}^{\infty} w(A)w(E_b(A,\tau)) \frac{\partial E_b}{\partial(\ln \tau)} dA,$$ 2.20

where $E_b(A, \tau)$ describe E_b dependence from potential asymmetry at given τ (derived from equation 2.16). From the potential asymmetry distribution function $w(A)$ local polarization distribution can be found:

$$w(p) = \frac{2k_BT}{\sqrt{2\pi}\sigma_A(1-p^2)} exp\left[-\frac{(a\tanh[p]-a\tanh[\bar{p}])^2}{2\sigma_A(2k_BT)^2}\right].$$ 2.21

This expression can be transformed into one obtained in RBRF model, when σ_A and A_0 are substituted as follows:

$$\sigma_A = 2J\sqrt{q_{AE+\tilde{\Delta}}}$$ 2.22

and $$A_0 = 2J_0\bar{p}.$$ 2.23

J is the Gaussian variance and J_0 is the average of the random interbond coupling, $\widetilde{\Delta} = \Delta/J^2$ is renormalized variance of the random local electric fields, $\bar{p}$ is the average polarization and q_{AE} – the Edwards-Anderson glass order parameter. The latter two are defined as follow:

$$\bar{p} = \int_{-1}^{+1} p w(p) dp \qquad \qquad 2.24$$

and

$$q_{AE} = \int_{-1}^{+1} p^2 w(p) dp. \qquad \qquad 2.25$$

This model allows extraction of microscopic local properties from dielectric permittivity measurements. Edwards-Anderson glass order parameter is the order parameter of dipolar glass systems like polarization in proper ferroelectrics.

Doped incipient ferroelectric have common features with dipolar glasses and relaxor ferroelectrics – extremely wide dielectric dispersion region and very broad relaxation times distribution [A56]. In doped canonical incipient ferroelectrics $SrTiO_3$ ($Sr_{1-1.5x}Bi_xTiO_3$) and $KTaO_3$ ($K_{1-x}Li_xTaO_3$) impurity ions Bi and Li occupies off-centered positions in perovskite lattice and forms reorientable dipoles [A57]. Dipole interactions with induced ferroelectric, antiferrodistortive regions and highly polarizable host lattice complicates dielectric relaxation spectrum in wide frequency range below soft mode response.
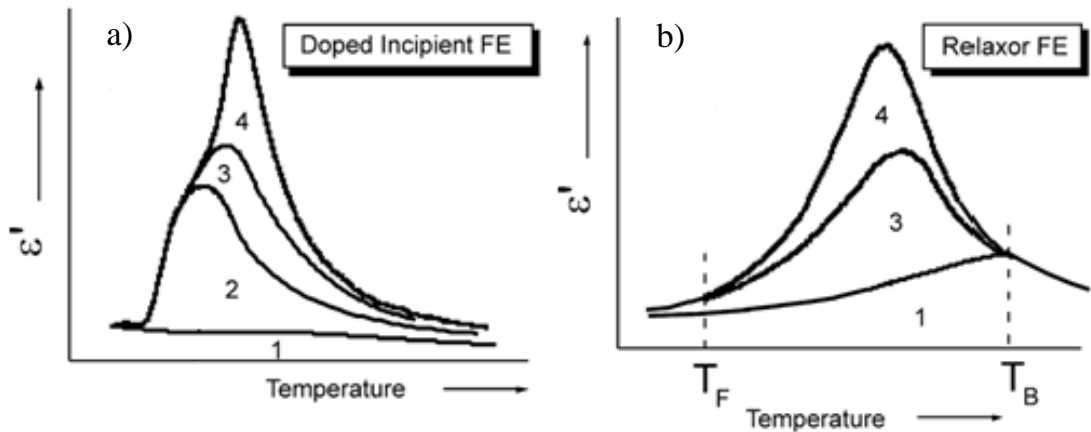
Fig. 2.3.9. Comparison of incipient and relaxor ferroelectrics dielectric spectra, adapted from [A57].

These interactions hardens soft mode (soft mode frequency stays finite at all temperatures) and induce formation of polar cluster similar to PNRs. Consequently the phonon contribution is much lower and not dominant as in pure $SrTiO_3$ and $KTaO_3$ (as depicted in Fig. 2.3.9 a) region 1).

A general structure of doped incipient ferroelectric dielectric spectra exhibits contribution from hopping of individual off-center ion (or vacancy in heterovalent dopant case) (Fig. 2.3.9 a) region 2) and two contributions (Fig. 2.3.9 regions 3 and 4) from polar cluster – "flipping" (region 4) and "breathing" (region 3). The contribution (2) dominates at low dopant concentrations while contributions of (3) and (4) prevail at higher concentrations [A57]. Phonon contribution becomes dominant only at low enough temperatures where all other contributions effectively freeze out - are no more contributing.

References

A1 Tagantsev A. K., Cross L. E., Fousek J. "Domains in ferroic crystals and thin films", Springer, ISBN 978-1-4419-1416-3 (2010).

A2 Granicher H., Muller K.A. *Mater. Res. Bull.* 6, 977 (1971).

A3 Toledano P., Dmitriev V. "Phase transitions in crystals and quasicrystals", World Scientific, ISBN: 978-981-4500-02-9, (1996).

A4 Dubovik, V. M., Tugushev, V. V. Phys. Rep.187, 145–202 (1990).

A5 Van Aken B. B., Rivera J. P., Schmid H., Fiebig M. *Nature* 449, 702 (2007).

A6 Bozorth R. M. "Ferromagnetism", Wiley, ISBN 0-7803-1032-2, (1993).

A7 Nye J. F. "Physical Properties of Crystals: Their Representation by Tensors and Matrices", Oxford Science Publications, ISBN: 978-0198511656 (1985).

A8 Rabe K. M., Ahn C. H., Triscone J. M. "Physics of Ferroelectrics A Modern Perspective", Springer, ISBN: 0303-4216 (2007).

A9 Sawyer C. B., Tower C. H., *Phys. Rev.* 35, 269 (1930).

A10 Grigas J. "Segnetoelektriniai reiškiniai ir faziniai virsmai", Vilnius Universitetas, UDK: 539.2(075.8) (1987).

A11 Kittel C. "Introduction to solid state physics", John Wiley & Sons, Inc., ISBN: 0-471-11181-3 (1996).

A12 Scott J. F. *Rev. Mod. Phys.*, 46, 83 (1974).

A13 Cochran W. *Phys. Rev. Lett.,* 3, 9, 412 (1959).

A14 Lyddane R. H., Sachs R. G., Teller E. *Phys. Rev.,* 59, 673 (1941).

A15 Muller K. A., Burkard H. *Phys. Rev. B,* 19, 7 3593 (1979).

A16 Barrett J. *Phys. Rev.,* 86, 118 (1952).

A17 Chaves A. S., Barretto P. C. S., Ribeiro L. A. A. *Phys. Rev. Lett.,* 37, 618 (1976).

A18 Pytte E. *Phys. Rev. B,* 9, 3758 (1972).

A19 Migoni R., Bilz H., Bauerle D. *Proceedings of the International Conference on Lattice Dynamics, Flammarion, Paris*, 650 (1977).

A20 Vendik O.G., Ter-Martirosyan L.T., Zubko S.P., *J. Appl. Phys.,* 84, 993 (1998).

A21 Kamba S., Savinov M., Laufek F., Tkac O., Kadlec C., Veljko S., John E. J., Subodh G., Sebastian M. T., Klementova M., Bovtun V., Pokorny J., Goian V., Petzelt J. *Chem. Mater.*, 21, 811 (2009).

A22 Gurevich V.L., Tagantsev A.K. *Adv. Phys.,* 40, 719 (1991).

A23 Buzin I.M. *Vestn. Mosk. Univ. Fiz. Astron.,* 18, 70 (1977).

A24 Tagantsev A.K. *Sov. Phys. JETP,* 59, 1290 (1984).

A25 Tagantsev A. K., Sherman V. O., Astafiev K. F., Venkatesh J., Setter N. *Journal of Electroceramics,* 11, 5, (2003).

A26 Garin B.M. *Sov. Phys. Solid State,* 32, 1917 (1990).

A27 Petzelt J., Ostapchuk T., Gregora I., Rychetsk I., Hoffmann-Eifert S., Pronin A.V., Yuzyuk Y., Gorshunov B.P., Kamba S., Bovtun V., Pokorn J., Savinov M., Porokhonskyy V., Rafaja D.,Vanek P., Almeida A., Chaves M.R., Volkov A.A., Dressel M.,Waser R., *Phys. Rev. B,* 64, 184111 (2001).

A28 Zhang S. T., Kounga A. B., Aulbach E., Ehrenberg H., Rodel J. *Appl. Phys. Lett.,* 91, 112906 (2007).

A29 Bokov A. A., Ye Z. G. *J. of Mat. Science,*41, 31 (2006).

A30 Smolenskii G. A., Isupov V. A., Agranovskaya A. I., Popov S. N. *Sov. Phys. Solid State*, 2, 2584 (1961).

A31 Chu F., Setter N., Tagantsev A. K. *J. Appl. Phys.*, 74, 5129 (1993).

A32 Stenger C. G. F., Burggraaf A. J. *Phys. Stat. Sol. (a),* 60, 653 (1980).

A33 Bokov A. A., Raevskii I. P., Smotrakov V. G. *Sov. Phys. Sol. Stat.,* 26, 1708 (1984).

A34 Bokov A. A., Leschenko M. A., Malitskaya M. A., Raevskii I. P. *J. Phys.: Condens. Matter,* 11, 4899 (1999).

A35 Shvartsman V. V., Lupascu D. C. *J. Am. Ceram. Soc.,* 95, 1 (2012).

A36 Vakhrushev S. B., Kvyatkovsky B. E., Nabereznov A. A., Okuneva N. M., Toperverg B. P. *Ferroelectrics,* 90, 173 (1989).

A37 Nabereznov A. A., Vakhrushev S. B., Dorner B., Strauch D., Moudden H. *Eur. Phys. J.,* 11, 13 (1999).

A38 Hirota K., Ye Z. G., Wakimoto S., Gehring P. M., Shirane G. *Phys. Rev. B* 65, 104105 (2002).

A39 Vakhrushev S. B., Nabereznov A. A., Sinha S. K., Feng Y. P., Egami T. *J. Phys. Chem. Solids,* 57, 1517 (1996).

A40 Wakimoto S., Stock C., Birgeneau R. J., Ye Z. G., Chen W., Buyers W. J. L., Gehring P. M., Shirane G. *Phys. Rev. B,* 65, 172105 (2002).

A41 Gehring P. M., Wakimoto S., Ye Z. G., Shirane G. *Phys. Rev. Lett.,* 87, 277601 (2001).

A42 Gehring P. M., Park S. E., Shirane G. *Phys. Rev. Lett.,* 84, 5216 (2000).

A43 Hlinka J., Kamba S., Petzelt J., Kulda J., Randall C. A., Zhang J. *Phys. Rev. Lett.,* 91, 107602 (2003).

A44 Bovtun V., Petzelt J., Porokhonskyy V., Kamba S., Yakimenko Y. *J. Eur. Ceram. Soc.,* 21, 1307 (2001).

A45 Uchino K., Nomura S. *Ferroelectr. Lett. Sect.,* 44, 55 (1982).

A46 Sherrington D., Kirkpatrick S. *Phys. Rev. Lett.,* 35, 1972 (1975).

A47 Tagantsev A. K. *Phys. Rev. Lett.,* 72, 7, 1100 (1994).

A48 Binder K., Young A. P. *Rev. Mod. Phys.,* 58, 801 (1986).

A49 Courtens E. *J. Physique Lett.,* 43, L199 (1982).

A50 Gonzalo J. A. Phys. Rev. B, 39, 16, 12297 (1989).

A51 Banys J., Lapinskas S., Kajokas A., Matulis A., Klimm C., Völkel G., Klöpperpieper A. *Phys. Rev. B,* 66, 144113 (2002).

A52 Banys J., Macutkevic J., Lapinskas S., Klimm C., Völkel G., Klöpperpieper A. *Phys. Rev. B,* 73, 144202 (2006).

A53 Pirc R., Tadic B., Blinc R., Kind R. *Phys. Rev. B,* 43, 4, 2541 (1991).

A54 Pirc R., Kutnjak Z., Novak N. *J. Appl. Phys.*, 112, 114122 (2012).

A55 Dolinšek J., Arčon D., Zalar B., Pirc R., Blinc R., Kind R. *Phys. Rev. B,* 54, R6811 (1996).

A56 Grigalaitis R., Banys J., Bagdzevičius Š., Sternberg A., Bormanis K. *Physica status solidi C,* 6, 12, 2743 (2009).

A57 Bovtun V., Porokhonskyy V., Savinov M., Pashkin A., Zelezny V., Petzelt J., *J. Eur. Ceram. Soc.,* 24, 1545 (2004).

3. Material processing.

3.1. Ceramic processing.

Four targets were used for PLD deposition of thin films: commercial single crystal $SrTiO_3$, ceramic $SrRuO_3$ (SRO) and $La_{0.8}Sr_{0.2}MnO_3$ (LSMO) for electrodes, and own made ceramic STO.

Commercially available (Inframat, Advanced Materials, USA) reagent grade $SrTiO_3$ nano powder was used as a starting material, powder properties are given in Table 3.1. Cubic phase and right stoichiometry was confirmed by powder x-ray diffraction (Fig. 3.1.1) with Bruker Discovery8 high resolution x-ray difractometer with $Cu_{K\alpha}$ radiation (λ=0.1542 nm). The scan range was from 15° to 115° with an increment step size of 0.05°. All Bragg peaks were indexed in the diffraction pattern according to Powder Diffraction File Card no. 00-035-0734 from The International Centre for Diffraction Data (ICDD) database, no unidentified ones.
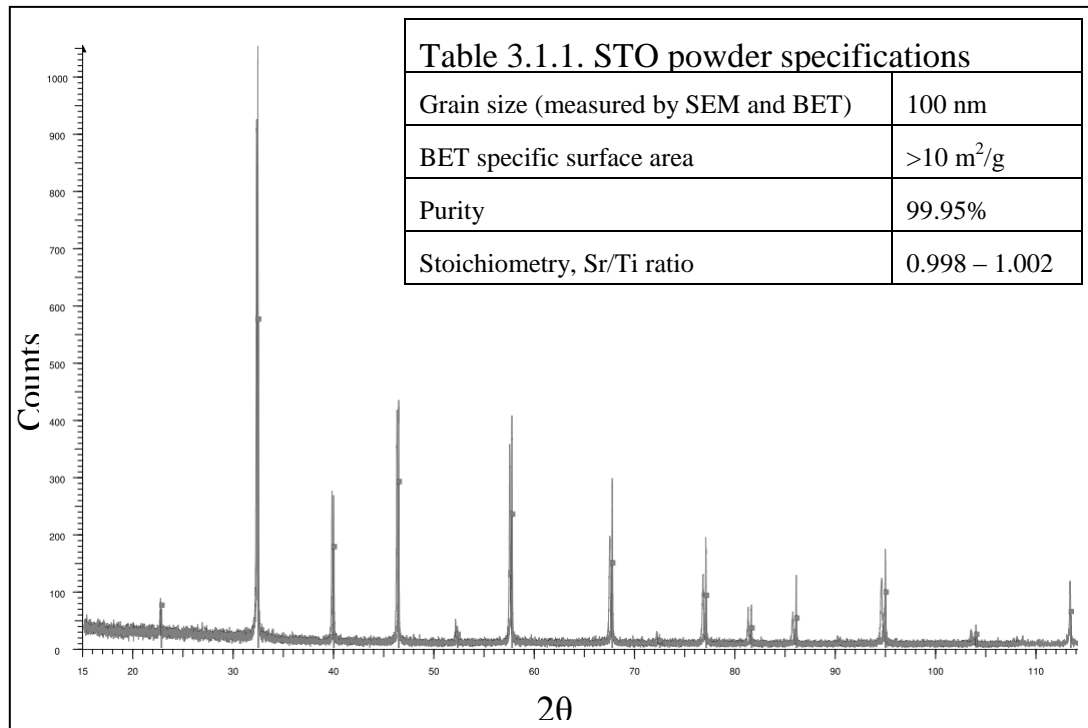

Table 3.1.1. STO powder specifications

Grain size (measured by SEM and BET)	100 nm
BET specific surface area	>10 m^2/g
Purity	99.95%
Stoichiometry, Sr/Ti ratio	0.998 – 1.002

Fig. 3.1.1. θ-2θ x-ray powder diffraction pattern from STO sintered ceramic (line) and Bragg peak positions from PDF card no. 00-035-0734 (dashes).

STO ceramic targets were processed as follows: 20 g of powder was mixed with 1 g of binder - PVA solution in water (4% of polyvinyl alcohol in water) by hand grinding in corundum mortar. The mixture was ball milled in 500 ml nylon jars with yttrium stabilized zirconia mini balls as the grinding media. Isopropanol as a suspension was added to the powders with the weight ratio 1:1 with powders + mini balls. The jars were set vertically in planetary milling machine and milled for 16 h (180 rpm speed) to thoroughly mix powder with binder and brake powder agglomerates.

After milling slurry was dried, separated from YSZ balls and pressed into the appropriate size pallets (PLD target dimensions: 25.6 mm – 1 inch diameter and 6.4 mm – 0.25 inch thickness). Uniaxially pressed (10 kN) pallets had density of about 1.76 g/cm^3, i.e. 34% of theoretical density (TD) and were not dense enough to promote even densification during sintering - this lead to cracked pallets after sintering. After uniaxial pressing it was used additional pressing step – isostatic (500 kN, 255 MPa) - to acquire sufficient green body density. It was achieved 2.56 g/cm^3 green body density (50% TD). After uniaxial and isostatic pressing obtained pallet was sintered at 1480°C for 4 h. Sintered pallet was analyzed by XRD (Fig. 3.1.1) and showed single cubic perovskite $SrTiO_3$ phase (at room temperature) and was 4.96 g/cm^3 density, i.e. 96.7% TD. Temperature regime during sintering: burning off binder at 600°C for 4 h (temperature ramp. rate 1°C/min), ceramic sintering at 1480°C for 4 h (temperature ramp. rate 2°C/min) and cool down to room temperature at ramp. rate 2°C/min.

Single crystal STO (001) target was purchased (CrysTec GmbH, Germany). SRO and LSMO ceramic targets were acquired (PI-KEM Ltd, United Kingdom). All commercial targets were scanned in XRD at room temperature and confirmed appropriate crystallographic structure and respective chemical elements stoichiometry.

$Sr_{1-1.5x}Bi_xTiO_3$ (incipient ferroelectric $SrTiO_3$ doped with heterovalent Bi), $(K_{0.5}Na_{0.5})(Nb_{x-1}Sb_x)O_3$ with 0.5 mol. % MnO_2 (ferroelectric sodium potassium niobate substituted with antimony and added sintering aid – MnO_2) and $0.4Na_{0.5}Bi_{0.5}TiO_3$-$(0.6-x)SrTiO_3$-$xPbTiO_3$ ceramics were prepared by ordinary solid state route by scholars of "Laboratory of Physics and Application of Functional Materials" [B1-3] in Institute of Solid State Physics, University of Latvia, Latvia.

3.2. Substrate treatment.

Strain free STO thin films were deposited on STO single crystalline substrates (homoepitaxial deposition) and strained thin films were deposited on LSAT substrate (heteroepitaxial deposition), which exerts moderate in plane strain ~ 1% on STO thin film, using PLD method.

Smooth substrate surfaces terminated with a single atomic plane are essential for perfecting the epitaxial growth of transition metal oxide films, including epitaxial $SrTiO_3$ thin films. Well established treatment method was used (developed by [B4-6]) to obtain single terminated $SrTiO_3$ substrates.

Commercial single crystal oxide wafers are prepared by so-called mechanochemical polishing with an alkaline solution containing colloidal silica particles. Commercial STO (100) (CrysTec GmbH, Germany) surface was smooth ($R_A < 0.5$ nm) but no ordered single unite cell size terraces were visible. Crystalline substrates were specially miscuted (Fig. 3.2.1, 0.1° off toward (001) direction by provider) to obtain well-ordered unite cell size ($a = 0.39046$ nm for $SrTiO_3$ at room temperature) terraces on the surface.
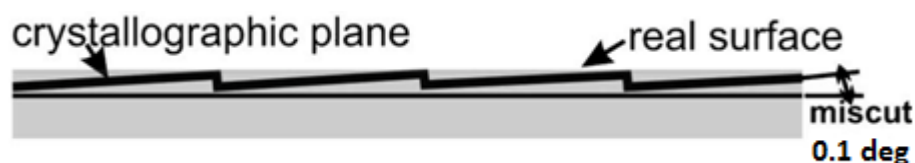

Fig. 3.2.1. Schematical representation of miscut angle, adapted from [B7].

STO is a perovskite and its structure consists from alternating non charged SrO and TiO_2 atomic layers. Calculations predicts a different surface energy for two possible surface terminations (in (100) orientation) [B8] and surface energy is dependent from the size of A-site ion. In $SrTiO_3$ the TiO_2 plane is more stable, consequently one expects preferential termination after some chemical or physical treatment. However cut or cleaved crystals have equal amount of AO and BO_2 terminated domains separated by half unite cell steps because $SrTiO_3$ does not have well denominated cleavage planes. Further polishing leads to formation of several kinds of defects and not well defined (at atomical scale) surface.

To obtain perfect single termination, according to [B5] substrate was soaked in H_2O for ~30 min to form Sr-hydroxide complex $Sr(OH)_2$. It is energetically unfavorable for water to react with chemically very stable TiO_2 [B9]. It is known that Sr-hydroxide complex can be dissolved in acidic solutions. After soaking step substrates were etched in buffered HF acid for ~25 s (typical AFM image of etched STO surface Fig. 3.2.2). In contrast to [B4] pH of acidic solution was not controlled.
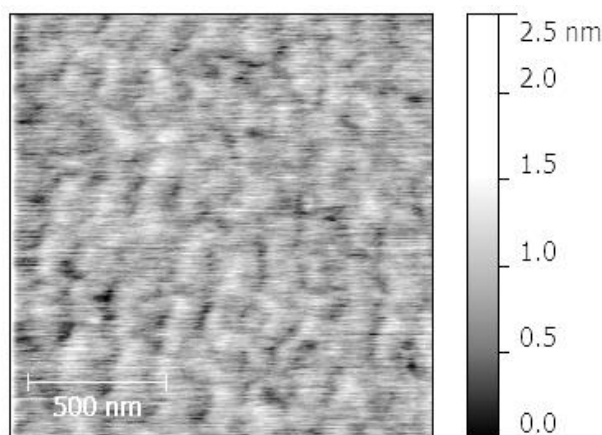

Fig. 3.2.2. AFM micrograph of $SrTiO_3$ (100) surface after BHF etching step.

After etching one assumes that crystal surface is terminated by TiO_2 atomic layers with one unite cell steps. As can be seen in Fig. 3.2.2 etched surface doesn't look well defined. To remove the remnants of previous etching and reconstruct surface a final annealing step is performed at 925°C for 1 h (with flowing O_2, to fully oxidize surface). After this treatment one obtains isolating single B-site terminated (TiO_2) STO substrate surface (Fig. 3.2.3).
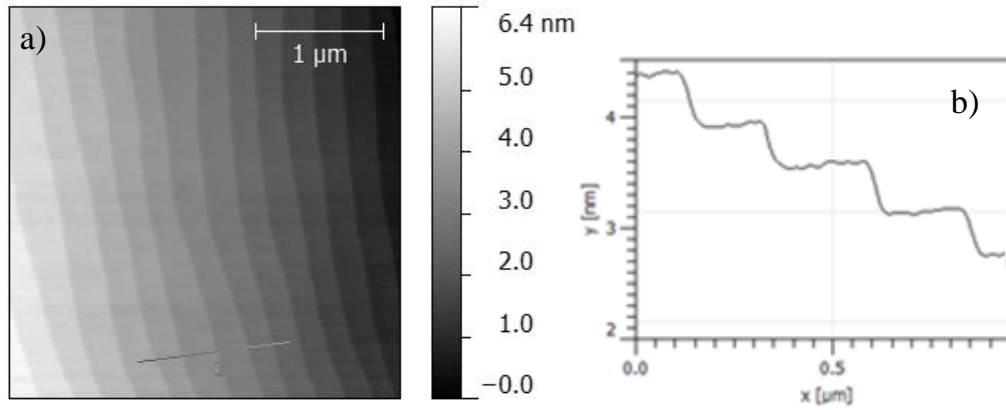
57

Fig. 3.2.3. AFM micrograph of treated STO (100) surface a) and line profile showing one unite cell height steps on the surface b).

Single termination is also confirmed by depositing few unite cell thickness SrRuO$_3$ layer. It is well known that SRO covers all surface and develops aligned terraces only if substrate is single terminated. This is a consequence of SRO growth rate dependence of substrate terminating layer – growth rate is different for A- and B- site terminated areas. When surface is mixed terminated SRO develops well-ordered configuration, but doesn't cover all surface (shown in Fig. 3.2.4 b)).
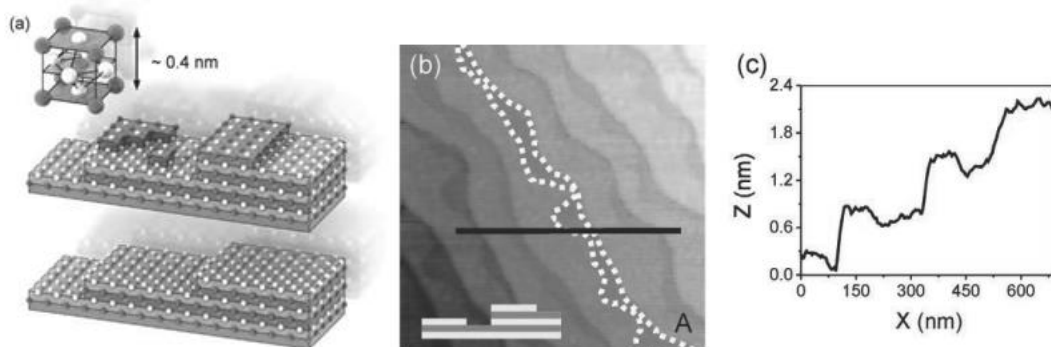

Fig. 3.2.4. A schematic representation of a mixed-terminated surface a) with steps of 0.2, 0.4, 0.6 nm high and single-terminated BO$_2$ surface with steps of 0.4 nm high. The dark grey blocks correspond to the AO layer and the light grey blocks to the BO$_2$ layer, respectively. Clear mixed termination b) and steps of 0.2, 0.4, and 0.6 nm high, marked by the dashed line and also shown in its corresponding line profile c). Adapted from [B10].

After depositing few unite cell thickness SRO layer, one can observe fully covered surface, without ½ and 1½ height steps (shown in Fig. 3.2.5). This observation confirms single site (according to [B5-6] B-site, TiO_2) terminated STO substrate after performed treatment procedure.
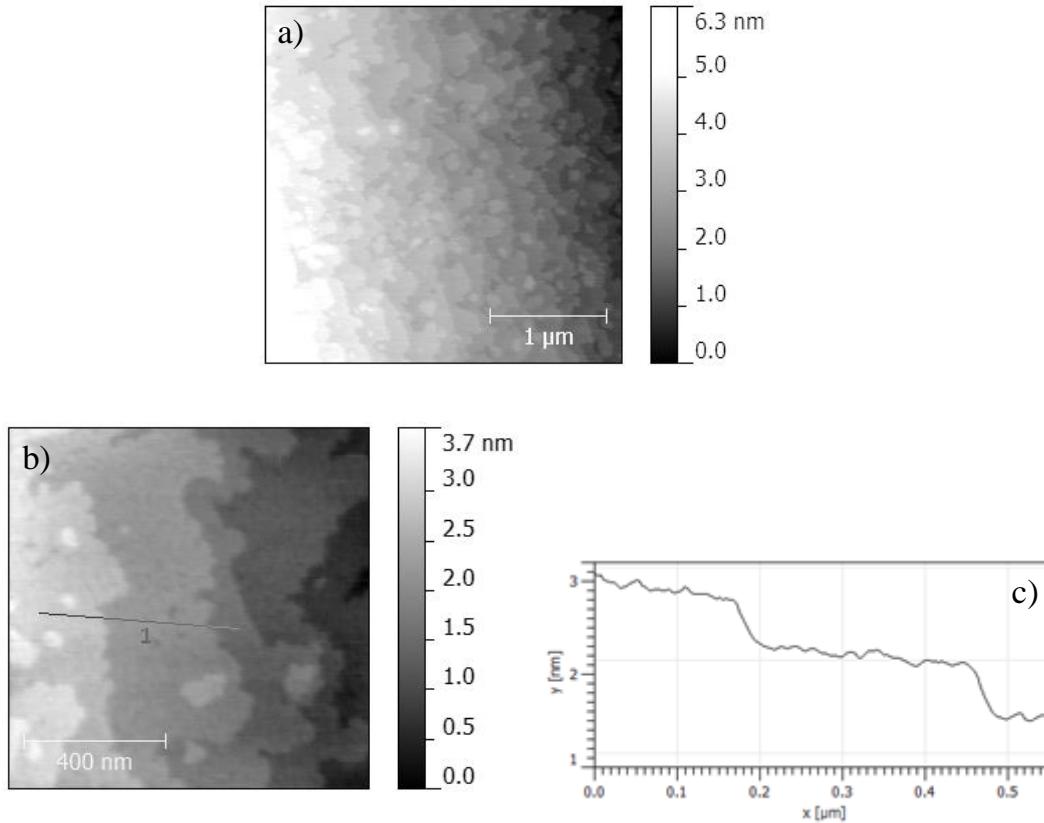

Fig. 3.2.5. AFM micrograph of deposited $SrRuO_3$ on treated STO a), zoomed in image b) and corresponding line profile showing one unite cell height steps c).

Another substrate used in this thesis was LSAT, $(LaAlO_3)_{0.3}$-$(Sr_2AlTaO_6)_{0.7}$ is a solid solution of perovskites $LaAlO_3$ and Sr_2AlTaO_6. It has cubic structure, low dielectric constant which makes it suitable substrate for thin film microwave measurements and appropriate substrate in microwave applications.

Well established treatment method developed for $SrTiO_3$ substrates (wet etching with HF acid and annealing at elevated temperatures) failed for LSAT substrates, because in LSAT (001) respective site (A- or B-site) terminated

surface still consists of two different ions – A-site from La and Sr and B-site from Al and Ta. Up to date there is no selective etchant found for LSAT to obtain single site terminated surface. To achieve single site termination it was tried annealing at elevated temperature [B11], but at 1250°C not only steps and terraces are formed, but also few nanometer height mounds (Fig. 3.2.6 a)) which can be partially etched away with BHF (Fig. 3.2.6 b)) after soaking in deionized water. This can be explained as follows: since La_2O_3, Al_2O_3, Ta_2O_5 are insoluble in water it follows that mounds are mainly consisting of SrO, which is soluble in water (forms $Sr(OH)_2$ hydroxide complexes) and later can be etched away.
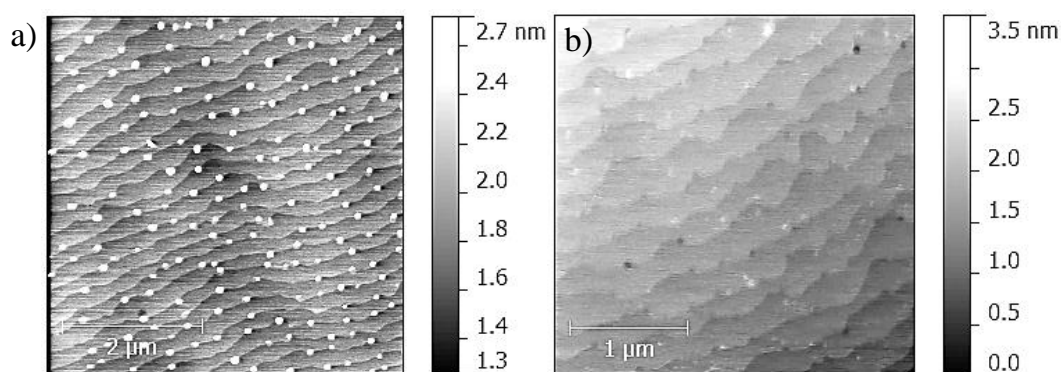

Fig. 3.2.6. AFM image showing steps (~0.4 nm height) and mounds of LSAT (001) substrate annealed at 1250ºC for 1.2 h in O_2 flow a) and the same substrate after etching in BHF for 1 min b).

SrO appearance on the surface indicates that at these temperatures A-site (consisting of La, Sr and O) decomposes and surface is La deficient (La evaporates or diffuses into the bulk of substrate). To prevent loss of La it was used method described by Ngai in [B12]:

Substrates were covered with $LaAlO_3$ and annealed (schematically shown in Fig. 3.2.7 a)).
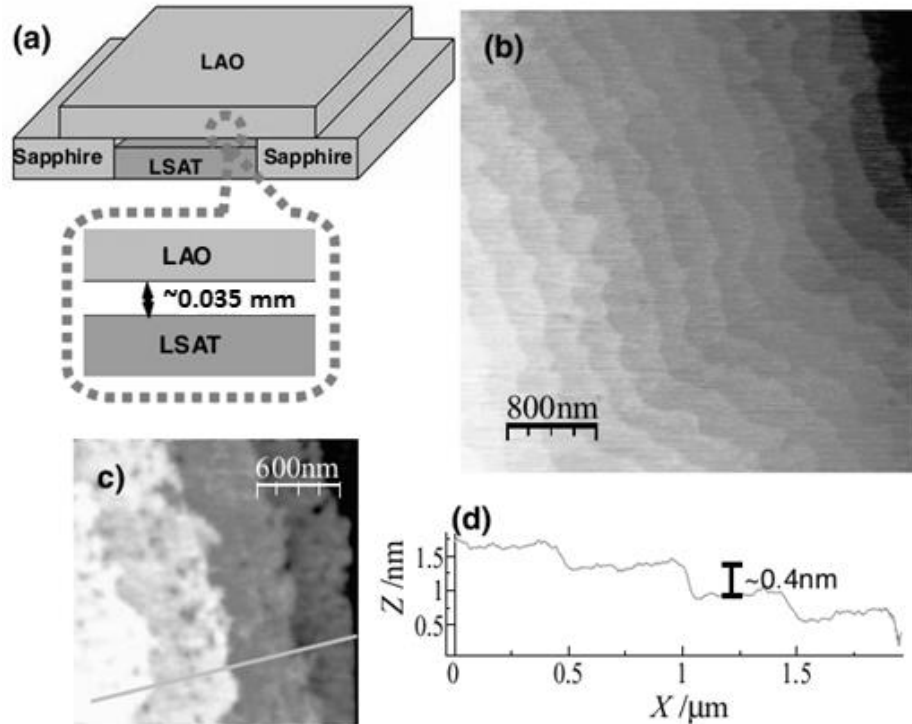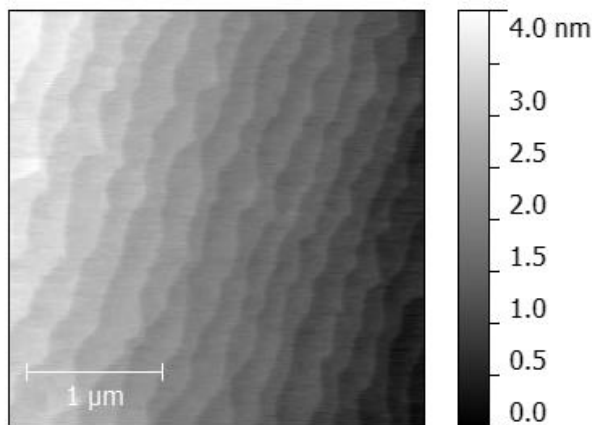
Fig. 3.2.7. LAO substrate, supported by sapphire rails, is placed in close proximity to the LSAT substrate a). AFM image of an LSAT substrate after annealing with an LAO cover substrate at 1300°C, showing well-ordered steps. Vertical scale: ~7 nm b). AFM image showing closer view of steps c). Line profile of the steps shown in c, indicating unit cell step heights d). Adapted from [B12].

3.2.8. AFM micrograph of LSAT (001) annealed at 1250ºC for 1.8 h (LaAlO$_3$ to LSAT distance 36 μm) and 0.5 l/min Ar flow.

LAO cover increases La vapor pressure at LSAT surface and prevents La evaporation (or diffusion). Inert gas like Ar in this case prevents Sr from oxidation and formation of SrO (in O$_2$ rich atmosphere decomposed A plane forms SrO). After optimizing annealing temperature single site terminated LSAT substrates with a single unite cell height steps were obtained (Fig. 3.2.8).

3.3. Pulsed laser deposition.

Major factors of the performance and novel properties (high-temperature superconductivity [B13], colossal magnetoresistance [B14]) of metal oxide structures and devices are the purity, structural perfection and homogeneity of constituent epitaxial layers, and the smoothness and abruptness of the heterointerfaces. Growth control on the atomic scale during thin film deposition process determines epilayers and interfaces perfection. Deposition process with an atomically controllable thickness is essential for high performance applications and can be achieved with one of physical vapor deposition techniques – pulsed laser deposition (PLD). Time resolved analysis during PLD deposition by reflection high energy electron diffraction (RHEED) allows direct in situ control of the growth dynamic and surface morphology.

Laser was first time demonstrated and publicized by the publication of the first optical maser in 1960 [B15]. Among the first experimental laser applications was ablation of various material (PLD) by intense ruby laser [B16], but did not received wide interest, because of worse quality of deposited materials in comparison with other deposition techniques like CVD or MBE. Rebirth of PLD occurred after famous PLD utilization in the growth of the high temperature superconducting material $YBa_2Cu_3O_{7-\delta}$ [B17] with superior quality. Since then PLD has emerged as a PVD technique for depositing epitaxial and nonepitaxial films of superconductors, metals, ferroelectrics, ferromagnetics and their multilayers.

3.3.1. Principle of PLD.

PLD is a physical vapor deposition technique based on the intense laser beam evaporation (ablation) of the target material. The most common laser used in PLD are excimer (ArF, KrF, XeCl etc.) and frequency multiplied solid state Nd:YAG lasers operating at 1-100 Hz repetition rates and UV wavelengths (KrF λ = 248 nm). Very short pulse (typically few tens of ns or

even less) highly energetic laser beam is focused on the target surface in order to obtain sufficiently high energy density needed for ablation (schematically depicted in Fig. 3.3.1).
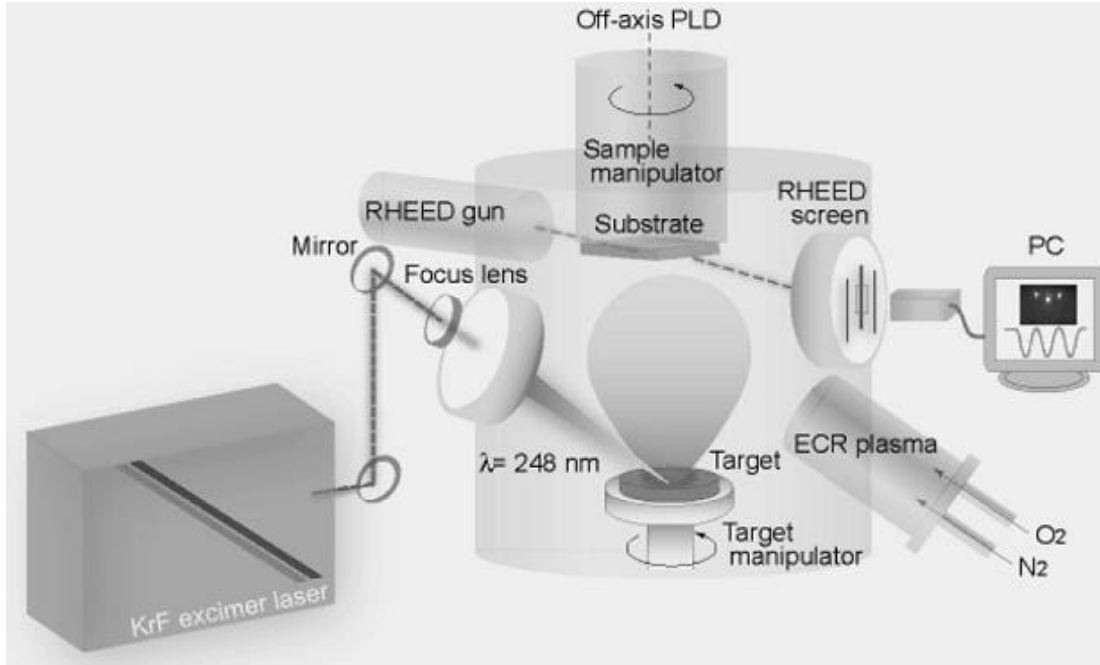

Fig. 3.3.1. Schematic diagram of a flexible oxide PLD system. Adapted from [B18]

The vaporized material will form highly directional plasma plume and part of the evaporated material will be deposited on the substrate. It is considered that material transfer in PLD is stoichiometric process provided certain minimum laser fluence is exceeded [B19]. However this assumption is not always valid and is depending on the ablated material and laser properties like the absorption coefficient, reflectivity, congruent melting, pulse duration, wavelength, fluence, all of them affects the laser beam interaction with target material. The laser target interaction is very complex and non-equilibrium physical phenomenon.

3.3.2. Ablation process.

Laser light and the solid material interact through the absorption of photons by the electronic subsystem. At high intensities achievable in short laser pulses ($>10^{13}$ W/cm^2 and above) ionization time for the dielectrics is just

a few femtoseconds [B20]. The electrons produced by the ionization then dominate absorption in the same way as the free carriers in metals – laser-mater interaction is similar independently of its initial material (metal, semiconductor or dielectric). Inverse Bremsstrahlung and resonant absorption becomes major mechanisms for both metals and dielectrics [B21].

Absorbed electromagnetic energy is immediately converted to electronic excitations in the form of plasmons, unbound electrons and in case of insulators excitons [B22]. Electric field amplitude of EM wave is expressed as:

$$E = \left(\frac{2\Phi}{cn\varepsilon_0}\right)^{1/2}, \qquad\qquad 3.1$$

Φ is the power density, c is the speed of light, n is refractive index and ε_0 is dielectric permittivity of free space (dielectric constant). Material with refractive index of 2 in radiation of 2×10^8 W/cm^2 power density will be subjected to the electric field strength of 0.2 MV/cm, high enough field to cause dielectric breakdown in many materials. Breakdown field is proportional to the square root of power density, which in turn is proportional to fluence and inversely proportional to the pulse length.
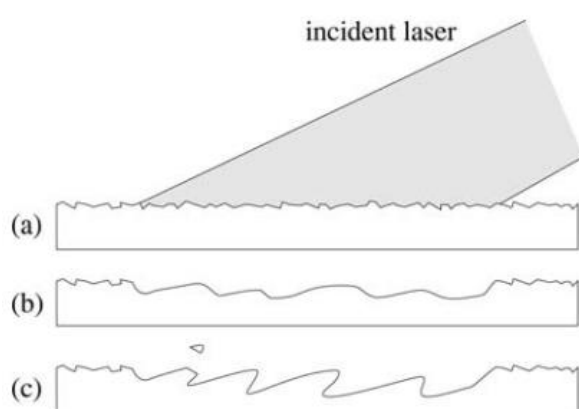
In general there are three possible ablation mechanisms:

- Electrostatic ablation. Electron energy loss due to electron-ion collisions and heat conduction are neglected for ultrashort ps and fs pulses, electrons escapes the solid and creates high electric field due to charge separation, this field electrostatically pulls out ions from the solid – ablation;

- Nonthermal ablation. Solid is transformed into vapor at higher than the equilibrium rate, equilibrium has no time to be established and ablation proceeds in nonequilibrium fashion;

- Thermal ablation-evaporation. Conditions are close to equilibrium and particles with energies $> E_b$ (binding energy) from the high-energy tail of the Maxwellian distribution can escape the solid [B23].

However in the most cases (when excimer laser is used with tens ns pulses) material ablation is controlled by the thermal conduction rate throughout the lattice. Excited electrons transfer their energy to the lattice within few picosecond and heating starts in the surface layer $1/\alpha$ (α optical absorption coefficient) [B22]. Due to high temperatures material will be evaporated (or ablated, depending on the pulse length and material heat conductivity) and it will absorb remainder of the laser pulse, which in turn will rise the plume temperature even higher. These effects leads to very high pressures at the target surface and due to pressure gradient plasma plume will expand in perpendicular to the target surface direction. The angular distribution of the produced plasma is forward directed and deposited film thickness can be well described by $\cos^{n}\theta$ formula (θ – angle with a surface normal) [B24], exponent n increases with increasing laser fluence and spot size.

Initially ablated species in plasma have wide distribution of kinetic energies (from ~1 eV to ~100 eV), during plume expansion ions collide in the plasma (and with process gas like O_2 or Ar if used) and cause redistribution of energy among the various degrees of freedom of the thermodynamical system of the laser generated plasma plume. The ablation spot on the target usually is ~ 1 mm^2 and will erode quickly if fired at the same spot (Fig. 3.3.2).

Fig. 3.3.2. Target surface erosion. Flat surface a) after prolonged exposure to the focused laser beam starts to form pillars b) which can break c) and form macroscopic particulates in deposited film. Adapted from [A8].

To avoid the excessive corrosion targets are rotated and raster scanned (shown in Fig. 3.3.3). Best results are

obtained when fine grain ceramic is used as targets, because in large grain ceramic and single crystal target thermal shock damages the surface and promotes creation of particulates.
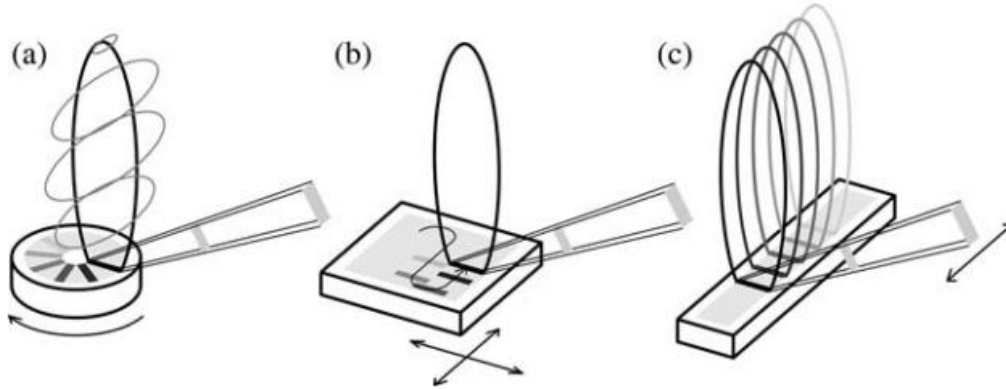

Fig. 3.3.3. Target rotation a) and raster scanning b), also laser beam scanning [A8].

3.3.3. Film nucleation and growth kinetics.

Couple interdependent processes happen after an adatom (molecule, ion or atom) arrives to the surface of substrate. First of all adatom might be elastically reflected back to gas phase – desorbed (as shown in Fig. 3.3.4). Another possibility is to be captured (after transferring its energy to the surface molecules – thermalized) on the substrate surface – adsorbed.
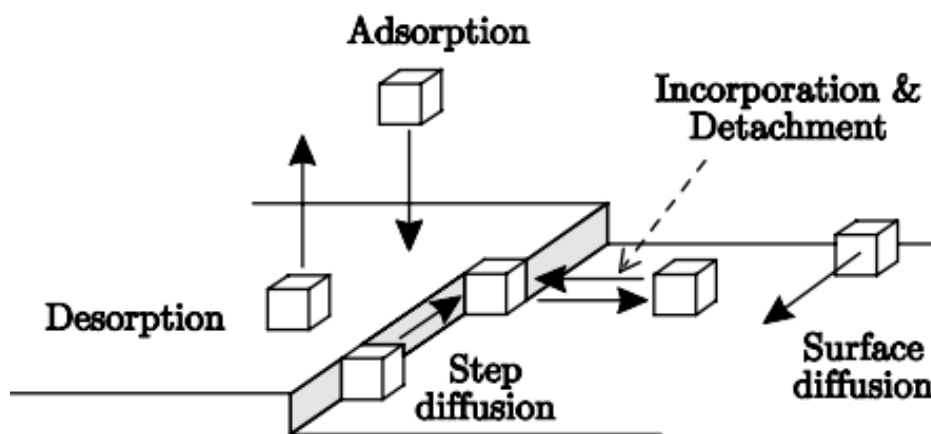

Fig. 3.3.4. Schematic view of processes in film nucleation. Adapted from [B25].

Once adsorbed adatom may change the surface site, migrate – surface diffusion depends on adatom energy, chemical surface composition and surface temperature. During surface diffusion adatoms might permute energetically favorable and unfavorable (interstitial) sites until is incorporated in the substrate surface, the same might be achieved in step diffusion, when adatoms move only along the surface steps. The nucleation behaviour strongly depends on the wetting of the substrate by the film material and raises different growth modes (shown in Fig. 3.3.5).
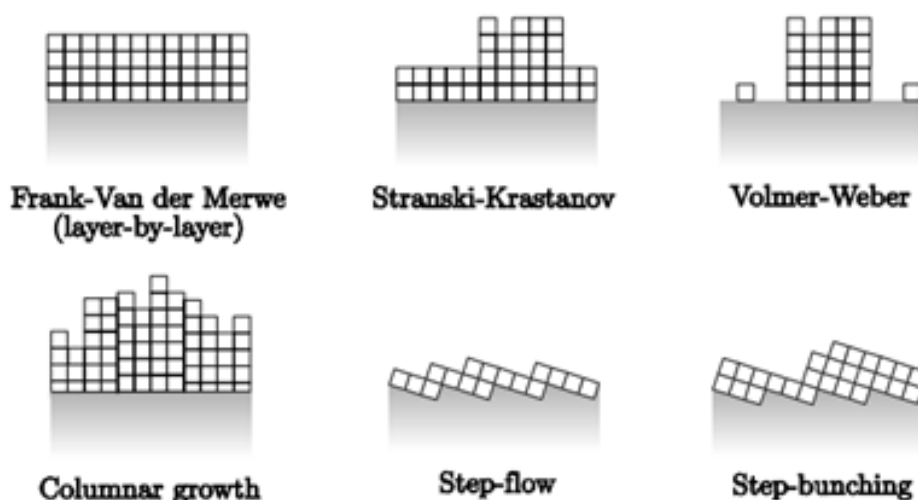

Fig. 3.3.5. Schematical view of crossection between film and substrate for different growth modes. Adapted from [B25].

Three classical growth modes and additional three modes might be observed in heteroepitaxial film deposition. Delicate balance between film γ_f (and substrate γ_s) surface and interface γ_i free energies causes different growth modes at the primary phase of film formation. When $\gamma_f + \gamma_i < \gamma_s$ strong bonding between film and substrate is expected and this leads to layer-by-layer growth mode (as described by Frank and Van der Merwe [B26]), shown in Fig. 3.3.5.

On the other extremity there is low bonding between film and substrate, growth proceeds in 3D mode and coalesce to form continuous film (Volmer–Weber growth mode [B27], or columnar growth). In heteroepitaxy growth mode might change from layer-by-layer to islands growth (Stranski–Krastanov

growth mode [B28]), because the lattice mismatch rise biaxial strain, resulting in elastic energy which increases with increasing layer thickness. Misfit dislocations are formed in exceed of critical thickness h_c to release elastic energy accommodated by misfit strain.

Miscut (surface misorientation from perfect crystallographic orientation) of the substrate gives one more controllable parameter in film deposition. Substrate can be intentionally miscuted to introduce steps on the surface. At the supersaturation (which is typical for PLD) the density of steps can be so large that other growth modes are suppressed and film grows in step-flow mode. Films grown in step-flow mode have relatively high structural perfection, because in this mode island coalescence is avoided. If the growth front moves with high velocity there is possibility that higher steps catch up with the lower ones and eventually bunched steps moves as an entity – step bunching happens.

In PLD the film is grown at highly not thermodynamic equilibrium and kinetic effects have to be considered. Because of the limited surface diffusion, the deposited material cannot fully rearrange for the surface energy minimization. The high supersaturation of the vapor leads to a large nucleation rate, and kinetic effects will lead to the occurrence of different growth modes [B21]. Another unique feature of PLD is the ability to combine very high deposition rates (after laser pulse) with intervals of no deposition (in between laser pulses), "healing effect", in periodic manner.

3.3.4. PLD deposition system used in this thesis.

"Surface" GmbH commercial "Laser star UHV" cluster system (shown in Fig. 3.3.6) equipped with "Coherent Compex 201" KrF laser ($\lambda = 248$ nm, pulse length 25 nm (FWHM), maximum repetition rate 10 Hz, maximum pulse energy 600 mJ and average power 5W) was used for the film growth.

PLD and RHEED chambers were equipped with turbo-molecular pumps and 10^{-7} mbar vacuum was achievable. The central chamber serves as transfer and storage unit and is equipped with ion-getter pump (vacuum better than 10^{-8} mbar). Substrates and targets are introduced through the load-lock that reduces pumping time and helps to preserve ultra-high vacuum and avoid contamination (all chambers are isolated by gate walves).
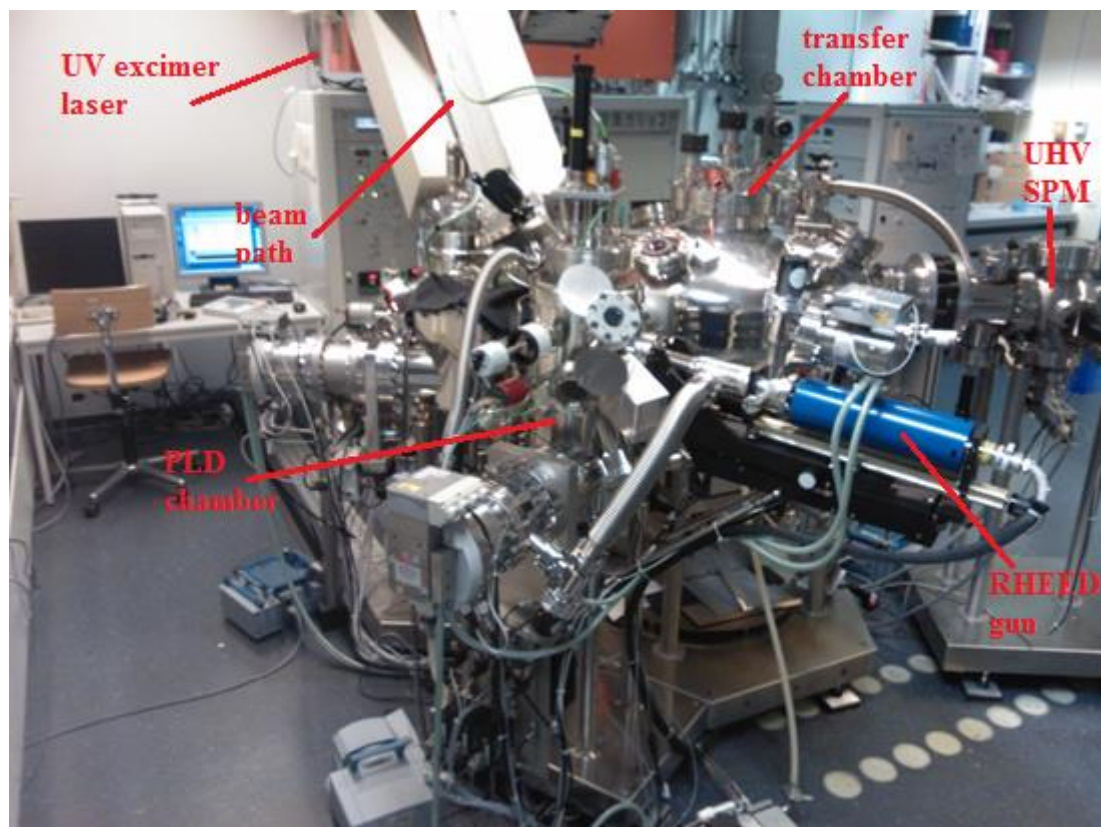

Fig. 3.3.6. Photo of the PLD start cluster in EPFL LC.

Laser radiated coherent light is guided through variable aperture to cut only the homogeneous flat-top part of the beam (excimer lasers suffer from inherent nonhomogeneous beam shape [B29]). Top-hat shaped beam is guided with UV graded fused silica optical elements (mirrors, lens, and windows) through the vacuum sealed window in to the deposition chamber. Laser spot is imaged on the target surface by imaging lenses to have a possibility to vary laser fluence. Because of the aperture, guiding optics and deposits on the chamber windows laser power is decreased befor the PLD chamber. In order to

know precise power it is measured not only in the laser but also after guiding path on the other side of the PLD chamber (power difference might be as large as 80% of nominal power).

Substrates were heated by IR laser (from room T up to 1000°C) and temperature was measured with a pyrometer (above 200°C). Three process gasses were available: pure O_2, N_2 and Ar. PLD deposition system included RHEED equipment for in situ monitoring of film growth. Schematical view of typical "Laser star UHV" cluster system is presented in Fig. 3.3.7 (different arrangement of constituent parts in comparison with EPFL LC tool).
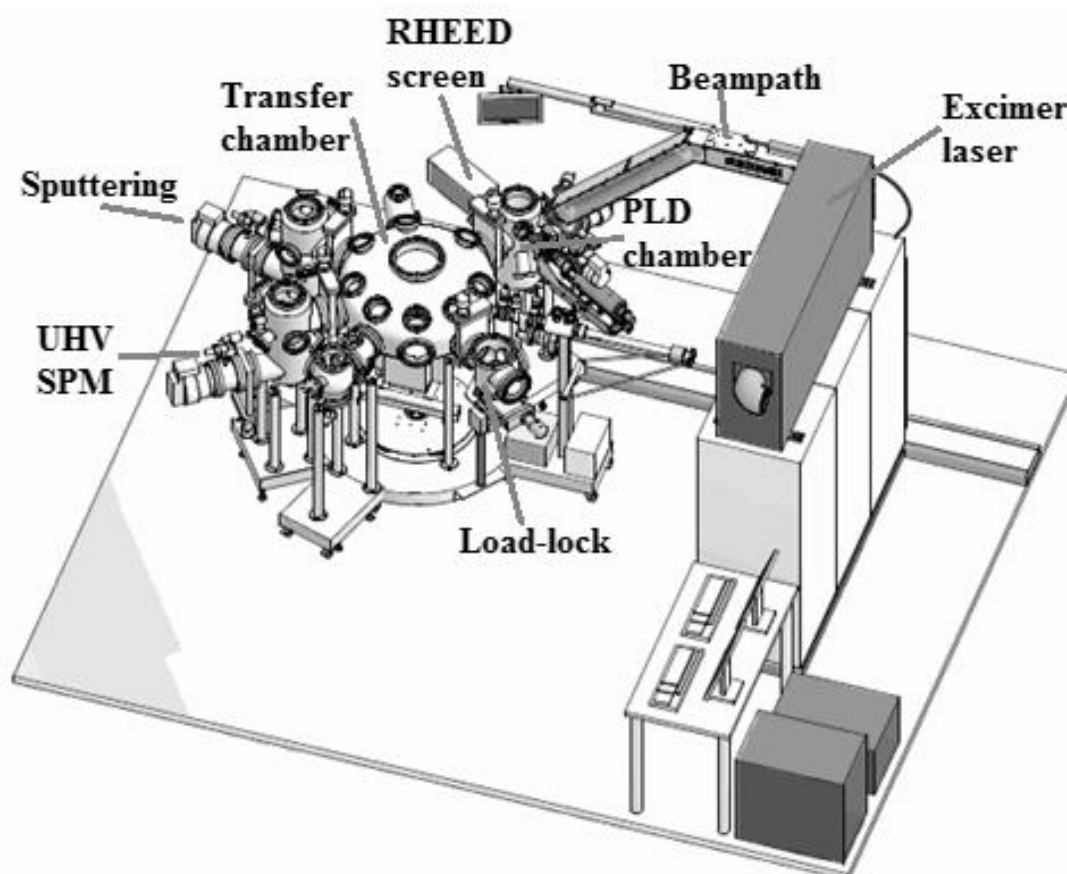
Fig. 3.3.7. Schematic of PLD start cluster, adapted from [B30].

References

B1 Private communication with dr. Karlis Bormanis (Karlis.Bormanis@cfi.lu.lv).

B2 Dambekalne M., Antonova M., Livinsh M., Kalvane A., Mishnov A., Smeltere I., Krutokhvostov R., Bormanis K., Sternberg A. *Integrated Ferroelectrics*, 102, 52 (2008).

B3 Dunce M., Birks E., Antonova M., Kundzinsh M., Sternberg A. Integrated Ferroelectrics, 108, 125 (2009).

B4 Kawasaki M., Takahashi K., Maedav T., Tsuchiya R., Shinoharav, Ishiyama O., Yonezawa T., Yoshimoto M., Koinuma H. *Science*, 226, 1540 (1994).

B5 Koster G., Kropman B. L., Rijnders G. J. H. M., Blank D. H. A., Rogalla H. *Appl. Phys. Lett.,* 73, 2920 (1998).

B6 Lippmaa M., Takahashi K., Ohtomo A., Ohashi S., Ohnishi T., Nakagawa N., Sato T., Iwatsuki M., Koinuma H., Kawasaki M. *Materials Science and Engineering,* B56, 111 (1998).

B7 Krainyukova N. V., Butskii V. V. *App. Surf. Scien.*, 235, 32 (2004).

B8 Henrich V. E., Cox P. A. "The Surface Science of Metal Oxides", Cambridge University Press, Cambridge, (1994).

B9 Komiyama M., Gu M. *Appl. Surf. Sci.,* 120, 125 (1997).

B10 Kleibeuker J. E., Koster G., Siemons W., Dubbink D., Kuiper B., Blok J. L., Yang C.-H., Ravichandran J., Ramesh R., Elshof J. E., Blank D. H. A., Rijnders G. *Adv. Funct. Mater.,* 20, 3490 (2010).

B11 Ohnishi T., Takahashi K., Nakamura M., Kawasaki M., Yoshimoto M., Koinuma H. *Appl. Phys. Lett.,* 74, 2531 (1999).

B12 Ngai J. H., Schwendemann T. C., Walker A. E., Segalv Y., Walker F. J., Altman E. I., Ahn C. H. *Adv. Mater.,* 22, 2945 (2010).

B13 Bednorz J.G., Müller K.A. *Z. Phys. B,* 64, 189 (1986).

B14 Von Helmolt R., Wecker J., Holzapfel B., Schultz L., Samwer K. *Phys. Rev. Lett.,* 71, 2331 (1993).

B15 Maiman T.H. *Nature*, 187, 493 (1960).

B16 Smith H.M., Turner A.F. *Appl. Opt.,* 4, 147 (1965).

B17 Dijkkamp D., Venkatesan T., Wu X.D., Shaheen S.A., Jisrawi N., Min-Lee Y.H., McLean W.L., Croft M. *Appl. Phys. Lett.,* 51, 619 (1987).

B18 Chambers S. A. *Adv. Mater.,* 22, 219 (2010).

B19 Dam B., Rector J. H., Johansson J., Huijbregtse J., de Groot D. G. *J. Appl. Phys.,* 83, 3386 (1998).

B20 Gamaly E. G., Rode A. V., Tikhonchuk V. T., Luther-Davies B. *Phys. Plasmas,* 9, 949 (2002).

B21 Eason R. "Pulsed laser deposition of thin films: applications-led growth of functional materials" John Wiley & Sons, Inc., ISBN-10: 0-471-44709-9 (2007).

B22 Willmott P. R., Huber J. *R. Rev. Mod. Phys.,* 72, 1 (2000).

B23 Landau L. D., Lifshitz E. M., Pitaevskii L. P. "Electrodynamics of Continuous Media", Pergamon, Oxford (1984).

B24 Anisimov S. I., Bauerle D., Luk'yanchuk B. S. *Phys. Rev. B,* 48, 12076 (1993).

B25 Huijben M., Interface Engineering for Oxide Electronics: Tuning electronic properties by atomically controlled growth, PhD thesis, University of Twente, The Netherlands, ISBN: 90-365-2351-6 (2006).

B26 Frank F.C., Van der Merwe J.H. *Proc. Roy. Soc. London A,* 198, 216 (1949).

B27 Volmer M., Weber A. *Z. Phys. Chem.,* 119, 277 (1926).

B28 Stranski I.N., Krastanov L. *Acad. Wiss. Math.-Naturw. Klasse IIb,* 146, 797 (1938).

B29 Delmdahl R., Pätzel R. *Phys. stat. sol. (c)* 5, 10, 3276 (2008).

B30 http://www.surface-tec.com/cluster.php (accessed on May 2014).

4. Characterization.

In order to determine the structural and functional relations between the fabrication process and the final thin films and ceramics, characterization is essential step. Thorough structural analysis is essential feedback mechanism in ceramic and thin film optimization. Thin film surface morphology was monitored during growth and after deposition by RHEED. To have high spatial resolution it was used scanning probe microscopy (SPM) and electron microscopy (SEM) to obtain information on the angstrom scale. The crystalline structure of ceramics and thin films were characterized by x-ray diffraction (XRD) and transmission electron microscopy (TEM). Chemical composition and stoichiometry can be derived from diffraction experiments but also can be obtained directly from SEM/TEM energy (or wavelength) dispersive x-ray analysis (EDX/WDX). Structural characterization was performed in EPFL LC (École Polytechnique Fédérale de Lausanne, Laboratoire de céramique) and EPFL CIME (École Polytechnique Fédérale de Lausanne, Centre interdisciplinaire de microscopie électronique).

Dielectric spectroscopy is powerful technique probing collective dielectric properties of a medium as a function of frequency. Modeling allows extracting microscopic data from macroscopic measurements; it is essential characterization technique of materials for electrical, electromechanical and electrochemical applications. Broadband dielectric spectroscopy and data analysis were done in Vilnius University, Faculty of Physics, Laboratory of Microwave Spectroscopy.

4.1. Structural characterization.

4.1.1. Reflection high energy electron diffraction.

RHEED is one of electron diffraction techniques and gives information about surface properties and symmetry. Diffraction conditions are expressed by

the Bragg's law, however due to geometrical arrangement (shown in Fig. 4.1.1) and electron energies, RHEED is only sensitive to material surface (few unite cell depth).
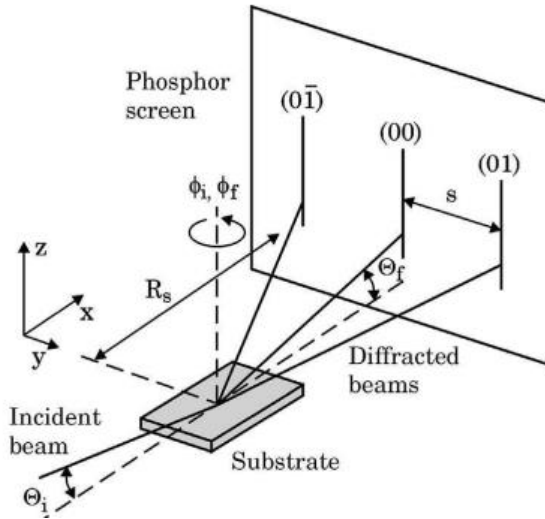

Fig. 4.1.1 Schematic view of RHEED setup. Adapted from [B21].

Due to surface sensitivity in RHEED only two conditions for diffraction have to be fulfilled (only two Laue equations instead of three as in three dimensional systems). A graphical representation of the diffraction conditions is Ewald sphere construction. Ewald's sphere is constructed about the beginning of the incident wave vector k and has radius k, schematically shown in Fig. 4.1.2 a).
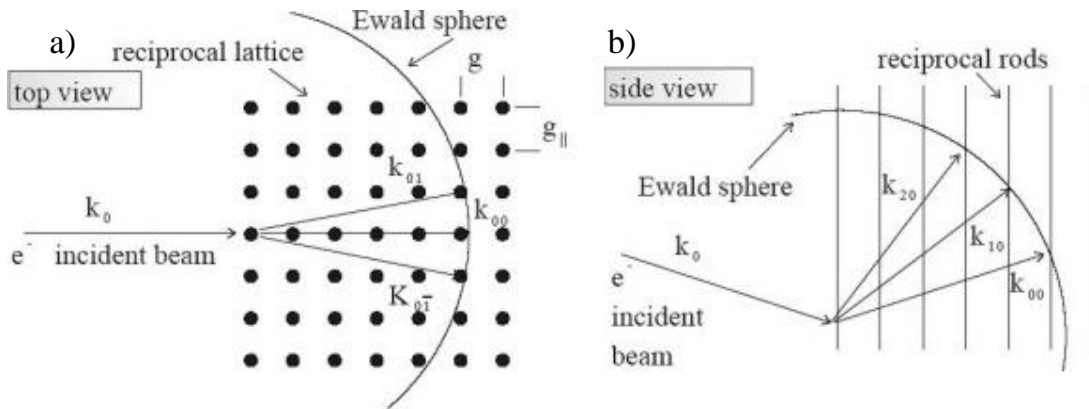

Fig. 4.1.2 Ewald sphere construction for RHEED experiment, top view a) and side view b). Reciprocal lattice is constructed from rods instead of spots as in 3D diffraction. Adapted from [C1].

For any reciprocal lattice point which sphere crosses, the line from the sphere center represents a diffracted beam. For diffraction process from two dimensional periodic system (surface) only the parallel to the surface

75

components of the wave vector are conserved – reciprocal space vectors have only two components and are represented as rods (Fig. 4.1.2 b)) in reciprocal space instead of points as in three dimensional case.

Surface sensitivity is obtained by grazing incidence angle (θ is usually from 0.5° to 5°, as shown in Fig. 4.1.1). Because of the high electron energies (up to 50 keV), incident wave vector is big in comparison with reciprocal lattice and Ewald sphere intersection with reciprocal rods are not zero dimensional points but rather 1D streaks shown in Fig. 4.1.3 a).

Fig. 4.1.3 RHEED images of the flat $SrRuO_3$ film surface a), of atomically smooth $SrTiO_3$ substrate b) and 3D diffraction from islands on the $SrTiO_3$ doped with Bi film surface c) (experiments in EPFL LC).

RHEED diffraction pattern is also influenced by many other factors like distribution of the lattice parameters (thin film case), focusing of electron beam etc. The diffraction pattern is a combination of diffraction from smooth surface and transmission-diffraction (as in bulk 3D case) from the particles on the surface. When first case is dominant – one observes spots (or streaks) lying on concentric Laue circles (in Fig. 4.1.3 b) shown first and second Laue circles). When diffraction through the particles dominates – 3D diffraction pattern is observable as in Fig. 4.1.3 c). Electrons are charged particles and strongly interact with a mater, thus it is difficult to interpret absolute intensities of diffraction pattern – it is studied by dynamical scattering theories, where electrons exhibit multiple scattering events in the solid.

One of the most useful RHEED application – in situ monitoring of the surface roughness and growth dynamics. In this experiment specular beam intensity is monitored and in 2D growth mode case, spot intensity is directly related to the growth rate (Fig. 4.1.4 c)). Here the surface is periodically roughened and smoothened during 2D nucleation and growth, as a result electrons are periodically scattered out of specular beam and intensity variations are observed.
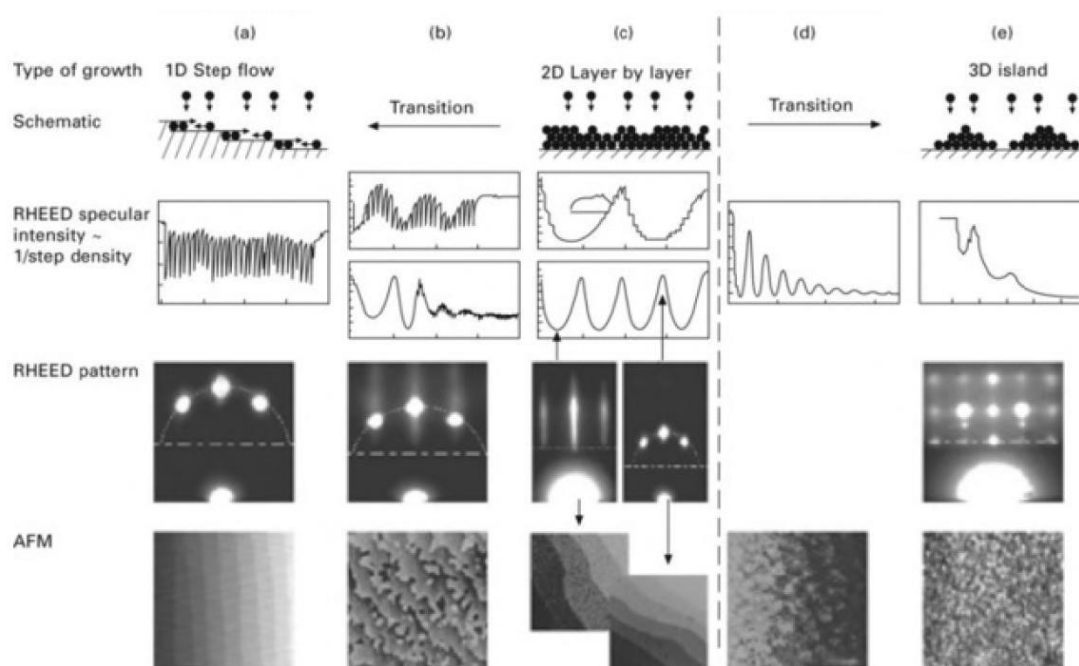

Fig. 4.1.4 Different growth modes during PLD. Step flow a), step flow like b), layer-by-layer c), transition from 2D to 3D growth d) and 3D growth e). Adapted from [C2].

Depending of surface reconstruction there is few more possibilities: stable (real 2D growth as in MBE), decaying (pseudo 2D observable in PLD, shown in Fig. 4.1.4 b) and d)) oscillations, also no oscillation (as in 3D growth mode) or relatively large intensity modulation of RHEED signal as in step-flow growth mode (Fig. 4.1.4 e) and a), respectively).

E-beam is attenuated at PLD pressures (even up to 1 mbar) by elastic and inelastic electron scattering. Two main requirements to combine PLD with

RHEED are low pressure in the electron source (usually $<10^{-6}$ mbar) and short e-beam path at high pressures. These requirements were satisfied by differentially pumped RHEED systems [C3], nowadays two-stage differentially pumped RHEED with small aperture is operated up to 0.5 mbar pressures (shown in Fig. 4.1.5).
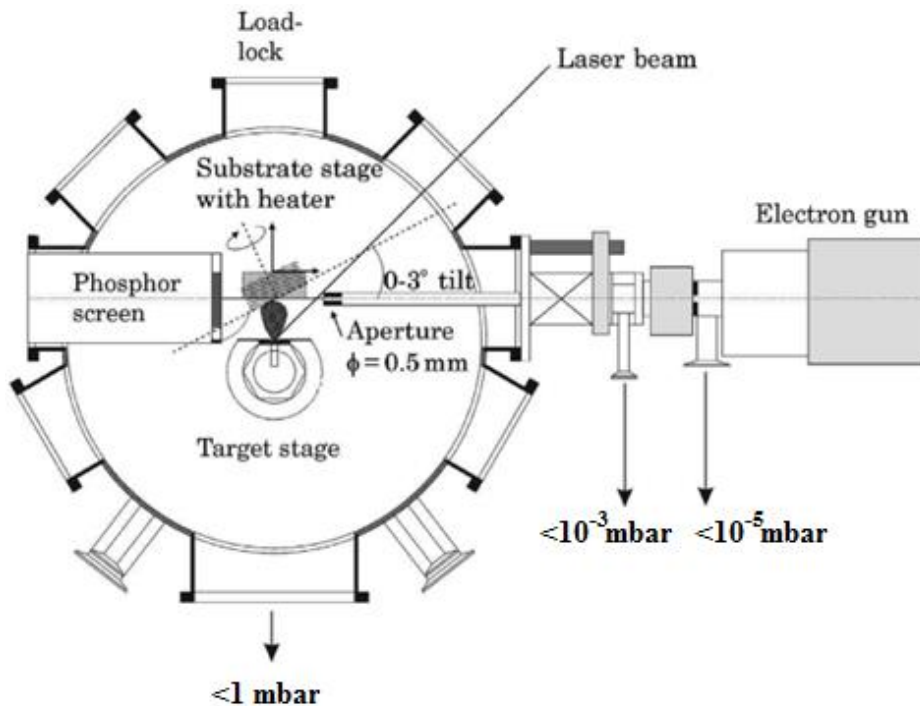

Fig. 4.1.5 PLD chamber equipped with two-stage differentially pumped RHEED system, adapted from [B21].

4.1.2. Scanning probe microscopy.

Scanning probe microscopy concept is - using the interaction of a small physical probe with a solid surface to obtain spatially resolved information about the surface. The probe is scanned across the sample (x, y spatial position) and the interaction is monitored (electron tunneling, electrostatic force, piezo force, conductivity etc.).

In atomic force microscopy (AFM) the tip is approached to the sample surface and the force acting on the tip can be approximated by the Hooke's law. The degree with which the probe is bended is controlled by feedback loop

– keeping the force constant i.e. keeping the distance between the tip and surface constant. There are two modes of operation in AFM – contact mode and tapping mode. In contact mode the tip is always at predefined distance (in contact with the sample at macroscopic scale), force between the tip and sample is kept constant (at setpoint value). In the tapping mode – the cantilever is oscillating near its resonant frequency (close to resonant frequency of the tip-sample surface system) with constant amplitude. The tip touches the surface only at the bottom of the swing, feedback loop keeps oscillation amplitude constant (at setpoint).
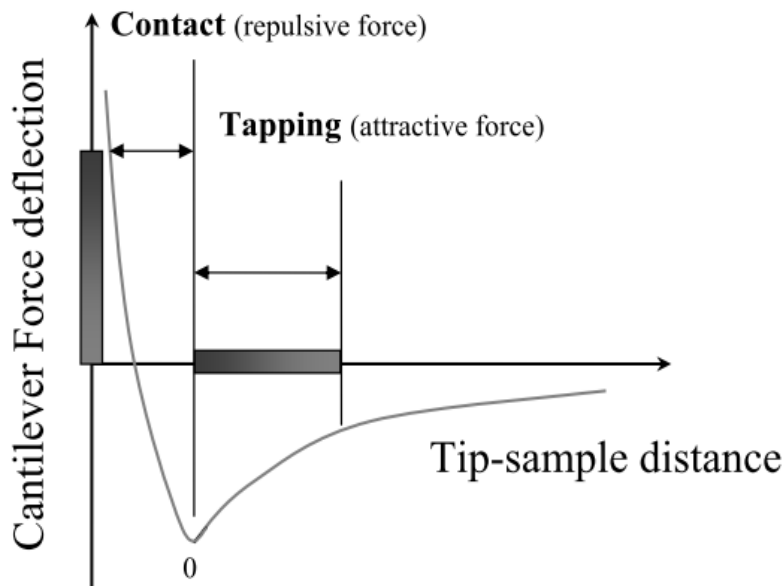
Forces acting on cantilever are shown in Fig. 4.1.6. Contact mode AFM works in repulsive force range and tapping mode – in the attractive force mode. The setpoints are labeled by two bars, and lighter gray corresponds to

Fig. 4.1.6 AFM tip-sample interaction [C4].

the decrease of either repulsive or attractive force. Contact mode is easier to implement, because of lack tracking the resonance frequency, but tapping mode less damages the tip itself and the imaging surface.

Ferroelectrics are special group of polar materials which possess the ability to switch their spontaneous polarization with an external electric field. The opposite ferroelectric domains have piezoelectric constants which are opposite in sigh – such a feature gives the foundation of piezo response

79

microscopy. This technique allows simultaneous detection and modification (if desired) of the ferroelectric polarization on the nanometer scale.

PFM (usually named piezo force microscopy) is based on the converse piezoelectric effect. Applied electric field to a ferroelectric material cause change of its dimensions and vice versus. For the detection of the polarization conductive cantilever is used as a top electrode.
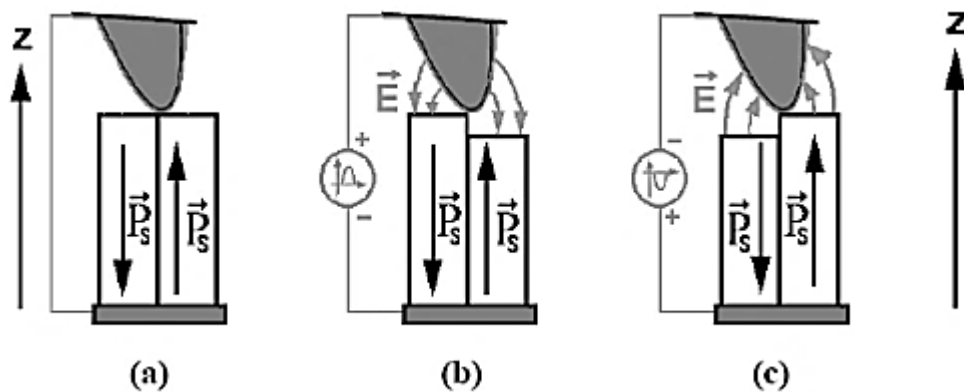

Fig. 4.1.7 Principle of PFM [C4].

When voltage is applied between the top electrode (the tip itself) and the bottom electrode, field is created inside the sample and depending on the initial direction of polarization sample is expanded (shown Fig. 4.1.7 b)) or contracted (Fig. 4.1.7 c)) due to converse piezoelectric effect, using constituent equations Δz is expressed:

$$\Delta z = -d_{ij} \cdot E_i \qquad 4.1$$

where d – piezoelectric coefficient and E – field. Depending on the polarization direction piezoelectric coefficient changes its sigh i.e. when $P_z > 0$ d_{33} is positive and when $P_z < 0$ - d_{33} is negative. Thus it is possible to distinguish between different polarization domains. Main problem is the absolute value of deformation which is usually at the limit of system sensitivity (for typical ferroelectric material's and applicable voltages). To overcome this issue it was developed AC method combined with lock-in detection system to improve signal-to-noise ratio. Instead of DC voltage (and field E), AC voltage

is applied. Different polarization states are distinguished by the fact that if dipole is oriented in opposite to the field (shown in Fig. 4.1.7 c)), the deformation of the surface is out of phase by 180° with the driving field. Schematic illustration of PFM system is given in Fig. 4.1.8.

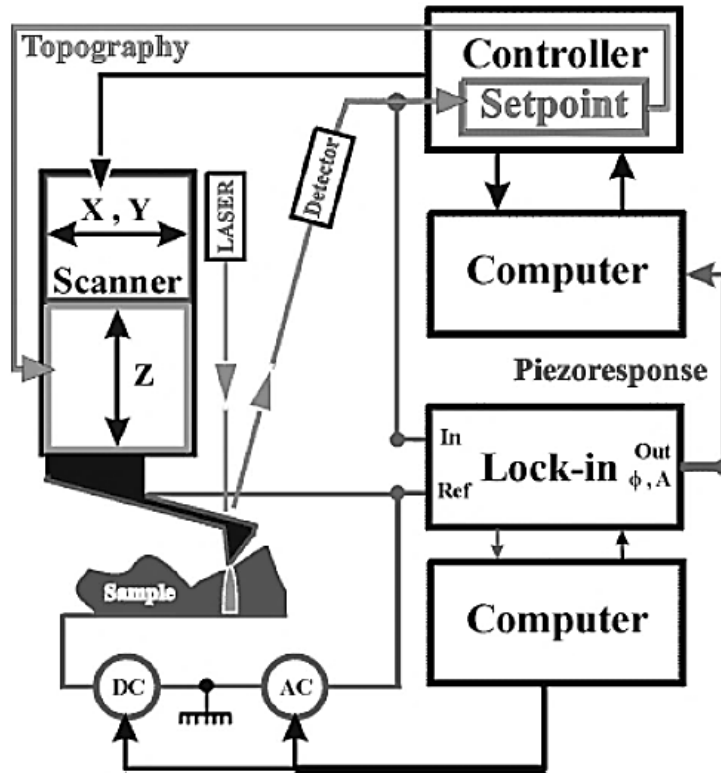

Fig. 4.1.8 Schematical picture of typical PFM setup [C4].

At the same time surface topology and piezoresponse is observed with very high resolution, an example is shown in Fig. 4.1.9.
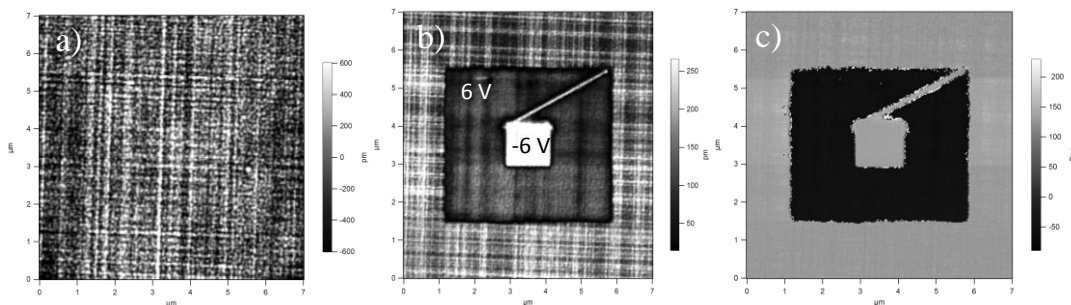

Fig. 4.1.9. Example of PFM. Measurements of ferroelectric $Ba_{0.7}Sr_{0.3}TiO_3$ thin film: topography (ferroelastics domains) a), amplitude b) and phase c) after poling experiment with 6 V voltage (experiment in EPFL LC).

AFM images were obtained using Autoprobe CP and CPII microscopes (Park Scientific Instruments, USA). For contact mode silicon ContAl-G probes (Innovative Solutions Bulgaria, Bulgaria) with nominal force constant $k = 0.2$ N/m were used.

PFM experiments were done with two systems. Room temperature experiments were done with multimode scanning probe microscope (Cypher, Asylum Research, USA) capable of measuring broad range of surface characteristic such as topography, piezo force, conductance, electrostatic force etc. with improved tapping mode – DART (dual AC resonance technique utilizing two lock-in amplifiers and two frequencies close to fundamental resonance frequency – ability to track resonance and enhance SNR). For DART-PFM it was used ASYELEC Ti/Ir coated conductive probes (Asylum Research, USA) with force constant $k = 42$ N/m, resonance freq. $= 300$ kHz and tip radius ~28 nm. Low temperature experiments were done with Cryogenic STM & SFM (Omicron NanoTechnology GmbH, Germany) capable to measure temperature dependent SPM down to 4 K temperature with atomic resolution (STM mode).

4.1.3. X-ray diffraction.

The structure and strain in thin films were determined by x-ray diffraction on high resolution triple axis difractometer (D8 Discover, Bruker, Germany) using monochromatic Cu K_α (filtered Cu K_β wavelength radiation) radiation source and position sensitive detector. Using different scan possibilities (*Θ-2Θ*, *ω-2Θ*, rocking curve *ω*, reciprocal space (hkl) maps etc.) layers thickness, lattice constant, crystallographic orientation and quality of thin films (and ceramic targets) were examined.

4.1.4. SEM/TEM electron microscopy.

Scanning electron microscopy images were taken on FEI XLF30-FEG (FEI, USA) with 1-30 kV Schottky field emission gun, imaging resolution

(using Everhart-Thornley secondary electron detector) was 2 nm at 30 kV and 8 nm at 1 kV. This SEM microscope had EDAX Si(Li) EDX detector with ultra-thin window for light element analysis.

Transmission electron microscopy images were taken with Philips CM300 (Philips, Netherlands), field emission electron source operated at 300 kV accelerating voltage. It has a point resolution of 0.2 nm and an information limit of 0.12 nm. The minimum focused probe size is 0.3 nm. Main applications of this microscope was bright field and dark field TEM imaging, high resolution TEM, selected area diffraction and energy dispersive x-ray spectroscopy (EDX).

Another TEM microscope was used FEI Tecnai Osiris (FEI, USA) analytical TEM instrument optimized for high speed and high sensitivity EDX measurements in STEM mode. Working voltage 80-200 kV with high brightness XFEG, 0.24 nm point resolution, 0.14 nm information limit, 0.18 nm HAADF scanning TEM resolution.
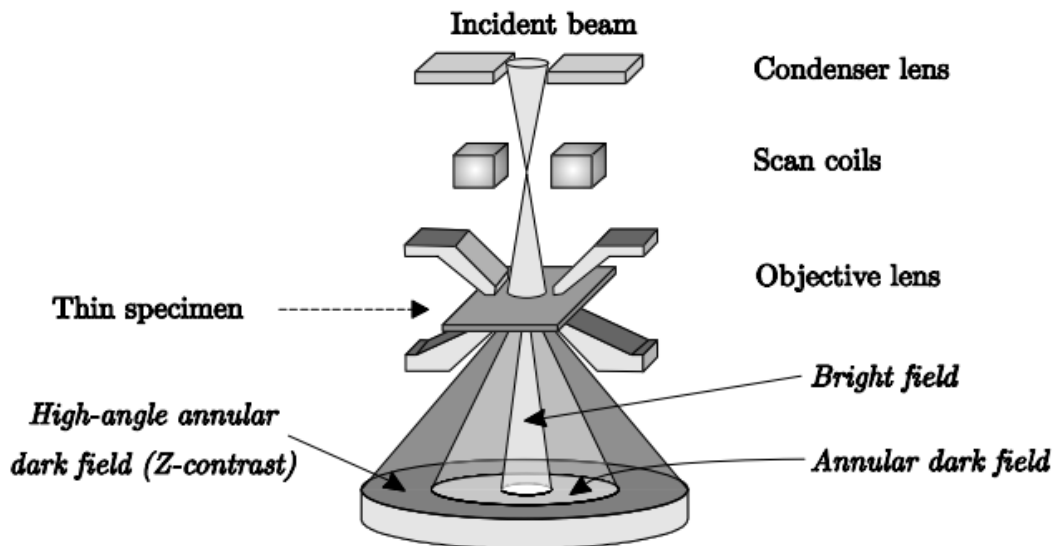

Fig. 4.1.10 Schematic view of TEM and STEM modes. Adapted from [B25].

The HAAD-STEM method employ scanning TEM microscopy with high angle scattered electron detector, thus Bragg scattered electron contribution is minimized and main contrast comes from incoherent thermal diffuse scattering,

83

also known as Z-contrast, schematically shown in Fig. 4.1.10 (Z is an average atomic number of the constituent atomic column below the electron beam). Such incoherent STEM imaging technique is less sensitive to defocus and thickness changes as in high resolution TEM.

All SEM/TEM characterization was done with the help of dr. Silviu Cosmin Sandu in EPFL CIME.

4.2. Dielectric characterization.

In this chapter measurement techniques and methods of dielectric spectroscopy will be described. All of them were used for bulk material characterization.

4.2.1. Low frequency region.

In the low frequency range from 20 Hz to 1 MHz sample capacitance and loss tangent were measured with the precision LCR meter HP4284 (Hewlett Packard, USA). In the ultralow frequency range from 10 μHz to 65 kHz Solartron 1250 (Solartron Analytical, UK) frequency response analyzer with a Solartron 1296 dielectric interface was used. At low frequencies also Novocontrol Alpha-analyzer (Novocontrol Technologies GmbH, Germany) with ZG-4 test interface was used.

Painted silver or platinum paste and magnetron sputtered gold, chrome/gold or platinum were used for contacts. At frequencies below 1 MHz inductance and resistivity of connecting cables and electrical contacts can be neglected, complex dielectric permittivity was calculated from the planar capacitor formulas:

$$\varepsilon' = \frac{(C\prime_m - C\prime_0)d}{\varepsilon_0 S} + 1, \qquad\qquad 4.2$$

$$\varepsilon'' = \varepsilon' tg\delta = \frac{C\prime_m tg\delta_m - C\prime_0 tg\delta_0}{C\prime_m - C\prime_0}, \qquad\qquad 4.3$$

where C'_m and $tg\delta_m$ are the capacitance and loss tangent of the system with the sample. C'_0 and $tg\delta_0$ are the capacitance and loss tangent of the system without the sample, d is the height of the sample, S is the area of the sample, ε_0 is dielectric permittivity of vacuum. The area of the sample was kept way larger than the thickness so that the fringing field effects were insignificant. Temperature was measured with different platinum RTDs and thermocouples depending on the temperature ranges. Measurements were performed on the cooling cycle with the typical 1 K/min cooling rate. Bulk ceramic samples were usually annealed to eliminate memory effects – to break frozen PNRs (where applicable) and to have the same initial conditions. Homemade furnace (from room T up to 500 K) and commercial furnaces (from room T up to 1000 K) were used for heating above the room temperatures. For cooling below the room temperature the vapor from liquid nitrogen (cooling down to 100 K) and closed cycle helium cryostat (down to 30 K) were used.
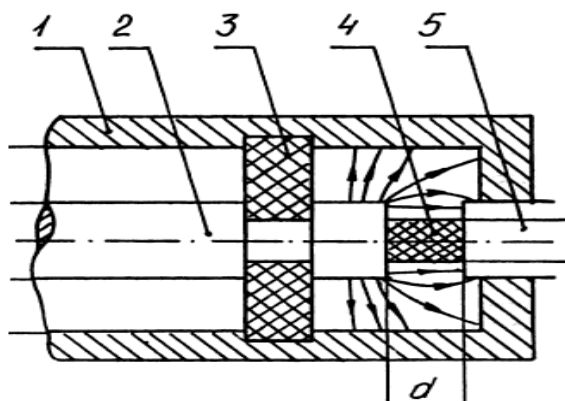
4.2.2. High frequency region.

Fig. 4.2.1. Dielectric specimen in a coaxial line spectrometer. 1and 2 - outer and inner conductors, 3 – dielectric spacer, 4 – sample and 5 - short piston with temperature sensor (RTD or thermocouple). Adapted from [C6].

High frequency dielectric measurements were performed with homemade spectrometer [C5]. The coaxial technique is most convenient for dielectric spectroscopy of solids in the frequency range from 1 MHz up to few GHz. The specimen is placed at the end of the coaxial transmission line between the inner conductor and the short piston (shown in Fig. 4.2.1), this way one obtains the capacitor.

Complex reflectivity coefficient $R^* = |R|\exp(i\varphi)$ was measured with Agilent 8714 ET (Agilent Technologies, USA) vector network analyzer in the frequency range from 1 MHz to 3 GHz. Coaxial lines have broadband transmission characteristic, there is no limitation from low frequency side and from high frequencies the condition for main TEM wave propagation is limiting factor, this condition is expressed [C5]:

$$\lambda > \pi(r_{in} + r_{out}), \qquad 4.4$$

here r_{in} and r_{out} are inner and outer diameters of coaxial line conductors respectively, λ is the length of electromagnetic wave. This condition implies that higher the measurement frequency – smaller the sample and coaxial line dimensions needs to be.

Complex reflection coefficient and complex impedance of measured capacitor are related to each other by following relationship:

$$R^* = \frac{Z_m^* - Z_0}{Z_m^* + Z_0}, \qquad 4.5$$

where Z_m^* and Z_0 are measured capacitor and the system impedances respectively. It is well known (neglecting inductance) that complex impedance is related to complex capacitance by relation:

$$Z_m^* = \frac{1}{\omega C_m^*}. \qquad 4.6$$

Having in mind parallel plate capacitor, 4.2 formula can be generalized as follows:

$$\varepsilon' - i\varepsilon'' = \frac{d}{\varepsilon_0 S}(C' - iC'') + 1. \qquad 4.7$$

From 4.5, 4.6 and 4.7 equations one obtains the formulas for calculating the real and imaginary parts of the complex dielectric permittivity ε^* for measured sample:

$$\varepsilon' = \frac{d}{\varepsilon_0 S_s}\left(\frac{-2R\sin\varphi}{\omega Z_0(1+2R\cos\varphi+R^2)} - C_0\right) + 1, \qquad 4.8$$

86

$$\varepsilon'' = \frac{d}{\varepsilon_0 S_S}\left[\frac{1-R^2}{\omega Z_0(1+2R\cos\varphi+R^2)}\right]. \qquad 4.9$$

where R and φ are modulus and phase of complex reflection coefficient (two directly measured quantities in vector network analyzer).

These equations are valid only when the field in the sample is homogeneous. This condition implies that sample geometrical dimension should be significantly smaller that exciting electromagnetic wave wavelength. At high frequencies (depending on the sample permittivity) field in the sample becomes inhomogeneously distributed (shown in Fig. 4.2.2) according to [C7]:

$$E = AJ_0\frac{kr}{\sqrt{\varepsilon'}}, \qquad 4.10$$

where A is model constant, depending on the geometry of the sample, r is the distance from disc-shaped sample center, J_0 − first order Bessel function and k is the wavenumber. Assuming that sample rod radius is 10 times smaller than first J_0 root, one might consider the field in the sample as quasihomogeneous (only small ~2% error is made).
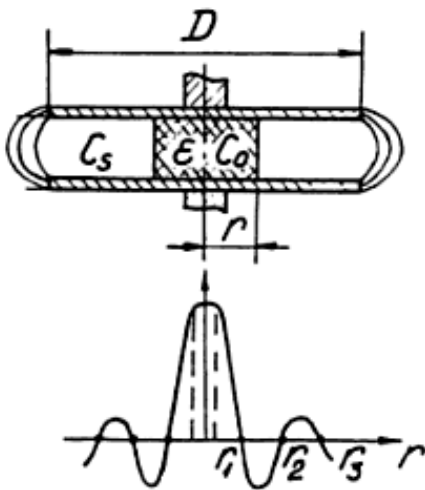

Fig. 4.2.2. High frequency electric field distribution in the specimen [C7]. C_S – spurious capacitance due to fringing field at the capacitor edges.

To fulfill quasihomogeneous field conditions, sample should be smaller than:

$$r \leq \frac{0.24\lambda}{2\pi\sqrt{\varepsilon'}}. \qquad 2.11$$

Inhomogeneities in the coaxial line and specimen holder entangle systematic errors (which influences to measurement precision increases with increasing frequency). These kinds of errors might be corrected invoking calibration procedures. In one port (reflection) coaxial line spectrometer SOL (short, open, load) calibration method was used to correct systematic errors.

4.2.3. Microwave region.

Dielectric spectroscopy at microwave frequencies have advantage over scattering techniques due to the possibility acquire both parts - real and imaginary - of dielectric permittivity instead of just imaginary part as in IR and other scattering experiments.

Displacive ferroelectric soft mode lies in the frequencies accessible by different kind of spectroscopic techniques like IR reflectivity/transmission, terahertz and Raman spectroscopy, but microwave spectroscopy allows measuring not only loss part but also the real part of dielectric permittivity. Waveguide dielectric spectroscopy method was used in this thesis for obtaining of dielectric properties at microwave frequencies.

Thin cylindrical rod was placed into the rectangular waveguide and modules of microwave transmission and reflection coefficients were measured with automatic dielectric spectrometer [C6], schematically shown in Fig. 4.2.3.
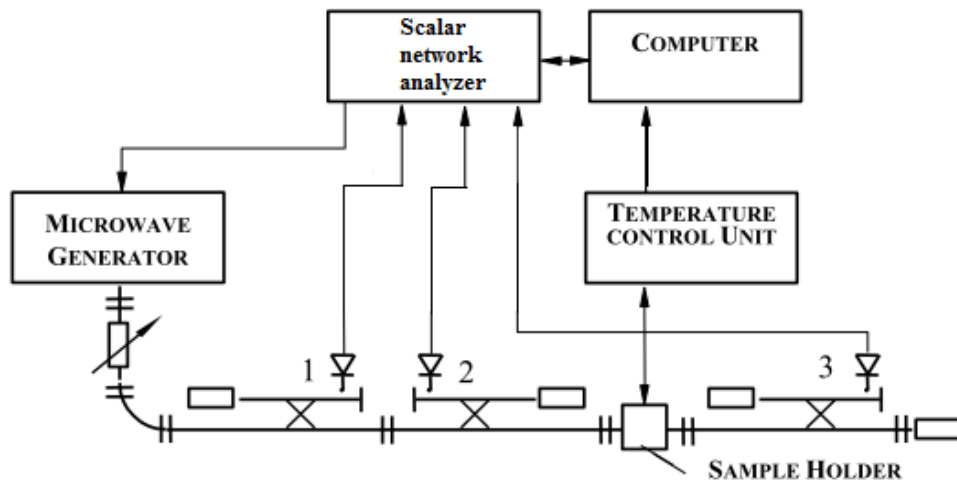

Fig. 4.2.3. Microwave dielectric spectrometer setup for reflection and transmission measurements with rectangular waveguide. Adapted from [C6].
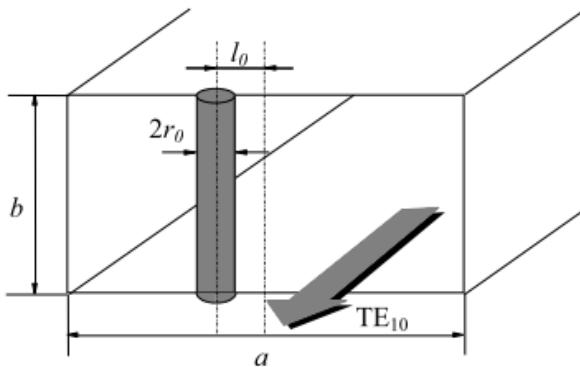
Generators (ГКЧ-61 for 8 – 12 GHz band, Р2-65 for 26 – 37 GHz band and Р2 – 68 for 37 – 53 GHz band) were used as variable microwave sources. Scalar network analyzers (Elmika R2400, Elmika, Lithuania) with different

cross-section rectangular waveguides allowed measuring scalar reflection and transmission coefficients in the frequency range from 8 GHz to 53 GHz.

Frequency dependent reflection $R(v)$ and transmission $T(v)$ coefficients were measured in all available frequency range, which was discretized to few hundred points and also scan was repeated coupled of times and values were averaged for systematic error elimination. After smoothening of the curves, selected frequency values of R and T were saved to personal computer for further analysis.

Dielectric permittivity was calculated according to the method of thin rectangular dielectric rod in the center of waveguide. The sample was glued into the sample holder (metallic insert, the same size as waveguide cross-section) in such way that after inserting the rod would be in the center of the wide waveguide wall, parallel to the electric field of the main TE_{10} mode (as shown in Fig. 4.2.4). Additional two metallic inserts were used for calibration (one as a short and another one as open references), thus allowing to eliminate systematic errors and verify the calibration during experiment.

Fig. 4.2.4. Thin cylindrical rod in a rectangular waveguide.

Complex dielectric permittivity $\varepsilon^*(v)$ can be estimated from nonlinear equations $\varepsilon^*=f(R^*)$ or $\varepsilon^*=f(R, T)$. When the specimen satisfies $\alpha_0=kr\ll1$ condition, the complex reflection coefficient is expressed as follows:

$$R^* = -\frac{4(\varepsilon^*-1)J_1(\beta_0)}{\pi\Delta_1\sqrt{\left(\frac{2a}{\lambda}\right)^2-1}},$$

4.12

$$\Delta_1 = \varepsilon^* J_1(\beta_0) \left[H_0^{(2)}(\alpha_0) + 2\sum_{m=1}^{\infty}(-1)^m H_0^{(2)}(mka) \right] - \sqrt{\varepsilon^*} J_0(\beta_0) H_1(\alpha_0), 4.13$$

where J_0, J_1 are the Bessel functions, $H_0^{(2)}$, H_1 are the Hankel functions, $\beta_0 = k_0\sqrt{\varepsilon}r$, a is the width of a waveguide wall and λ – wavelength in vacuum.

When losses of the specimen are zero then the TE_{10} wave is fully reflected at $$\upsilon_0 = \frac{c}{2\pi r\sqrt{\varepsilon}}$$ frequency. 4.14

When dielectric losses increase, the reflection and transmission coefficients dependence from the real part of permittivity becomes shallower (dependence decreases) as shown in Fig. 4.1.15 a). Precision of this method extremely decreases at higher than υ_0 frequencies. Optimal range for determination of ε^* is $0.2 < R < 0.85$, as shown in Fig. 4.2.5.
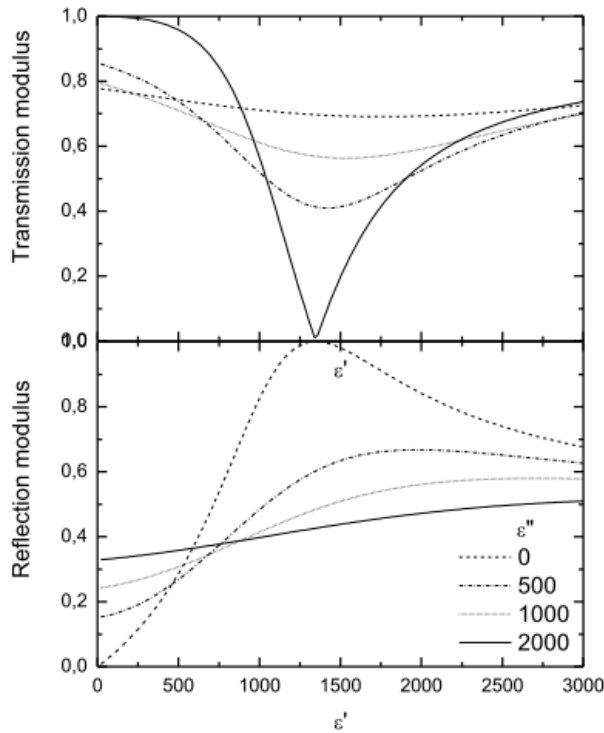
Fig. 4.2.5. Microwave transmission and reflection coefficient module dependence from the complex dielectric permittivity of the specimen, when $\upsilon = 10$ GHz and sample radius $= 100$ µm.

Newton method was used to calculate dielectric permittivity. This method allows converting nonlinear equations: $R = f_1(\varepsilon', \varepsilon)$ and $T = f_2(\varepsilon', \varepsilon)$ (4.15) into linear form.

The limits and initial values of ε^* were chosen approximately and iteration was stopped when:

$$R - f_1(\varepsilon', \varepsilon'') < \delta \text{ and } T - f_2(\varepsilon', \varepsilon''),\qquad 4.16$$

where δ is the accuracy of calculations, δ was usually selected of 0.001, because measurements accuracy was smaller.

4.2.4. Theoretical models.

One of the main attribute of disordered materials like ferroelectric relaxors, dipolar glasses and incipient ferroelectrics is very broad dielectric dispersion close to some critical temperature. In ferroelectrics dispersion can be approximated by Debye formula [C7] fairly well:

$$\varepsilon^*(\omega) = \varepsilon_\infty + \frac{\Delta\varepsilon}{1+i\omega\tau}, \qquad\qquad 4.17$$

where ε_∞ is a contribution from all higher frequency processes, like electronic and ionic polarization, $\Delta\varepsilon$ is the strength of relaxator and ω is cyclic frequency.

In disordered materials dielectric dispersion is very broad and cannot be described by one relaxation time, thus an ensemble of Debye type processes is considered:

$$\varepsilon'(\omega) = \varepsilon_\infty + \Delta\varepsilon \int_{-\infty}^{+\infty} \frac{f(\ln\tau)}{1+(\omega\tau)^2} d(\ln\tau), \qquad 4.18$$

$$\varepsilon''(\omega) = \Delta\varepsilon \int_{-\infty}^{+\infty} \frac{f(\ln\tau)(\omega\tau)}{1+(\omega\tau)^2} d(\ln\tau). \qquad 4.19$$

These two equations (first kind Fredholm integral equations) define relaxation time distribution function $f(\tau)$. Different relaxation time distribution function $f(\tau)$ can fulfill 4.18 and 4.19 equations at the same $\varepsilon^*(\omega)$ value, thus such integral equations represent ill-posed problem. One of the method for solving 4.18 and 4.19 system of equations is to choose such $f(\tau)$, that it would be possible to integrate analytically. There are few predefined relaxation time distribution functions; one of them is Cole-Cole function [C9]:

$$f(\tau) = \frac{\sin\alpha_{cc}\pi}{\cosh\left[(1-\alpha_{cc})\ln 2\pi\frac{\tau_{cc}}{\tau}\right]-\cos\alpha_{cc}\pi}, \qquad 4.20$$

where $0 \leq \alpha_{cc} \leq 1$ is a parameter describing the width of the Cole-Cole function and τ_{cc} is mean and the most probable relaxation time. Inserting 4.20 into the 4.18 and 4.19 one obtains following expression of $\varepsilon^*(\omega)$:

$$\varepsilon^*(\omega) = \varepsilon_\infty + \frac{\Delta\varepsilon}{1+(i\omega\tau_{CC})^{1-\alpha_{cc}}} . \qquad 4.21$$

This formula describes dielectric permittivity when relaxation time distribution function is symmetric. When this function is asymmetric one can use superposition of Cole-Cole functions or another asymmetric function like Cole-Davidson [C10]:

$$f(\tau) = \frac{sin\gamma\pi}{\pi}\left(\frac{\tau}{\tau_{CD}-\tau}\right)^\gamma, \tau < \tau_{CD}, f(\tau) = 0 \; when \; \tau > \tau_{CD} . \quad 4.22$$

Where τ_{CD} is most probable relaxation time according to Cole-Davidson function and γ is a parameter describing asymmetry. From 4.18, 4.19 and 4.22 one obtains:

$$\varepsilon^*(\omega) = \varepsilon_\infty + \frac{\Delta\varepsilon}{(1+i\omega\tau_{CD})^\gamma} , \qquad 4.23$$

Summing Cole-Cole and Cole-Davidson formulas one obtains Havriliak-Negami function, which is useful describing very broad and asymmetric dielectric permittivity dispersions [C11-12]:

$$\varepsilon^*(\omega) = \varepsilon_\infty + \frac{\Delta\varepsilon}{(1+(i\omega\tau_{HN})^{1-\alpha_{cc}})^\gamma} \qquad 4.24$$

and relaxation time distribution function:

$$f(\tau) = \frac{1}{\pi}\frac{\left(\frac{\tau}{\tau_{HN}}\right)^{(1-\alpha_{cc})\gamma} sin(\gamma\Theta)}{\left[\left(\frac{\tau}{\tau_{HN}}\right)^{2(1-\alpha_{cc})}+2\left(\frac{\tau}{\tau_{HN}}\right)^{(1-\alpha_{cc})}cos\pi(1-\alpha_{cc})+1\right]^{\gamma/2}} , \qquad 4.25$$

$$\Theta = arctan\frac{sin\pi(1-\alpha_{cc})}{\left(\frac{\tau}{\tau_{HN}}\right)^{(1-\alpha_{cc})}+cos\pi(1-\alpha_{cc})} . \qquad 4.26$$

Havriliak-Negami function describes dielectric dispersion in disordered materials the best of previously mentioned functions. Major difficulty of using

all these functions (Cole-Cole, Cole-Davidson, Havriliak-Negami, and many more [C13]) is that relaxation time distribution function needs to be known a prior, what sometimes is very difficult or inefficient.

To overcome this nuisance one should solve 4.18 and 4.19 equations without a priori defined relaxation time distribution functions. One of the ways solving these equations is to use numerical methods – discretize and convert to a set of linear nonhomogeneous algebraic equations. Method, described in [C14] employing Tikhonov regularization technique for solving 4.18 and 4.19 equation, was used and relaxation distribution function was extracted from experimental data.

The temperature dependence of the mean relaxation time (from Cole-Cole, Cole-Davidson, Havriliak-Negami functions and relaxation times distribution function) can be approximated by Arrhenius (Eq. 4.27) or Vogel-Fulcher laws (Eq. 2.15) $\tau = \tau_0 exp\left(\frac{E_a}{k_B(T-T_f)}\right)$, where τ_0 is the attempt relaxation time at very high temperature, E_a is the activation energy for the analyzed process and T_f is freezing (or critically slowing down) temperature. This expression diverges at positive temperatures and at $T=T_f$ thermally activated dipole reorientation becomes impossible, unlike divergence at $T=0$ in Arrhenius law:

$$\tau = \tau_0 exp\left(\frac{E_a}{k_B T}\right). \qquad\qquad 4.27$$

Arrhenius law typically describes ferroelectric materials with independently relaxing dipoles and Vogel-Fulcher law (originally developed for glass viscosity description [C15]) better depicts disordered material behaviour, like dipolar glass freezing phenomena or critical slowing down in nonergodic ferroelectric relaxors phase at positive temperatures [C16].

References

C1 http://www.wmi.badw.de/methods/leed_rheed.htm (accessed on June 2014).

C2 Koster G., Rijnders G. "In Situ Characterization of Thin Film Growth" Woodhead Publishing, ISBN: 978-1-84569-934-5 (2011).

C3 Karl H., Stritzker B. *Phys. Rev. Lett.,* 69, 2939, (1992).

C4 Feiming Bai, Structure-property relationships of multiferroic materials – A nano perspective, PhD thesis, Virginia Polytechnic Institute and State University, USA (2006).

C5 Brilingas A., Davidovich R. L., Grigas J., Lapinskas S., Medkov M. A., Samulionis V., Skritskii V. *Physica Status Solidi (a),* 96, 101 (1986).

C6 Brandt A. "Issledovanie Dielektrikov Na Sverchvysokich Castotach", Fizmatgiz, Moscow, 1963.

C7 Grigas J. "Microwave Dielectric Spectroscopy of Ferroelectrics and Related Materials", Overseas Publishers Association, Amsterdam (1996).

C8 Jonscher A. K. "Dielectric relaxation in solids" Chelsea Dielectric Press, London (1983).

C9 Cole K. S., Cole R. H. *J. Chem. Phys.,* 9, 341 (1941).

C10 Davidson D. W., Cole R. H. *J. Chem. Phys.,* 19, 1484 (1951).

C11 Havriliak S., Negami S. *J. Polym. Sc. C.,* 14, 99 (1966).

C12 Havriliak S., Negami S. *Polymer.,* 8, 161 (1967).

C13 Zorn R. *J. Chem. Phys.,* 116,   8, 3204 (2002).

C14 Macutkevic J., Banysv, Matulis A. *Nonlin. Anal.: Modelling and Control*, 9, 75 (2004).

C15 Dagdug L. *J. Phys.: Condens. Matter,* 12, 9573 (2000).

C16 Levstik A., Kutnjak Z., Filipic C., Pirc R. *Phys. Rev. B.,* 57, 11204 (1998).

5. Results and discussion.

5.1. SrTiO₃ – an incipient quantum paraelectric.

Bulk $SrTiO_3$ (single crystal and ceramic) is well known and widely investigated material. STO have a cubic perovskite structure at room temperature with a space group Pm3m [D1]. Perovskites ABO_3 consist from 1-, 2- or 3-valent A-site cation and 5-, 4- or 3-valent B-site cation, and 2-valent anion. In STO case A-site is occupied by divalent Sr at the cube corners, in B-site is relatively small tetravalent Ti (at the cube center) and divalent O anions fill each of six cube faces. As indicated in space group Pm3m, STO lattice is primitive with one chemical base unite (Z=1, Z – is a number of formula units) per primitive cell (as shown in Fig. 5.1.1).
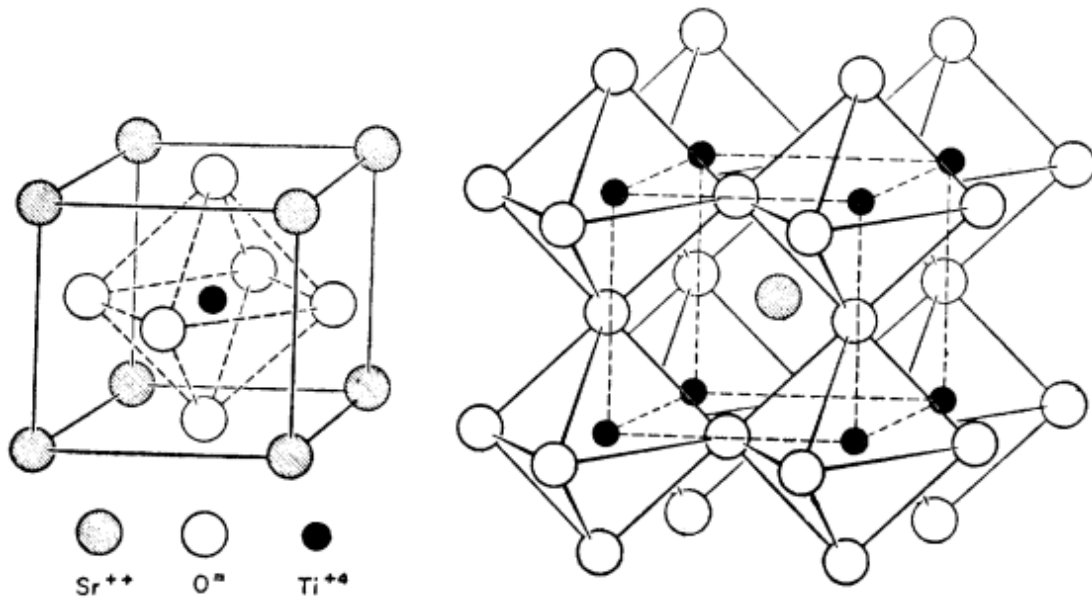
Fig. 5.1.1. Ideal perovskite structure – cubic $SrTiO_3$ at room temperature. Adapted from [D2].

At room temperature bulk STO lattice parameter is a=0.39046 nm [D3-4], also usually rounded to 0.3905 nm [D5 and many other]. When the temperature decreases down to ~105 K [D1] STO undergoes a structural phase transition from cubic to tetragonal symmetry phase with space

group I4/mcm [D6] and $a \approx \sqrt{2}a_0, c \approx 2a_0$. a and c lattice parameters variation as a function of temperature are shown in Fig. 5.1.2.
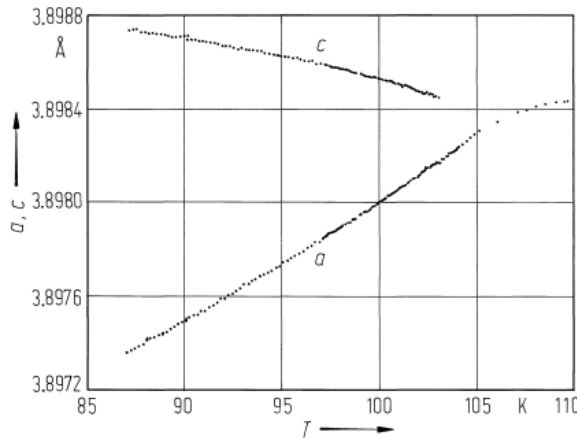

Fig. 5.1.2. Temperature dependence of STO a and c lattice parameters close to antiferrodistortive transition at 105 K, cell doubling is neglected [C7].

At antiferrodistortive phase transition temperature oxygen octahedra rotates in antiphase around one of the cubic axes [001] in as shown in Fig. 5.1.3. Structure changes from high temperature cubic to low temperature tetragonal, yet centrosymmetric, phase due to condensation of Brillouin zone (BZ) boundary phonon at R-point , confirmed by EPR [D6, D12], Raman scattering [D8], Brillouin scattering [D9], neutron inelastic scattering [D10] and ultrasonic measurements [D11].
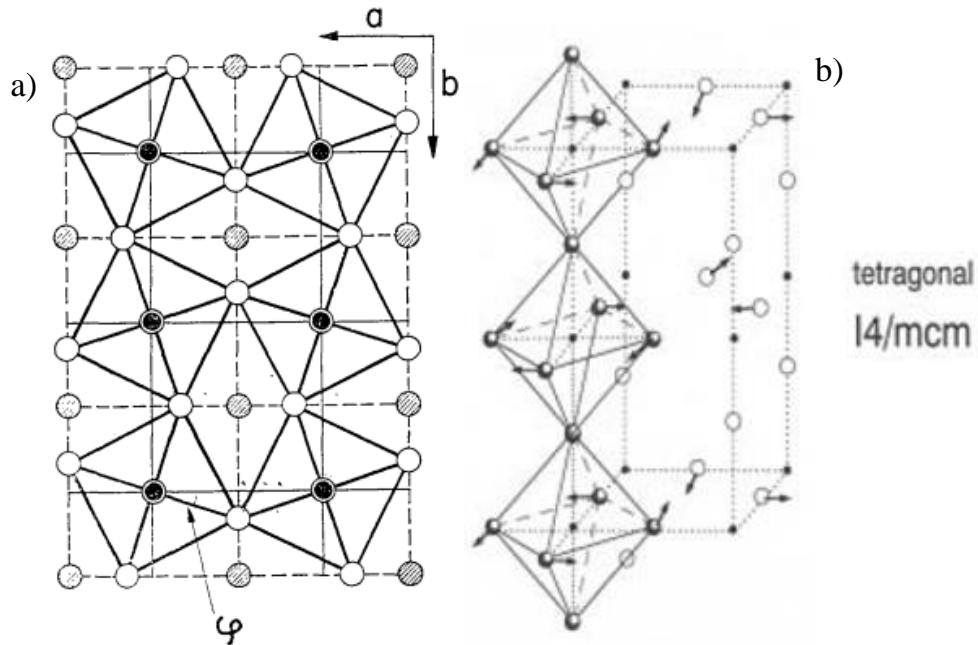
Fig. 5.1.3. The oxygen octahedra distortion in the plane perpendicular to the c-axis a) [D6] and in the plane parallel to c-axis b) [D18].
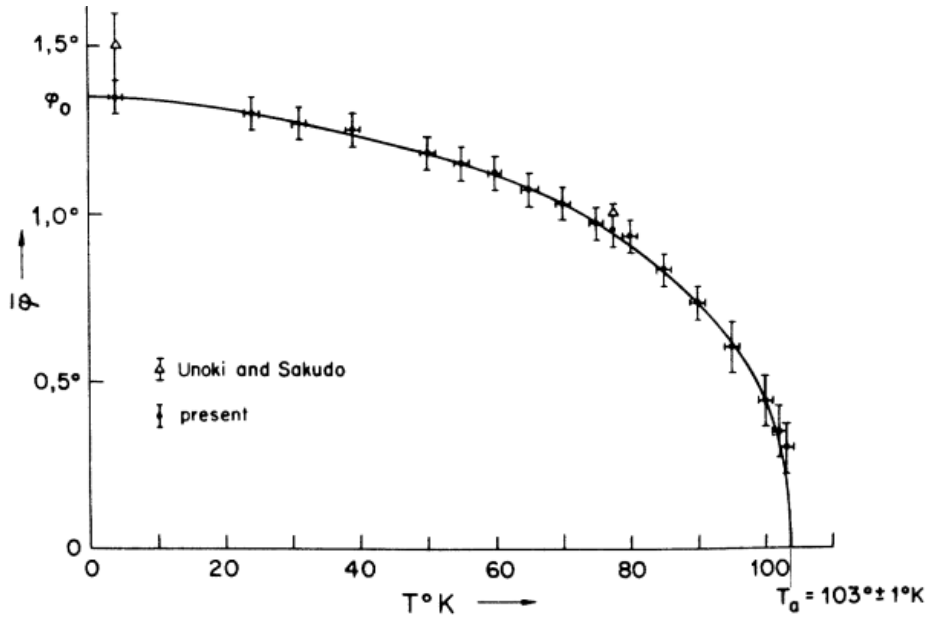
Fig. 5.1.4. Octahedron rotation angle obtained by EPR experiments [D6, D12].

Phonon accountable for the transition condensates at the R-point of BZ, thus phase transition is not a ferroelectric one, meaning no polarization is induced in low temperature phase. Order parameter of such transition is rotation angle γ (as shown in Fig. 5.1.3 and 5.1.4) .There is no unambiguous observation of dielectric permittivity anomaly related to this phase transition.

Unit cell doubles at T_a, Z = 1 (one formula unite per cell) in the cubic phase and Z = 4 (four formula unites per cell) in the tetragonal phase. This implies folding BZ so that R (zone corner [111]) point becomes zone center (Γ point) and triple degenerated phonon splits to two, as shown in Fig. 5.1.5.

Zone boundary phonon softens in accordance with Cochran law, with additional temperature independent term [D10]:

$$\frac{1}{\hbar^2\omega^2} = a + \frac{c}{(T-T_a)},\qquad 5.1$$

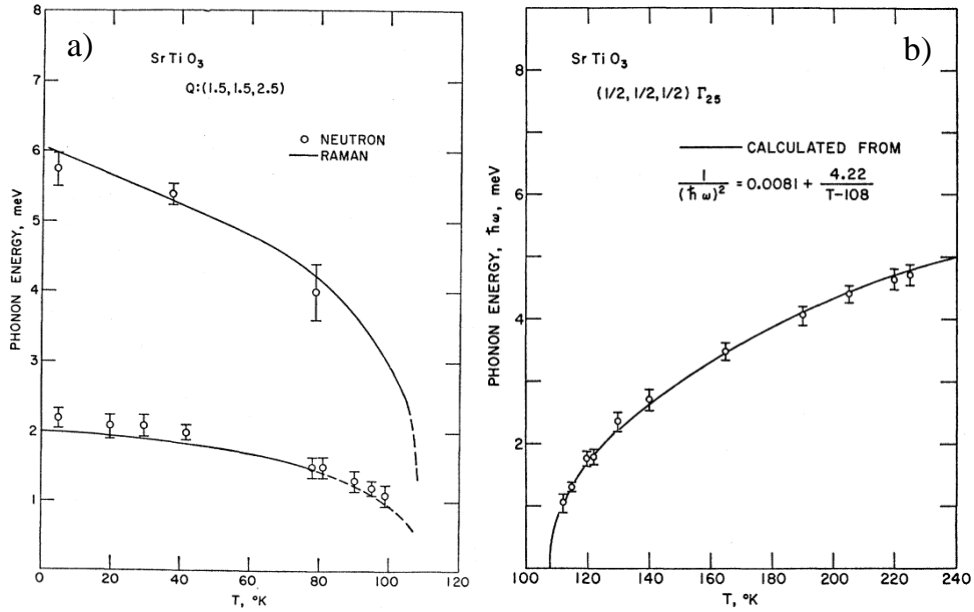with T_a = 108°C obtained from experimental data approximation from high temperature side.

Fig. 5.1.5. Temperature dependence of the F_{2u} (Γ_{25}) triple degenerated soft antiferrodistortive mode above T_a b). Below T_a triply degenerated mode F_{2u} splits to Raman active modes: A_{1g} and double degenerated E_g a). Adapted from [D10].

SrTiO$_3$ is very interesting, model system, because there are two instabilities simultaneous active. Another instability manifests itself by large and anisotropic (below T_a) dielectric constant, which saturates at liquid He temperatures with dielectric permittivity $\varepsilon_a \approx 40000$ (in ab plane) and $\varepsilon_c \approx 10000$ (along the tetragonal axe) [D13-15], shown in Fig. 5.1.6. This instability is considered ferroelectric one, because lowest energy BZ center optical phonon softens to very low (but not zero) energies at cryogenic temperatures. This behaviour was explained by quantum fluctuations (or zero point motion of Ti ion) [D15], which suppress complete mode softening and ferroelectric phase transition never happens.

Intrinsic quantum paraelectric behaviour was explained by Barrett's [A15-16] model, which is a quantum version of microscopic theory of Slater [D17], experimental dielectric permittivity data can be approximated by 2.7 and 2.8 formulas.
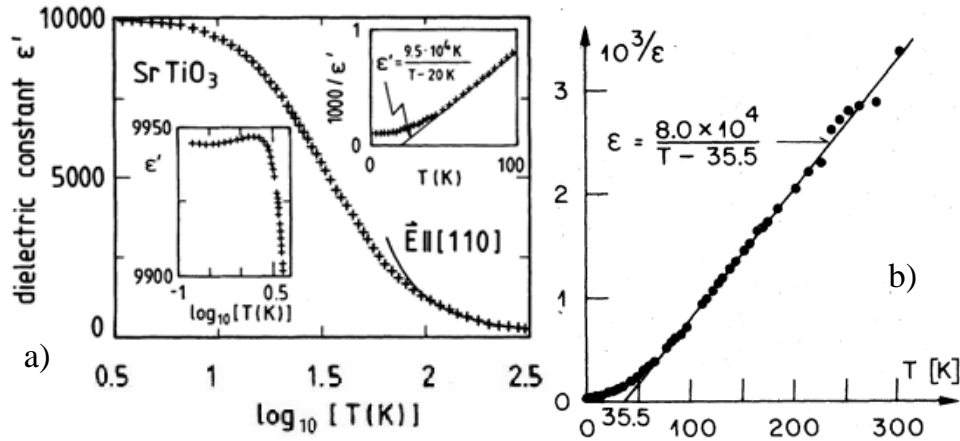
Fig. 5.1.6. Temperature dependence of dielectric permittivity a) [D16] and inverse dielectric permittivity b) [D15]. As can be seen in a) and b) departure from Curie-Weiss law starts to emerge at low temperatures.

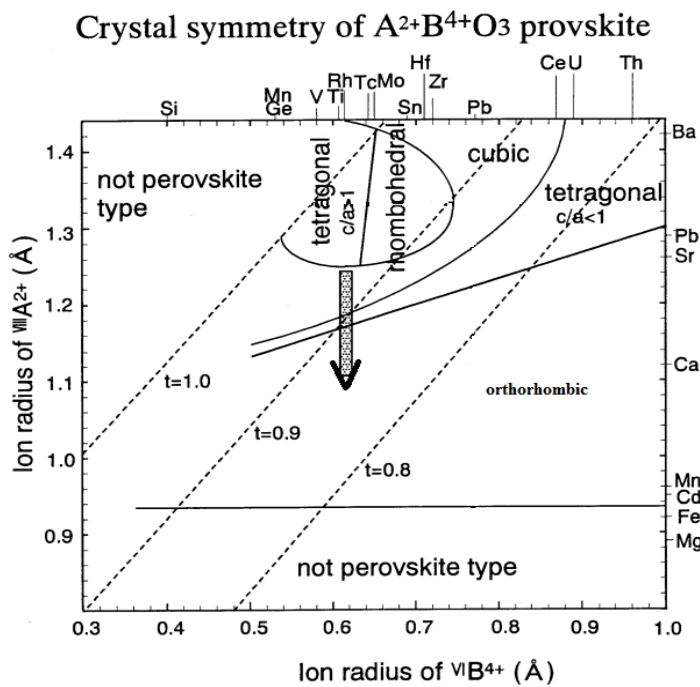## 5.1.1. Strain effects on the phase diagram and ferroelectricity.

Fig. 5.1.7. Structure of ABO_3 perovskites at ambient conditions. Arrow indicates the structure change at elevated pressures. Adapted from [D18].

Strontium titanate has a structure tolerance factor ≈ 1 (Fig. 5.1.7). This fact makes both phase transition to be very sensible to external stimulus like pressure [D14] and electric field [D19].

Biaxial strain can be induced in epitaxial thin films by the presence of a lattice mismatched substrate. Lattice mismatch, also known as in-plane

elastic strain or misfit strain, for short, between film and substrate is expressed as:

$$\epsilon_P(T) = \frac{a_s(T) - a_f(T)}{a_f(T)},$$
5.2

where $\epsilon_P(T)$- is parent misfit strain, $a_s(T)$ and $a_f(T)$ temperature dependent substrate and film lattice parameters respectively.
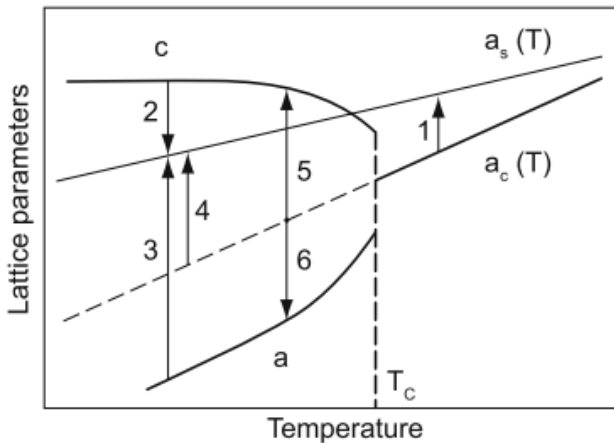

Fig. 5.1.8. Illustration for the concept of misfit and parent misfit strains [A1].

Material with a cubic/tetragonal phase transition at T_c is considered in Fig. 5.1.8. The temperature dependences of its lattice constants are shown: $a_c(T)$ - for the cubic phase, a and c - for the tetragonal phase. An epitaxial (001) film of this material deposited onto a (001) cubic substrate without formation of misfit dislocations is considered. The temperatures dependence of the substrate lattice constant is shown as $a_s(T)$. The variation of the lattice constants corresponding to the natural spontaneous strain (5, 6), misfit strain (1, 2, and 3) and parent misfit strain (1, 4) are shown with arrows [A1].

In the case of ferroelectrics misfit strain and clamping by substrate changes phase transition temperatures (T_c increases for $BaTiO_3$ and $PbTiO_3$) and character – from a first order (in bulk material) to a second order in thin film form. This behaviour was explained by *Pertsev et. al.* using Landau-Ginzburg-Devonshire formalism in [D20-21]. The same group of authors also developed strain-temperature phase diagram for $SrTiO_3$ (shown in Fig. 5.1.9).
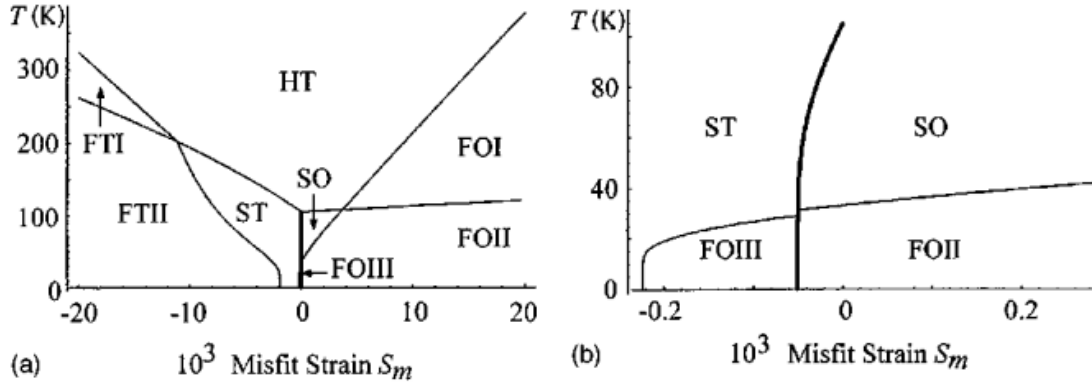
Fig. 5.1.9. Phase diagram of (001) - oriented single-domain SrTiO3 thin films epitaxially grown on different cubic substrates a) and its enlarged section near zero misfit strain b). The second- and first-order phase transitions are shown by thin and thick lines, respectively. Adapted from [D22].

Model predicted additional phases, instead just two as in bulk STO (high temperature cubic and low temperature tetragonal): HT - high temperature tetragonal phase, ST - "structural" tetragonal states SO - "structural" orthorhombic states, FTI - ferroelectric tetragonal phases, FOI - ferroelectric orthorhombic phases, FTII, FOII, and FOIII - "mixed" states where both P and q (structural order parameter) differ from zero (see Table 5.1.1. for details).

Table 5.1.1. Nonzero components of the polarization P and the structural order parameter q in different stable phases forming in $SrTiO_3$ epitaxial thin films grown on cubic substrates [D22].

Phase	HT	ST	SO	FTI	FTII	FOI	FOII	FOIII
P				P_3	P_3	P_1 or P_2	P_1 or P_2	P_1 or P_2
q		q_3	q_1 or q_2		q_3		q_2 or q_1	q_3

Another discovery by *Pertsev et al.* and consequence of delicate counterbalance of structural and polar orders was that STO film stays in paraelectric phase down to 0 K only in a narrow range of a small negative strain as shown in Fig. 5.1.9 a). Main hurdle for experimental confirmation of this theory was lack of high quality single crystalline (epitaxial) thin films – polycrystalline films could not sustain sufficient strain and sensitive effect was

overwhelmed by grain boundaries [D23] and other effects bound to ceramics. Only with the development of thin film deposition techniques *Haeni et al.* experimentally showed ferroelectric STO thin films at room temperatures [D24], as shown in Fig. 5.1.10.
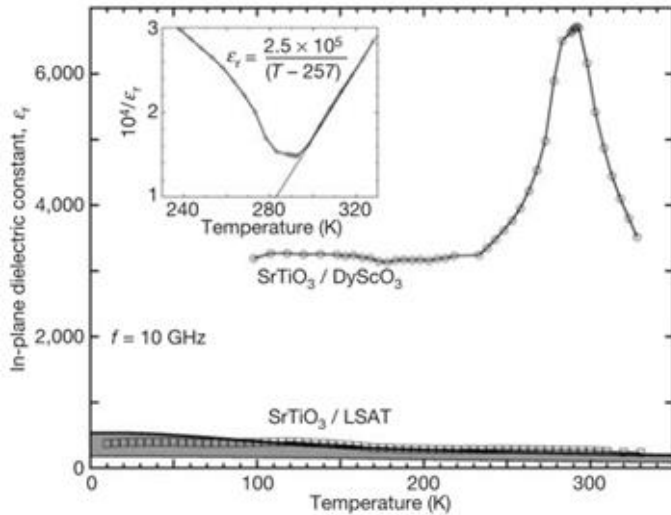

STO thin films with considerable tunability [D25], high dielectric permittivity [D26] and very low losses [D19] in paraelectric phase have attracted a lot of efforts in employing it as a tunable material (or in solid solutions and composites) for microwave applications.

Fig. 5.1.10. In-plane ε' of strained epitaxial STO films, epitaxially grown by MBE on DyScO$_3$ and on LSAT substrates, as a function of temperature at 10 GHz. The inset shows a Curie-Weiss fit to 1/ε' [D24].

Not too long ago *Tagantsev et al.* [I1] predicted that "the antiphase domain boundaries of strontium titanate SrTiO$_3$ that exist at temperatures below the antiferrodistortive transition, <…> are similar to Neel domain walls, as an additional component of the order parameter develops within them. <…> that at low temperatures, typically below 40 K, such boundaries becomes unstable with respect to the development of a ferroelectric polarization. This ferroelectric transition might provide the much needed explanation for several anomalies that are experimentally observed in SrTiO$_3$ in this temperature region". This model predicts two types of boundaries (APB – antiphase boundary) – "easy" and "hard" in the free energy context.

"Easy" APBs are perpendicular to tetragonal "c" axis, they are quite thin (full width $2t_w \approx 2a_0$) and energetically favorable. Such boundaries were experimentally observed by high resolution TEM experiment [D27], shown in Fig. 5.1.11.
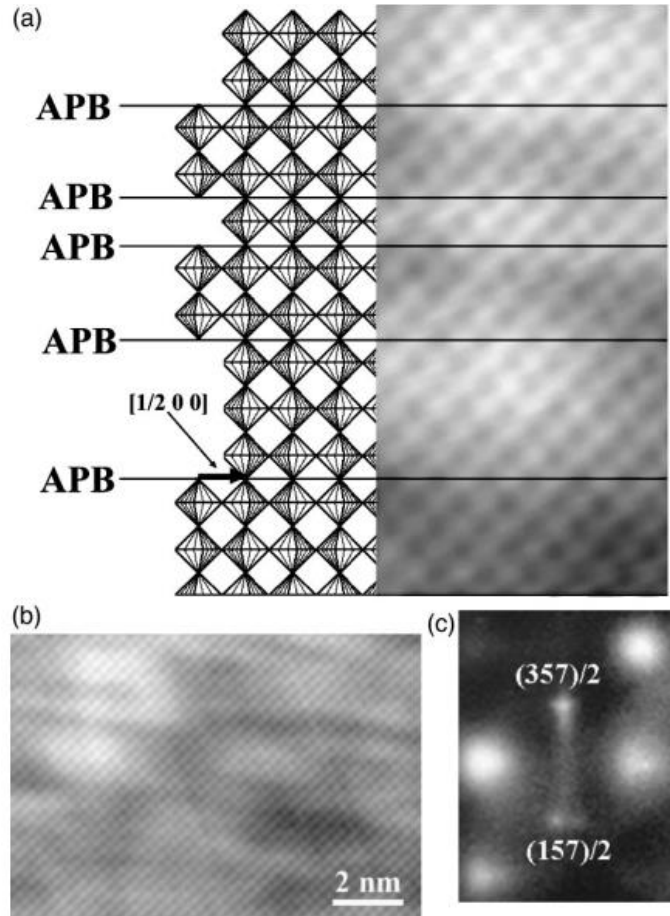

Fig. 5.1.11. (a) Left: structural model of the antiphase domains in the tetragonal $SrTiO_3$. Each orientational variant consists of very thin plates of domains, parallel to the a-b plane, and stacked along the c axis. The translation vector between two neighboring plates is <1/2 0 0>, using $2a_p$ as the edge length of the unit cell. Right: projection of a high-resolution image of $SrTiO_3$, showing black dots as Sr/O columns and white dots as Ti/O columns. Note, the black and white bands are antiphase domains with their interfaces as antiphase boundaries running parallel to the a axis. (b) High resolution image from a larger area similar to that in (a). (c) Corresponding diffraction pattern of (b), showing a diffuse streak perpendicular to the antiphase boundaries [D27].

103

"Hard" APBs contain the "c" axis (are parallel to "c" axis) and are Neel type [I1]. They are more energetically costly and are wider $2t_w \approx 20$ to $25a_0$. In [I1] *Tagantsev et al.* have shown that these boundaries are unstable with respect to the development of a spontaneous polarization parallel to "c" axis, this transition should occur between 35 K and 40 K with developed polarization of ~ 4 $\mu C/cm^2$. This APB is schematically shown in Fig. 5.1.12.
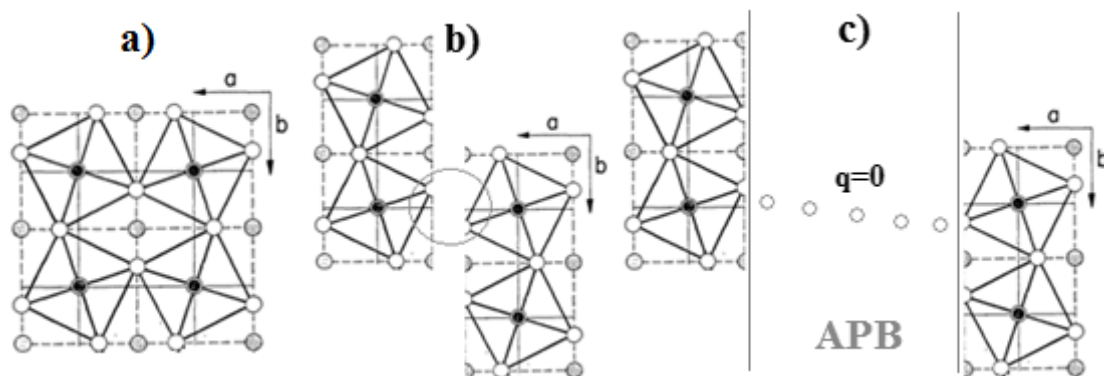

Fig. 5.1.12. Schematical view of "hard" APB.

This result might explain numerous anomalies already reported in STO at 30 K to 40 K temperature range.

5.1.2. Non-strained STO thin films.

The aim of PLD deposition of STO epitaxial thin film was experimental verification of existence of "hard" APBs and ferroelectricity inside them. One of the straightforward experimental technique capable probing polar nature of these boundaries is PFM. Due to experimental difficulties to conduct PFM experiments at 30 K temperature, it was considered another way of proving (or disproving) the theory: enhance ferroelectric and antiferrodistortive phase transitions to higher temperatures (already verified by few group of authors e.g. [D24] for ferroelectric phase transition and [D28] for antiferrodistortive structural phase transition) by biaxial epitaxial straining and clamping the STO film by properly chosen substrate. All previous condition doesn't contradict the assumption that polarity in "hard" APBs should also occur at elevated temperatures.

First of all PLD deposition was started from non-strained thin STO films. This was done to optimize deposition conditions and obtain initial results, also check the possibility to deposit single crystal quality fully epitaxial thin films with EPFL LC PLD equipment. Previous investigators [D29] using PLD deposited epitaxially strained films with a large number of threading dislocations due to high misfit strain between the film and the substrate.

Strain free STO thin films were deposited on $SrTiO_3$ substrates – using homoepitaxy. Substrates of STO (001) with low miscut angle were treated as explained in 3.2. Chapter, AFM micrographs are shown in Fig. 5.1.13.
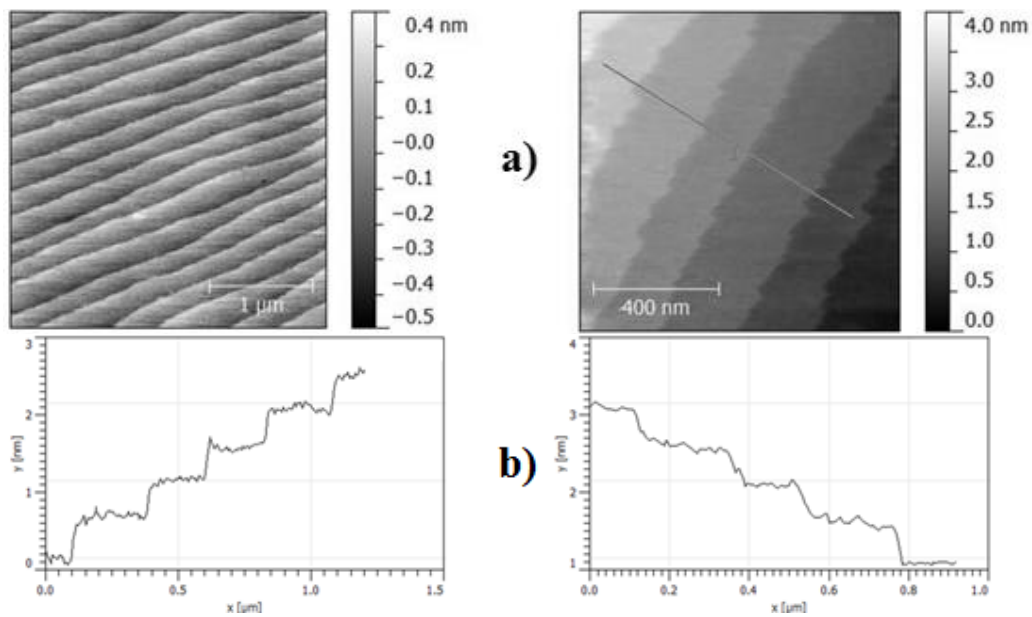
Fig. 5.1.13. AFM images of the $SrTiO_3$ (001) substrates after treatment a). Cross-sectional profile (perpendicular to the terraces) b).

Smooth substrate surface with one unite cell height steps is visible (Fig. 5.1.13) after substrate treatment, surface is terminated by TiO_2 plane according to [B11]. Primarily single crystalline commercial $SrTiO_3$ target was used (CrysTec GmbH, Germany).

Best quality homoepitaxial films were obtained at 800 °C deposition temperature, with 2 Hz laser repetition rate and 30-32 mJ energy, calculated laser fluence was 0.54 - 0.58 J/cm^2 on the target. The oxygen pressure was 0.1 mbar during deposition and was raised to 1 mbar during cool down to fully

105

oxidize the film. STO homoepitaxial thin (77nm, Fig. 5.1.14) film still has the same step and terrace surface (shown in Fig. 5.1.15), indicating perfect 2D growth and superb film quality (XRD STO 001 reflex rocking curve FWHM was 0.014°).
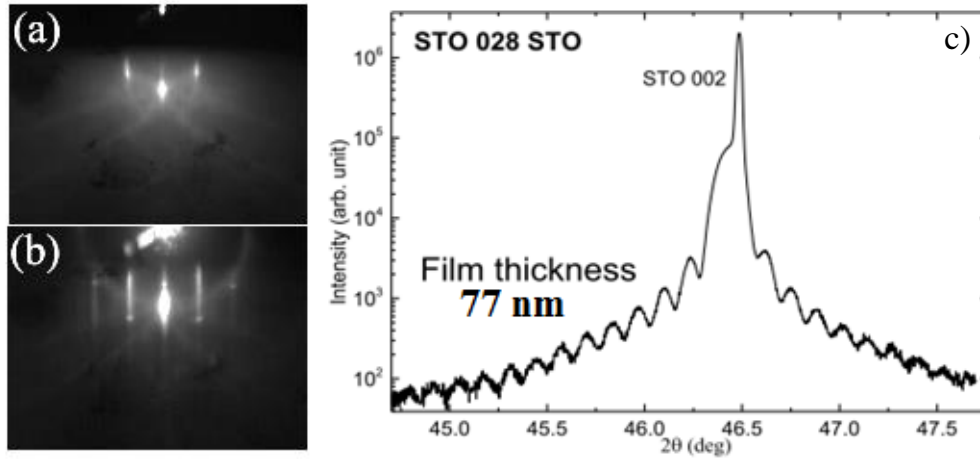

Fig. 5.1.14. RHEED image of STO substrate a) and RHEED image of 77 nm thick SrTiO$_3$ film b). XRD 2Θ-ω scan of STO thin film on STO substrate showing a high intensity SrTiO$_3$ 002 peak with Laue oscillations c).
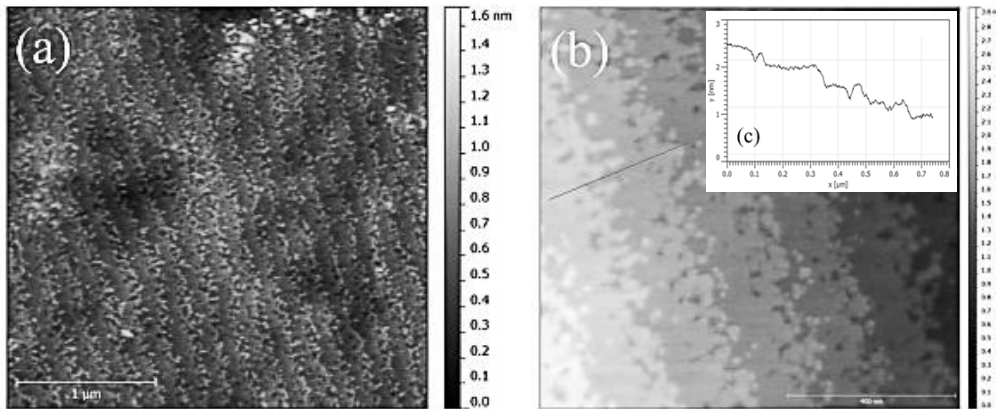

Fig. 5.1.15. AFM images of the 77 nm thick SrTiO$_3$ film a) and b), cross-sectional profile c). Micrograph b) - image size 1x1 μm^2 and the full contrast correspond to 3 nm.

Homoepitaxial STO 002 film and substrate 002 peaks should coincide in Fig. 5.1.14 c), but one can observe small STO film lattice expansion by 0.006 Å. According to literature [D30 and D31] (Fig. 5.1.16 a)) such lattice expansion is negligible small and STO film could be considered as almost stoichiometric with Sr/(Sr+Ti)=50%.
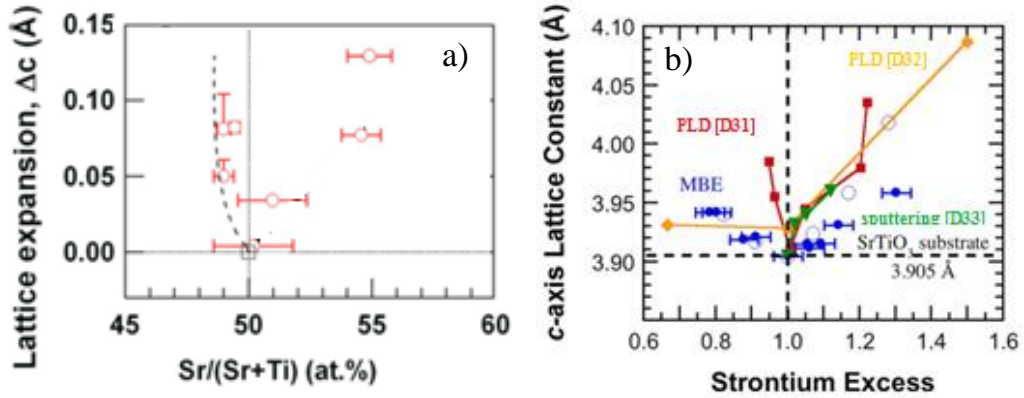
Fig. 5.1.16. Lattice expansion as a function of Sr cationic ratio a), adapted from [D31]. Comparison of out-of-plane lattice constant as a function of strontium excess x in $Sr_{1+x}TiO_{3+\delta}$ for sets of homoepitaxial films grown by MBE, PLD ([D31] and [D32]), and rf magnetron sputtering [D33] b). The circles are from films grown by MBE in this study. The open circles were grown by codeposition, while the closed circles were grown by alternately shuttered monolayers. Adapted from [D34].

Another investigation (homoepitaxial $SrTiO_3$, grown by MBE [D34]), concluded that STO lattice will expand in either cases when film has Sr excess or deficit, shown in Fig. 5.1.16 b) and Fig. 5.1.17.
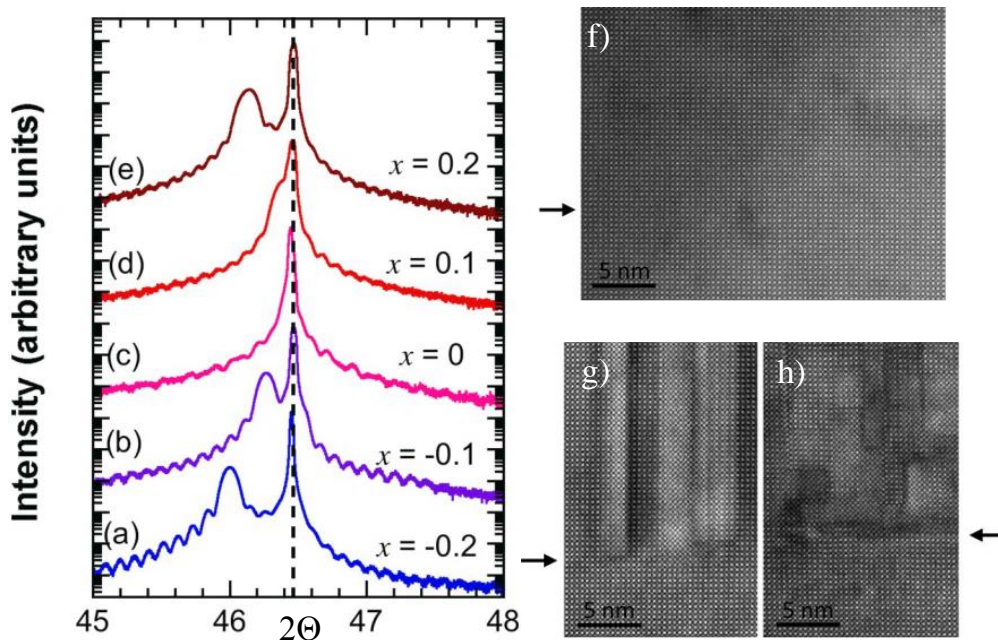
Fig. 5.1.17. Out-of-plane XRD data taken around the 200 peak of $Sr_{1+x}TiO_{3+\delta}$ films with x= -0.2 a), -0.1 b), 0 c), 0.1 d) and 0.2 e). The vertical dashed line

107

marks the 200 peak of the SrTiO$_3$ (001) substrate. STEM images of the interface between the SrTiO$_3$ (100) substrate and film for Sr$_{1+x}$TiO$_{3+\delta}$ films with x= 0 f), 0.1 g) and 0.2 h). An arrow indicates the interface. Adapted from [D34].
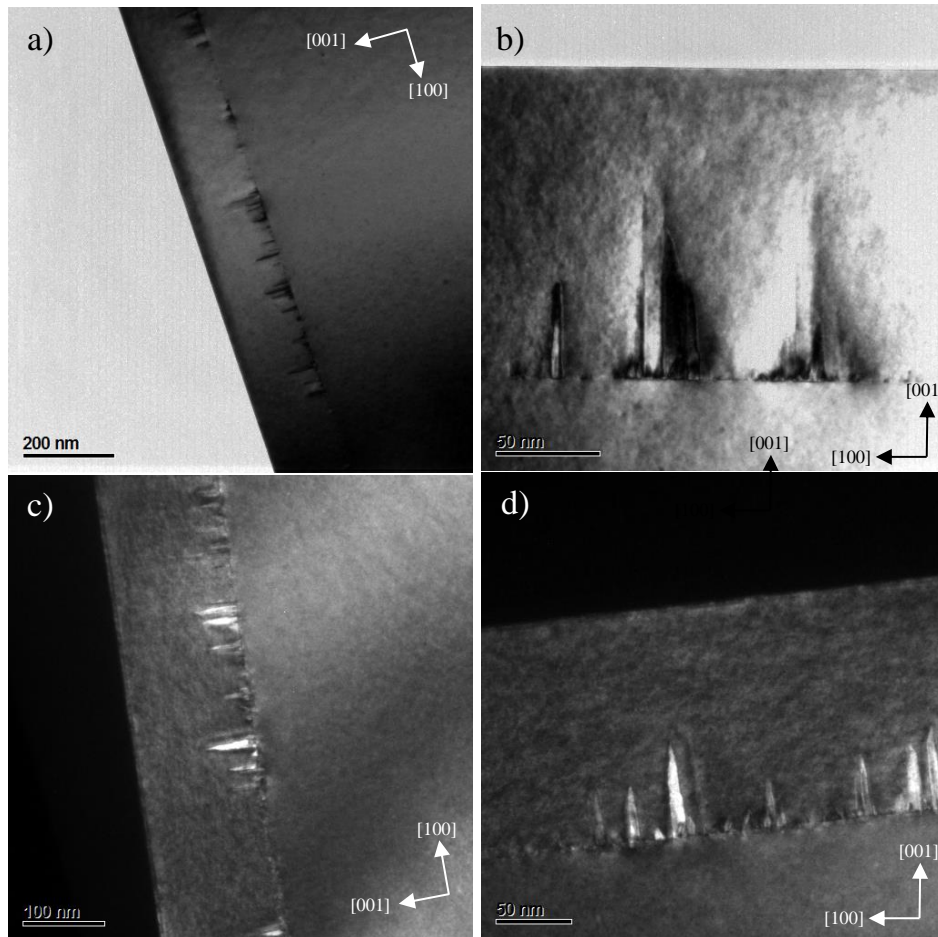

Fig. 5.1.18. Homoepitaxial STO thin film bright field TEM images a) and b), dark field TEM images c) and d). Acknowledgments dr. Cosmin Sandu.

Another sample of strain free STO was investigated by TEM, measured film thickness was 149 nm. In TEM and HRTEM images one can observe contrast coming from defects or strain fields inside the film, shown in Fig. 5.1.18 – 5.1.23. Selected area electron diffraction experiment (Fig. 5.1.19) showed that both regions have the same crystallographic orientation, thus contrast is not from differently oriented grains as in the polycrystalline materials (for instance ceramics), but from dislocations as confirmed by Fig. 5.1.20 - 5.1.23.

Comparison of HRTEM (Fig. 5.1.20) with STEM (Fig. 5.1.19 g) images allows concluding that homoepitaxial STO thin films (deposited from single crystal STO target) are slightly off-stoichiometric. Possibly less than x=0.05 Sr rich ($Sr_{1+x}TiO_{3+\delta}$) and dislocations might appear due to the Ruddlesden–Popper planar faults [D35], as seen in both Fig. 5.1.19 g) and Fig. 2.1.18 – 2.1.20.
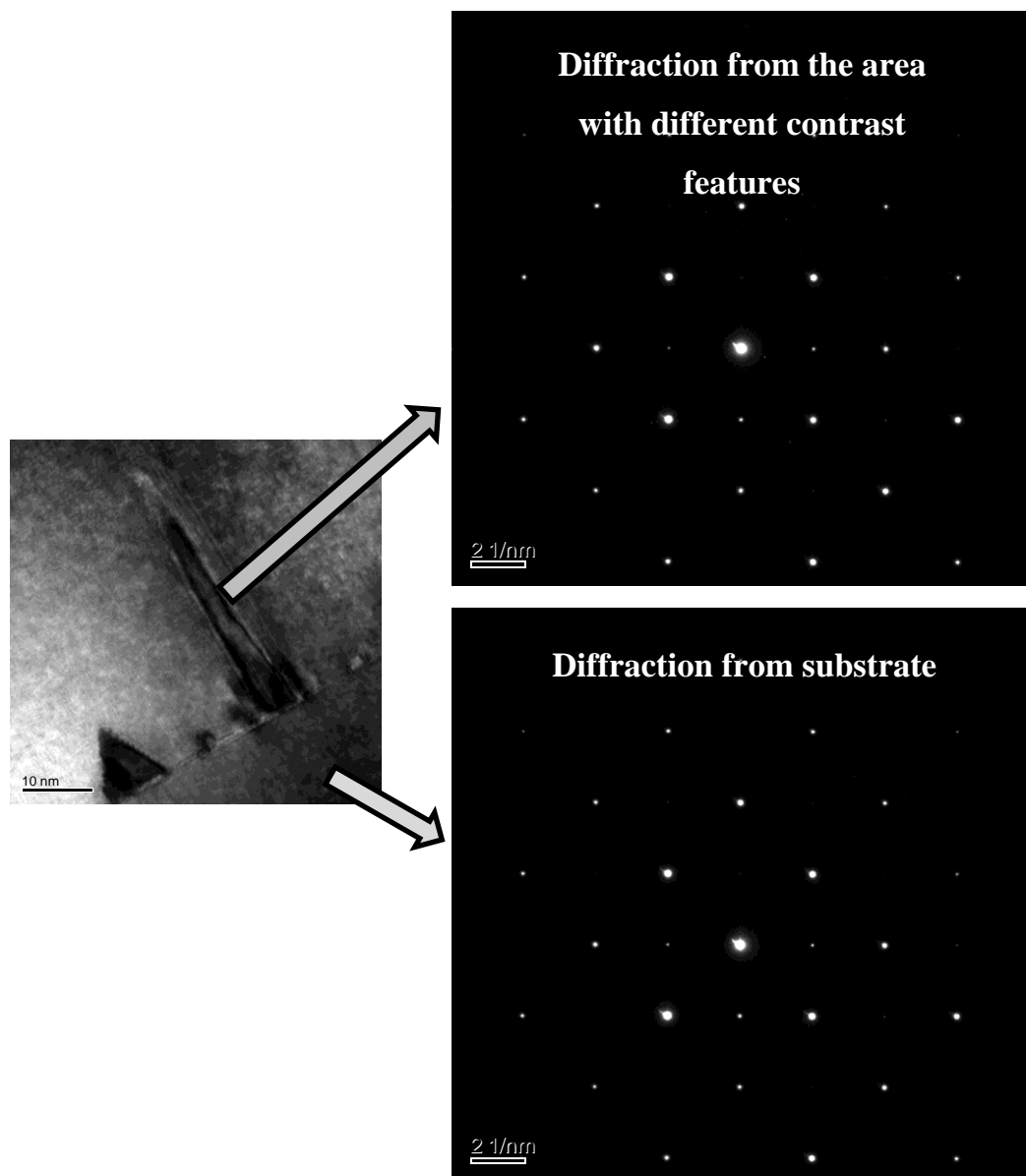

Fig. 5.1.19. SAED electron diffraction from STO thin film and from STO substrate. Acknowledgments dr. Cosmin Sandu.
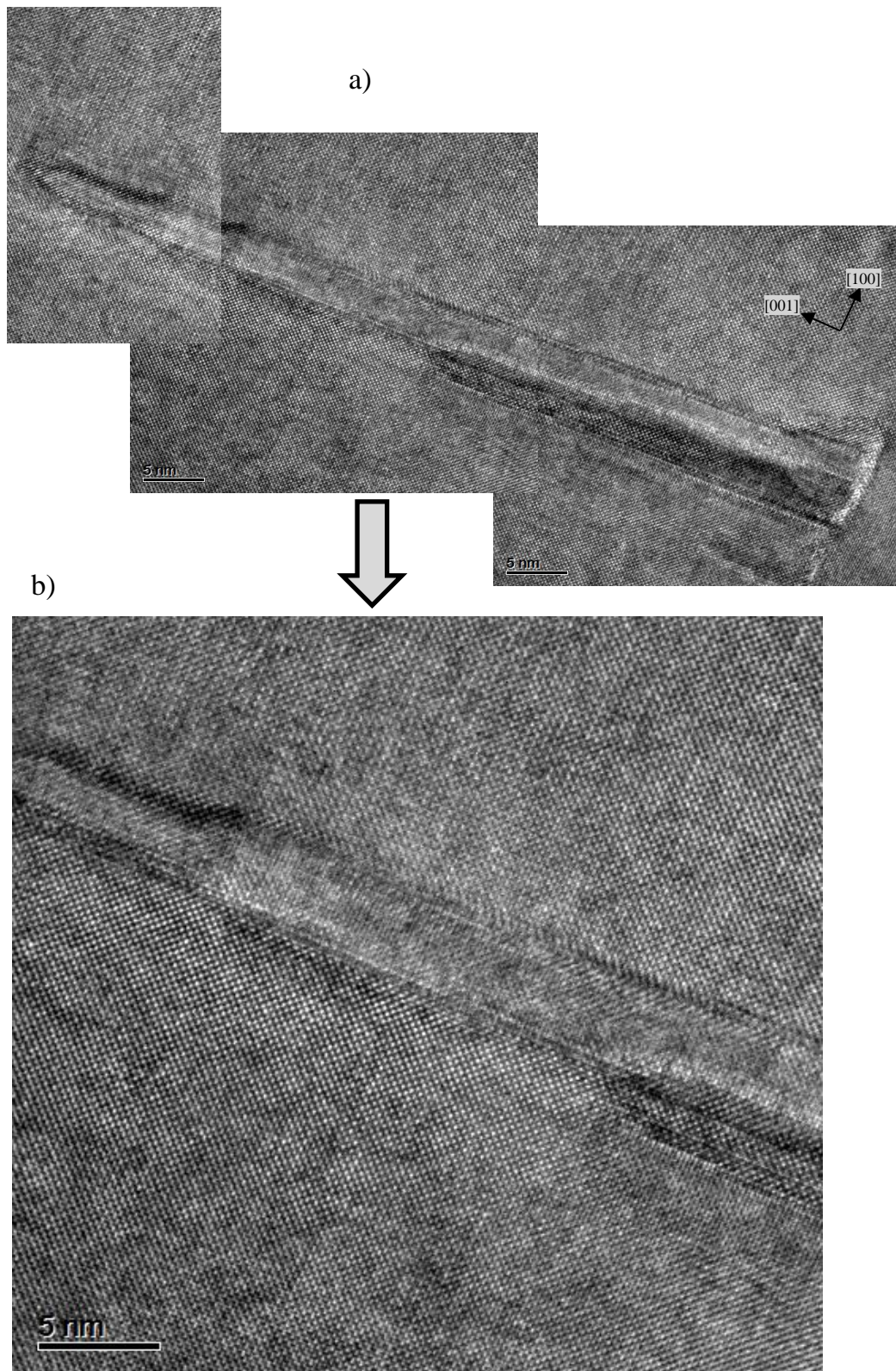
Fig. 5.1.20 HRTEM image of the region with a treading dislocations a) enlarged image b). [100] zone axis, 300 kV accelerating field.

Mathematically the objective lens in TEM performs a Fourier transform (Fourier analysis) that creates the diffraction pattern of the object in the back focal plane and an inverse Fourier transform (Fourier synthesis) that makes the interference of the diffracted beams back to the real space image in the image plane – one obtains real space lattice image, schematical shown in Fig. 5.1.21.
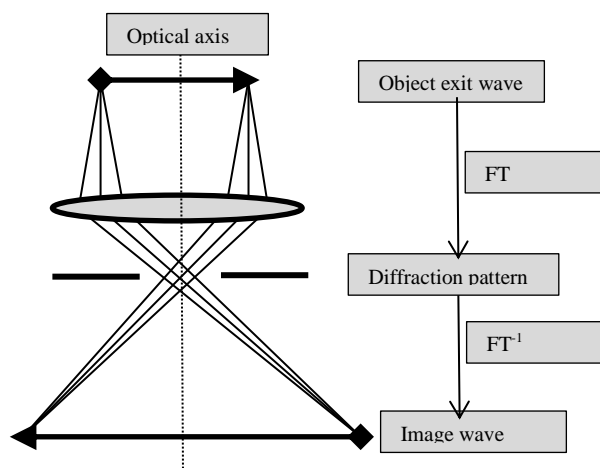

Fig. 5.1.21. Basic ideas behind Fourier transform analysis of dislocations in HRTEM.

HRTEM image processing in Fourier space is performed in a similar way as image formation in the TEM. The FFT of an HRTEM image is calculated. Periodic structures from atoms rows give rise to sharp spots in the resulting diffraction pattern. With the mask one selects which diffracted beams should contribute to the image formed by inverse Fourier transform – thus obtaining spatially filtered image, with just one type of planes contributing.

Obtained HRTEM image (shown in Fig. 5.1.20 b) was transformed by FFT to diffraction pattern (Fig. 5.1.22 a) and all diffraction spots were indexed according to substrate and film orientation (STO_{film} [001]//$STO_{substrate}$ [001]). Lowest order diffraction points of interest, corresponding to diffraction from planes (100), (101), (001) and (-101) (as shown in Fig. 5.1.22 b), were selected by mask and inverse FFT was performed. Thus obtained images represent lattice planes of different orientation - (100) planes in Fig. 5.1.22 c), (101) planes in Fig. 5.1.22 d), (-101) planes in Fig. 5.1.23 a) and (001) planes in Fig. 5.1.23 b).
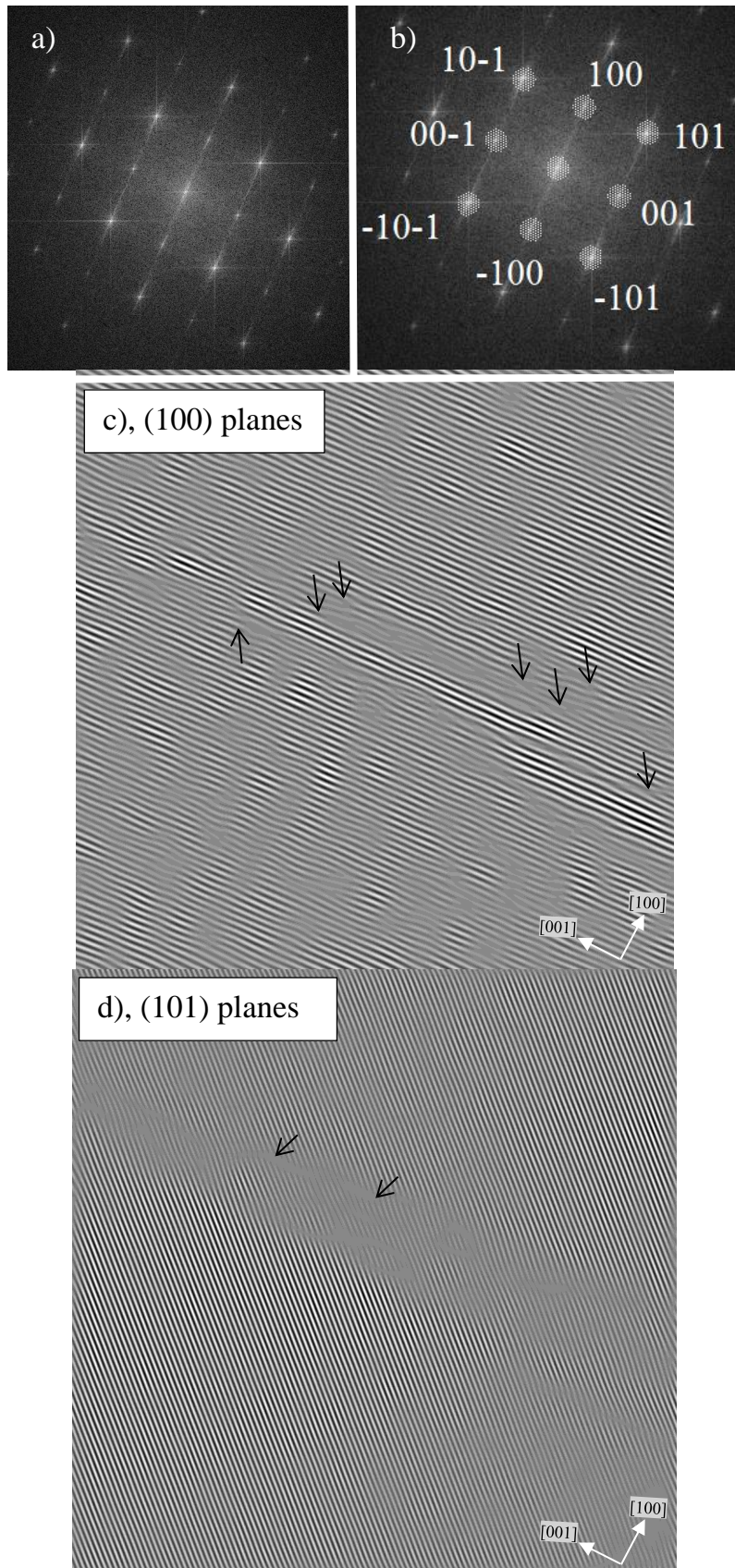
Fig. 5.1.22. HRTEM image Fourier analysis of the same area as in Fig. 5.1.20 b). Arrows indicates edge dislocations.
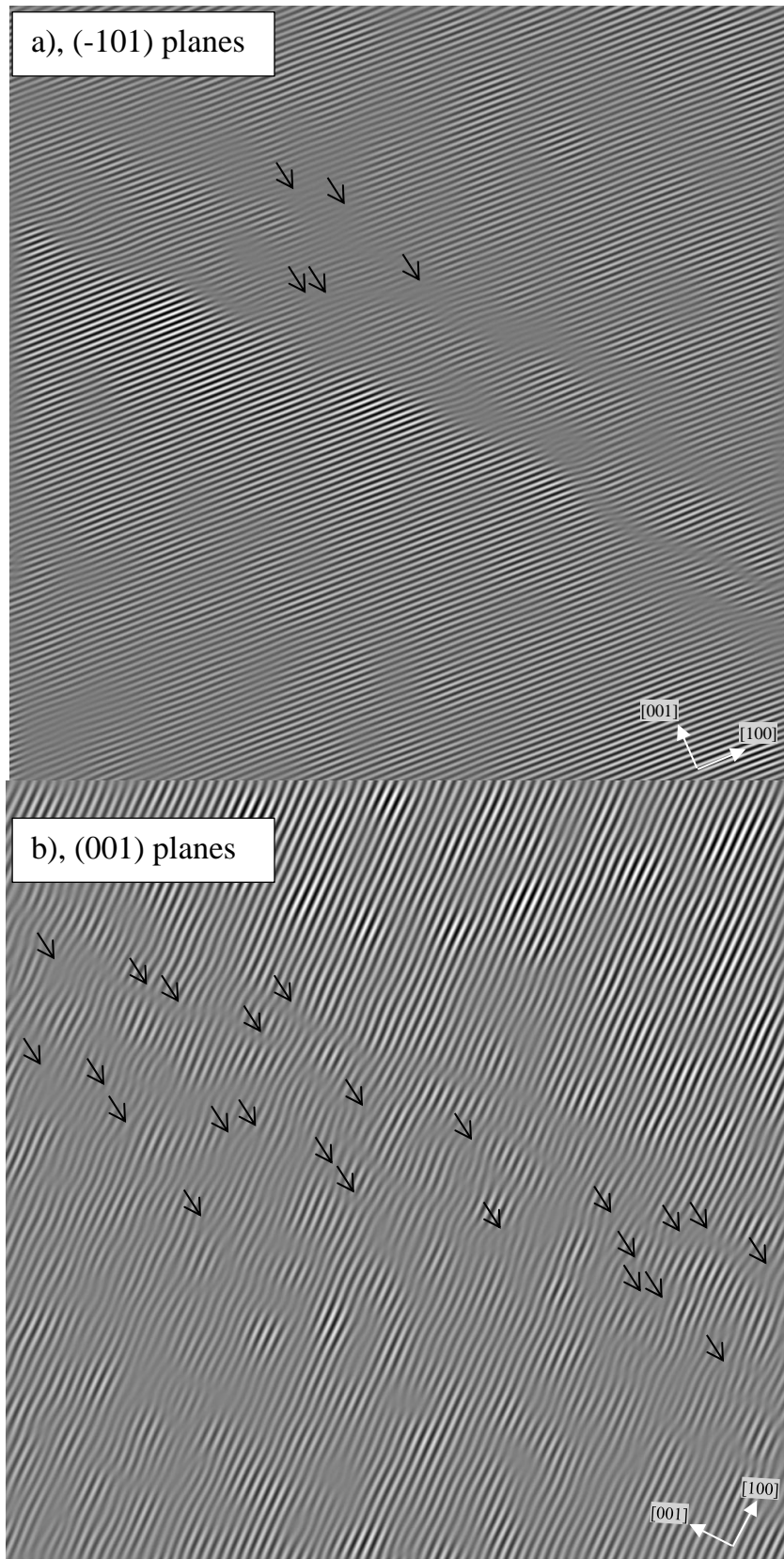
Fig.5.1.23. HRTEM image Fourier analysis of the same area as in Fig. 5.1.22.
Arrows indicates edge dislocations.

Fourier analysis showed that homoepitaxial STO thin film have two type edge dislocations with Burgers vector b = a<001> and b = a<110>. These findings are confirmed by the extinction criterion, which states:

$$g \cdot b = 0, \qquad\qquad 5.3$$

where g is diffraction vector, b – Burgers vector.

Treading dislocations with b = a[001] are visible in Fig. 5.1.26 b), but are absent in Fig. 5.1.25 c), which indicates that imaging vector and Burgers vector are perpendicular to each other. The same applies to dislocations with b = a[-101] as in Fig. 5.1.26 a), they are absent in Fig. 5.1.25 d) and vice versus. Such dislocation networks were already observed in $SrTiO_3$ thin films deposited on $LaAlO_3$ (001) substrates [D36], graphically described in Fig. 5.1.24.
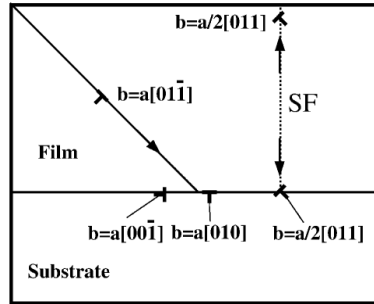

Fig. 5.1.24. Possible formation of misfit dislocation (left part) and partial dislocations, accompanied by a stacking fault [D36].

Such dislocation network releases elastic energy accumulated due to lattice parameter difference, as shown in Fig. 5.1.25. Dislocations with b = a[001] are energetically favored because dislocation energy is proportional to the square of Burgers vector [D36] and $\left|b_{(001)}\right| < \left|b_{(-101)}\right|$.
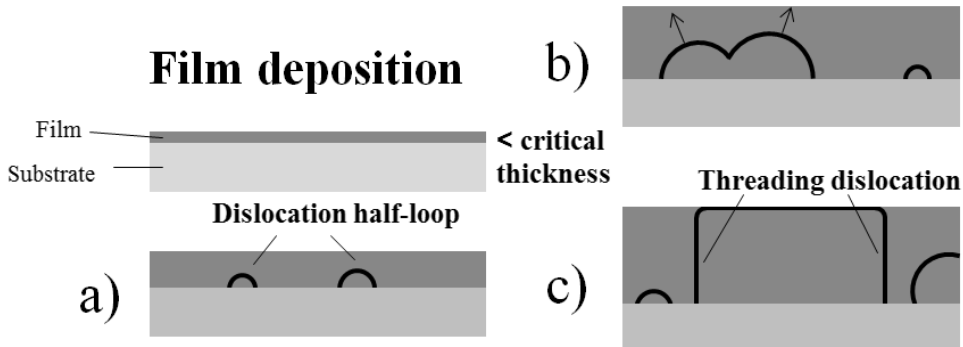

Fig. 5.1.25. Schematical view of treading dislocation formation.

Stoichiometry of the STO film was probed also by TEM EDX technique (with Philips CM300 microscope). Obtained results are shown in Fig. 5.1.26 and Table 5.1.2, they have not confirmed off-stoichiometry, because no significant Sr and Ti content deviation from the average was found.
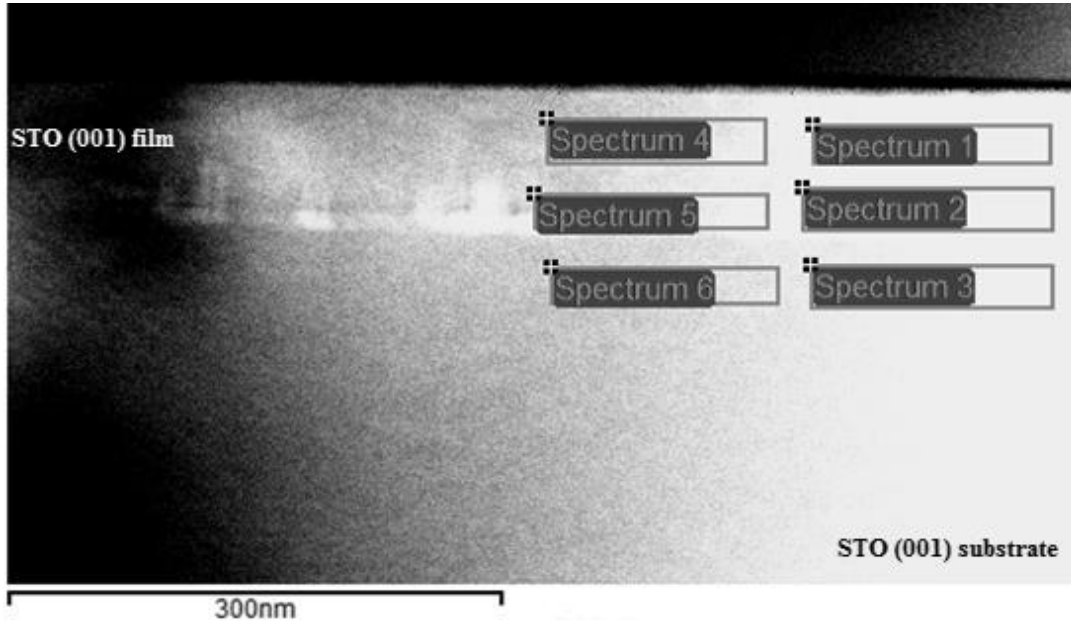

Fig. 5.1.26. TEM EDX measurement of SrTiO$_3$ homoepitaxial thin film. Acknowledgments dr. Cosmin Sandu.

Table 5.1.2. Elemental analysis of the area imaged in Fig. 5.1.29. All results are in atomic %.

Spectrum	O	Ti	Sr
Spectrum 1	60.66	19.61	19.74
Spectrum 2	59.43	20.31	20.26
Spectrum 3	60.89	19.78	19.33
Spectrum 4	59.95	20.33	19.72
Spectrum 5	64.31	18.26	17.43
Spectrum 6	61.48	19.51	19.01
Mean	61.12	19.63	19.25
Std. deviation	1.72	0.76	0.98
Max.	64.31	20.33	20.26
Min.	59.43	18.26	17.43

STO thin films deposited from single crystalline STO target had small, but very important off-stoichiometry, which caused film lattice to slightly expand and created treading dislocation networks to release elastic energy (result obtained from HRTEM analysis). STO epitaxial film (deposited from single crystal of STO) stoichiometry dependence from laser fluence was found in literature [D37-39]. All other parameters were optimized during PLD deposition. Due to technical EPFL LC PLD setup limitation it was too difficult to change laser fluence and optimize deposition for perfect stoichiometry. Further STO deposition was carried out from ceramic STO target (made in the EPFL LC laboratory, described in the 3.1. Chapter), that helped avoiding before mentioned nuisance related to single crystal target [D38 and D30].

To perform PFM experiments on thin film one needs a conducting layer between the film and the substrate. Well established and close lattice match to $SrTiO_3$ is $SrRuO_3$ (SRO) [D39]. At low temperatures $SrRuO_3$ is a Fermi liquid [D40] and at ambient temperatures it exhibits bad metal behaviour [D41].

Best SRO electrodes were deposited by PLD on treated STO (001) substrates at following conditions: 650°C deposition temperature, 2 Hz laser repetition rate, 32 mJ impulse energy, at 0.142 mbar O_2 pressure. Usually deposited SRO electrodes repeated substrate morphology e.g. aligned step-and-terrace surface (shown in Fig. 5.1.27), just some of the samples showed flat surface without steps and terraces (Fig. 5.1.28).
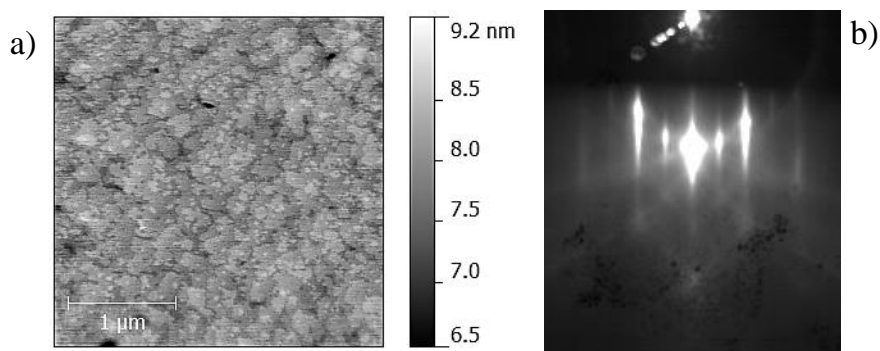

Fig. 5.1.27. AFM images of the 22 nm thick $SrRuO_3$ electrode a) and RHEED image of SRO electrode at room temperature b).
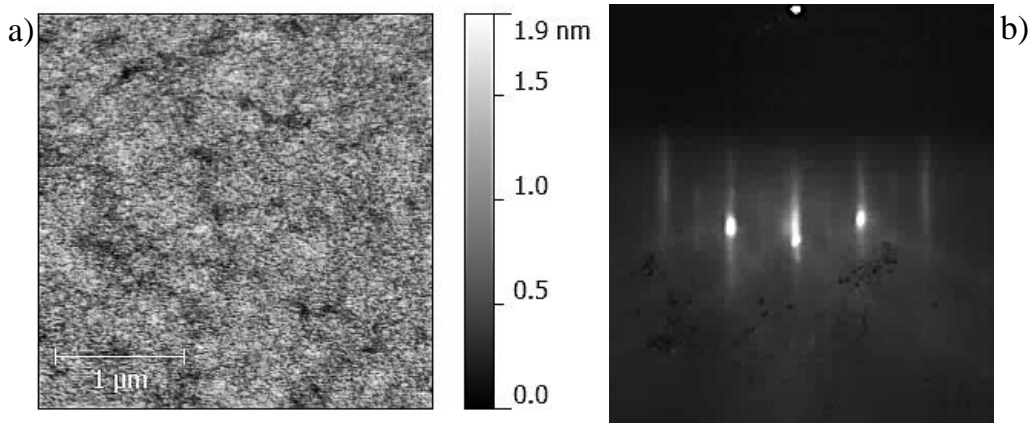
116

Fig. 5.1.28. AFM images of the 22 nm thick SrRuO$_3$ electrode a) and RHEED image of SRO electrode at room temperature b).

Further step of PLD experiments was deposition of STO non-strained film on STO substrate with electrode – STO/SRO//STO. Best quality homoepitaxial STO thin films with SRO electrodes were deposited from ceramic STO target at following conditions: 800°C deposition temperature, with 2 Hz laser repetition rate and 32 mJ laser energy (0.1 mbar O$_2$ pressure during deposition and 1 mbar during cool down). In comparison with STO films deposited from single crystal STO target, deposition rate increased twice, keeping the other deposition parameters the same. The SRO layer surface morphology (step-and-terrace or flat surface, as seen in Fig. 5.1.27 a) and Fig. 5.1.28 a)) had no impact on STO thin film nucleation and growth. This could be explained by SRO layer reconstruction, because STO layer was deposited at way higher temperatures – SRO at 650°C and STO at 800°C.
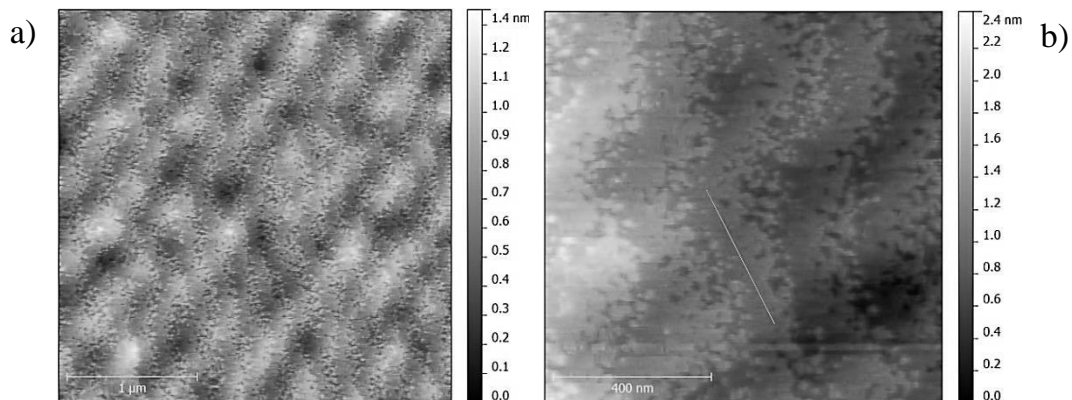

Fig. 5.1.29. AFM images of the 68 nm thick STO thin film a) zoomed in image b) (central part of a)).

As can be seen in Fig. 5.1.29, 68 nm (calculated from XRD Laue oscillations, Fig. 5.1.30 a)) STO thin films still have the same step and terrace surface as a substrate, indicating perfect 2D growth and superb structural quality (XRD STO 001 reflex rocking curve FWHM was 0.011°).

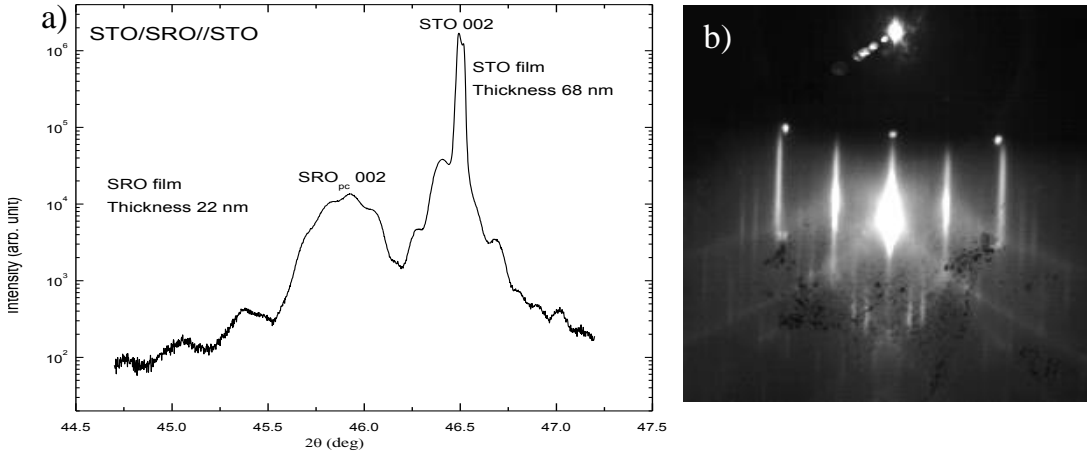Fig. 5.1.30. XRD 2Θ-ω scan of STO/SRO//STO heterostructures showing $SrRuO_3$ 002 and $SrTiO_3$ 002 peaks with Laue oscillations a). RHEED image of 68 nm thick $SrTiO_3$ film b).

Additional RHEED streaks, shown in Fig. 5.1.30 b), are due cooling down in vacuum (only 1 mbar O_2) [D42] and possible surface reconstruction [D43]. After exposing the fresh STO film surface to ambient conditions, additional streaks as in Fig. 5.1.30 b) have disappeared.

5.1.3. Strained STO thin films.

Mechanical coupling between thin films and their substrates strongly influences the film properties. Recently *Yamada et al.* [D44] experimentally showed that compressive ~ -1% strain enhances AFD phase transition in STO thin films from 108 K (as in bulk crystal) to 360 K (biaxially strained thin films) temperature. The same enhancement was theoretically predicted by Pertsev et al. in [D22], however *Yamada et al.* [D44] showed that AFD phase transition is enchanted more than 100°C above theoretical predictions (Fig. 5.1.31).
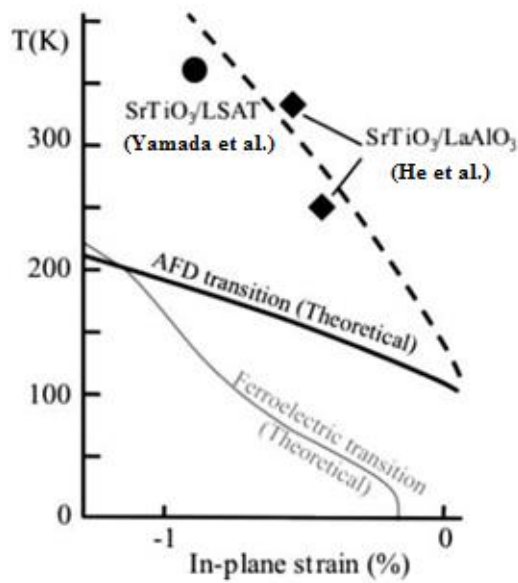
Fig. 5.1.31. Dependence of AFD transition temperature and ferroelectric transition temperature in SrTiO$_3$ film on the in-plane compressive strain. Solid lines show the theoretical predictions [D22]. The AFD transition temperatures experimentally observed by He et al. [D45] and [D44] study are plotted as dots. Adapted from [D44].

Considering *Tagantsev et al.* [I1] prediction for ferroelectricity inside the anti-phase boundaries (APB) in the antiferrodistortive STO phase and phase transition temperature enhancement predicted by *Pertsev et al.* [D22] and confirmed experimentally by *Yamada et al.* [D44] strained STO thin films were deposited by PLD and properties were examined looking for possible ferroelectricity in APB at the ambient temperatures.

Ceramic STO was used as a target, $(LaAlO_3)_{0.3}$-$(Sr_2AlTaO_6)_{0.7}$ (LSAT) was chosen as the substrate. LSAT has a lattice parameter of 0.3868 nm at room temperature, thus STO deposited on LSAT substrate would be compressively (~ -1%) strained. Both phase transitions of STO should be at higher temperatures and ferroelectricity in APB might appear around room temperature, what makes such a phenomenon [I1] feasible for another type of ferroelectric memory applications.

First of all one needs conductive layer between the substrate and the film for PFM and dielectric measurements in MIM configuration. SrRuO$_3$ deposition conditions on LSAT substrates were optimized, because SRO is well established electrode material in heteroepitaxial thin oxide films [D39].

At optimized conditions (625°C, 2 Hz laser repetition rate, 39 mJ energy, 0.15 mbar O_2) SRO nucleates and grows in ordered shapes, but is not fully covering the surface, as shown in Fig. 5.1.32.
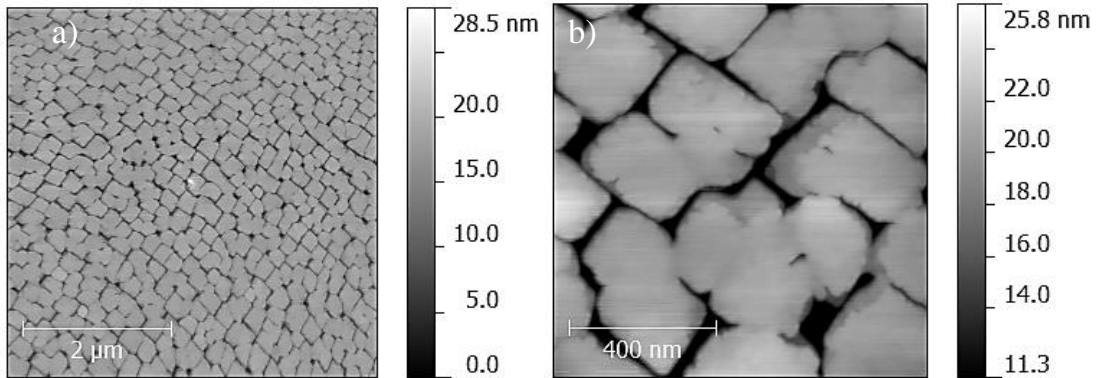

Fig. 5.1.32. AFM images of the SRO layer on LSAT substrate a) zoomed in image b) (central part of a)). SRO//LSAT.

Such behaviour can be explained as follows: LSAT (001) substrates were treated according to [B12], and should have A-site terminated surface. However surface is still terminated with different ions A-site – Sr, La (and if it is terminated by B-site – Al, Ta) in the best case and is terminated by all of them if it is not completely single site terminated surface.
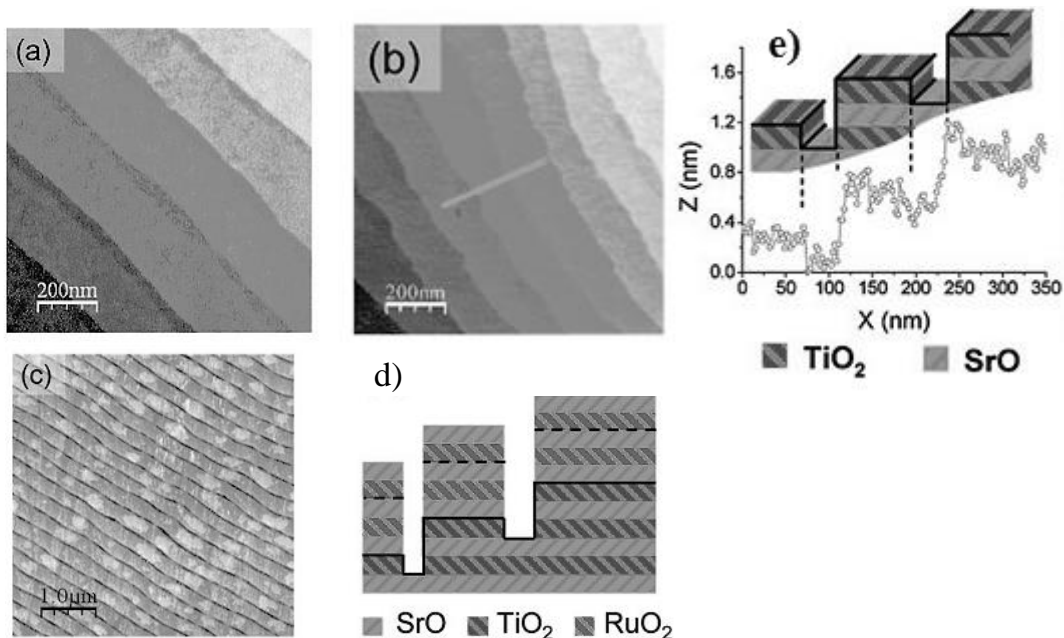

Fig. 5.1.33. AFM topographic images of bare $SrTiO_3$ (001) substrate after annealing at 1200°C for 2 h a) and b). A sketch of the deduced surface

nanostructure and possible termination e). 5 × 5 μm^2 area of a SrRuO$_3$ film (7 ML) deposited on (a) shown in c) and the sketch of the corresponding atomic layers are shown in d). Adapted from [D46].

It is well known that SRO grows in a step flow mode and develops single unite cell height terraces only if the substrate (STO 001 as an example) is single terminated [D46]. If the substrate is mixed terminated – one obtains situation depicted in Fig. 5.1.33 d) and e). The same applies to SRO//LSAT heteroepitaxial layer, because the growth rate at different ion terminated surface is different and finally one obtains film shown in Fig. 5.1.32.

To overcome the wetting problem of SRO was used two strategies:

1) deposit a buffer layer, which could be made single terminated, on LSAT;

2) use another electrode material without such a problems as SRO on LSAT.

Obviously STO was tried as a buffer layer in SRO/STO//LSAT heterostructure. Thin STO buffer layer was deposited at 780°C, 1 Hz laser repetition rate and 38 mJ laser energy (0.1 mbar O$_2$ pressure during deposition and 1 mbar during cool down), shown in Fig. 5.1.34 a). Deposited buffer was treated as ordinary STO substrate according to recipe described in 3.2. Chapter: hydrolyzed, etched in BHF and annealed at high temperature in O$_2$.
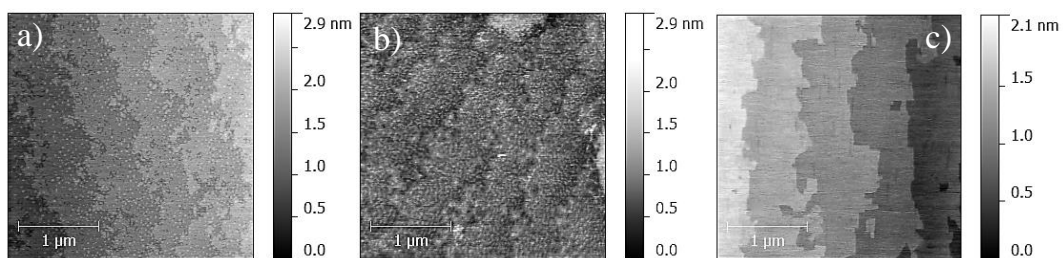

Fig. 5.1.34. AFM micrographs of deposited STO buffer layer (~10 nm) a), BHF etched for 12 s b) and annealed at 925°C for 1 h (0.6 l/min O2 flow) c).

According to [B11] and others investigations, surface of STO//LSAT should be single site (B-site) terminated as conventional STO substrate. Single

site termination is supported by AFM image (Fig. 5.1.34 c), where one can observe one unite cell size steps. SRO was deposited on LSAT substrate with intermediate STO buffer, however SRO did not cover the entire surface and did not developed step-and-terrace surface, shown in Fig. 5.1.35 a). Insufficient SRO electrode quality was confirmed by RHEED, showing spotty, 3D-like diffraction pattern (Fig. 5.1.35 b)).
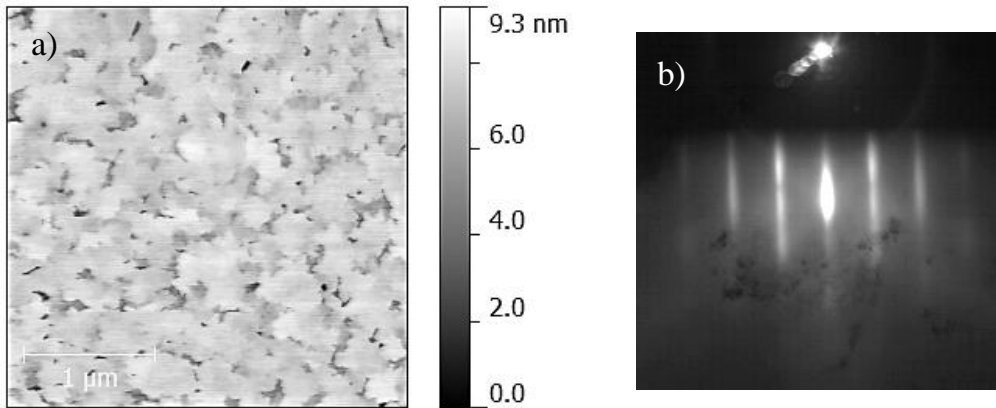
Fig. 5.1.35. AFM images of the SRO layer on STO//LSAT a), SRO was deposited at 625°C, 2 Hz laser repetition rate, 38 mJ laser energy and 0.143 mbar O_2, RHEED image of SRO/STO//LSAT b).
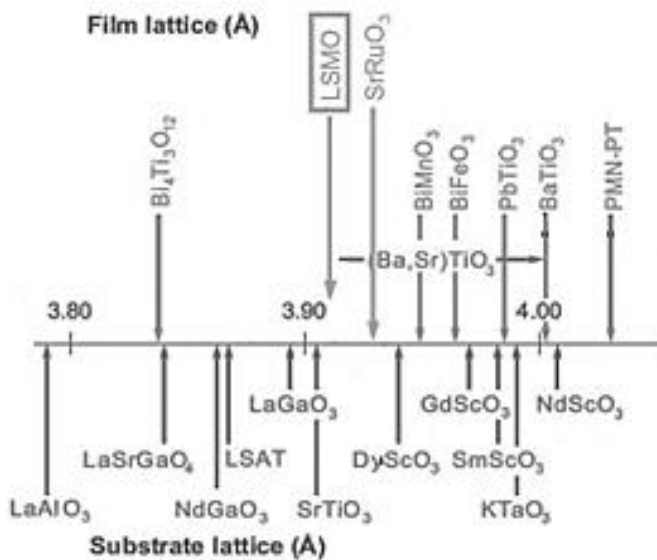
Fig. 5.1.36. Lattice parameters of cubic or pseudocubic perovskites at ambient conditions.

Low quality SRO growth tendency and surface morphology might be a consequence of mixed termination of STO buffer layer or too high negative misfit strain exerted by LSAT substrate.

Another approach was to use different

122

electrode material system, $La_{1-x}Sr_xMnO_3$ (LSMO) – was chosen. $L_{0.8}Sr_{0.2}MnO_3$ (bulk lattice parameter 0.3909 nm [D47]) is closely matched to $SrTiO_3$, and has not too high (~ -1%) negative misfit with LSAT substrate (Fig. 5.1.36), what helps to stabilize LSMO continuous layer.

Metal-insulator transition temperature of LSMO on LSAT substrate is at 345 K [D48], so this material is appropriate as an electrode in STO/LSMO//LSAT heterostructures. Conductivity is electronic and due hole-doping of the initial charge transfer insulator [D47].
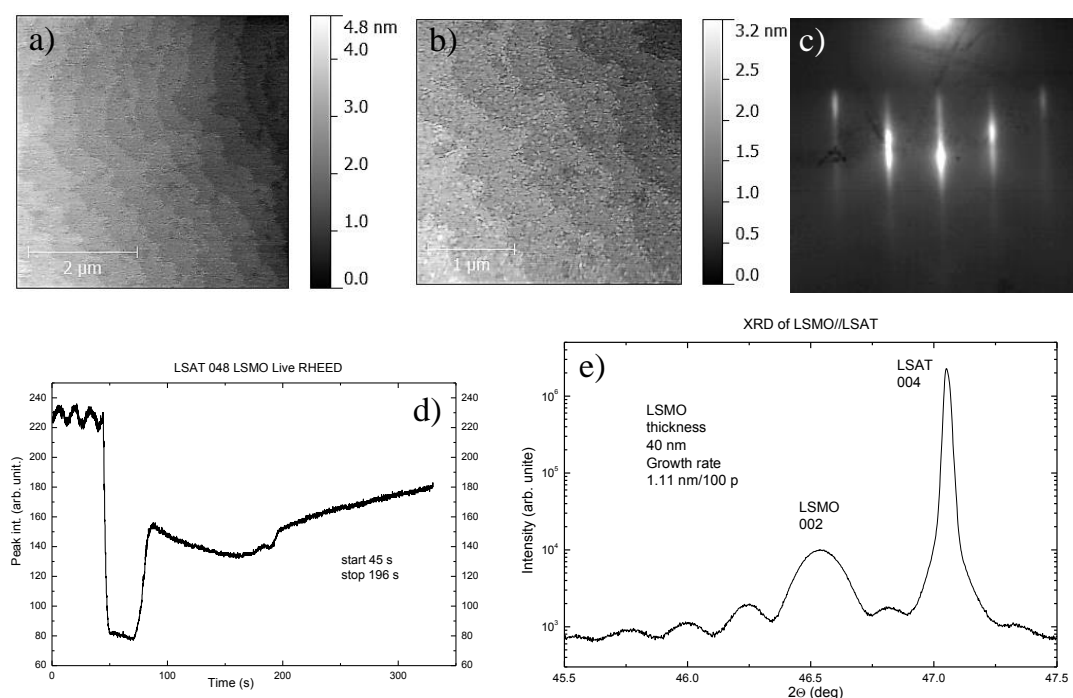
Fig. 5.1.37. AFM micrograph of LSMO layer grown on LSAT substrate a) and b), RHEED image of LSMO//LSAT c) and RHEED oscillations during LSMO deposition d). XRD 2Θ-ω scan of LSMO//LSAT heterostructures showing LSMO 002_{pc} peaks with Laue oscillations e).

Despite lower conductivity than SRO, LSMO grows (on LSAT substrate) in step flow mode (shown in Fig. 5.1.37 d)) and covers the entire substrate surface (shown in Fig. 5.1.37 a) and b)). Optimized LSMO electrodes were deposited from ceramic LSMO target at following conditions: 750°C deposition temperature, with 2-3 Hz laser repetition rate and 39 mJ laser

energy, 0.15 mbar O_2 pressure during deposition and 1 mbar during cool down. Later it was observed that exposing freshly deposited LSMO layer to ambient conditions strongly deteriorates deposited STO thin films. For this reason growth rate (1.11 nm per 100 pulse) was calibrated from Laue oscillations observed in XRD 2Θ-ω scan (Fig. 5.1.37 e)) and used to calculate LSMO layer thickness depending on the laser pulse count without exposing LSMO layer to atmosphere. Later LSMO growth rate was confirmed by HFTEM experiments.

At optimized deposition conditions layer-by-layer growth of strained STO (STO/LSMO//LSAT) was achieved. STO thickness was controlled by RHEED oscillations and all heterostructure thickness was kept below 100 nm attaining full strain without relaxation.

Best structural quality fully strained STO thin films were obtained at 780°C deposition temperature, with 2 Hz laser repetition rate and 39 mJ energy. The oxygen pressure was 0.1 mbar during deposition and was raised to 1 mbar during cool down to fully oxidize the film. STO layer in heterostructure of STO/LSMO//LSAT at before mentioned conditions grew in 2D layer-by-layer mode (Fig. 5.1.38 a)). Film thickness was *in-situ* monitored by RHEED oscillations (Fig. 5.1.38 b)) and later confirmed by XRD (Fig. 5.1.39) and HRTEM experiments.

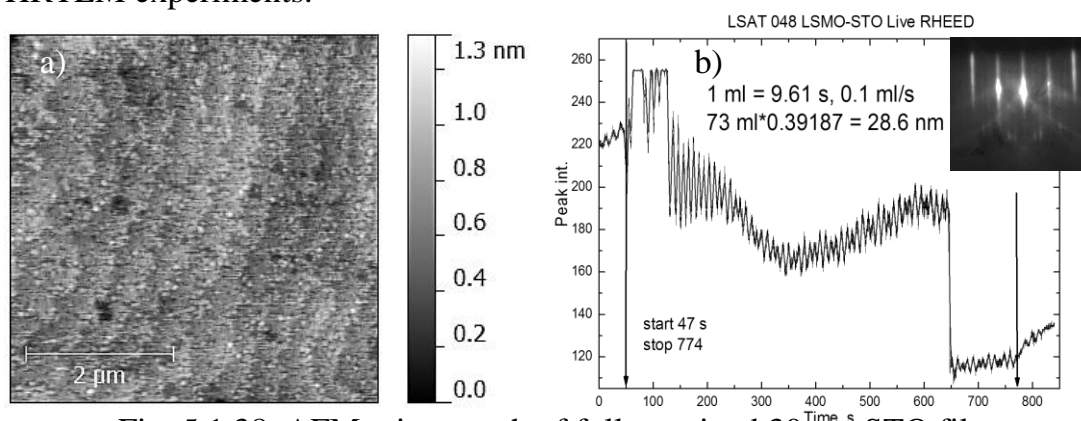Fig. 5.1.38. AFM micrograph of fully strained 30 nm STO film (STO/LSMO//LSAT) a), *in situ* RHEED oscillations during STO film deposition (RHEED image of STO film after deposition, insert) b).
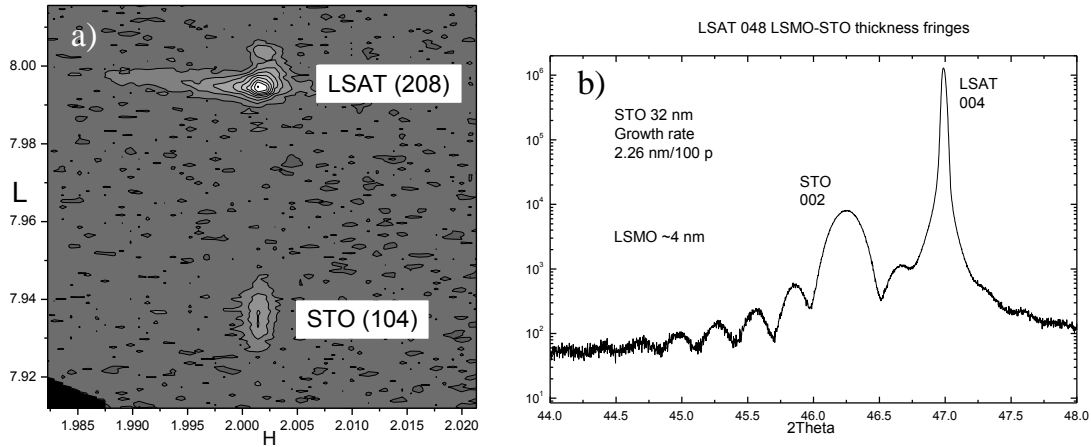
Fig. 5.1.39. XRD asymmetric reciprocal space map (RSM) scan around LSAT (208) and STO (104) a) and XRD 2Θ-ω scan of STO/LSMO//LSAT heterostructures showing STO 002 and LSMO 002$_{pc}$ peaks with Laue oscillations b).

XRD asymmetric reciprocal space map (RSM) (shown in Fig. 5.1.39 a)) revealed fully strained STO thin film with STO lattice parameters: a=0.38675 nm, c=0.39256 nm and 0.539 % tensile out of plane and -0.949 % compressive in plane strains. At this strain state STO thin film should be in antiferrodistortive phase, what is confirmed by formation of fine "a/c" domain pattern (shown in Fig. 5.1.40 a).
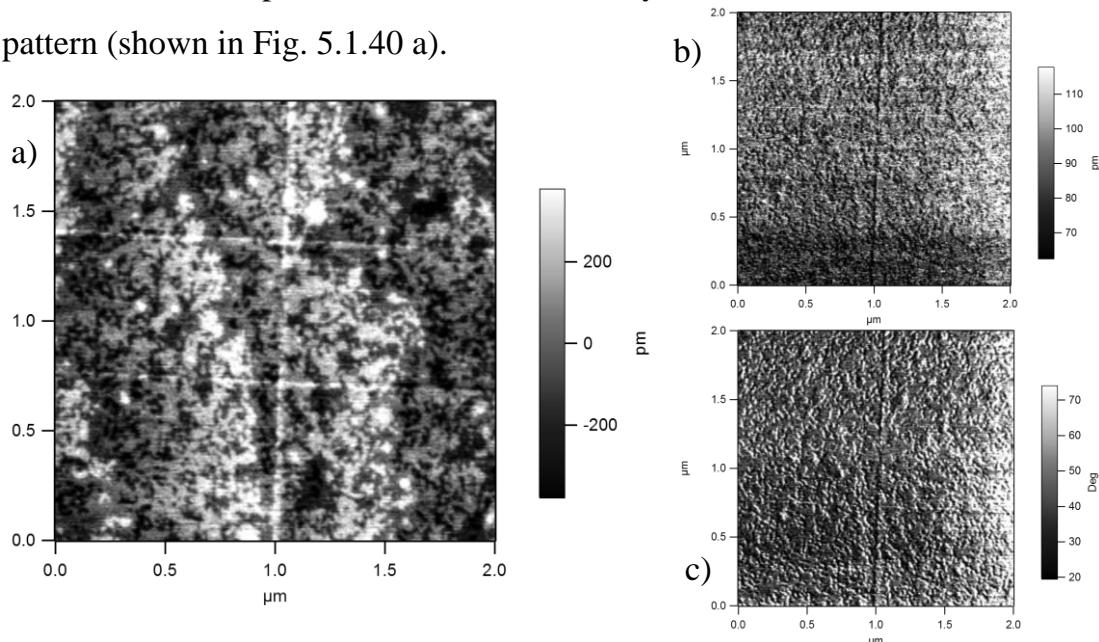
Fig. 5.1.40. PFM (dual AC resonance tracking mode – DART mode) images of fully strained 30 nm STO thin film at room temperature: topography a), PFM out of plane amplitude b) and PFM phase c).

Fig. 5.1.41. Diagram shows the domain states or domain patterns having the minimal average (macroscopical) elastic energy in a (001) tetragonal ferroelectric film deposited on cubic substrate as functions of the relative coherence strain Φ. Adapted from [A1].
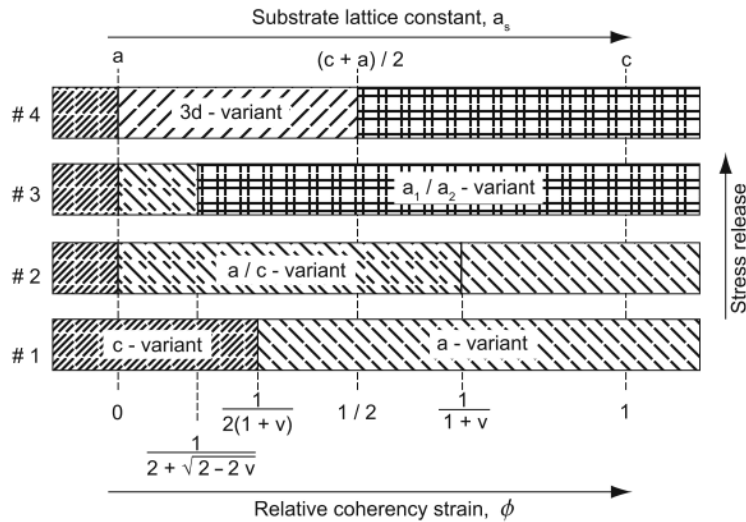
Surface rumpling corresponding to elastic "a/c" domains can be observed in AFM and PFM topography (Fig. 5.1.40 a). Lack of piezoresponse, no change in piezoresponse amplitude (Fig. 5.1.45 b) and phase (Fig. 5.1.45 c), indicates that STO thin film is in antiferrodistortive phase and not in ferroelectric phase yet (at room temperature). No features which could be attributed to ferroelectricity in APB were observed also - vertical lines in Fig. 5.1.40 b) and c) is a crosstalk in the different signaling channels of lock-in amplifier.

Formation of "a/c" elastic domain pattern was predicted in [A1] due to relaxation of elastic energy, shown in Fig. 5.1.41. Diagram displays the domain states or domain patterns having the minimal average (macroscopical) elastic energy. STO thin film is in metastable monodomain ("c" axis oriented out of plain direction) state (shown in Fig. 5.1.38 a) corresponding to Fig. 5.1.41 #1 c-variant, immediately after cool down from deposition temperature. During few days metastable monodomain state transforms to a/c -variant depicted in Fig. 5.1.41 #2 and #3 a/c-variant. Heating up to 100°C on the hotplate (at ambient conditions) accelerates this process (heating up closer to AFD phase transition) and instead of few days – few minutes is enough to obtain twinned ("a/c" elastic domain pattern) STO thin films (shown in Fig. 5.1.42).
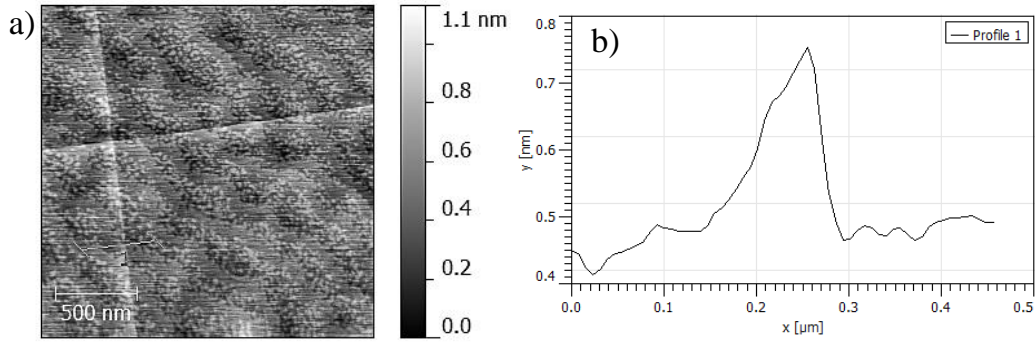
Fig. 5.1.42. AFM of the twinned 90 nm fully strained (-0.987 % compressive in plane strain) STO thin film a) and corresponding cross-sectional profile b).

Observable surface rumpling (Fig. 5.1.42 b) due to formation of "a/c" twins can be graphically explained by Fig. 5.1.43, just omitting ferroelectric polarization P_{ferro} (strained STO film is not in ferroelectric state at room temperature) and possibly flexoelectric polarization P_{flexo} (need additional investigations, not concerned in this thesis).
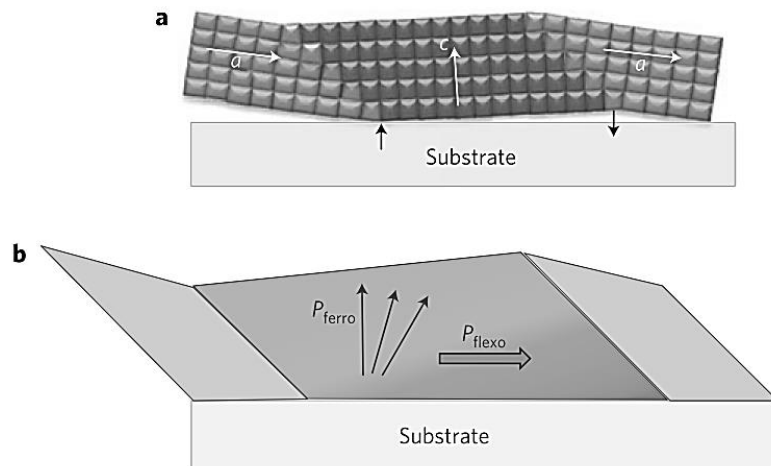
Fig. 5.1.43. Sketch of stresses, strain gradients and polar vectors in the twinned film. Schematic representation of the domain structure in a film with a/c domains a). The black arrows represent the stresses that must be applied to the twinned film to flatten it onto the substrate. The flexoelectric polarization (grey) induces a rotation of the ferroelectric polarization of the c domain (blue) b). Adapted from [D49].

Further investigation step was to deposit thicker STO thin film and partially relax the elastic strain (at the same time changing both phase transition

temperatures), trying to observe ferroelectricity at ambient conditions by PFM and TEM experiments. Strain relaxation was done controlling electrode LSMO layer and STO film thickness [A1]. Thicker LSMO electrode (16 nm) and STO film (90 nm) were deposited at the optimized (described before) deposition conditions for STO/LSMO//LSAT heterostructure. AFM, XRD and RHEED structural investigation results are presented in Fig. 5.1.44. No ferroelectricity manifestation is observed in PFM images of twinned STO thin film (Fig. 5.1.45) at room temperature. Conductivity was also checked − no conductivity difference was observed in the film and at the twin walls (Fig. 5.1.46).
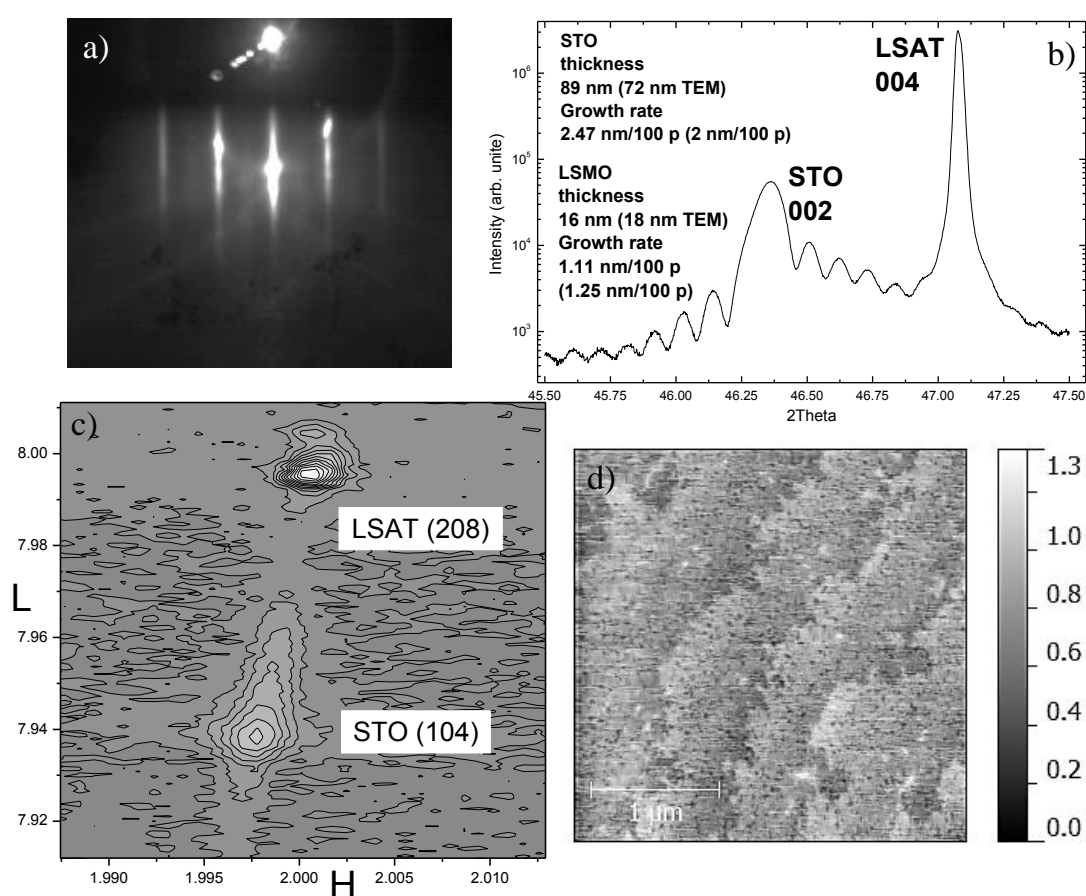
Fig. 5.1.44. RHEED image a) and XRD 2Θ-ω scan of STO/LSMO//LSAT heterostructure b). XRD asymmetric RSM around LSAT (208) and STO (104) (partially relaxed STO layer) c) and AFM image of 90 nm STO thin film in the metastable monodomain state d) (scale is in nm).
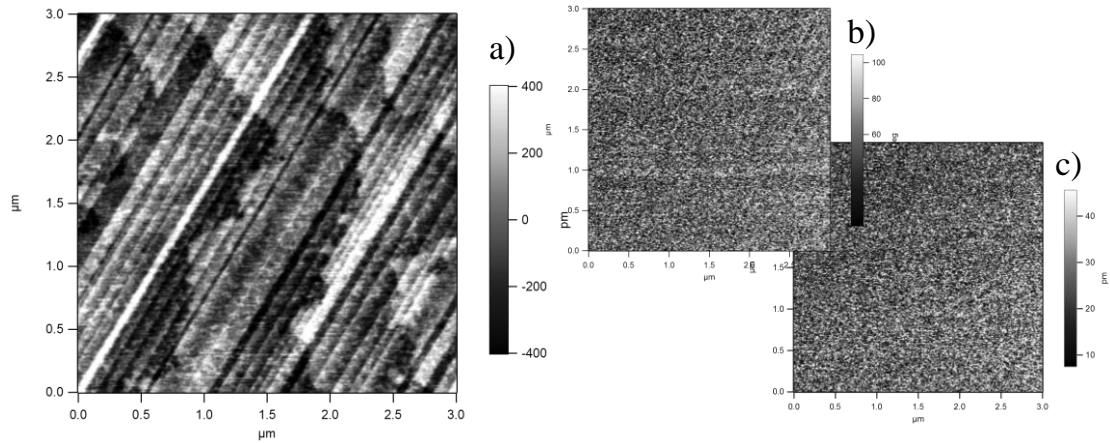
Fig. 5.1.45. PFM (DART mode) images of partialy relaxed twinned 90 nm STO thin film at room temperature: topography a), PFM phase b) and PFM out of plane amplitude c).
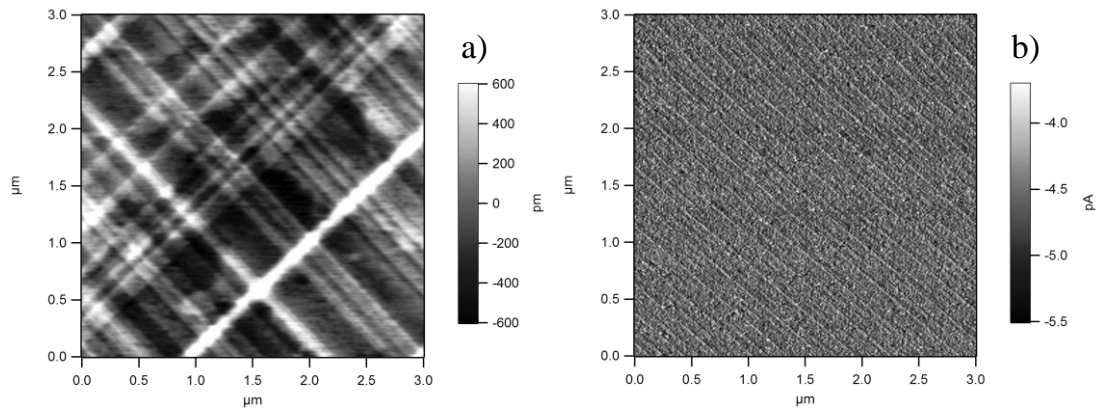
Fig. 5.1.46. Conductive AFM (cAFM) measurement of 90 nm partially relaxed STO film. Topography a) and corresponding current map b).
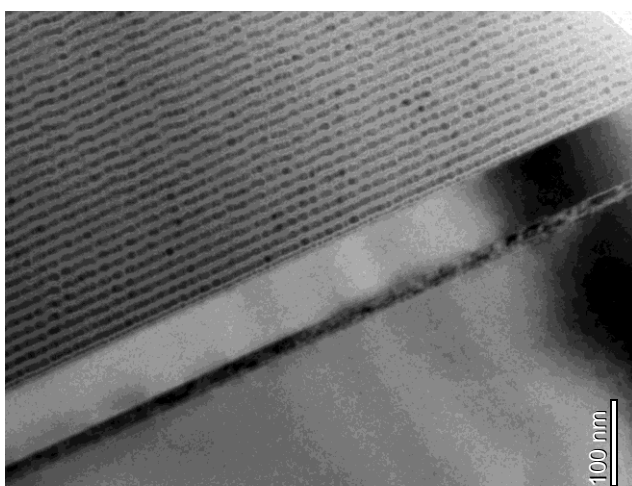
Fig. 5.1.47. Heteroepitaxial strained STO thin film bright field TEM image. Acknowledgements dr. Cosmin Sandu.

Lattice parameters of STO calculated from XRD asymmetric RSM – a=0.38789 nm (in plane) and c=0.39245 nm (out of plane). These values correspond to negative -0.6 % in plane strain. At this strain state STO is in the AFD phase, as confirmed by

129

PFM experiment – observed surface rumpling (also observed in the literature [D44]). No "a/c" elastic domains (elastic twins) were observed in TEM (Fig. 5.1.47).

Due to AFD phase transition STO lattice multiplies – real space volume doubles. Multiplication consequence is additional diffraction peaks (superlattice peaks) appearing in diffractogram, Yamada et al. [D44] observed such additional peaks in diffraction experiments with synchrotron radiation.
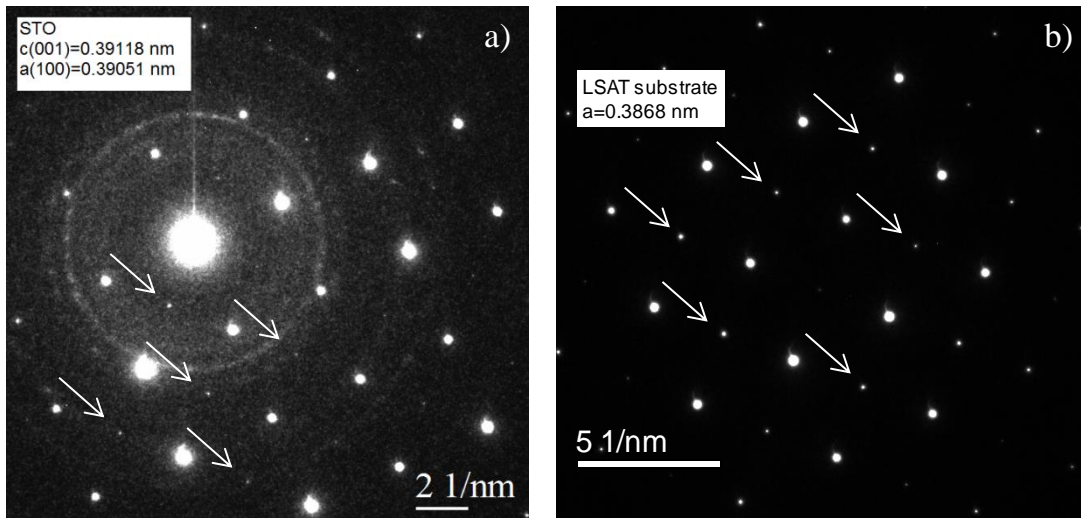
Fig. 5.1.48. SAED electron diffraction from 72 nm STO thin film and from LSAT substrate (heterostructure STO/LSMO//LSAT). Arrows indicate superlattice peaks. Acknowledgements dr. Cosmin Sandu.

TEM SAED diffractogram revealed such superlattice peaks due to lattice multiplication at (½, ½, ½) indices (Fig. 5.1.48 a). Peaks at (½, ½, ½) in Fig. 5.1.48 b) are due to the fact that LSAT substrate counting as a pseudocubic with lattice constant $a_{pc} = 0.3868$ nm is wrong. In reality LSAT has a space group Pn-3m (224) with a double unite cell and lattice constant $a = 0.3868 \cdot 2 = 0.7736$ nm - ordered fcc LSAT. In fcc structure it is not allowed reflections with mixed odd and even indices, thus to distinguish between fcc and simple cubic structures it is used {2h+1, 2k+1, 2l+1}fcc family of reflections because they do not have integral indices and therefore do not exist simple cubic case [D50].

HRTEM experiment on the same lamella as in Fig. 5.1.47 was used for clarification of the phase. Obtained micrographs are presented in Fig. 5.1.49.
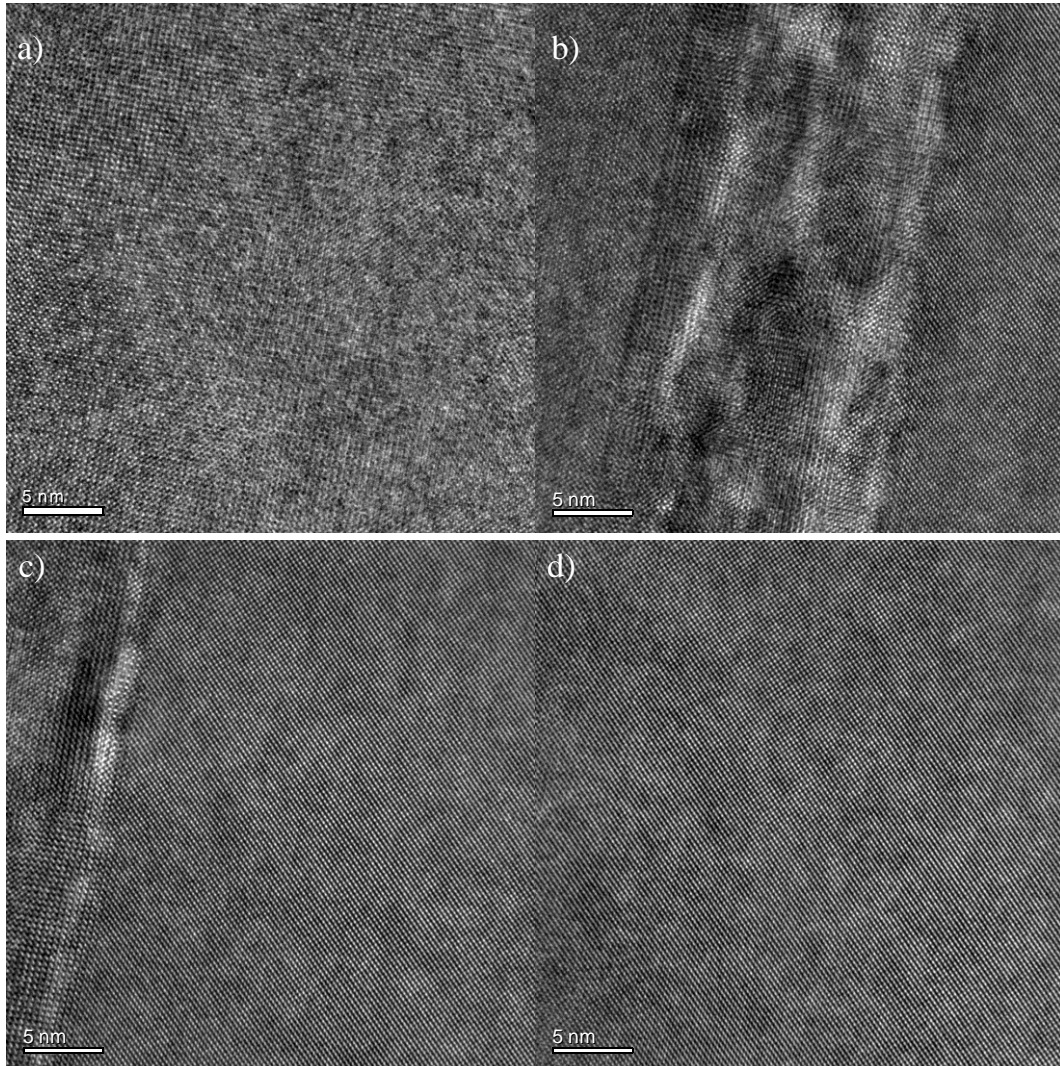
Fig. 5.1.49. HRTEM image of STO/LSMO//LSAT, the same lamella as in Fig. 5.1.53. LSAT substrate a), LSMO layer in between substrate and STO film b), LSMO and STO interface c) and strained STO layer closer to LSMO electrode d). [100] zone axis, 300 kV accelerating field. Acknowledgements dr. Cosmin Sandu.

No contrast due to "a/c" elastic domains (twinning) is observed in Fig. 5.1.49. b), c) and d). Only contrast, observable in Fig. 5.1.49 b) and c) (in LSMO layer), is due to elastic strain relaxation forming dislocation network (confirmed by Fourier analysis of HRTEM LSMO layer). FFT of STO layer (Fig. 5.1.49 d) present superlattice peaks (not shown in Fig. 5.1.49) also. In conclusion even negative -0.6 % in plane strain, as in TEM investigated

sample, increases AFD phase transition to higher than room temperatures in agreement with [D40].

5.1.4. AFD phase transition and ferroelectricity in APB of strained STO thin films.

Antiferrodistortive phase transition temperature in strained STO thin films (biaxial negative -1 % strain, exerted due to clamping by LSAT substrate) is enhanced up to 360 K [D44]. This phase transition manifests in additional ferroelastic strain and small but physically important change of unite cell dimensions (in bulk STO change from cubic to tetragonal symmetry). Change from cubic to tetragonal symmetry (and obvious lattice parameter change from only one "a" to two "a" and "c") makes a possibility for elastic strain relaxation by forming fine "a/c" elastic 90° domains in thin film of STO (twinning). "a/c" domain pattern was observed in STO thin film (STO/LSMO//LSAT heterostructures) at room temperature by AFM/PFM topography. Phase transition temperature estimated to be around 370 K, by high temperature AFM experiments done in prof. Elisabeth Soergel group at Institute of
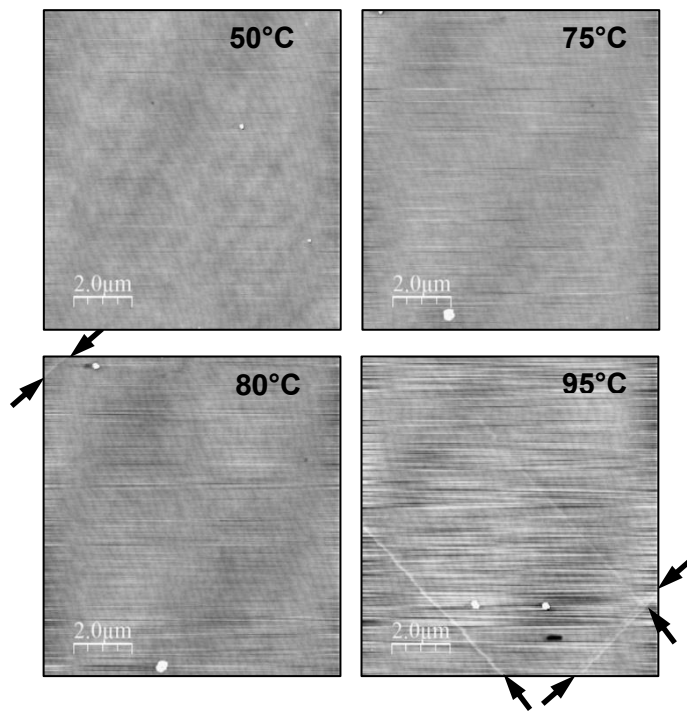

Fig. 5.1.50. AFM topography images at increasing temperature shows the onset of the development of ferroelastic domains. The "a" domains can be discerned by thin topographical features that follow strict crystallographic directions i.e. <100>pc and are highlighted by black arrows. Acknowledgements dr. Leo Mc Gilly.

132

Physics, University of Bonn (Bonn, Germany) by dr. Leo Mc Gilly. Temperature dependent AFM/PFM setup used in these experiments is described in [D51].

While the films under study were actually within the tetragonal antiferrodistortive monodomain state (metastable) at room temperature, heating up to 100°C (close to AFD transition temperature) gave impulse for "a/c" elastic domain formation (due to minimization of elastic energy), this strain relaxation mechanism is observed at room temperatures (monodomain STO thin films relaxes to polydomain state in few days), but at temperatures close to the AFD phase transition this relaxation happens in few minutes instead of days. Unfortunately technical limitations did not allowed to observe vanishing of the surface rumpling (what should happen at temperatures higher than AFD transition temperature), limiting temperature was 100°C. "a" domain formation is shown in Fig. 5.1.50., while heating STO/LSMO//LSAT from room temperature up to 95°C. This experiment gives indirect confirmation of AFD phase transition temperature enhancement up to 100°C.

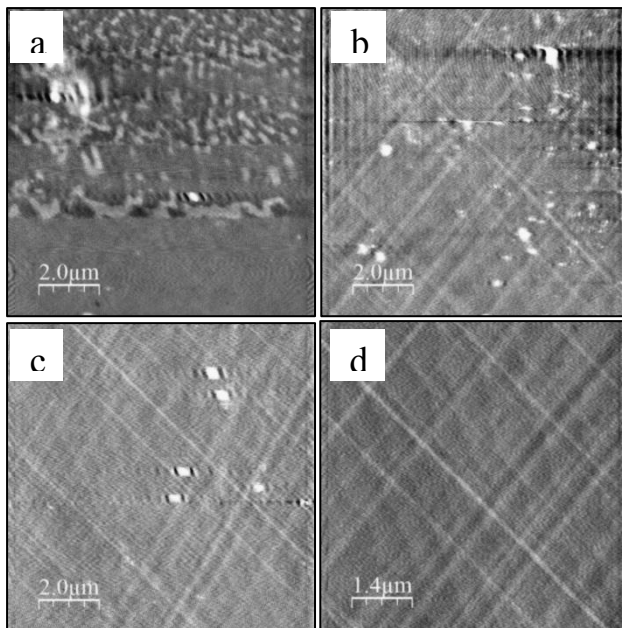Fig. 5.1.51. Low-temperature AFM topography images taken at -70°C which shows the formation of ice a) which acts to obscure the true surface features which can be seen in b) and after several successive scans to clean the area c) and d). Acknowledgements dr. Leo Mc Gilly.

After unsuccessful attempts to find ferroelectricity in APB (and anti-phase boundaries) of strained STO (STO/LSMO//LSAT) at room temperatures

(shown in previous 5.1.3.2 Chapter) we decided to try the same experiment at temperature below 0°C i.e. on cooling down from room temperatures. Results of this investigation are presented in Fig. 5.1.51 (AFM/PFM measurements accomplished in Bonn, Germany).

On cooling the sample the minimum temperature attained was -70°C. Several experimental obstacles presented themselves whilst trying to work at such low temperature. Firstly, even though the AFM enclosure had been flushed with dry nitrogen for up to an hour before cooling in order to remove as much moisture as possible the formation of ice was still observed as can be seen in Fig. 5.1.51 a). This posed a major problem as it prevented good contact between the conductive tip and the film surface which is essential for performing PFM and it also acted to obscure the ferroelastic topographical features. A method to overcome this problem was to simply repeatedly scan the same area to allow for the tip to remove the ice from the scan area (Fig. 5.1.51 b), c) and d)). No evidence of a polar APB was found across the entire temperature range either commensurate with the existing ferroelastic domain structure or otherwise.

An attempt at inducing the polar nature of the film by the application of an electric field across the scanning probe and the bottom electrode was done. The tip was scanned across the surface whilst at the same time 10 V of alternating polarity was applied. The expectation was to bring about a field-induced transition to the polar APBs as the limit to temperature had been reached. While initially it seems that domains have been poled in the film (Fig. 5.1.52 a)) it would seem unlikely on further consideration. The observed contrast in the PFM images could appear from charge-injection into the film considering the thickness of the film (approx. 100 nm) and the large applied bias (±10 V). Furthermore the contrast persisted until room temperature (Fig. 5.1.52 b)) where the ferroelectric phase is far from expected.
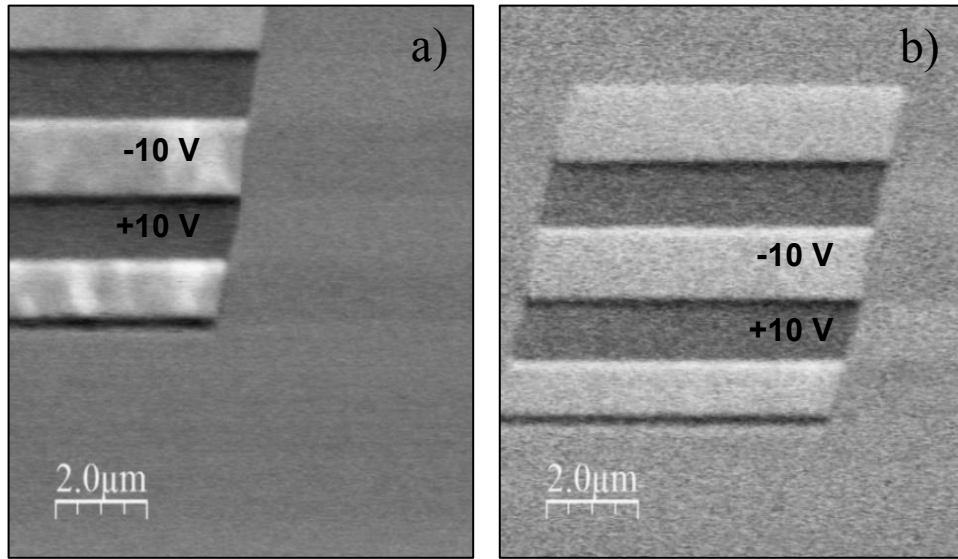
Fig. 5.1.52. Attempts at poling with alternate application of positive and negative voltages to the tip results in the observed PFM 'domain' structure at -70°C a) which then persists to room temperature b). This is thought to likely be an example of charge injection into the film and not true polarization reversal. N.B. the image in a) is shifted off-center due to drift compared to that seen in b). Acknowledgements dr. Leo Mc Gilly.

Absence of polar APB in strained STO thin films down to -70°C forced us to change AFM/PFM equipment to more capable one. Final PFM experiment was done in EPFL LC, with Cryogenic STM & SFM (Omicron Nanotechnology GmbH, Germany) capable to measure temperature dependent SPM down to 4 K. Fully strained (-0.88% biaxial in-plane strain, calculated from asymmetric RSM) 80 nm STO heterostructure (STO/LSMO//LSAT) was placed into the high vacuum chamber and slowly cooled down by radiative emission down to 150 K. Chamber walls were cooled by liquid nitrogen flowing in capillary system. No water vapor was in the chamber, thus no ice formed even down to 150 K temperatures. PFM response was observed at fixed temperatures down to the lowest attained temperature – 153 K. Low temperature PFM experiment results are shown in Fig. 5.1.53.

Topography	**PFM amplitude**	**PFM phase**	
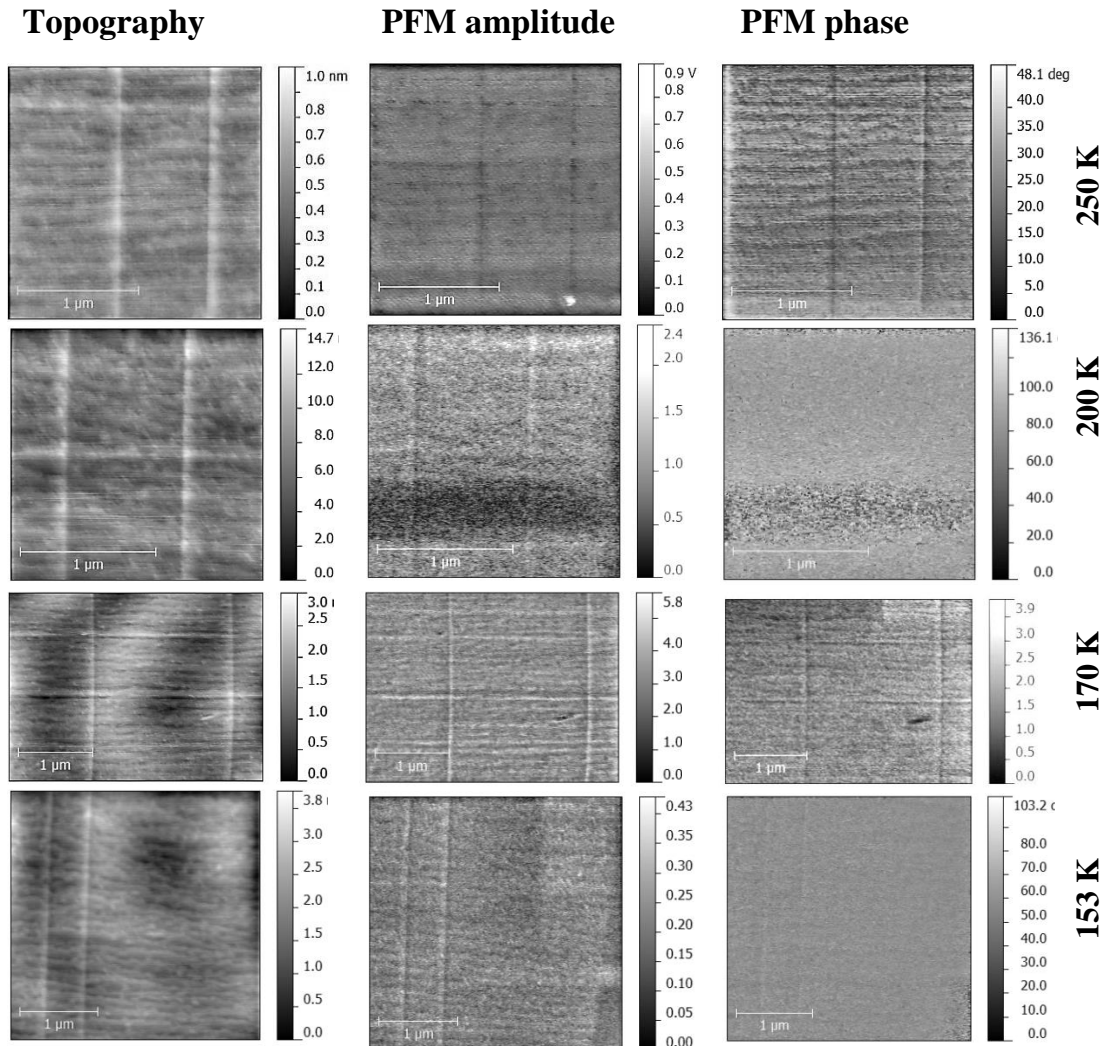
Fig. 5.1.53. Low temperature PFM topography, amplitude and phase images, taken on cooling from room temperature at 250 K, 200 K, 170 K and 153 K. The unites are the same as in 250 K images. Acknowledgements dr. Leo Mc Gilly and dr. Igor Stolichnov.

No evidence of polar response of APB was observed even to the lowest achieved temperatures. Surface rumpling due to "a/c" domain pattern persists to the lowest temperatures with no evidence of ferroelectric phase transition. In Fig. 5.1.53 PFM amplitude and phase images one can observe the features coming from the crosstalk between topography and PFM amplitude/phase channels.

In summary, high structural quality strain free homoepitaxial STO thin films were deposited at optimized conditions by PLD. Atomically smooth surfaces and interfaces, also defect free films were deposited from ceramic STO target in agreement with before accomplished studies on STO and other materials [D30-31, D37-39]. STO thin films deposited from single crystal target were slightly off-stoichiometric (in comparison with literature non-stoichiometry was negligible [D34]), less than x=0.05 in $Sr_{1+x}TiO_{3+\delta}$. Non-stoichiometry was discovered while analyzing HRTEM images, which revealed treading dislocation networks created to release elastic energy accommodated in thin films due to lattice expansion (Sr/Ti off-stoichiometry).

Strained STO thin films were deposited from ceramic target (avoiding Sr/Ti off-stoichiometry) on LSAT substrates with LSMO electrodes at optimized conditions by PLD. Structural and local characterization by XRD, TEM, RHEED and AFM revealed that STO thin films in STO/LSMO//LSAT heterostructures were in-plane compressively strained. In-plane compressive strain state were controlled by changing LSMO electrode layer and STO thin film thicknesses, it was possible to relax strained STO thin films from -1% to -0.5% in-plane strain in controllable manner.

Strained STO thin films were in AFD phase at room temperature, confirmed by AFM topography – surface rumpling due to elastic twinning (90° elastic domains) and superlattice peaks obtained analyzing HRTEM images. In fully strained STO thin films phase transition from paraelectric to AFD phase occur at approximately 373 K (instead of 108 K as in bulk STO), observed by high temperature AFM experiment. Initially elastic monodomain STO thin film splitted into polydomain (90° elastic domains, twinning) approaching 373 K on heating. This could be explained by elastic energy release by forming elastic twins. Approaching phase transition temperature twinning proceeds way faster than at temperatures far away from transition. The same twinning was observed in the films which were never heated (after deposition) above the

room temperature. Splitting from monodomain into polydomain state proceeded during few weeks at room temperature.

Tagantsev et al. [I1] predicted that "hard" (parallel to tetragonal axis) APBs in bulk STO should develop instability in respect to polarization. *Pertsev et al.* [D22] calculated strain-temperature phase diagram of STO thin films (epitaxially strained and clamped by substrates) and predicted phase transition temperature increase with induced in-plane compressive and tensile strain (experimentally confirmed by *Haeni et. al.* [D24]). Having both facts in mind it was assumed that at -1% in plane strained STO thin films should develop ferroelectricity in APBs at higher temperatures than originally predicted by *Tagantsev* (35 K to 40 K). Increase in the phenomenon temperature would be beneficial from application and scientific point of view. No polar response in the antiphase boundaries (no predicted ferroelectricity in APBs [I1]) was observed in the temperature range from 150 K up to 370 K by PFM. There are few possibilities:

1. There is no APBs in strained STO thin films (no APBs were observed in HRTEM investigation);
2. There is no ferroelectricity in APB at 150 K to 370 K temperatures;
3. APBs density is negligible small to be observable by PFM studies;
4. APBs width is too small to be observed by PFM (predicted "hard" APBs width $2t_w \approx 20$ to $25a_0$ [I1] should be thick enough to be observed by PFM, tip radius ~28 nm).

References

D1 Rimai L., DeMars G.A. *Phys. Rev.,* 127, 702 (1962).

D2 Last J. T. *Phys. Rev.,* 105, 6, 1740 (1957).

D3 Lytle F.W. *J. Appl. Phys.,* 35, 2212 (1964).

D4 Okazaki A., Kawaminami M. *Mater. Res. Bull.,* 8, 545 (1973).

D5 Mitsui T., Westphal W.B. *Phys. Rev.,* 124, 1354 (1961).

D6 Unoki H., Sakudo T. *J. Phys. Soc. Jpn.,* 23, 546 (1967).

C7 Sato M., Soejima Y., Ohama N., Okazaki A., Scheel H.J., Müller K.A. *Phase Transitions,* 5, 207 (1985).

D8 Fleury P.A., Scott J.F., Worlock J.M. *Phys. Rev. Lett.,* 21, 16 (1968).

D9 Laubereau A., Zurek R. *Z. Naturforsch.,* 25a, 391 (1970).

D10 Shirane G., Yamada Y. *Phys. Rev.,* 177, 858 (1969).

D11 Okai B., Yoshimoto J. *J. Phys. Soc. Jpn.,* 39, 162 (1975).

D12 Müller K.A., Berlinger W., Waldner F. *Phys. Rev. Lett.,* 21, 12, 814 (1968).

D13 Sakudo T., Unoki H. *Phys. Rev. Lett.,* 26, 851 (1971).

D14 Uwe H., Sakudo T. *Phys. Rev. B,* 13, 271, (1976).

D15 Müller K. A., Burkard H. *Phys. Rev. B,* 19, 3593, (1979).

D16 Viana R., Lunkenheimer P., Hemberger J., Bohmer R., Loidl A. *Phys. Rev. B,* 50, 1, 601 (1994).

D17 Slater J.C. *Phys. Rev.,* 78, 748 (1950).

D18 Yamanaka T., Hirai N., Komatsu Y. *American Mineralogist*, 87, 1183 (2002).

D19 Tagantsev A. K., Sherman V. O., Astafiev K. F., Venkatesh J., Setter N. *J. Electroceramics,* 11, 5 (2003).

D20 Pertsev N.A., Zembilgotov A.G., Tagantsev A.K. *Phys. Rev. Lett.,* 80, 1988 (1998).

D21 Pertsev N., Zembilgotov A.G., Hoffman S., Waser R., Tagantsev A. K. *J. Appl. Phys.,* 85, 1698 (1999).

D22 Pertsev N.A., Tagantsev A.K., Setter N. *Phys. Rev. B,* 61, R825 (2000).

D23 Petzelt J., Ostapchuk T., Gregora I., Rychetský I., Hoffmann-Eifert S., Pronin A. V., Yuzyuk Y., Gorshunov B. P., Kamba S., Bovtun V., Pokorný J., Savinov M., Porokhonskyy V., Rafaja D., Vaněk P., Almeida A., Chaves M. R., Volkov A. A., Dressel M., Waser, R. *Phys. Rev. B,* 64, 18, 184111 (2001).

D24 Haeni J.H., Irvin P., Chang W., Uecker R., Reiche P., Li Y.L., Choudhury S., Tian W., Hawley M.E., Craigo B., Tagantsev A.K., Pan X.Q., Streiffer S.K., Chen L.Q., Kirchoefer S.W., Levy J., Schlom D.G. *Nature*, 370, 758 (2004).

D25 Yamada T., Astafiev K., Sherman V., Tagantsev A., Su D., Muralt P., Setter N. *J. Appl. Phys.*, 98, 054105 (2005).

D26 Yamada T., Astafiev K., Sherman V., Tagantsev A., Muralt P., Setter N. *Appl. Phys. Lett.,* 86, 142904 (2005).

D27 Wang R., Zhu Y., Shapiro S. M. *Phys. Rev. B,* 61, 8814 (2000).

D28 Yamada T., Kiguchi T., Tagantsev A.K., Morioka H., Iijima T., Ohsumi H., Kimura S., Osada M., Setter N., Funakuboo H. *Integrated Ferroelectrics,* 115, 57 (2010).

D29 Yamada T., Astafiev K. F., Sherman V. O., Tagantsev A. K., Su D., Muralt P., Setter N. *J. Appl. Phys.,* 98, 054105 (2005).

140

D30 Ohnishi T., Yamamoto T., Meguro S., Koinuma H., Lippmaa M. *J. Phys.: Conf. Ser.,* 59, 514 (2007).

D31 Ohnishi T., Shibuya K., Yamamoto T., Lippmaa M. *J. Appl. Phys.,* 103, 103703 (2008).

D32 Suzuki T., Nishi Y., Fujimoto M. *Philos. Mag. A,* 80, 621 (2000).

D33 Fuchs D., Adam M., Schweiss P., Gerhold S., Schuppler S., Schneider R., Obst B. *J. Appl. Phys.,* 88, 1844 (2000).

D34 Brooks C. M., Fitting Kourkoutis L., Heeg T., Schubert J., Muller D. A., Schlom D. G. *App. Phys. Lett.,* 94, 162905 (2009).

D35 Ruddlesden S. N., Popper P. *Acta Crystallogr.*, 10, 538 (1957); 11, 54 (1958).

D36 Qin Y.L., Jia C.L., Urban K., Hao J.H., Xi X.X. *J. Mater. Res.,* 17, 12, 3117 (2002).

D37 Dam B., Rector J. H., Johansson J., Kars S., Griessen R. *App. Surf. Scien.,* 96-96, 679 (1996).

D38 Dam B., Rector J. H., Johansson J., Huijbregtse J., De Groot D. G. J. *Appl. Phys.*, 83, 3386 (1998).

D39 Koster G., Kleinv, Siemons W., Rijnders G., Dodge J. S., Eom C.-B., Blank D. H. A., Beasley M. R. *Rev. Mod. Phys.,* 84, 253 (2012).

D40 Mackenzie A. P., Reiner J. W. , Tyler A. W. , Galvin L. M. , Julian S.R., Beasley M. R., Geballe T. H., Kapitulnik A. *Phys. Rev. B,* 58, R13318 (1998).

D41 Klein L., Dodge J. S., Ahn C. H., Snyder G. J., Geballe T. H., Beasley M. R., Kapitulnik A. *Phys. Rev. Lett.,* 77, 2774 (1996).

D42 Naito M., Sato H. *Physica C,* 229, 1 (1994).

D43 Herger R., Willmott P. R., Bunk O., Schlepütz C. M., Patterson B. D., Delley B., Shneerson V. L., Lyman P. F., Saldin D. K. *Phys. Rev. B,* 76, 195435 (2007).

D44 Yamada T., Kiguchi T., Tagantsev A. K., Morioka H., Iijima T., Ohsumi H., Kimura S., Osada M., Setter N., Funakubo H. *Integr. Ferroelectr.,* 115, 57 (2010).

D45 He F., Wells B. O., Shapiro S. M. *Phys. Rev. Lett.,* 94, 176101 (2005).

D46 Bachelet R., Sanchez F., Santiso J., Munuera C., Ocal C., Fontcuberta J. *Chem. Mater.,* 21, 12, (2009).

D47 Urushibara A., Moritomo Y., Arima T., Asamitsu A., Kido G., Tokura Y. *Phys. Rev. B,* 51, 14103 (1995).

D48 Yang F., Kemik N., Biegalski M. D., Christen H. M., Arenholz E., Takamura Y. *Appl. Phys. Lett.,* 97 , 092503 (2010).

D49 Catalan G., Lubk A., Vlooswijk A. H. G., Snoeck E., Magen C., Janssens A., Rispens G., Rijnders G., Blank D. H. A., Noheda B. *Nature Mat.,* 10, 963 (2011).

D50 Li H., Salamanca-Riba L., Ramesh R., Scott J. H. *J. Mater. Res.,* 18, 7, 1698 (2003).

D51 Lilienblum M., Hoffmann Á., Soergel E., Becker P., Bohatý L., Fiebig M. *Rev. Sci. Instrum.,* 84, 043703 (2013).

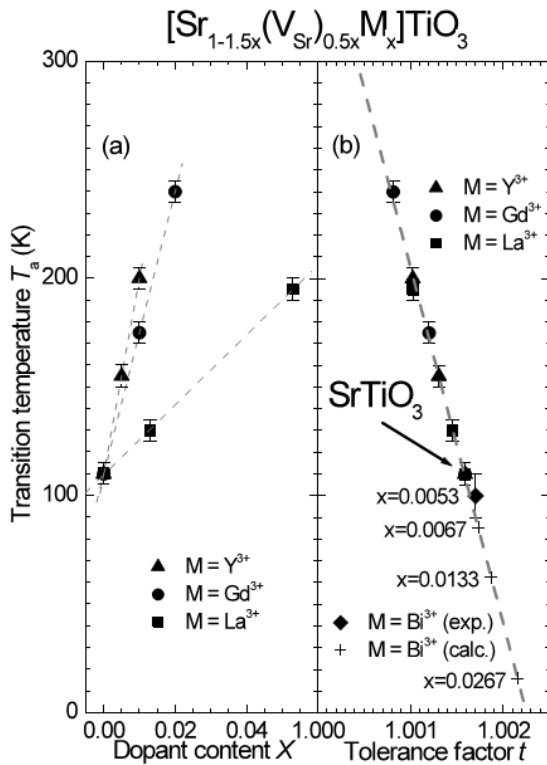## 5.2. Chemical doping effects and changed lattice dynamics in $(Sr_{1-1.5x}Bi_x)TiO_3$ ceramics.

Fig. 5.2.1. Transition temperature T_a of Y-, Gd-, and La-doped STO vs. dopant content x in $[Sr_{1-1.5x}(V_{Sr})_{0.5x}M_x]TiO_3$ a) and tolerance factor t b). Dashed lines are linear fits to the experimental data. Solid diamond marks T_a for Bi-doped STO with x=0.0053, taken from data of [E8], while crosses show T_a for x=0.0067, 0.0133, and 0.0267 following the linear fit to the aforesaid data (dashed line) as a function of t. Adapted from [E9].

Ferroelectricity in $SrTiO_3$ can be induced as a result of small concentrations of dopants [E1], isotopic substitution in the oxygen octahedra [E2], applied high enough electric field [E3], or mechanical pressure [D14]. The properties are extremely sensitive to external perturbations and dopants, due to the tolerance factor t ≈ 1 (using *Shannon* radii [E4]). Induced biaxial strain and clamping by the substrate (STO thin films) influence on STO phase transitions and properties were analyzed in previous chapters. In this chapter doping effects on $SrTiO_3$ dielectric properties will be explored by broadband dielectric spectroscopy accomplished in Laboratory of Microwave Spectroscopy, Vilnius University (Vilnius, Lithuania).

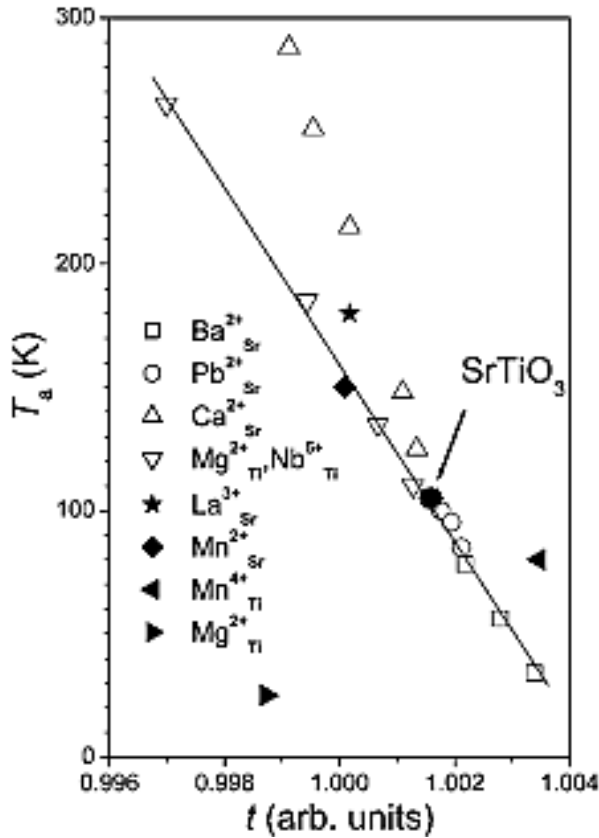Even the smallest amount of constituent isovalent dopants, like Ba^{2+}, Pb^{2+}, Cd^{2+} [E5] or Ca^{2+}

Fig. 5.2.2. Improper ferroelastic phase transition temperature T_a for STO based materials with Sr^{2+} substituted by Ba^{2+}, Pb^{2+}, Ca^{2+}, Mn^{2+}, and La^{3+} and Ti^{4+} substituted by Mn^{4+}, Mg^{2+}, and $Mg^{2+}_{1/3}$ $Nb^{5+}_{2/3}$ as a function of the tolerance factor t. Several data points are included for some substituents because t varies with the dopant concentration. Data points marked by solid symbols correspond to [E10] work; open symbols are taken from [E11, E12 and [E13]. Adapted from [E10].

[E6] can induce polar state in $SrTiO_3$. Heterovalent doping with rare-earth ions induces anomalies in the dielectric response with considerable frequency dispersion [E7] – doping changes STO structure from centrosymetric to noncentrosymetric or even polar one.

Recently it was shown in [E9] that for heterovalent dopants on a perovskite A-site the AFD phase transition temperature T_a decreases by the increasing Goldschmidt tolerance factor t (shown in Fig. 5.2.1). Similar trend was observed also in another experiment [E10], therein was shown that T_a increases with decreasing t and vise versus (shown in Fig. 5.2.2).

Before-mentioned investigations allow concluding, that doping effects might be treated in the same manner as straining of $SrTiO_3$ lattice. These strains develops due to different radii ions (or vacancies) introduced into very sensitive STO lattice (tolerance factor $t \approx 1$). Different substituent ion (vacancies) radii change STO lattice parameters and tolerance factor, thus

144

doping affects both phase transition temperatures. Increased lattice constant due to A-site doping leads to decrease of T_a and appearance of T_C (or Tm as in relaxor ferroelectrics).

Bismuth was tried for improvement of $SrTiO_3$ properties. Selection of bismuth can be rationalized by the fact that STO A-site doping with ion (like Pb or Ba) larger than Sr induces ferroelectricity and enhance functional properties by effecting phase transitions temperatures. Bi doping could be used for enhancement of giant piezoelectric effect [E14] temperatures from cryogenic 1 K temperature to more applicable ones by increasing T_a, in a similar manner considered in [E15] for increasing piezoelectric properties of Sr doped PZT (due to extrinsic contribution to piezoelectric properties by elastic domain walls).

Heterovalent Bi^{3+} doping on A-site of $SrTiO_3$ leads to considerable lattice expansion. This is contradictory, because Bi^{3+} ionic radii (extrapolated to $N_c=12$) estimated size of 1.45 Å is just slightly larger than 1.44 Å for Sr^{2+} [E4]. This discrepancy might be explained by the fact that due to Bi^{3+} doping, there should appear V_{Sr} in the lattice maintaining overall charge neutrality. In [E9] V_{Sr} size was estimated to be 1.54 Å, this value fits before-mentioned model (phase transition temperature dependency from lattice size, internal strain and tolerance factor) very well (shown in Fig. 5.2.1). Lattice expansion was confirmed by XRD measurements [E14], shown in Fig. 5.2.3.

$(Sr_{1-1.5x}Bi_x)TiO_3 \rightarrow [Sr_{1-1.5x}(V_{Sr})_{0.5x}Bi_x]TiO_3$

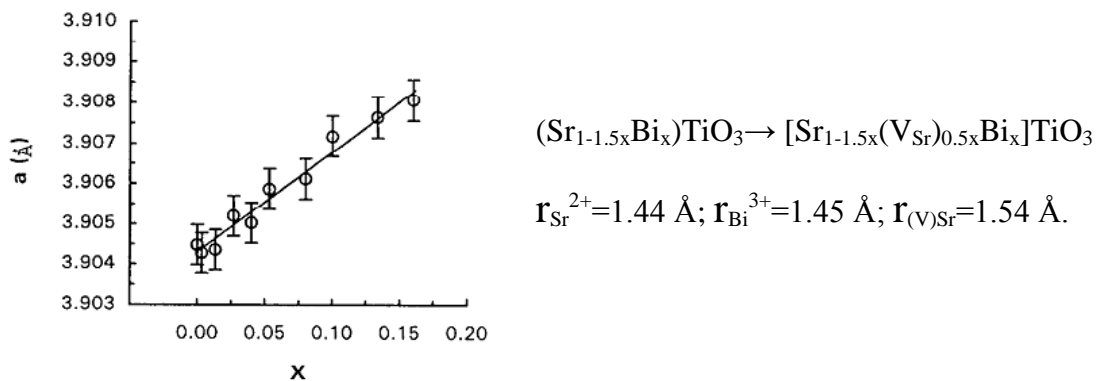$r_{Sr}^{2+}=1.44$ Å; $r_{Bi}^{3+}=1.45$ Å; $r_{(V)Sr}=1.54$ Å.

Fig. 5.2.3. The lattice parameter "a" of $(Sr_{1-1.5x}Bi_x)TiO_3$ as a function of x, measured by XRD diffraction. Adapted from [E16].

145
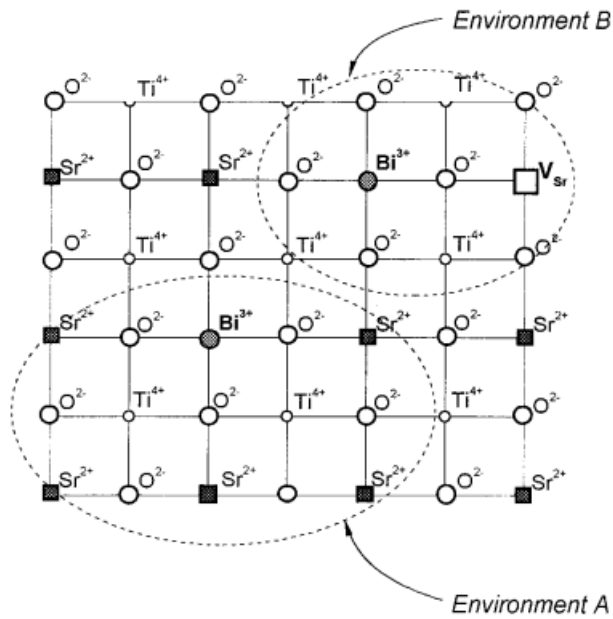
Fig. 5.2.4. Schematic projection on the (100) plane for $(Sr_{1-1.5x}Bi_x)TiO_3$ showing two types of local environments of Bi ions [E17].

Bi doping induces formation of local antiferrodistortive and polar regions due to different Bi environments, shown in Fig. 5.2.4.

In environment B, Bi^{3+} ion is close to V_{Sr}, thus STO lattice is expanded and polar anomaly is expected (due to off-center Bi ion and ferroelectric distortion of the lattice). In environment A, there is no V_{Sr} in close proximity, thus lattice is contracted, tolerance factor t decreases and antiferrodistortive anomaly takes places.

Even the minute Bi doping induces two dielectric anomalies, denoted as modes A and B in Fig. 5.2.5. On Bi concentration increase these modes gain the strength, but T_m remains intact, and only at x=0.0033 third mode appears (in Fig. 5.2.5 denoted as mode C). T_m and dielectric strength of this mode increase with increasing Bi concentration and on further increasing Bi concentration mode C starts dominating the dielectric spectra.

Sometimes there is observed and fourth dielectric anomaly, shown in Fig. 5.2.6. This anomaly is related to oxygen vacancies, because its strength strongly depends on annealing atmosphere. Reducing atmosphere during anneal increases its strength and oxidizing – completely suppresses the anomaly.
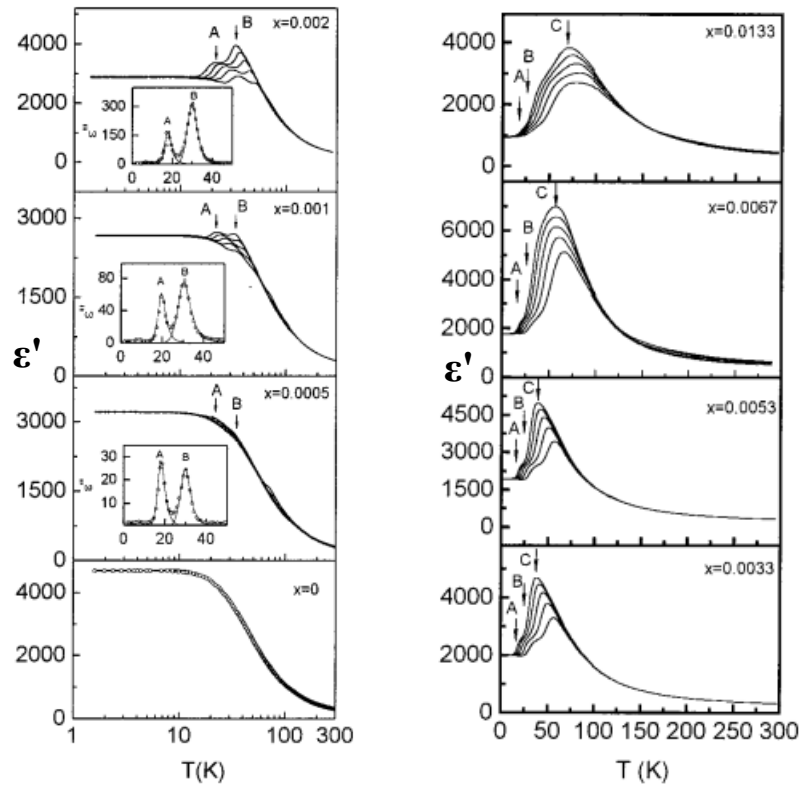
Fig. 5.2.5. Temperature dependence of ε' for $(Sr_{1-1.5x}Bi_x)TiO_3$ with different x at 0.1, 1, 10, 100 and 1000 kHz (from top to bottom). The insets show the temperature dependence of ε'' at 0.1 kHz. Adapted from [E17].
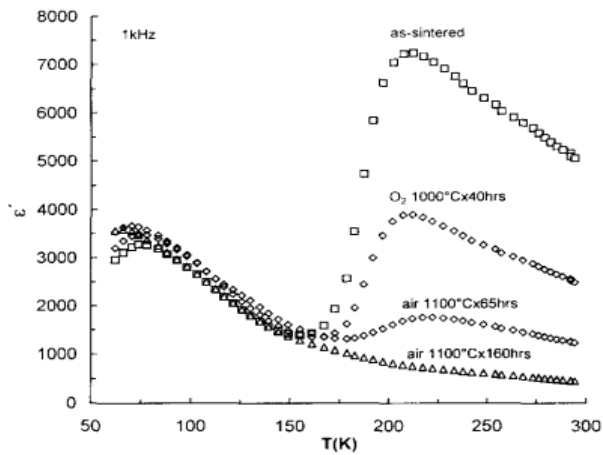
Fig. 5.2.6. Temperature dependence of ε' under different annealing conditions (atmosphere, temperature and time) for $(Sr_{1-1.5x}Bi_x)TiO_3$ ceramics with x=0.0133. Adapted from [E18].

A lot of studies have already been done to obtain dielectric properties of pure and doped SrTiO$_3$. Among the early investigators strontium-bismuth titanate system was first reported by Skanavi et al. [E19]. Researchers discovered that $(Sr_{1-1.5x}Bi_x)TiO_3$ ceramic with small to moderate Bi content exhibits dispersion similar to relaxor ferroelectrics. They tried to

explain this behavior on the basis of hopping ions model. The later investigations confirmed relaxor-ferroelectric-like behavior of strontium-bismuth titanate (SBT for sh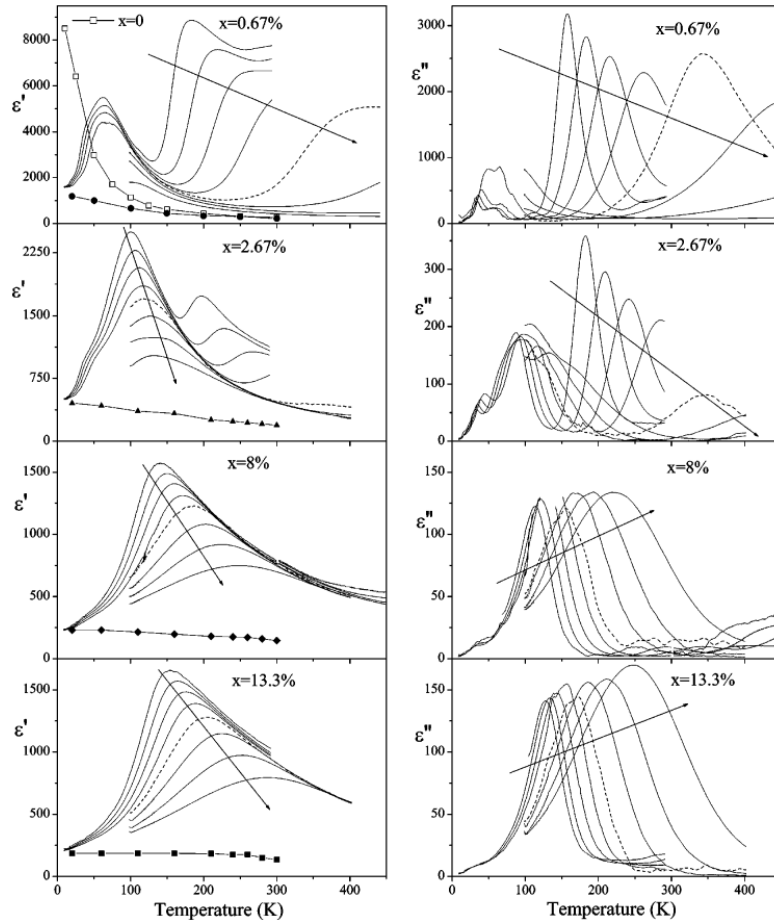ort) [E16, E18, E20-22]. Broadband dielectric studies (Fig. 5.2.7) of this material (up to $x \leq 0.17$) [E23-24] showed that Bi doping induces formation of local antiferrodistortive and polar regions. This causes a complex relaxational dynamics below the phonon frequency range.

Fig. 5.2.7. Temperature dependence of the real and imaginary parts of dielectric function of $(Sr_{1-1.5x}Bi_x)TiO_3$ for $x = 0.67\%$, 2.67%, 8%, 13.3% at selected frequencies 10^2, 10^3, 10^4, 10^5, 10^6 (dashed), 10^7, 10^8, and 10^9 Hz. The total phonon contribution is denoted by symbols (full circles for $x = 0.67\%$ and open squares for $x = 0$). Arrows indicate the evolution of the spectra with increasing frequency. Adapted from [E23].

Relaxor-like materials have been extensively studied over last decades, typical relaxors are $Pb(Mg_{1/3}Nb_{2/3})O_3$ (PMN) crystal [E25] or ceramic [E26]. Very intense investigation by the broadband dielectric spectroscopy of various solid solutions of $PbMg_{1/3}Nb_{2/3}O_3$-$PbSc_{1/2}Nb_{1/2}O_3$-$PbZn_{1/3}Nb_{2/3}O_3$ (PMN-PSN-PZN) was reported [E27]. Dielectric spectra of these solutions were

investigated in a broad frequency range from 20 Hz to 100 THz by a combination of dielectric spectroscopy (20 Hz - 53 GHz), time-domain THz spectroscopy (0.1–0.9 THz) and infrared reflectivity (20–3000 cm^{-1}). Very strong and broad dielectric relaxation observed below the phonon frequencies was analyzed in terms of distribution of relaxations times, using Tikhonov regularization method. It revealed slowing down of the longest and mean relaxation times in agreement with the Vogel-Fulcher (4.27 equation) and the Arrhenius laws (4.28 equation), respectively. In all these materials, which we can call classical relaxors, the splitting of the relaxation time distribution function into two parts was observed [E25-29]. One peak of the relaxation time distribution function remains at THz frequencies and another one broadens and goes down to the lowest frequencies. Creation of polar nanoregions below the Burns temperature is manifested by the appearance of the dielectric relaxation in the THz range, by temperature dependence of the A_{1g} component of the ferroelectric soft mode and by splitting of all polar modes in the infrared spectra.

Moreover the nearly ferroelectric-like behavior in $(Sr_{1-1.5x}Bi_x)TiO_3$ (SBT for short) compounds with small bismuth content [E16, E23] witch transforms to the relaxor-like one when bismuth amount increases causes considerable scientific interest. The aim of this investigation is to extend the investigation of dielectric dispersion in SBT with x ranging from 0.05 to 0.25 and calculate relaxation times distribution functions. No broadband dielectric studies (to our knowledge) have been carried out for compositions with x = 0.25 and 0.2, no relaxation times distribution functions (without any *a priori* statements) were calculated for $(Sr_{1-1.5x}Bi_x)TiO_3$ at all.

Dielectric properties of SBT ceramics were investigated in the broad frequency (from 10 mHz to 36 GHz) and temperature (from 30 K to 450 K) ranges. The SBT solid solution was synthesized by solid state reaction from high-grade oxides in the Laboratory of Physics and Application of Functional Materials [B1], Institute of Solid State Physics, University of Latvia, Latvia, from $SrCO_3$ (99.5% purity), TiO_2 (99.5% purity) and Bi_2O_3 (99% purity).

Calcination was done at 1000°C (900°C for $0.75SrTiO_3$-$0.25Bi_{2/3}TiO_3$) for 1 hour, sintering was done at 1360°C (1250°C for $0.75SrTiO_3$-$0.25Bi_{2/3}TiO_3$) for 1 hour, all thermal treatment was done in a platinum crucible in ambient atmosphere. Silver paste was used for electrodes on perpendicular surfaces of samples (which dimensions were chosen according to measurement frequency) to produce a good electrical contact. The samples were annealed in atmosphere at 450 K before each measurement to avoid memory effects. The measurements data have been collected on cooling with the cooling rate less than 2 K/min.

Temperature dependence of the real and imaginary parts of the dielectric permittivity of $(Sr_{0.625}Bi_{0.25})TiO_3$ ceramics are presented in the Fig. 5.2.8.
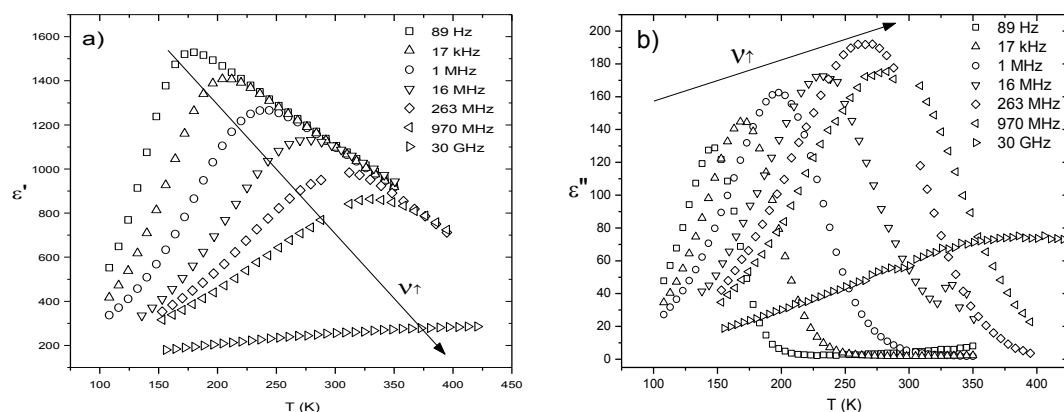

Fig. 5.2.8. Temperature dependence of the real a) and imaginary b) parts of dielectric permittivity of SBT (x = 0.25) ceramic at fixed frequencies.

Experimental data shows pronounced dielectric dispersion below 500 K temperature. The maximum of the real and imaginary parts of dielectric permittivity shifts to the higher temperatures on the frequency increase. This resembles the dielectric behaviour similar to the dipolar glasses e.g. BP-BPI [A52]. The frequency dependences of dielectric permittivity (Fig. 5.2.9) exhibit large dispersion which broadens and shifts toward lower frequencies on cooling.
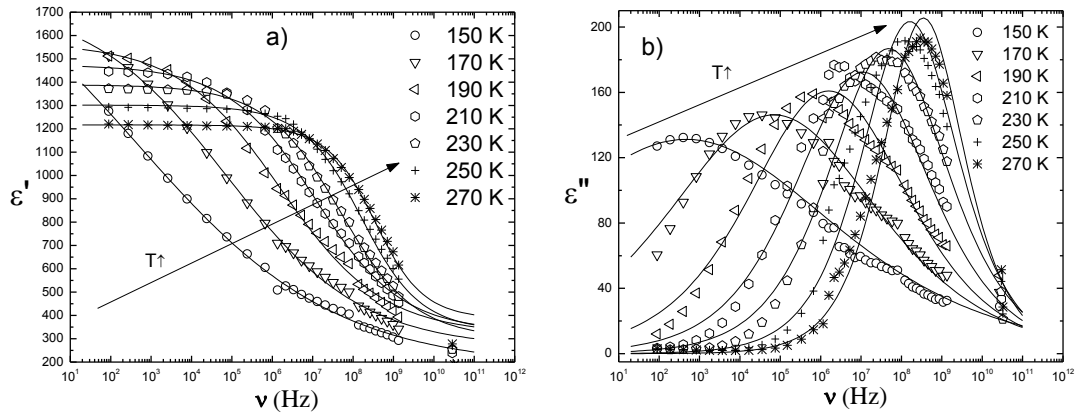
Fig. 5.2.9. Frequency dependence of the real a) and imaginary b) parts of dielectric permittivity of SBT (x = 0.25) ceramic at fixed temperatures. Solid lines are the best fits by Cole-Cole formula (4.21).
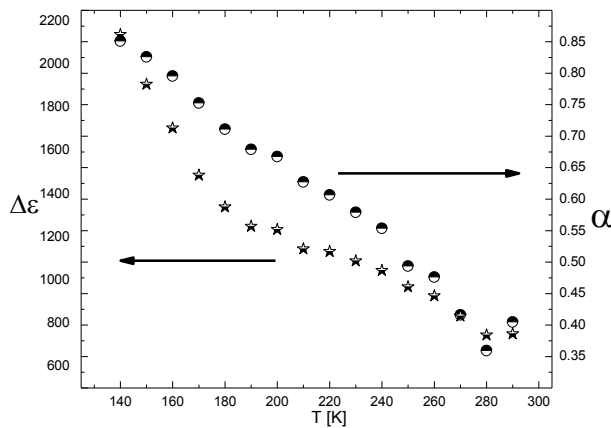

Fig. 5.2.10. The Cole-Cole fit parameters as temperature dependence: the relaxation times distribution parameter α (circles) and the strength of relaxator $\Delta\varepsilon$ (stars).

From Fig. 5.2.9 it is clearly seen that this dispersion is much broader than the Debye-type dispersion thus there is a distribution of relaxation times. Cole-Cole formula approximates the frequency dependent experimental data rather well (shown in Fig. 5.2.9), just at low temperatures dispersion becomes anomalously broad and asymmetric, thus Cole-Cole fits starts to deviate from experiment. Broader than the Debye-type dispersion is also confirmed by Cole-Cole fit α value (Fig. 5.2.10, circles). It reaches up to 0.85, which means extremely broad distribution of the relaxation times.

Dielectric strength (shown in Fig. 5.2.10, stars) of the relaxational process monotonically increases in a manner already observed in disordered materials, no dielectric strength maximum was observed agreeably with the fact that no phase transition was observed in $(Sr_{0.625}Bi_{0.25})TiO_3$ ceramics.

151

In order to extract more detailed information from frequency dependences of SBT (x = 0.25) ceramics we calculated the real distribution of relaxation times as a superposition of independent individual Debye-type processes. Eq. 4.18 and 4.19 were numerically solved using Tikhonov regularization method, calculation method is described in [C12]. Relaxation times distribution model fits experimental dielectric permittivity data very well, as shown in Fig. 5.2.11.
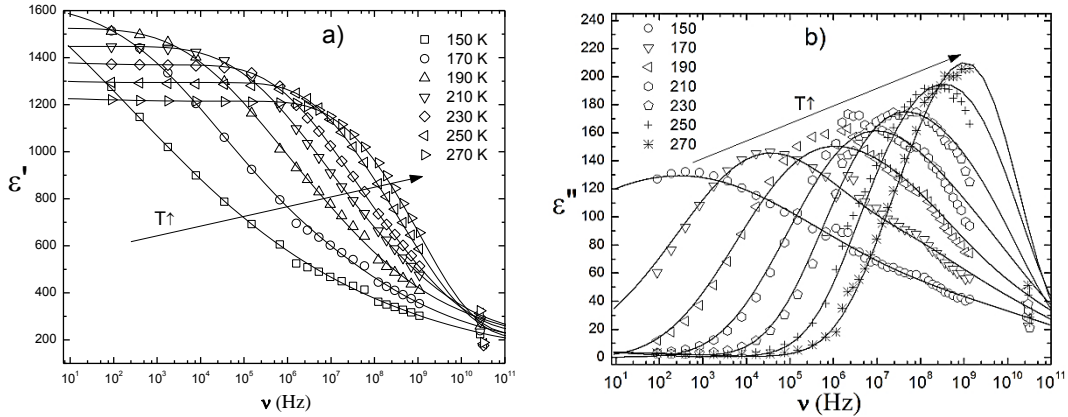
Fig. 5.2.11. Frequency dependence of the real and imaginary parts of dielectric permittivity of SBT (x = 0.25) ceramic at fixed temperatures. Solid lines are the distribution of relaxation times fits (Eq. 4.18 and 4.19).

Fig. 5.2.12. Relaxation time distribution function $f(\tau)$ of SBT (x=0.25) ceramics at different temperatures a). Solid lines represent the double-well potential fits. The most probable relaxation times from Cole-Cole fit (diamonds) and the longest relaxation times from $f(\tau)$ fit (circles) fitted with the Vogel-Fulcher relationship b).

152

The calculated $f(\tau)$ curves (Fig. 5.2.12) revealed a broad distribution of relaxation times in this ceramic. At high temperatures the distribution appears 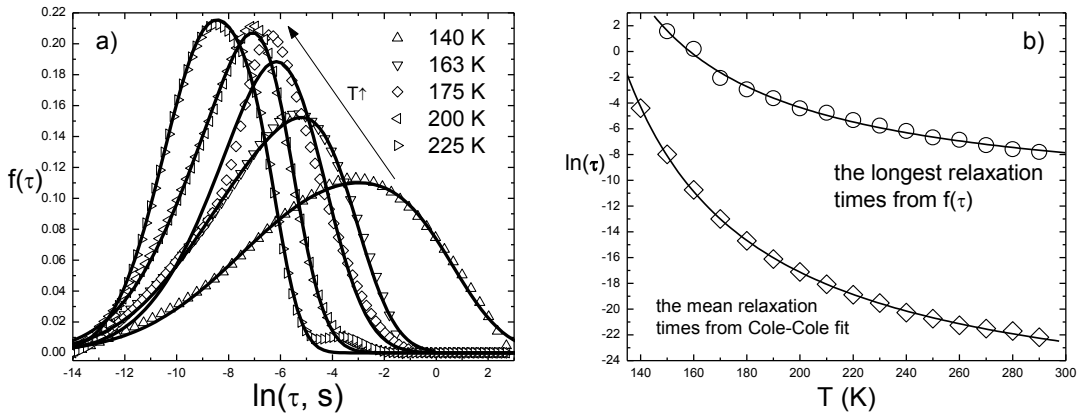to be nearly symmetrical however on cooling it not only broadens toward longer relaxation times but also becomes more asymmetrical. Such behaviour gives a hint that interaction between PNRs and AFD regions and the volume of them increases on temperature decrease.

The longest relaxation times (from $f(\tau)$ fits) and the mean relaxation times (from Cole-Cole formula fits) (shown in Fig. 5.2.12 b) can be approximated by the empirical Vogel-Fulcher relationship with the parameters presented in 5.2.1 table.

Table 5.2.1. Parameters of relaxation times approximation with the Vogel-Fulcher relationship ($(Sr_{0.625}Bi_{0.25})TiO_3$).

	τ_0 (s)	E_a/k_B (K)	T_0 (K)
The longest relaxation times from f(τ)	$7.36 \cdot 10^{-6}$	843	87
The mean relaxation times from Cole-Cole formula fits	$3.26 \cdot 10^{-13}$	1328	85

Obtained Vogel-Fulcher (VF) relationship parameter τ_0 (of the mean relaxation times from Cole-Cole formula) let assume that system dynamic at very high temperatures becomes close to phonon contribution i.e. in comparison to relaxor-ferroelectrics, SBT system should transform to homogeneous paraelectric phase, although no phase transformation was observed by dielectric measurements. The longest relaxation times from $f(\tau)$ (shown in Fig. 5.2.12 b, circles) varies in agreement with VF relationship also, with lower activation energy and twice lower τ_0 – meaning different PNR and AFD regions dynamic from lattice phonons.

We also tried to compare obtained results with the well-known dipolar glass model (described in Chapter 2.3.3) in which the dipoles are moving in asymmetric double well potential. This allows us to find the height and asymmetry of the potential as well as the distributions of these parameters. More details about this model can be found in [A51-52]. Double-well potential model fit to the $f(\tau)$ curves are seen as solid lines in Fig. 5.2.12 a.

Although this fit looks rather well, the obtained double-well parameters are not compatible with this model - the asymmetry of double-well potential is about twice bigger as the height of the potential itself.

PFM investigation of SBT (x = 0.25) was used for material assignment to relaxor-ferroelectrics. PFM was done in prof. dr. A. Kholkin group (Department of Ceramics and Glass Engineering/CICECO, University of Aveiro, Aveiro, Portugal) by dr. R. Grigalaitis.

In PFM experiment out-of-plane and in-plane polarization components were obtained, confirming piezoelectric nature of this response [E30]. No labyrinth-like structures were observed (Fig. 5.2.13) as in canonical relaxor-ferroelectrics (for example in PMN [E31]), thus it was made a conclusion that SBT (x = 0.25) is not in the ferroelectric relaxor (neither ergodic neither nonergodic) state at room temperature.
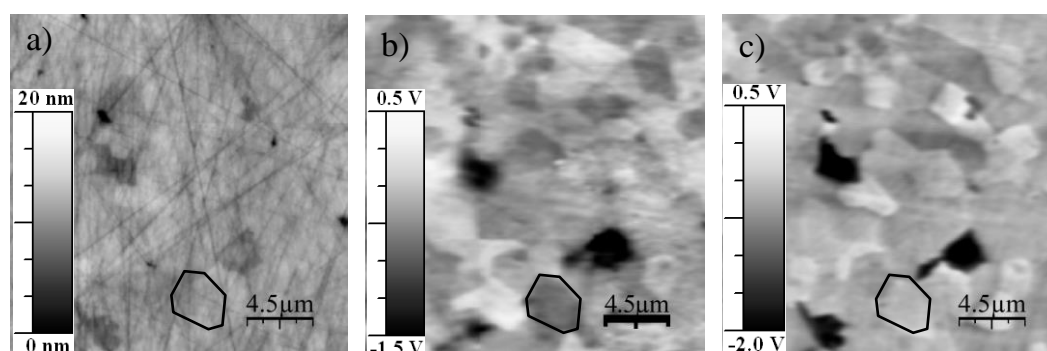
Fig. 5.2.13. Surface topography a), out-of-plane (OPP) b) and in-plane (IP) c) local piezoresponse data of $0.75SrTiO_3$-$0.25Bi_{2/3}TiO_3$ ceramics ($U_{AC} = 40V$, $U_{DC} = 20V$, $f = 50$ kHz). The green contour marks one of the grain boundaries in both OPP and IP images [E30]. Acknowledgements dr. Robertas Grigalaitis.

The temperature dependences of complex dielectric permittivity of $Sr_{1-1.5x}Bi_xTiO_3$ (x = 0.2 and 0.15) ceramics are displayed in Fig. 5.2.14. Dielectric spectra were measured in broad frequency (from 20 Hz to 36 GHz) and temperature (from 25 K to 450 K) ranges.

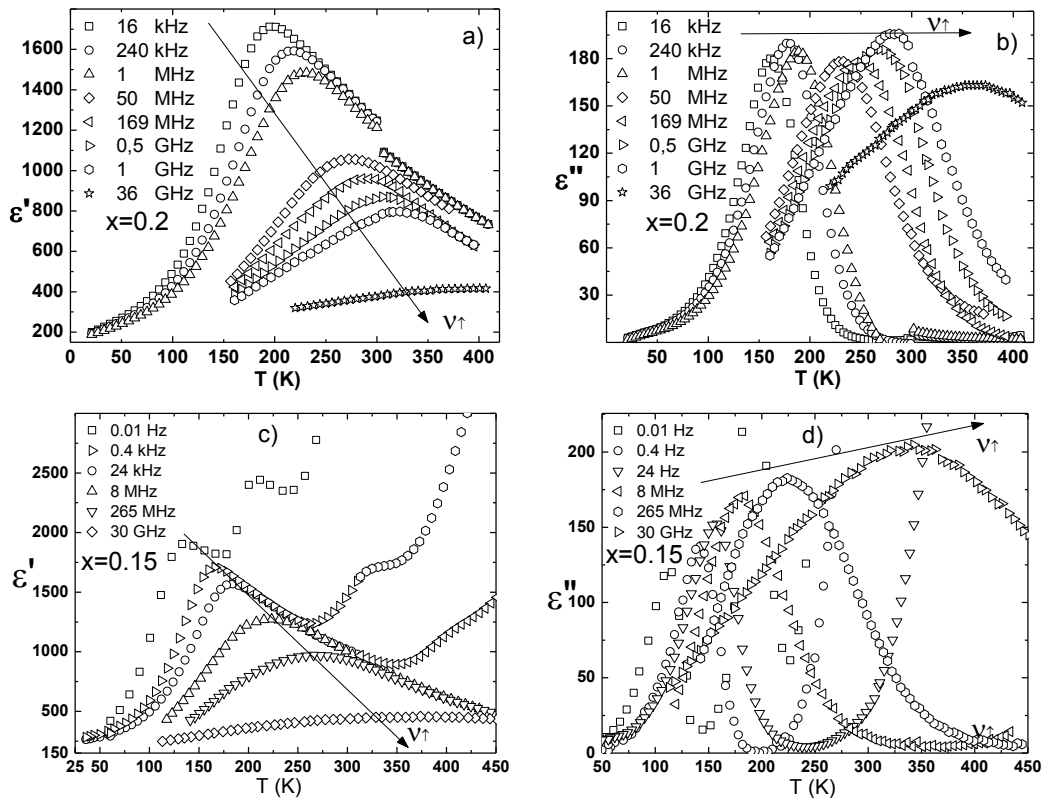Fig. 5.2.14 Complex dielectric permittivity temperature dependences of $Sr_{1-1.5x}Bi_xTiO_3$, with x = 0.2 (a and b) and 0.15 (c and d).

Experimental data reveals pronounced dielectric dispersion. The maximum of real and imaginary parts of dielectric permittivity shifts to higher temperatures with the frequency increasing and broadens anomalously in the same manner as in $(Sr_{0.625}Bi_{0.25})TiO_3$ ceramics. The difference from pure relaxors can be seen in the Fig. 5.2.14 b and d, where the temperature curves of imaginary part of dielectric permittivity at different frequencies cross each other and coincide only at temperatures below 50 K.

The frequency dependences of the dielectric permittivity of these materials (Fig. 5.2.15) exhibits large dispersion which broadens and shifts toward lower frequencies on cooling. Obtained frequency dependences were fitted with empirical Cole-Cole (x = 0.2) and Havriliak-Negami (x = 0.15) formula (not shown) and relaxation times distribution model (Fig. 5.2.15 solid lines). The calculated $f(\tau)$ curves (Fig. 5.2.16) revealed a broad distribution of relaxation times in these ceramics also. At high temperatures the distribution is

155

almost symmetrical, as in relaxors [E25-26], on cooling it does not only broaden toward longer relaxation times but also becomes more asymmetric.
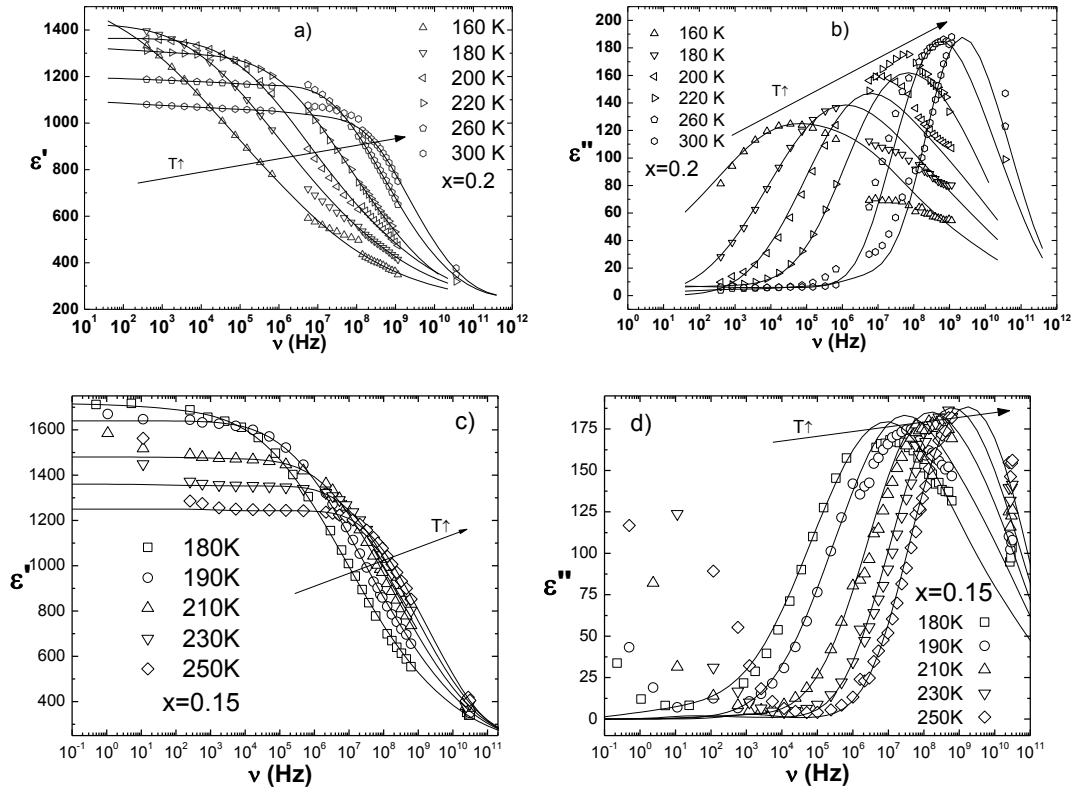

Fig. 5.2.15. Complex dielectric permittivity frequency dependences of $Sr_{1-1.5x}Bi_xTiO_3$, with x = 0.2 (a and b) and 0.15 (c and d), at fixed temperatures. Solid lines are the distribution of relaxation times fits (Eq. 4.18 and 4.19).

The most probable relaxation times as calculated from the first moment of the distribution function follow the Vogel-Fulcher relationship which is characteristic of dipolar glasses or relaxor-ferroelectrics in nonergodic phase (parameters are shown in Table 5.2.2 for x = 0.2).

Table 5.2.2. Parameters of relaxation times approximation with the Vogel-Fulcher relationship $((Sr_{0.7}Bi_{0.2})TiO_3)$.

	T_0 (K)	E_a/k_B (K)	τ_0 (s)
Most probable relaxation times fit	65	1718	$5.5 \cdot 10^{-14}$
Longest relaxation times fit	70	2560	$7 \cdot 10^{-14}$
Mean relaxation times fit	17	2770	$4.5 \cdot 10^{-15}$

The dielectric spectroscopy of the SBT (x = 0.25, 0.2 and 0.15) ceramics revealed extremely broad dispersion of dielectric permittivity in these materials. In contrast to the proposals of Porokhonskyy et al. [E23], which claimed that the dispersion SBT ceramics looks relaxor-like, we have to point its close similarity to the dispersion typically found in dipolar glasses (see e.g. [E29]).
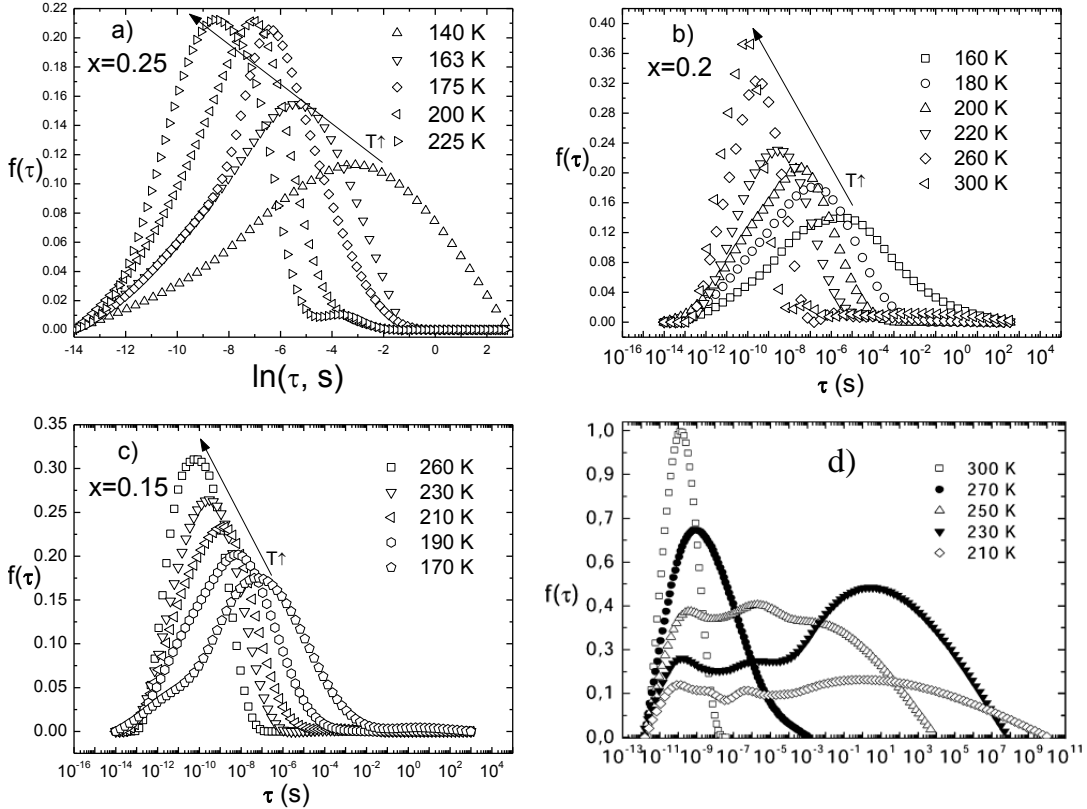

Fig. 5.2.16. Calculated relaxation time distribution function f(τ) of $Sr_{1-1.5x}Bi_xTiO_3$ ceramics and canonical relaxor PMN at different temperatures. $(Sr_{0.625}Bi_{0.25})TiO_3$ a), $(Sr_{0.7}Bi_{0.2})TiO_3$ b), $(Sr_{0.775}Bi_{0.15})TiO_3$ c) and $Pb(Mg_{1/3}Nb_{2/3})O_3$ d) [E26].

The calculated distribution of relaxation times confirms our findings because no splitting into the two parts of *f(τ)* can be seen even at low enough temperatures (Fig. 5.2.16 a, b and c). However the dipolar glass model, applied on the distribution of relaxation times gave us unphysically big values of double-well potential asymmetry. This leads to conclusion that SBT (with x = 0.25, 0.2 and 0.15) is not the true dipolar glass. The reason for such behaviour could be the formation of polar nano regions which typically are

157

responsible for the huge dielectric dispersion in ferroelectric relaxors like PMN crystals [E25] or ceramics [E26]. However in case of SBT these polar regions should be small enough and do not emerge into one another on cooling but cause only the distortions of above mentioned double-well potential due to the long-range interactions between them.

On further decrease of Bi (x = 0.15 to 0.05) content one observes additional dispersion region (Fig. 5.2.17 a) and c) region B, also Fig. 5.2.14 c). This dispersion look similar to one already observed in [E18, E23] and could be related to ceramic annealing conditions i.e. oxidizing or reducing atmosphere during ceramic sintering. Appearing additional dispersion could be related to oxygen deficiency in low Bi content ceramic, caused by loss of oxygen from the crystal lattice at high sintering temperatures (> 1350°C).

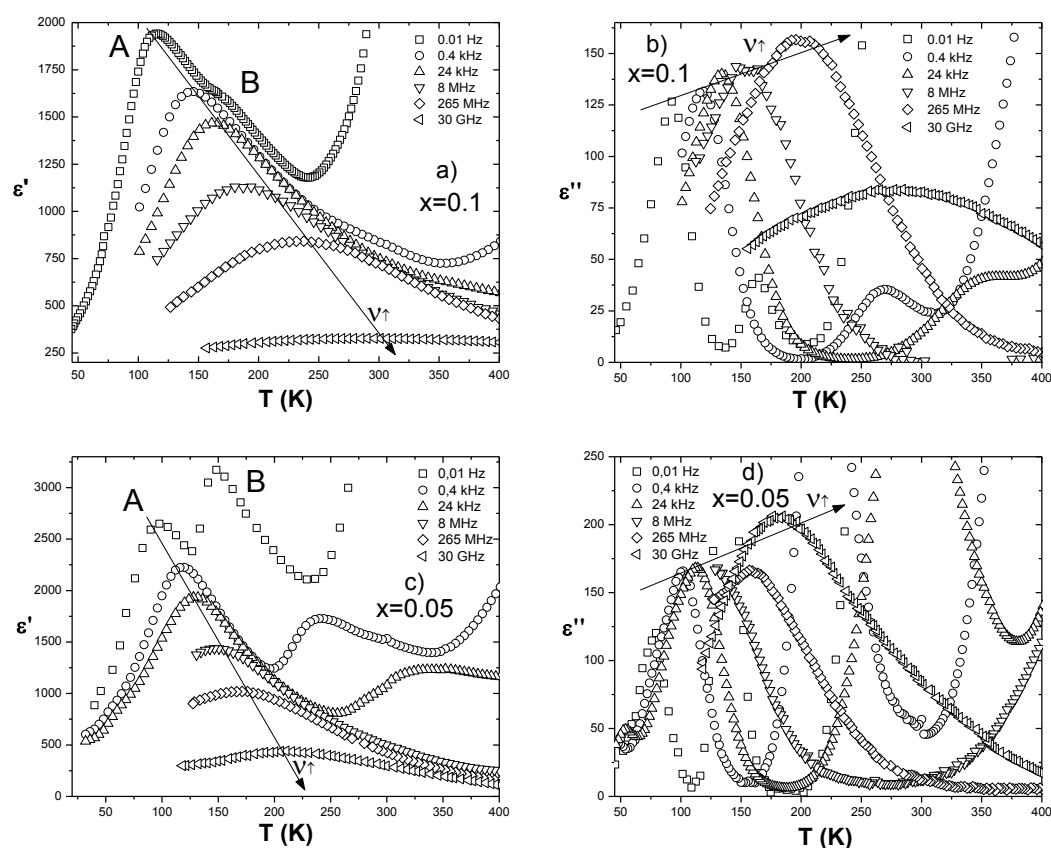Fig. 5.2.17. Complex dielectric permittivity temperature dependences of $Sr_{1-1.5x}Bi_xTiO_3$, with x = 0.1 (a and b) and 0.05 (c and d).

The experimental data of SBT (x = 0.1 and 0.05) ceramics shows broad dielectric dispersion localized at lower temperatures in comparison to SBT (x = 0.25 to 0.15). Dispersion region moves towards lower temperatures with decreasing Bi doping. The maximum of the real and imaginary parts of dielectric permittivity shifts to higher temperatures as frequency increases (Fig. 5.2.18 a) and c) region A) in the same manner as already observed in higher Bi content ceramics. The two relaxation processes are observed. One is attributed to dipole relaxation (Fig. 5.2.17 a) and c) region A) and another relaxation is attributed to in-grain conductivity (Fig. 5.2.17 a) and c) region B).
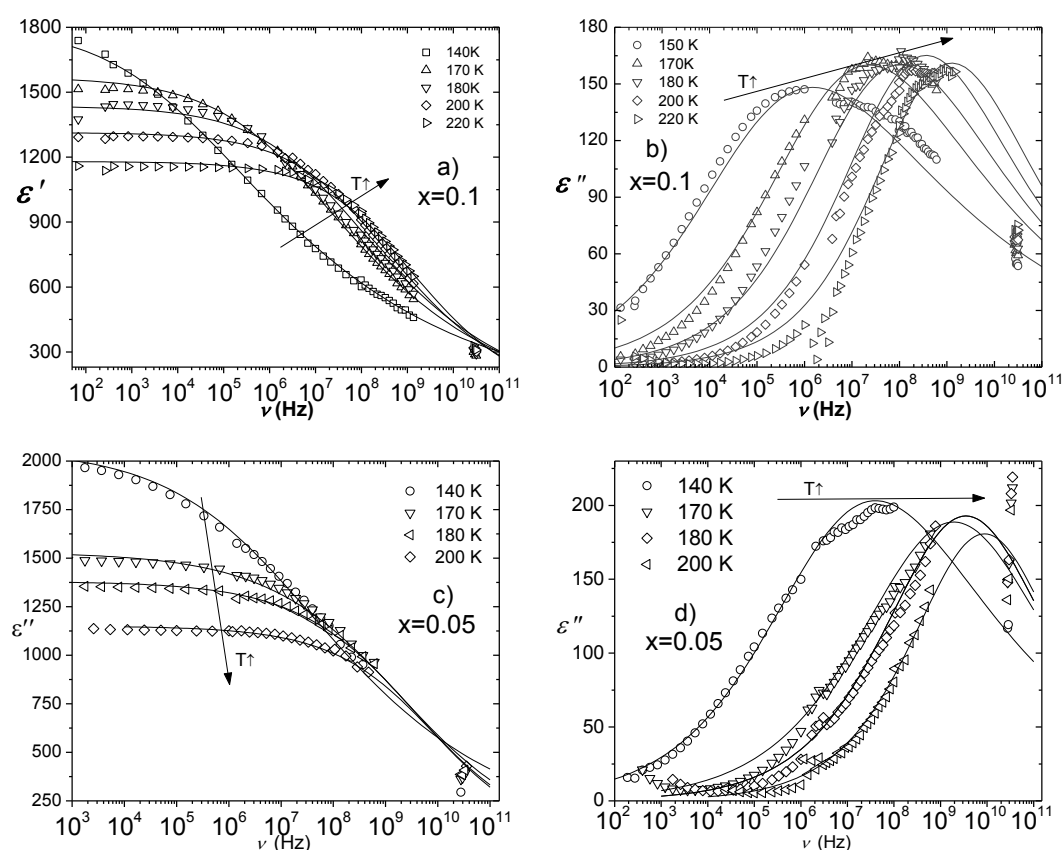

Fig. 5.2.18. Complex dielectric permittivity frequency dependences of $Sr_{1-1.5x}Bi_xTiO_3$, with x = 0.1 (a and b) and 0.05 (c and d). Solid lines are Havriliak-Negami fits (Eq. 4.24).

Frequency dependencies of dielectric permittivity (Fig. 5.2.18) have been analysed in terms of Havriliak-Negami formula (Eq. 4.24). Obtained mean

relaxation times from Havriliak-Negami formula fits fulfil the Vogel-Fulcher relationship with parameters showed in the 5.2.3 table.

Table 5.2.3. Parameters of relaxation times approximation with the Vogel-Fulcher relationship (($Sr_{0.85}Bi_{0.1}$)TiO_3 and ($Sr_{0.925}Bi_{0.05}$)TiO_3).

	x = 0.1	x = 0.05
τ_0 (s)	$9.7\cdot10^{-14}$	$2.2\cdot10^{-14}$
T_0 (K)	60 ± 16	19 ± 41
E_a/k_B (K)	950 ± 280	1196 ± 896

From Fig. 5.2.18 b) one can observe that even asymmetric Havriliak-Negami relaxation times distribution formula do not fit experimental data well enough. To obtain real relaxation times distribution we used the same approach as with before described SBT ceramics (x = 0.25 to 0.15) – Eq. 4.18 and 4.19 were numerically solved using Tikhonov regularization method [C12].
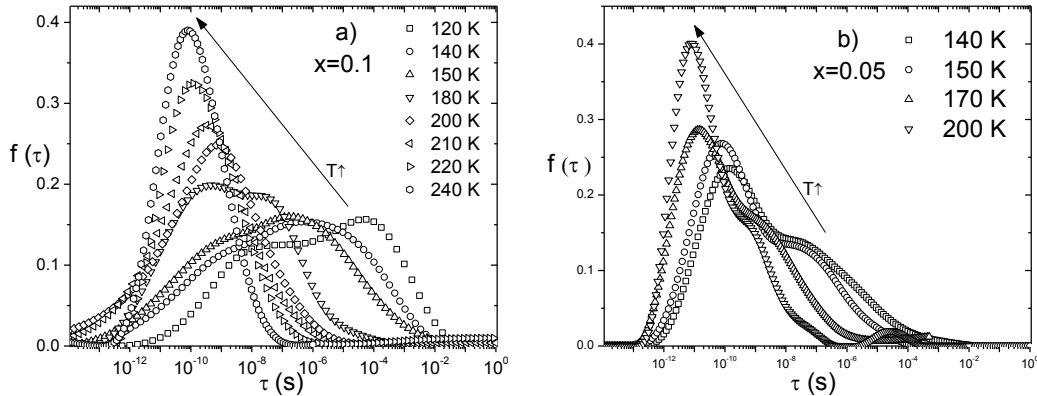
Fig. 5.2.19. Calculated relaxation time distribution function $f(\tau)$ of $Sr_{1-1.5x}Bi_xTiO_3$ ceramics. x = 0.1 in a) and x = 0.05 in b).

Additional feature (not observed in higher Bi content ceramics), seen in Fig. 5.2.19 is that calculated relaxation times distribution function splits into two parts. One peak of the relaxation time distribution function remains at THz frequencies and another one broadens and goes down to the lowest frequencies. Such behaviour is a clear indication that ($Sr_{0.85}Bi_{0.1}$)TiO_3 and ($Sr_{0.925}Bi_{0.05}$)TiO_3 dispersion reassembles dielectric dispersion observed in relaxor-ferroelectrics [E25-26].

Additional dispersion region at low frequencies (Fig. 5.2.17 region B) was approximated by Havriliak-Negami formula (Eq. 4.24).
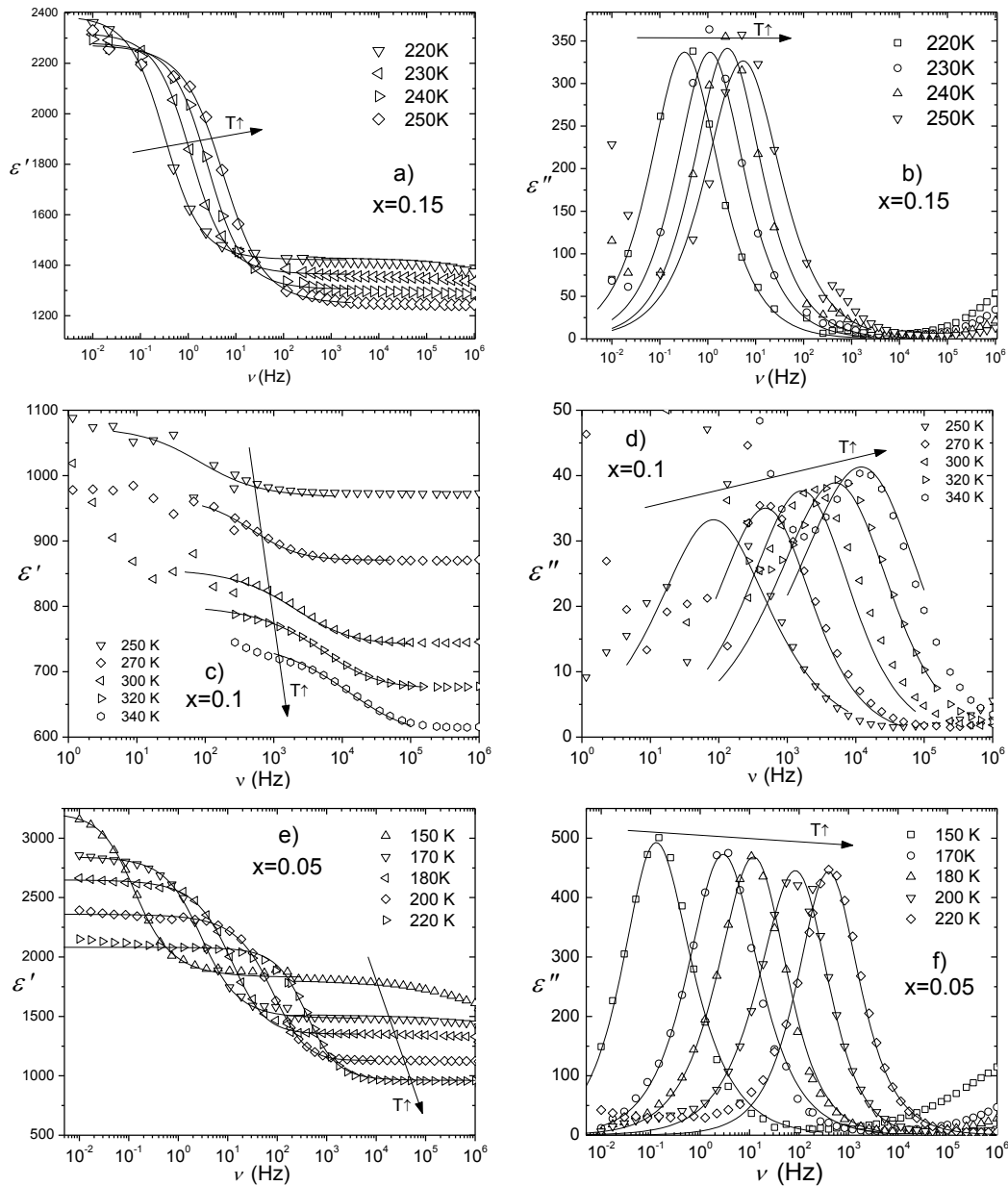
Fig. 5.2.20. Frequency dependences of the real a), c) and e) as well as imaginary b), d) and f) parts of dielectric permittivity of $Sr_{1-1.5x}Bi_xTiO_3$ceramics at low frequencies (relaxation region B) for x = 0.15, 0.1 and 0.05 respectively. Solid lines are Havriliak-Negami formula fits (Eq. 4.24).

Havriliak-Negami fit parameter γ, describing relaxation times distribution asymmetry (shown in Fig. 5.2.21 a), is equal to one and just at higher temperatures starts deviating from the unity (for x = 0.1). Such γ behaviour

indicates that distribution is fully symmetric (for compositions with x = 0.15 and x = 0.05). The fit parameter α (shown in Fig. 5.2.21 b) for all three compositions is close to zero (less than 35%, up to 300 K) meaning narrow relaxation times distribution, such behaviour could be related to the small deviation of the grain sizes in sintered ceramics.

Fig. 5.2.21. The Havriliak-Negami fit parameters as temperature dependence: the relaxation times distribution parameter γ a) and α b) for $Sr_{1-1.5x}Bi_xTiO_3$ (x = 0.15, 0.1, 0.05).

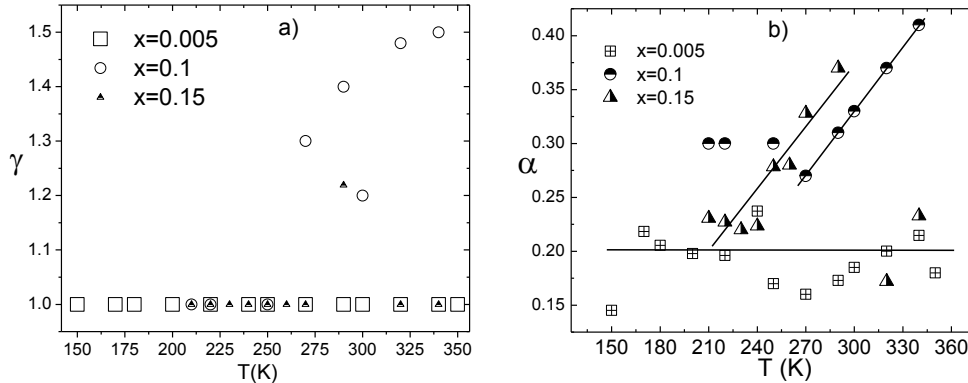Obtained relaxation times from Havriliak-Negami fits were converted to mean and most probable values in accordance to [C11]. The most probable relaxation times follow Vogel-Fulcher relation with parameters presented in Table 5.2.4.

Table 5.2.4. Parameters of relaxation times approximation with the Vogel-Fulcher relationship (for $Sr_{1-1.5x}Bi_xTiO_3$ (x = 0.15, 0.1, 0.05)).

	x = 0.05	x = 0.1	x = 0.15
τ_0 (s)	$8.23*10^{-11}$	$4.7*10^{-11}$	$9.1*10^{-11}$
E_a/k_B (K)	3159±141	3995±1698	4561±1246
E_a/k_B (eV)	0.27±0.012	0.34±0.14	0.39±0.1
T_0 (K)	14.58±4.43	0±54.77	15.62±33.22

Narrow distribution of τ_0 and activation energies gives a hint that relaxation is related to the same entities – in this case to charge carriers inside the ceramic grains and narrow grain size distribution. Conductivity in SBT is thermally activated process (the same as in the semiconductors) this is confirmed by the VF freezing temperature, which is approximately equal to zero (in the margin of systematic error). Charge carriers probably are electrons from

single or double ionized oxygen vacancies [E32], because no ionic conductivity was ever reported at such a low temperatures (below the room temperatures). In summary the low frequency dispersion is caused by electronic conductivity inside the grains – it was observed the space charge polarization mechanism in SBT (x = 0.15 to x = 0.05).

In summary, investigated SBT ceramics obey dielectric dispersion which is similar to one observable in disordered materials like dipolar glasses [E28-29] and relaxor ferroelectrics [E25-27]. SBT dielectric dispersion is due Bi doping induced formation of local antiferrodistortive and polar regions. This causes a complex relaxational dynamics below the phonon frequency range. Ceramics with the highest Bi content (x = 0.25 to 0.15) possess relaxation times distribution function which does not spilt into two parts as observed in canonical relaxor ferroelectric PMN [E25-26]. Applied dipolar glass model [A51-52] gives unphysical model parameters, thus cannot by applicable at all. Having this in mind, ceramic with high Bi content (x $\geq$ 0.15) can be attributed to a relatively new class of materials intermediate between dipolar glasses and ferroelectric relaxors.

SBT ceramic with lower Bi doping (x = 0.1 and x = 0.05) exhibit the splitting of relaxation times distribution function, thus could be classified as materials with relaxor ferroelectric-like dielectric properties [E25]. Splitting of relaxation time distribution function in canonical relaxor ferroelectrics is related to two separated contributions, one from nonpolar matrix and one from PNRs. On cooling PNRs contribution to dielectric dispersion gets weaker (PNRs gets frozen and below particular temperatures does not contribute to dielectric and other properties [A57]) – calculated $f(\tau)$ peak broadens and goes down to the lowest frequencies. $f(\tau)$ splitting observed in SBT (x < 0.15) could be related to couple physical reasons: one could be the fact that $SrTiO_3$ lattice is highly polarizable (it is possible to induce ferroelectric phase transition by electric field, stress etc.), thus lower amount of Bi dopants induces smaller

disorder (due to Bi dopants itself and lower amount of V_{Sr}) and below some critical dopant level (0<x<0.15) off-centered Bi ions promote creation PNRs, which collective response (mediated by highly polarizable $SrTiO_3$ lattice) to electric field gives broad dielectric dispersion and observed *f(τ)* splitting (an extra peak at long relaxation times) as in usual relaxor ferroelectrics. Another reason could be related to the smaller correlation size of PNRs, when bismuth doping is high (x ≥ 0.15). Polar regions become too small and do not emerge into one another on cooling but cause the distortions of double-well potential (described by dipolar glass model in Chapter 2.3.3 and [A51-52]) due to the long-range interactions between them, what is manifested by just the one peak in the relaxation time distribution function.

High sintering temperature of SBT ceramics induce oxygen loss, what is confirmed by additional relaxation region which can be reduced by annealing in oxidizing atmosphere [E18] and Maxwell–Wagner type relaxation observed in dielectric spectrum at low frequencies (below 1 MHz).

In $A^{2+}B^{4+}O_3$ perovskites increasing tolerance factor suppress AFD transition and strengthens polar anomaly. This manifests as induced AFD regions and PNRs in $Sr_{1-1.5x}Bi_xTiO_3$ ceramic due to locally increased (V_{Sr} bigger that Sr^{2+} ion radius) or decreased (Bi^{3+} smaller than Sr^{2+} ion radius) tolerance factor.

References

E1 Lemanov V. V. *Ferroelectrics,* 226, 133 (1999).

E2 Itoh M., Wang R., Inaguma Y., Yamaguchi T., Shan Y-J., Nakamura T. *Phys. Rev. Lett.,* 82, 17, 3540 (1999).

E3 Fleury P. A., Worlock J. M. *Phys. Rev.,* 174, 2, 174 (1968).

E4 Shannon R. D. *Acta Crystallogr. Sect. A,* 32, 751 (1976).

E5 Lemanov V.V. *Ferroelectrics*, 302, 169 (2004).

E6 Bednorz J.G., Müller K.A. *Phys. Rev. Lett.*, 52, 2289 (1984).

E7 Johnson D. W., Cross L. E., Hummel F. A. *J. App. Phys.*, 41, 2828 (1970).

E8 Almeida A., Teles P., Chaves M. R., Vilarinho P. M., Baptista J. L. *Ferroelectrics*, 294, 49 (2003).

E9 Tkach A., Almeida A., Agostinho Moreira J., Correia T. M., Chaves M. R., Okhay O., Vilarinho P. M., Gregora I., Petzelt J. *App. Phys. Lett.,* 98, 052903 (2011) .

E10 Tkach A., Vilarinho P. M., Kholkin A. L., Reaney I. M., Pokorny J., Petzelt J. *J. Chem. Mater.,* 19, 6471 (2007).

E11 Lemanov V. V., Sotnikov A. V., Smirnova E. P., Weihnacht M. *Phys. Solid State,* 44, 2039 (2002).

E12 Smirnova E. P., Sotnikov A. V., Kunze R., Weihnacht M., Kvyatkovskii O. E., Lemanov V. V. *Solid State Commun.,* 133, 421 (2005).

E13 Ranjan R., Pandey D., Lalla N. P. *Phys. Rev. Lett.,* 84, 3726 (2000).

E14 Grupp D. E., Goldman A. M. *Science*, 276, 392 (1997).

E15 Zheng H., Reaney I. M., Lee W. E., Jones N., Thomas H. *J. Am. Ceram. Soc.,* 85, 2337 (2002).

E16 Yu Zhi, Ang Chen, Vilarinho P. M., Mantas P. Q., Baptista J. L. *Journal of the Eur. Cer. Soc.,* 18, 1613 (1998).

E17 Ang Chen, Yu Zhi *J. Appl. Phys.,* 91, 1487 (2002).

E18 Yu Zhi, Ang Chen, Vilarinho P. M., Mantas P. Q., Baptista J. L. *J. Eur. Cer. Soc.,* 18, 1621 (1998).

E19 Skanavi G. I., Ksendzov Ya. M., Trigubenko V. A., Prokhvatilov V. V., *JETP*, 33, 320 (1957).

E20 Yu Zhi, Ang Chen, Vilarinho P. M., Mantas P. Q., Baptista J. L. *J. Eur. Ceram. Soc.,* 18, 1629 (1998).

E21 Ang Chen, Yu. Zhi, Vilarinho P. M., Baptista J. L. *Phys. Rev. B,* 57, 7403 (1998).

E22 Ang Chen, Yu. Zhi, Cross L. E., *Phys. Rev. B,* 62, 228 (2000).

E23 Porokhonskyy V., Pashkin A., Bovtun V., Petzelt J., Savinov M., Samoukhina P., Ostapchuk T., Pokorný J., Avdeev M., Kholkin A., Vilarinho P. *Phys. Rev. B*, 69, 144104 (2004).

E24 Ang Chen, Yu. Zhi, Hemberger J., Lunkenheimer P., Loidl A. *Phys. Rev. B,* 59, 6665 (1999).

E25 Grigalaitis R., Banys J., Kania A., Slodczyk A. *J. De Physique IV*, 128, 127 (2005).

E26 Grigalaitis R., Banys J., Sternberg A., Bormanis K., Zauls V. *Ferroelectrics*, 340, 147 (2006).

E27 Macutkevic J., Kamba S., Banys J., Brilingas A., Pashkin A., Petzelt J., Bormanis K., Sternberg A. *Phys. Rev. B,* 74, 104106 (2006).

E28 Banys J., Macutkevic J., Brilingas A., Grigas J., Bormanis K., Stenberg A. *Ferroelectrics*, 318, 141 (2005).

E29 Banys J., Lapinskas S., Kajokas A., Matulis A., Klimm C., Volkel G., Klopperpieper A. *Phys. Rev. B*, 66, 144113 (2002).

E30 Grigalaitis R., Bagdzevicius S., Banys J., Tornau E., Bormanis K., Sternberg A., Bdikin I., Kholkin A. L. *submitted to Lithuanian Journal of Physics* (2013).

E31 Kalininv S. V., Rodriguez B. J., Budai J. D., Jesse S., Morozovska A. N., Bokov A. A., Ye Z.-G. *Phys. Rev. B,* 81, 064107 (2010).

E32 Long S. A., Blumenthal R. N. *J. Am. Ceram. Sot.,* 54, 577 (1971).

E33 Eror N. G., Balachandran U. *J. Sol. State Chem.,* 40, 85 (1981).

5.3. Ferroelectric $(K_{0.5}Na_{0.5})NbO_3$ and doping effects in $(K_{0.5}Na_{0.5})(Nb_{1-x}Sb_x)O_3$ ceramics.

For a long time the major part of piezoelectric ceramics has been lead-based materials, particularly lead-zirconate-titanate ($Pb(Zr_{1-x}Ti_x)O_3$ or PZT). PZT is used with a composition close to morphotropic phase boundary (MPB) in general. MPB is a phase bound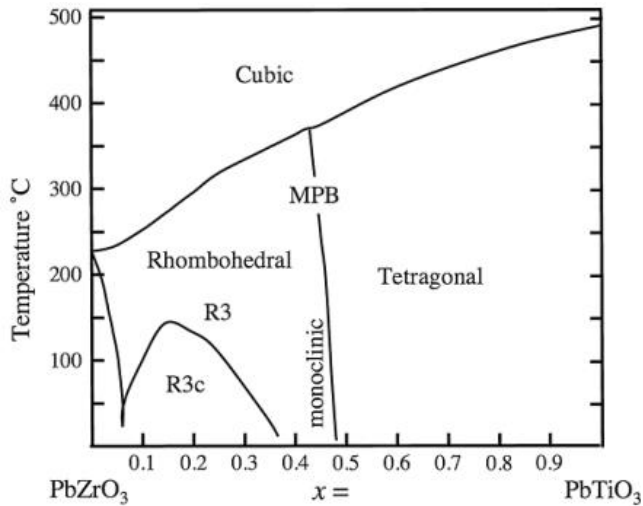ary, where changing chemical composition changes the structure – compositionally induced phase transition. MPB in PZT is around $x = 0.52$ (shown in Fig. 5.3.1), where properties such as piezoelectric coefficients, dielectric permittivity and mechanical coupling factors are maximized [F1].

Fig. 5.3.1. Phase diagram of PZT [F2].

Due to superior properties (also tunable by different Zr/Ti ratio and by dopants) the market for piezoelectric ceramics is dominated by PZT and PZT derived materials containing more than 60 wt. % lead. Lead and lead oxide are toxic to human and non-environment friendly materials, thus it has become a great concern eliminating the use of PZT (due to Pb [F3]) by replacing it with lead-free materials while maintaining competing piezoelectric properties.

Lots of work has already been done in order implementing EU directives [F1-2, F4 and references therein]. Usually there is future working direction envisaged for improved piezoelectric properties (in some cases comparable to PZT). One of them is to mimic PZT chemical composition with its end members antiferroelectric $PbZrO_3$ and ferroelectric $PbTiO_3$.
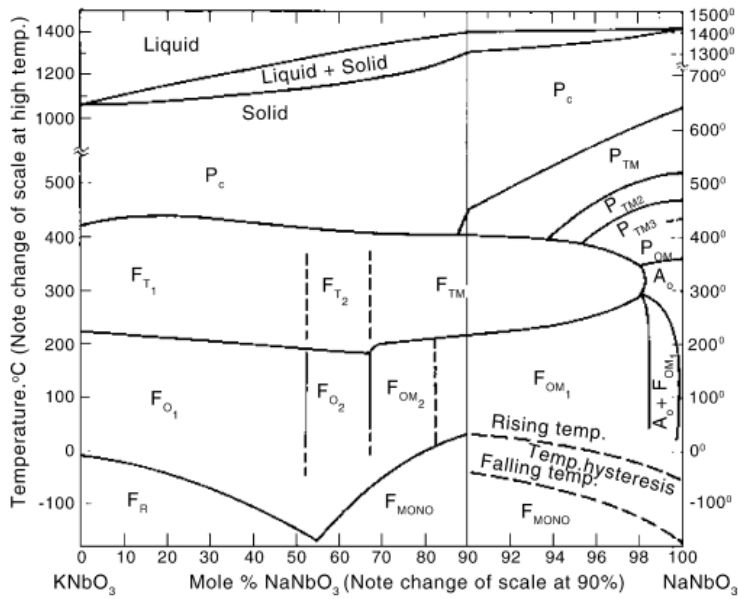
Fig. 5.3.2. Phase diagram for KNN, the system KNbO$_3$–KNaO$_3$.This system shows a relatively high degree of complexity, e.g. in comparison with the well-known PZT system [F6].

Sodium potassium niobate (K$_{0.5}$Na$_{0.5}$NbO$_3$, KNN for short) is considered as one of the most promising candidates. Since *Saito* et al. [F5] KNN again attracted science and industry attention with properties equal to PZT (d$_{33}$ = 416 pC/N [F5]). Highest properties are achieved at specific composition (close to 50/50 of constituents) in a solid solution of antiferroelectric NaNbO$_3$ and ferroelectric KNbO$_3$ (shown in Fig. 5.3.2). This composition is close to the MPB between two orthorhombic phases [F6] (or monoclinic and orthorhombic [F7]), resembling the PZT system.

First reported as ferroelectric by *Shirane* et al. [F8] KNN was investigated in detail by *Egerton and Dillon* [F9]. The phase diagram, shown in Fig. 5.3.2, is much more complex than that of PZT [F2] with several thermally induced phase transitions (polymorphic phase transitions - PPTs) and MPBs summarized by *Ahtee* et al. [F10-11]. High T_c temperature, high electromechanical coupling factor, existence of MPBs and PPTs in junction with environmentally friendly (and economically attractive) constituents makes KNN system appealing for various applications. However a few drawbacks still presents in producing this solid solution. The material is difficult to sinter using ordinary conditions and also the reactant powders require special care

169

[F12]. Volatility of the alkali species at high temperatures [F13] and hygroscopic nature of the reactant powders [F12] leads to nonstoichiometric, inhomogeneous compositions. All these problems require carefully controlled manufacturing conditions and low reaction temperatures [F2].

KNN exhibits poor densification under pressure-less sintering [F14]. Densification improvement via addition of CuO, MnO_2 [F15], and CeO_2 [F16] has been reported to enhance the sintered ceramic density and temperature stability of the doped KNN ceramics. Such additives are called sintering aids and usually believed playing no significant role in KNN ceramic after sintering. The incorporation of such liquid phase sintering aids promotes densification with up to 97.5% [F2] theoretical densities and reduced sintering temperatures what helps maintaining overall stoichiometry. Another approach involves substitution of A- (Li^+, Ba^{2+}, La^{3+}, Bi^{3+}, etc.), and B- (Ti^{4+}, Sb^{5+} or Ta^{5+}, etc.) sites in the ABO_3 structure of the KNN solid solution [R17 to R19]. Doping by isovalent and heterovalent dopants let fine-tune phase transition (and PPTs) temperatures closer to room (or other necessary) temperature, thus enhancing functional properties. Doping enhance functional properties but also induce disorder in the KNN lattice, which manifests in diffused phase transitions and even appearance of relaxor-ferroelectric behaviour.

KNN is a solid solution of $KNbO_3$ (KN) and $NaNbO_3$ (NN) and has a perovskite structure. The first time ferroelectricity in KNN was reported by *Shirane* et al. [F8], later the investigators announced excellent piezoelectric properties and high Curie temperature above 670 K [F9]. Both components: KN and NN are orthorhombic at room temperature. Sodium niobate is antiferroelectric below 753 K [F20-21], potassium niobate is ferroelectric below 709 K and there are three phase transitions similar to $BaTiO_3$ in potassium niobate. Structural changes in potassium niobate appear at higher temperatures than in barium titanate [F20-21].

The major problem with KNN ceramic is the sintering: it is complicated to sinter a dense KNN ceramic using an ordinary sintering process because of the high volatility of alkaline elements at high temperatures [B2]. In order to produce well sintered and dense ceramic with one phase and improved dielectric properties, there was introduced small amount of Sb in KNN ceramic (as sintering aid was also added 0.5 mol% MnO_2). KNN doping by Sb forms a solid solution with a single perovskite structure if solid solubility limit is not exceeded. MnO_2 increases the solid solubility limit of Sb^{5+} in KNN thereby suppressing the formation of secondary phases [F22].

$(K_{0.5}Na_{0.5})(Nb_{1-x}Sb_x)O_3+0.5$mol. % MnO_2 (with x=0.02 to 0.1, KNN-Sb_x for short) ceramics were produced by conventional solid state reaction in the Laboratory of Physics and Application of Functional Materials, Institute of Solid State Physics, University of Latvia, Latvia, by Dambekalne et al. [B2] from high purity (over 99.5%) carbonates and oxides: K_2CO_3, Na_2CO_3, Nb_2O_5, Sb_2O_5 and MnO_2. Na_2CO_3 and particularly K_2CO_3 are hygroscopic, thus an extra care was put avoiding water during ceramic processing. All starting powders were dried at 220°C for 2 days and after drying were kept in desiccator. Weighted powders were agate ball milled in agate jars for 24 h within the pure anhydrous ethanol suspension and calcined at 880°C for 5 h. After calcination MnO_2 was added and the powder was ball milled again. 5 wt. % PVA solution in water was added as binder. Obtained powder was uniaxiallly pressed into the pallets under 100 MPa pressure. Pressed pallets were sintered in alumina crucibles with a Pt foil in between the pallet and alumina bottom support to prevent the reaction, because potassium vapour is strongly alkaline and corrosive. Pallet sintering was done in atmosphere in the temperature range from 1110°C to 1140°C depending on introduced Sb dopant quantity [B2] and ceramic density after sintering reached 4.4 g/cm^3 (97.6% of TD).

Obtained KNN-Sb_x samples were characterized by XRD (X'Pert PRO MPD, Netherlands) and SEM (Carl Zeiss EVO 50 XVP, Germany).
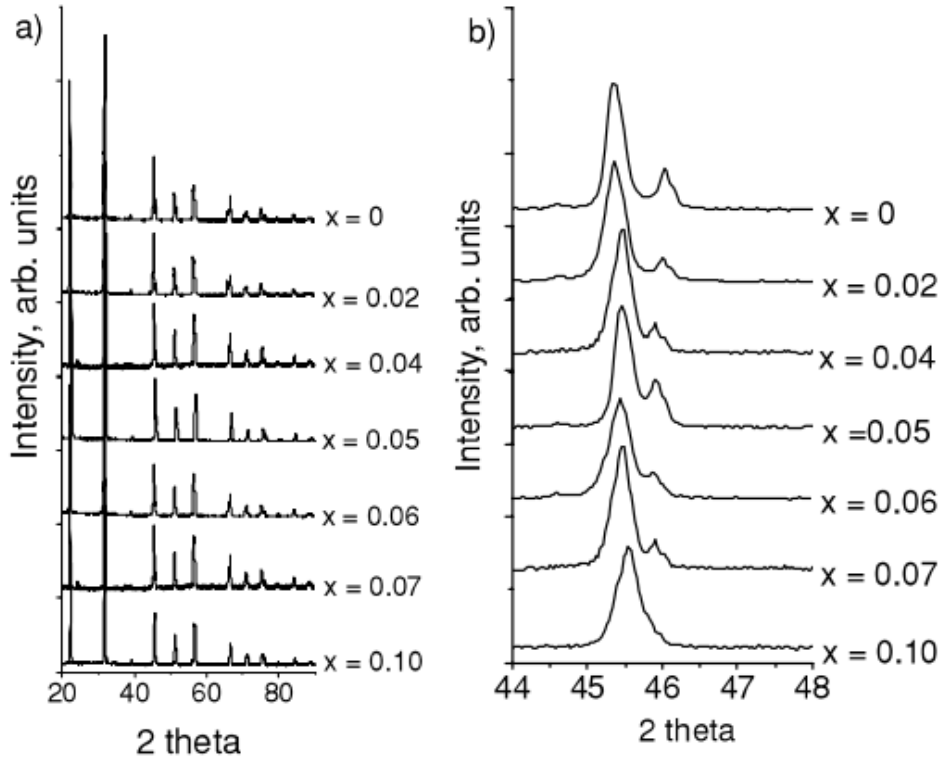
Fig. 5.3.3. X-ray diffraction patterns of sintered ceramic KNN-Sb$_x$ (x = 0 to 0.1) [B2].

XRD patterns (shown in Fig. 5.3.3) confirmed the formation of solid solution without any secondary phases. Diffraction peaks at $2\Theta = 45.7°$ are splitted for compositions x < 0.1, indicating orthorhombic distortion of the perovskite structure. (202) and (020) peak merging (shown in Fig. 5.3.3 b)) indicates phase transformation, however it is considered that phase at x = 0.1 is also orthorhombic [F6] with decreased lattice parameter differences [F22].
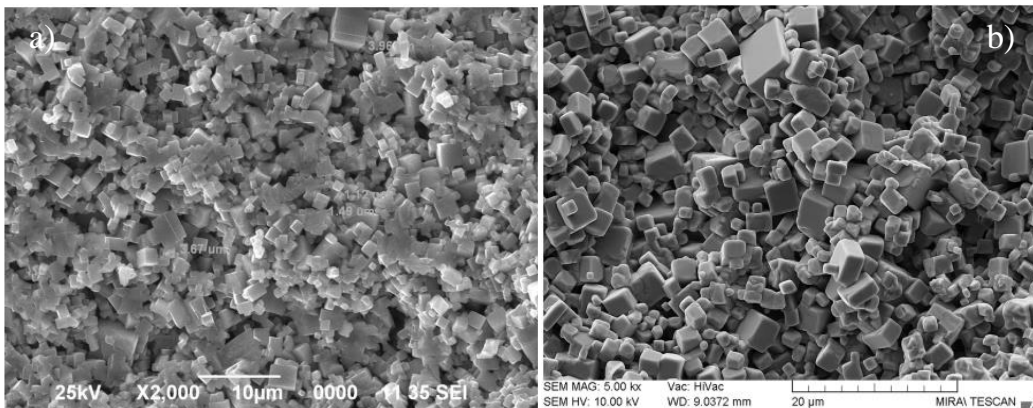

Fig. 5.3.4. Scanning electron micrographs (SEM) of the $(K_{0.5}Na_{0.5})(Nb_{1-x}Sb_x)O_3$+0.5mol.% MnO_2 with x = 0.06 (without MnO_2), sintered at 1140°C a) and x = 0.06, sintered at 1130°C b) [B2].

SEM micrographs showed homogeneously distributed cuboidal grains with average size from 2 μm to 4.5 μm (shown in Fig. 5.3.4 b)). Grain size increased with addition of MnO_2 in comparison to KNN-Sb_x ceramic without sintering aid (Fig. 5.3.4 a), average grain size 1 μm to 2 μm).

Dielectric properties of KNN-Sbx ceramics were investigated in the broad frequency (from 20 Hz to 38 GHz) and temperature (from 30 K to 800 K) ranges. For good electrical contacts there were used sputtered platinum and painted silver on the perpendicular surfaces of samples. The complex permittivity and conductivity were measured in the low frequency range from 1 Hz to 1 MHz, using HP 4284 precision LCR meter and impedance analyser (Novocontrol alpha-analyser with ZG-4 test interface) with a furnace (temperature from 300 K to 800 K) and continuous-flow He cryostat (temperature from 26 K to 300 K). The high frequency range from 1 MHz to 3 GHz was covered using Agilent 8714ET network analyser with a homebuilt coaxial dielectric spectrometer. The gigahertz region from 8 GHz to 54 GHz was covered by a waveguide setup with scalar network analyser R2400, which is produced by "Elmika" company.

Results of complex dielectric permittivity measurements at 1 kHz frequency are displayed in Fig. 5.3.5. In undoped KNN ceramic three phase transitions were established at 677 K (T_{C-T}, cubic to tetragonal phase transition), 464 K ((T_{T-O}, tetragonal to orthorhombic phase transition) and 165 K (T_{O-R}, orthorhombic to rhombohedral phase transition) [F23].
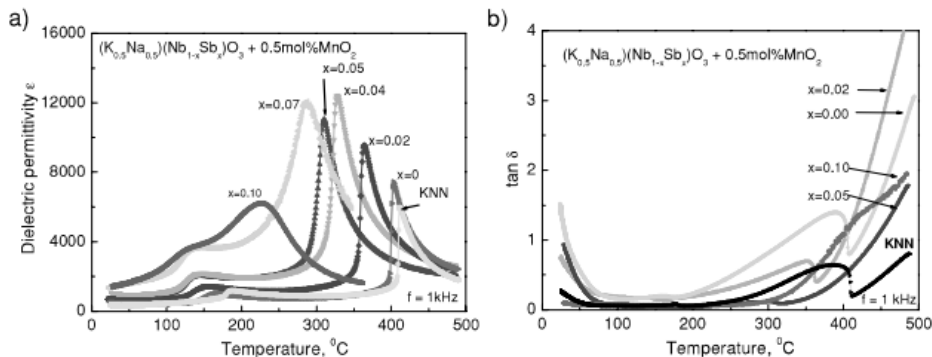

Fig. 5.3.5. Temperature dependence of the complex dielectric permittivity for $(K_{0.5}Na_{0.5})(Nb_{1-x}Sb_x)O_3+0.5mol.\%$ MnO_2 with x = 0.02 to 0.1 [B2].
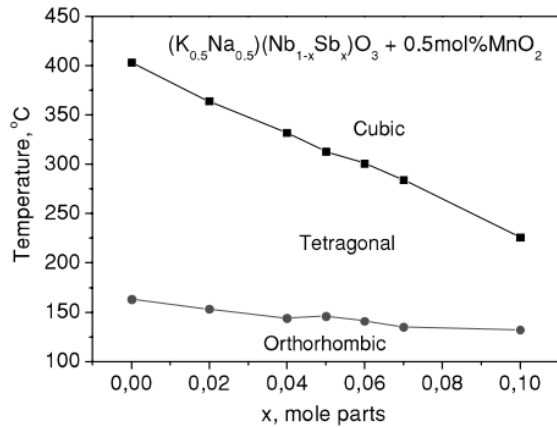
Fig. 5.3.6 Phase transition temperatures from dielectric measurements at 1 kHz frequency [B2].

After the partial Nb^{5+} substitution with Sb^{5+} both phase transitions (above room temperature) are shifted to lower temperatures (Fig. 5.3.5 and 5.3.6).

On increased Sb doping both T_{C-T} and T_{T-O} are brought closer to ambient temperature and piezoelectric properties are improved (shown in Fig. 5.3.7). With increasing Sb dopant content all phase transitions becomes diffused, especially lowest temperature phase transition (T_{O-R}) looks like one usually observed in disordered materials. From dielectric measurements it is evident that KNN-Sb$_x$ material shows gradual transformation from classical ferroelectric to relaxor-ferroelectric or dipolar glass.

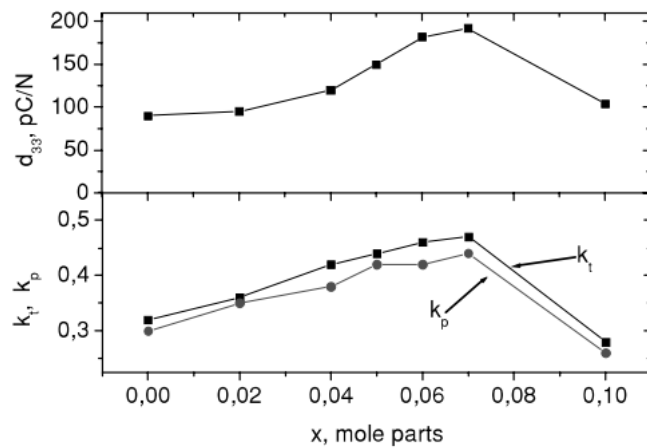Fig. 5.3.7. Variation of piezoelectric properties (d_{33}, k_p and k_t) with x in KNN-Sb$_x$ ceramic [B2].

When there is introduced more antimony (x>0.02) in KNNSbx+0.5Mn ceramic, the ferroelectric properties below room temperature changes to the behaviour, which is observed in disordered materials like dipolar glasses [E28-29] or ferroelectric relaxors [E25-27]). For this reason it was carefully investigated

KNN-Sb$_x$ with x = 0.1 to 0.07 and x = 0.06 to 0.02. The highest piezoelectric and dielectric properties were obtained with x = 0.7, thus KNN-Sb$_x$ investigation was started from this composition.
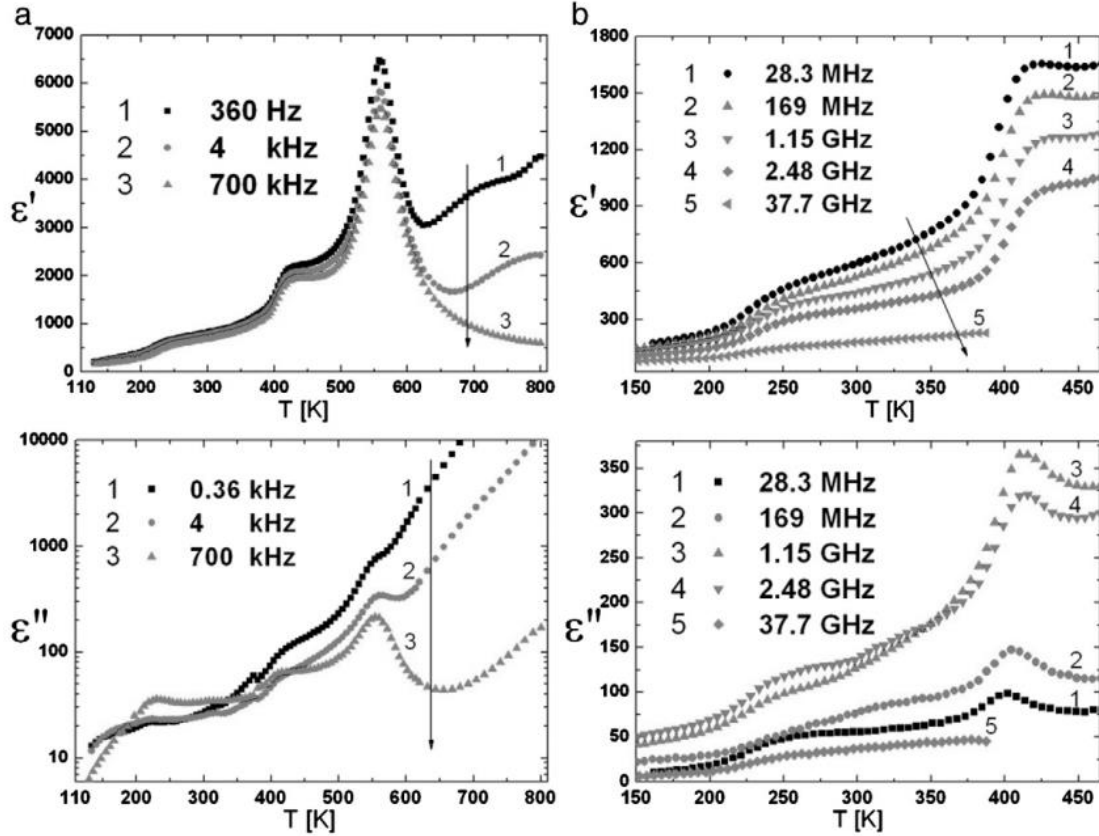

Fig. 5.3.8. Temperature dependences of the real and imaginary parts of dielectric permittivity of (K$_{0.5}$Na$_{0.5}$)(Nb$_{0.93}$Sb$_{0.07}$)O$_3$ ceramic for different frequencies below 1 MHz a) and above 1 MHz b).

The temperature dependences of the real and imaginary parts of (K$_{0.5}$Na$_{0.5}$)(Nb$_{0.93}$Sb$_{0.07}$)O$_3$ ceramic complex dielectric permittivity below 1 MHz frequency are presented in Fig. 5.3.8 a). There are displayed the same dependences above 1 MHz frequency in Fig. 5.3.8 b). In doped KNN three phase transitions were observed at 560 K (T_{C-T}, cubic to tetragonal phase transition), 425 K ((T_{T-O}, tetragonal to orthorhombic phase transition) and diffused one around 190 K (T_{O-R}, orthorhombic to rhombohedral phase transition) [F23]. Even small amount of Sb^{5+} ions, substituting Nb^{5+}, shift two of these phase transitions to lower temperatures compared with undoped KNN

ceramic. One more dielectric permittivity anomaly can be disclosed below room temperature. It could be attributed to the diffused phase transition, which corresponds to the structural transition observed in pure KNN from orthorhombic into rhombohedral ferroelectric state at $T_{O-R} = 165$ K [F23].

Careful examination of the dielectric dispersion below room temperature reveals its close similarity to the one, which is usually, founded in disordered materials like relaxor ferroelectric [E25-27] or dipolar glasses [E28-29]. Dielectric dispersion takes place in a broad temperature region in disordered materials. Peaks of dielectric permittivity ε' and ε'' shift towards higher temperatures on increasing frequency. As it is shown in Fig. 5.3.8 a), the temperature curves of the imaginary part of dielectric permittivity cross each other and coincide much below 100 K, it agrees with the behaviour of dipolar glasses [E28-29].
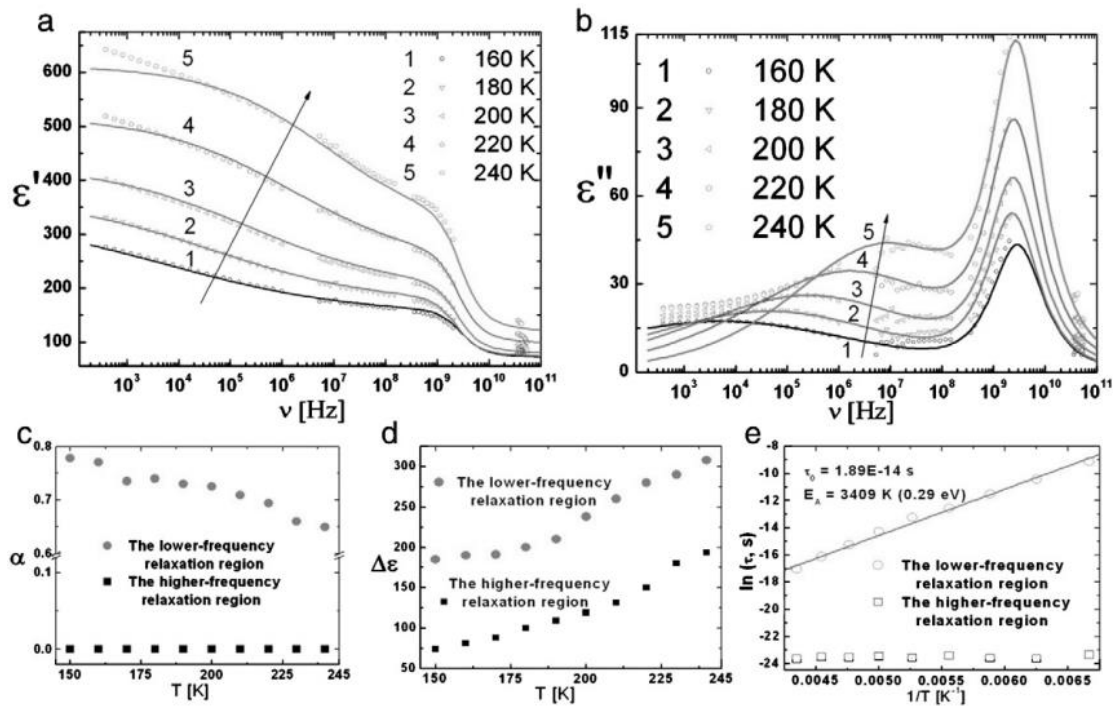

Fig. 5.3.9. Frequency dependences of the real a) and imaginary b) parts of dielectric permittivity of $(K_{0.5}Na_{0.5})(Nb_{0.93}Sb_{0.07})O_3$ ceramic at different temperatures. The solid lines in a) and b) are Cole–Cole formula (Eq. 4.21) fits. The Cole–Cole fit parameters: the relaxation times distribution parameter α,

176

shown in c) and the strength of relaxator $\Delta\varepsilon$ in d) are displayed as temperature dependence. Relaxation times from Cole–Cole formula are shown in e). The solid line is fit of the Arrhenius relationship (Eq. 4.27) to this dependence.

The frequency dependences of complex dielectric permittivity, represented in Fig. 5.3.9 a) and b), reveal at least two well separated processes. A sharp loss peak in GHz range does not change its location with respect to the frequency in the whole investigated temperature range. The maximum of the imaginary part of dielectric permittivity in MHz range broadens and shifts to lower frequencies on cooling. Obtained KNN frequency dependences were fitted with two superimposed Cole–Cole relaxation formulas.

In order to extract activation energy it used the Arrhenius formula (Eq. 4.27). Obtained activation energy $E_a = 3409$ K ($E_a/k_B = 0.29$ eV) from the fit. The higher frequency relaxation region (shown in Fig. 5.3.9 a) and b)) probably could be attributed to domain-wall dynamic and can be well described by Debye model, because distribution of relaxation times is nearly zero (Fig. 5.3.9 c)) and the mean relaxation time (Fig. 5.3.9 e)) lies almost constantly in the region of tenths of GHz.

The real part of complex dielectric permittivity is related to the imaginary part according to Kramers–Kronig relations:

$$\varepsilon'(\omega) = \varepsilon(\infty) + \frac{2}{\pi}\int_0^\infty \varepsilon''(\omega')\frac{\omega'}{\omega'^2-\omega^2}d\omega';$$
$$\varepsilon''(\omega) = -\frac{2}{\pi}\int_0^\infty [\varepsilon'(\omega') - \varepsilon(\infty)]\frac{\omega}{\omega'^2-\omega^2}d\omega' . \qquad 5.3$$

At low frequencies and high temperatures dielectric losses increase and cause an increase of the real part of dielectric permittivity as can be seen in Fig. 5.3.8 a). Such effect could be explained by high conductivity because the complex conductivity is related to the complex dielectric permittivity by following relations:

$$\sigma^* = \sigma_0 + \varepsilon_0 \varepsilon^* \omega = \sigma' + i\sigma'';$$
$$i\varepsilon_0 \omega(\varepsilon' - i\varepsilon'') = \sigma' + i\sigma'';$$
$$\varepsilon' = \frac{\sigma''}{\varepsilon_0 \omega}; \quad \varepsilon'' = \sigma_0 + \frac{\sigma'}{\varepsilon_0 \omega} \quad . \qquad\qquad 5.4$$

Obtained conductivity results are presented in Fig. 5.3.10 a) and b). At low frequencies and high temperatures conductivity shows frequency independent nature (Fig. 5.3.10 b)).
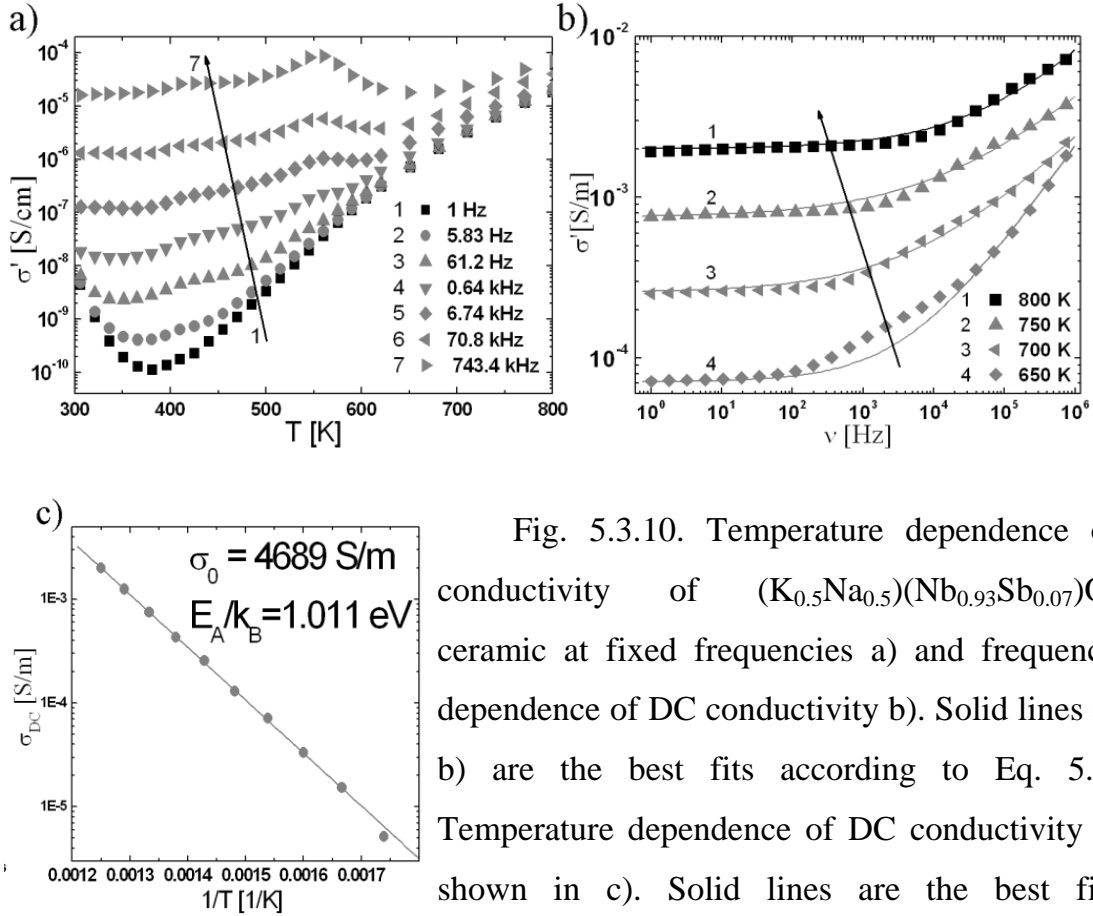

Fig. 5.3.10. Temperature dependence of conductivity of $(K_{0.5}Na_{0.5})(Nb_{0.93}Sb_{0.07})O_3$ ceramic at fixed frequencies a) and frequency dependence of DC conductivity b). Solid lines in b) are the best fits according to Eq. 5.6. Temperature dependence of DC conductivity is shown in c). Solid lines are the best fits according to Eq. 5.7.

This behavior can be addressed to DC conductivity which arises from the random diffusion of the ionic charge carriers via activated hopping process [F24]. At higher frequencies the conductivity reveals dispersion as could be seen in Fig. 5.3.10 b). The conductivity increases in a power-low and finally it becomes almost linear dependent from frequency.

The frequency dependence of the conductivity was analyzed using Almond-West type power law [F25] with a single exponent:

$$\sigma = \sigma_{DC} + A\omega^S,\qquad\qquad 5.5$$

where σ_{DC} is the DC conductivity and $A\omega^S$ is the AC conductivity.

As can be seen in Fig. 5.3.10 b), experimentally obtained conductivity data can by described according to Eq. 5.6 adequately well. Obtained σ_{DC} dependence from temperature was fitted with the Arrhenius formula for conductivity:

$$\sigma_{DC} = \sigma_0 exp(-E_A/k_B T).\qquad\qquad 5.6$$

In paraelectric phase the calculated parameters are $E_A = 11733.78$ K ($E_A/k_B = 1.011$ eV) and $\sigma_0 = 4689$ S/m.

Dielectric permittivity (and similarly conductivity) is related to the electrical modulus $M^*(\omega)$ by expression:

$$M^*(\omega)=1/\varepsilon^*(\omega)=M'(\omega)+iM''(\omega).\qquad\qquad 5.7$$

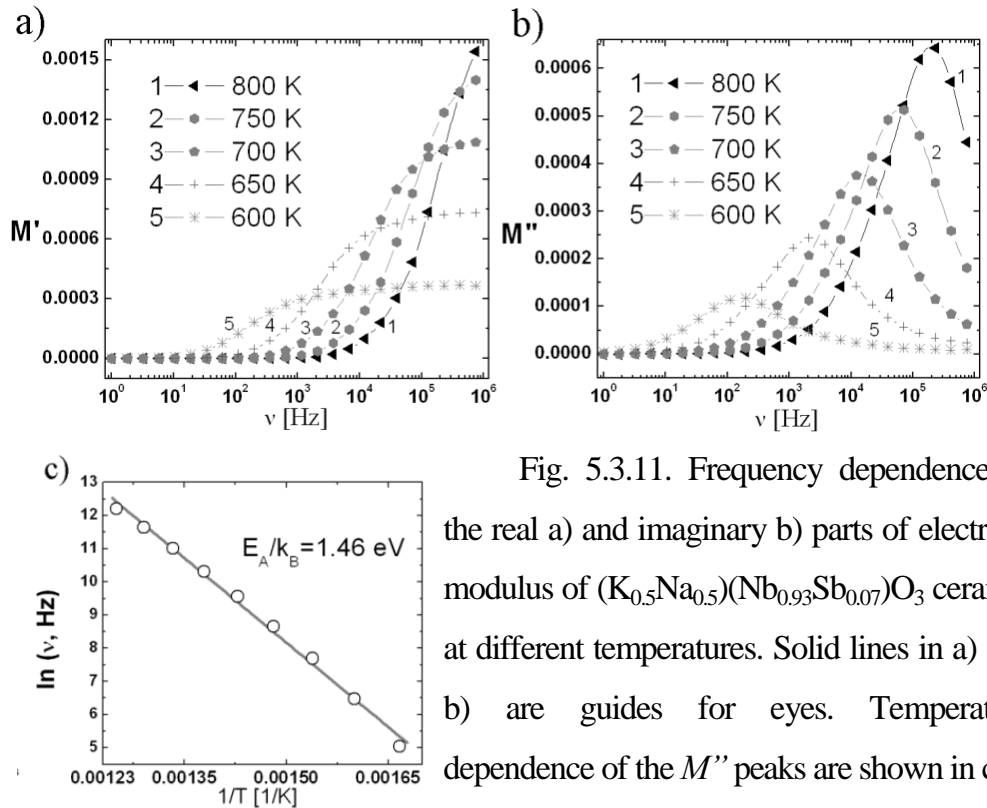Fig. 5.3.11 a) and b) display frequency dependence of M' and M''.

Fig. 5.3.11. Frequency dependence of the real a) and imaginary b) parts of electrical modulus of $(K_{0.5}Na_{0.5})(Nb_{0.93}Sb_{0.07})O_3$ ceramic at different temperatures. Solid lines in a) and b) are guides for eyes. Temperature dependence of the M'' peaks are shown in c).

At low frequencies M' value reaches zero, which indicates a lack of the restoring force for the electric field induced mobile ions (probably sodium ions). As the frequency increases, ions move shorter and shorter distances until the electric field changes to fast, then the ions oscillate only within the confinement of their potential energy well. From that it is following – M' increases to a maximum asymptotic value $M(\infty)=1/\varepsilon(\infty)$. Imaginary part of the modulus, displayed in Fig. 5.3.11 b) has symmetric peak centered in the dispersion region of M'. The most ions are mobile over long distances and are able to suppress applied electric field for frequencies to the lower frequency side of the M'' peak ($\omega\tau_\sigma < 1$), and the most ions are spatially confined in their potential wells and also can suppress applied electric field for the higher frequency side of the M'' peak ($\omega\tau_\sigma > 1$). Frequency region where $\omega\tau_\sigma = 1$ indicates a transition from long to short range ions mobility and the M'' peak frequency corresponds to the average electric field (or conductivity) relaxation time $1/\tau_\sigma$ [F26]. In order to calculate activation energy, M'' peak frequencies were plotted against temperature Fig. 5.3.11 c). The activation energy was calculated using this plot.

Results of the real and imaginary parts of dielectric permittivity of KNN-Sb_x (x = 0.08 and 0.1) ceramics are presented in Fig. 5.3.12. Above room temperature obtained results shows two diffused phase transitions near T_C = 532 K and T_{T-O} = 375 K (for $(K_{0.5}Na_{0.5})(Nb_{0.92}Sb_{0.08})O_3$) and T_C = 500 K and T_{T-O} = 400 K (for $(K_{0.5}Na_{0.5})(Nb_{0.9}Sb_{0.1})O_3$) which could be attributed to phase transitions from paraelectric cubic into ferroelectric tetragonal state and from tetragonal into orthorhombic state because in undoped $K_{0.5}Na_{0.5}NbO_3$ ceramic the same sequence of transitions was observed with T_c = 677 K and T_{T-O} = 464 K respectively [F23].

The frequency dependences of complex dielectric permittivity (Fig. 5.3.13) reveal two well separated processes.
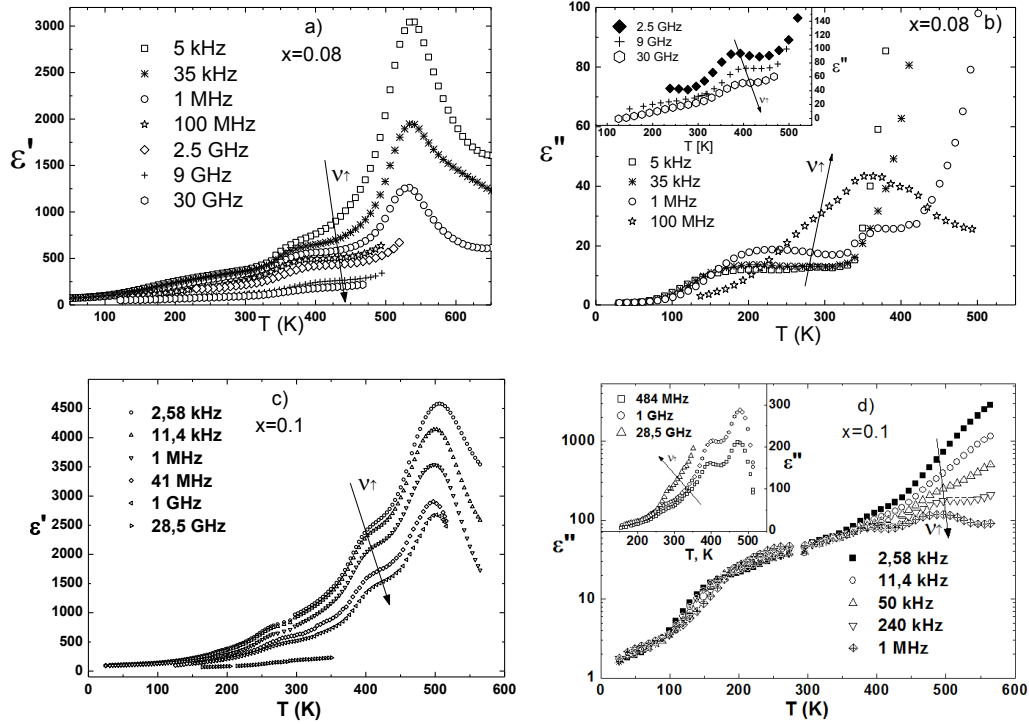
5.3.12. Temperature dependences of the real a), c) and imaginary b), d) parts of dielectric permittivity of $(K_{0.5}Na_{0.5})(Nb_{1-x}Sb_x)O_3$ ceramic at fixed frequencies, for x = 0.08 and 0.1 respectively.
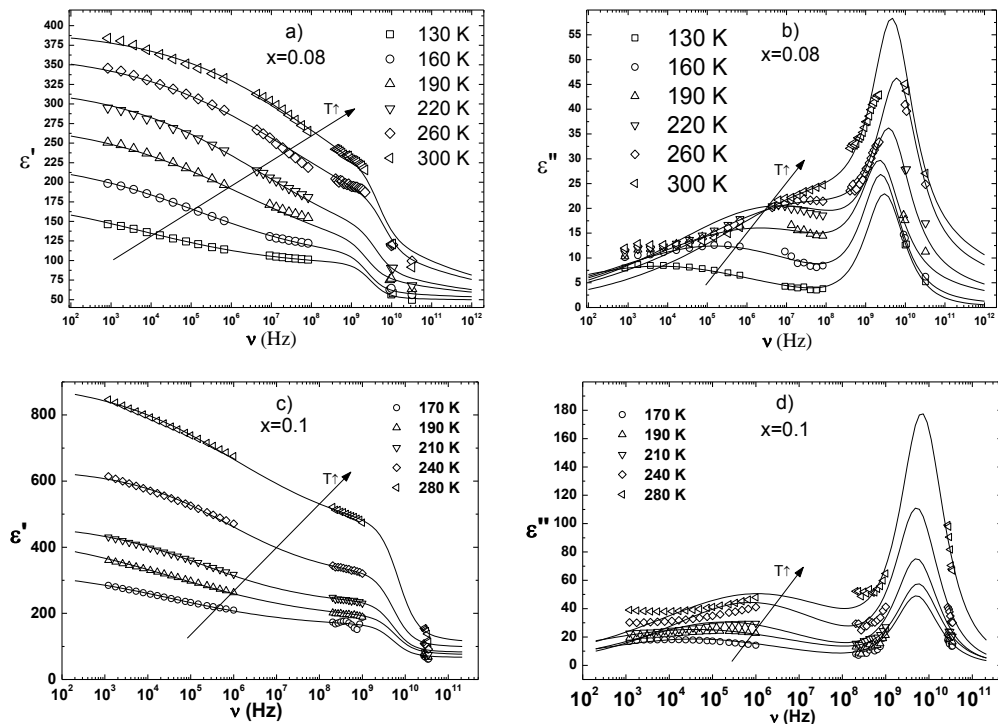
5.2.13. Frequency dependences of the real a), c) and imaginary b), d) parts of dielectric permittivity of $(K_{0.5}Na_{0.5})(Nb_{1-x}Sb_x)O_3$ ceramic at different

temperatures, for x = 0.08 and 0.1 respectively. The solid lines are Cole-Cole formula fits.

A sharp loss peak in GHz range does not change its location with respect to the frequency in the whole investigated temperature range. The maximum of imaginary part of dielectric permittivity in MHz range broadens and shifts to lower frequencies on cooling. To obtain additional information from this sequence of dispersions the measured frequency dependences were fitted with a superposition of two Cole–Cole relaxation formulas.

The results of Cole-Cole fits are demonstrated in Fig. 5.3.13 as the solid lines. Obtained Cole-Cole fit parameters are presented in Fig. 5.3.14.
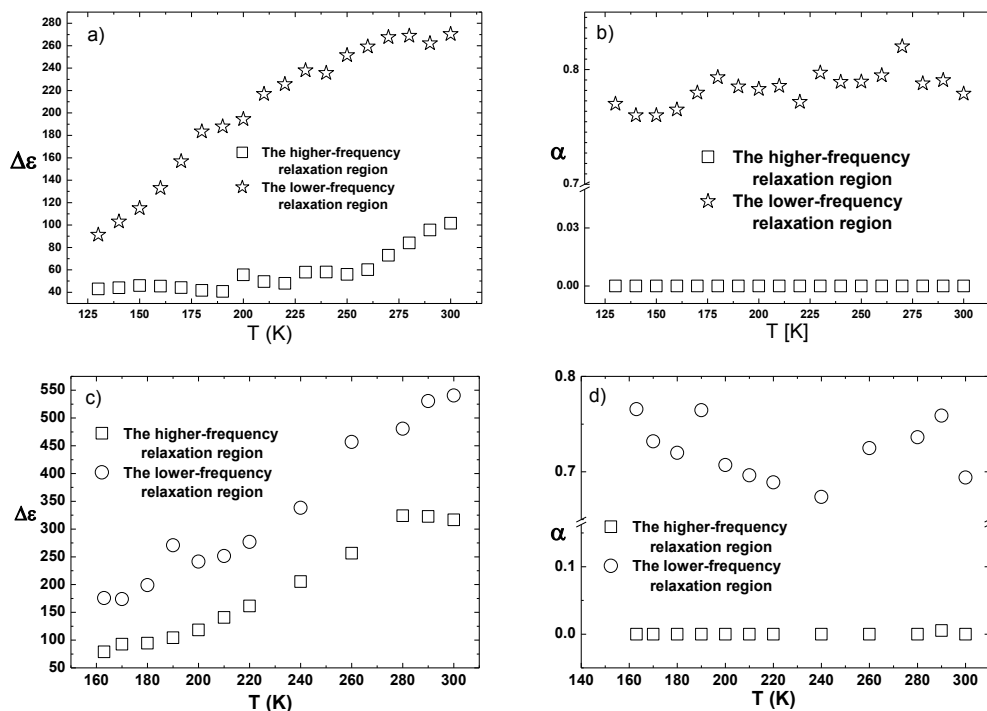
Fig. 5.3.14. The temperature dependence of Cole – Cole fit parameters $\Delta\varepsilon$ a), c) and parameter α, shown in b), d), for x = 0.08 and 0.1 respectively.

As it can be seen from Fig. 5.3.14 a) and c), in low-frequency relaxation region (up to hundreds of MHz) dielectric strength monotonically increases and starts to saturate but do not reach the maximum, because the transition from paraelectric to ferroelectric phase occurs at much higher temperatures (at about $T_C = 540$ K and 500 K, for x = 0.08 and 0.1 respectively). The relaxation is thermally activated and strongly differs from Debye type model, α reaches

182

almost 0.8 value, shown in Fig. 5.3.14 b) and d). The mean Cole-Cole relaxation time from MHz relaxation region diverges according Arrhenius (Eq. 4.27) relationship (shown in Fig. 5.3.15) for both investigated compositions. From the fit we have obtained activation energy $E_a = 2282$ K and $E_a = 1543$ K, for x = 0.08 and 0.1 respectively.
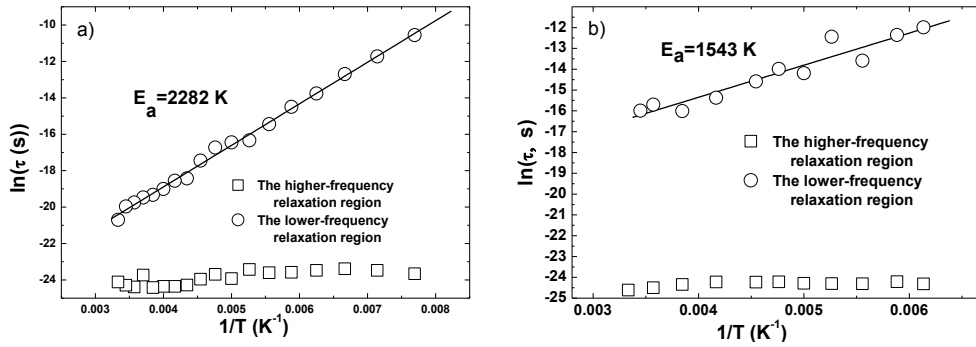
5.3.15. The temperature dependences of relaxation times from Cole–Cole formula for KNN-Sb$_x$, x = 0.08 a) and x = 0.1 b). The solid line is the fit of the Arrhenius relationship to lower-frequency relaxation process.

The higher frequency relaxation region (shown in Fig. 5.3.13) probably could be attributed to domain-wall dynamic and can be well described by Debye model, because distribution of relaxation times is nearly zero and the mean relaxation time (Fig. 5.3.14) lies almost constantly in the region of tents of GHz (shown in Fig. 5.3.15)

When there is introduced less than optimal amount of antimony dopant (x < 0.07) in KNNSbx+0.5Mn ceramic dipolar glass properties at low temperatures (below room temperature) are less evident than in higher Sb content ceramic (x ≥ 0.07), ferroelectric phase transitions above room temperature are less diffused for lower Sb content ceramics (x < 0.07) also. For this reason it was only investigated KNN-Sb$_x$ with x = 0.06 to 0.02 dielectric permittivity temperature dependences.

The temperature dependences of the real and imaginary parts of $(K_{0.5}Na_{0.5})(Nb_{1-x}Sb_x)O_3$ (x = 0.06, 0.04 and 0.02) ceramics complex dielectric permittivity ε^* are presented in Fig. 5.3.16. Niobium substitution with

antimony in $(K_{0.5}Na_{0.5})(Nb_{1-x}Sb_x)O_3$ (x = 0.06, 0.04 and 0.02) ceramics shifts T_c and T_{T-O} to lower temperatures in the same manner as already observed in higher Sb (x = 0.1, 0.08 and 0.07) concentration ceramics. All phase transition becomes less diffused and lowest temperature T_{O-R} transition becomes similar to higher temperature (T_c and T_{T-O}) phase transitions, i.e. no significant frequency dependence at x = 0.02 (shown in Fig. 5.3.16 e) and f)).
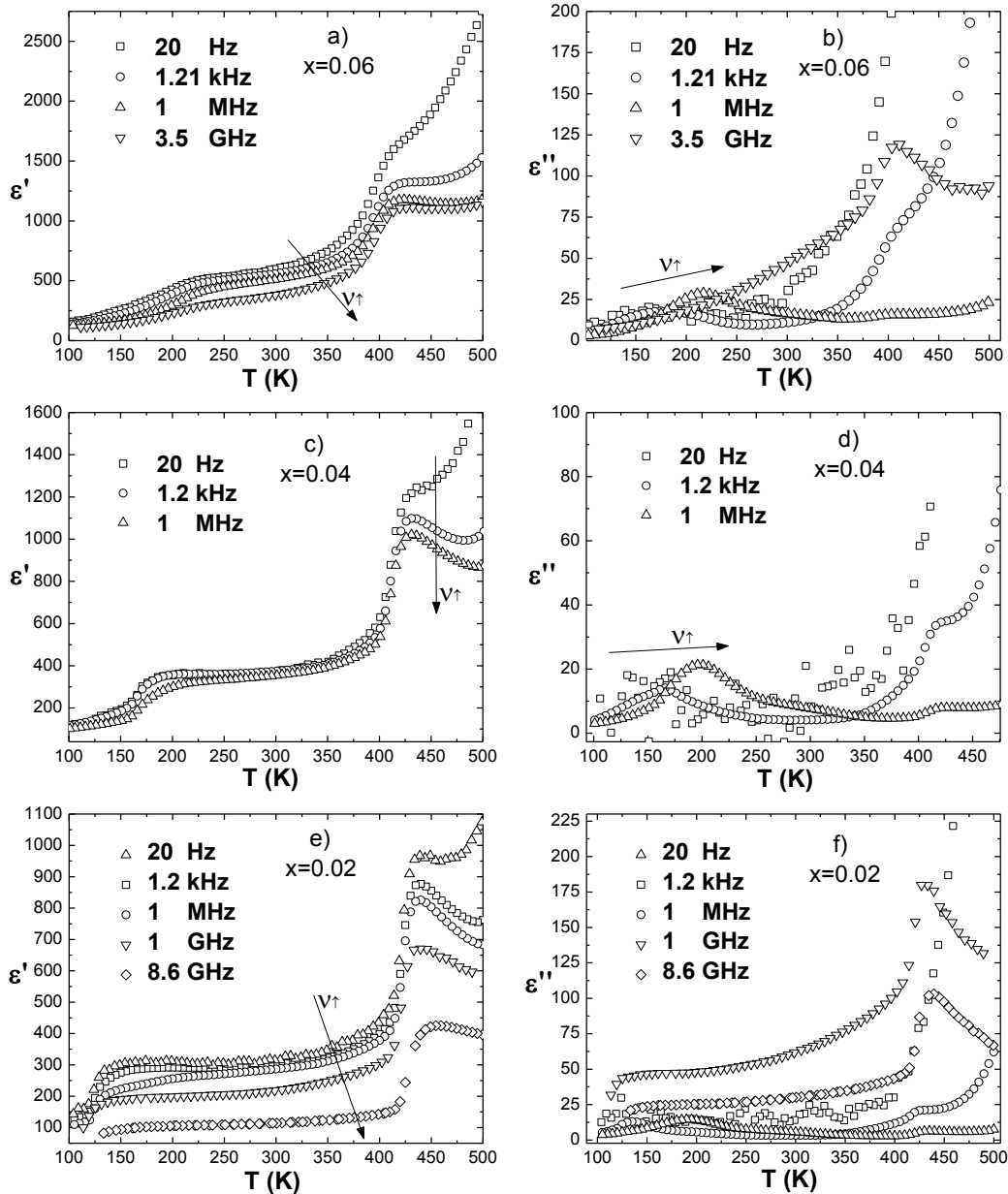

Fig. 5.3.16. Temperature dependences of the real a), c), e) and imaginary b), d), f) parts of dielectric permittivity of $(K_{0.5}Na_{0.5})(Nb_{1-x}Sb_x)O_3$ ceramic at fixed frequencies, for x = 0.06, 0.04 and 0.02 respectively.
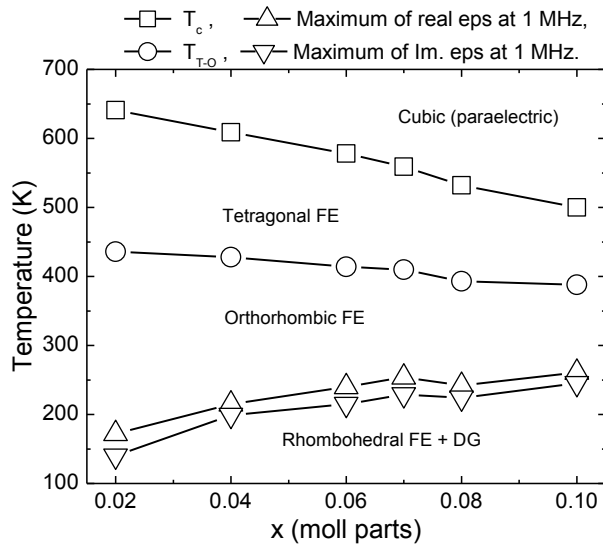
Fig. 5.3.17. Phase diagram of $(K_{0.5}Na_{0.5})(Nb_{1-x}Sb_x)O_3 + 0.5mol.\% MnO_2$ with $x = 0.02$ to 0.1. Lines are guide for eyes.

In summary, dielectric measurements showed two phase transitions located above room temperature (Fig. 5.3.17). Introduced antimony ions strain the lattice and shift both of these phase transitions to lower temperatures compared with undoped KNN ceramic [F23]. One more dielectric permittivity dispersion can be observed below room temperature. This complex dielectric permittivity dispersion is similar to one observed in disordered materials like relaxor ferroelectric [E25-26] or dipolar glasses [E27-29]. The temperature curves of imaginary part of dielectric permittivity cross each other at different frequencies and coincide only at very low temperatures (below liquid N_2), this claims in favor for the dipolar glass-like behavior.

Broadband dielectric investigation revealed two relaxation regions in MHz and GHz ranges. The lower relaxation is thermally activated and shows a broad distribution of the relaxation times. Activation energy for this process was calculated using Arrhenius relationship.

In $(K_{0.5}Na_{0.5})(Nb_{1-x}Sb_x)O_3+0.5mol.\%$ MnO_2 system decreasing B-site radius (Sb^{5+} is smaller than Nb^{5+} ion) increases tolerance factor, but ferroelectric anomaly temperature decreases. Such behaviour might be a consequence of different interaction between ions (less covalent bonding in the lattice) because KNN-Sb_x is $A^+B^{5+}O_3$ type perovskite.

185

References

F1 Rödel J., Jo W., Seifert K., Anton E. M., Granzow T. *J. Am. Ceram. Soc.,* 92 [6], 1153 (2009).

F2 Coondoo I., Panwar N., Kholkin A. *J. Adv. Dielect.,* 3, 1330002 (2013).

F3 Directive 2002/95/EC of the European Parliament and of the Council of 27 January 2003 on the restriction of the use of certain hazardous substances in electrical and electronic equipment, EC (2003).

F4 Shvartsman V. V., Lupascu D. C. *J. Am. Ceram. Soc.,* 95 [1], 1 (2012).

F5 Saito Y., Takao H., Tani T., Nonoyama T., Takatori K., Homma T., Nagaya T., Nakamura M. *Nature*, 432, 84 (2004).

F6 Ringgaard E., Wurlitzer T. *J. Eur. Ceram. Soc.,* 25, 2701 (2005).

F7 ACerS-NIST Phase Equilibria Diagrams Database, accessed on 2009.

F8 Shirane G., Newnham R., Pepinsky R. *Phys. Rev.,* 96 [3], 581 (1954).

F9 Egerton L., Dillon D. M. *J. Am. Ceram. Soc.,* 42 [9], 438 (1959).

F10 Ahtee M., Glazer A. M. *Acta Crystallogr., Sect. A: Found. Crystallogr.,* 32, 434 (1976).

F11 Ahtee M., Hewat A. W. *Acta Crystallogr., Sect. A: Found. Crystallogr.,* 34, 309 (1978).

F12 Hollenstein E., Davis M., Damjanovic D., Setter N. *Appl. Phys. Lett.,* 87, 182905 (2005).

F13 Maeder M. D., Damjanovic D., Setter N. *J. Electroceram.,* 13, 385 (2004).

F14 Du H. L., Li Z. M., Tang F. S., Qu S. B., Pei Z. B., Zhou W. C. *Mater. Sci. Eng. B,* 131, 83 (2006).

F15 Yin Q., Yuan S., Dong Q., Tian C. *J. Alloy Compd.,* 491, 340 (2010).

F16 Gao D., Kwok K. W., Lin D., Chan H. L. W. *J. Mater. Sci.,* 44, 2466 (2009).

F17 Ahn C. W., Park C. S., Choi C. H., Nahm S., Yoo M. J., Lee H. G., Priya S. *J. Am. Ceram. Soc.,* 92, 2033 (2009).

R18 Hagh N. M., Kerman K., Jadidian B., Safari A. *J. Eur. Ceram. Soc.,* 29, 2325 (2009).

R19 Jiang M., Liu X., Chen G., Zhou C. *Mater. Lett.,* 63, 1262 (2009).

F20 Wood E.A. *Acta Crystallogr.,* 4 [4], 353 (1951).

F21 Matthias B.T., Remeika J. P. *Phys. Rev.,* 82 [5], 727 (1951).

F22 Lin D., Kwok K. W., Tian H., Wong H., Chan L.-W. *J. Am. Ceram. Soc.*, 90, 1458 (2007).

F23 Buixaderas E., Bovtun V., Kempa M., Savinov M., Nuzhnyy D., Kadlec F., Vanek P., Petzelt J., Eriksson M., Shen Z. *J. Appl. Phys.,* 107, 014111 (2010).
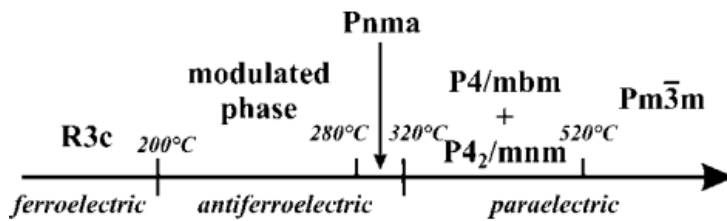
F24 Sidebottom D. L., Roling B., Funke K. *Phys. Rev. B,* 63, 024301 (2000).

F25 Almond D. P., Hunter C. C., West A. R. *J. Mat. Sc.,* 19, 3236 (1984).

F26 Dziaugys A., Banys J., Kezionis A., Samulionis V., Studenyak I. *Sol. Stat. Ion.,* 179, 168 (2008).

5.4. Broadband dielectric investigation of $Na_{0.5}Bi_{0.5}TiO_3$ solid solution with $SrTiO_3$ and $PbTiO_3$.

Among ferroelectric systems, $Na_{0.5}Bi_{0.5}TiO_3$ (NBT) occupies a special place. First of all, it is a lead-free material which exhibits promising electrical and electromechanical properties [G1]. Secondly, sodium bismuth titanate exhibits an unique sequence of phase transitions which are not completely understood despite thorough study and still attract much attention (schematically shown in Fig. 5.4.1). Many questions are still unanswered about the ferroelectric–

Fig. 5.4.1. Schematical representation of most resent phase diagram of NBT (structure and dielectric properties) [G3].

antiferroelectric phase transition which occurs over a broad temperature interval (from 200°C to 320°C). This phase transition is not even mentioned in some publications.

Dorcet et al. showed by transmission electron microscopy studies that the appearance of antiferroelectric phase is a consequence of a modulated phase [G2]. Relaxor-like behaviour in NBT is due to the ability of cations to occupy two kinds of positions which have nearly the same energy. Such two positions are defined by the local structure of the R3c blocks and the Pnma sheets [G2-3]. In this [G2] purely theoretical model, the driving force leading to the modulation is a torsion strain. Each of the two isolated parts of a crystal is symbolized by an octahedron. The initial state within the R3c crystal. No torsion is applied and all crystallographic directions symbolized by arrows remain constant. The chosen direction is arbitrary (shown in Fig. 5.4.2 a)). A torsion involving a crystalline rotation of 180° is applied. The involved strain between the two crystal parts is progressively accommodated by slight

elementary rotation of each octahedron. The lattice strain propagates within the overall crystal, and this feature case is not energetically favorable and therefore structurally unrealistic (Fig. 5.4.2 b)). A torsion involving a crystalline rotation of 180° is applied, but in this case the overall lattice strain is abruptly accommodated within a single plane. The strain is localized and minimized withi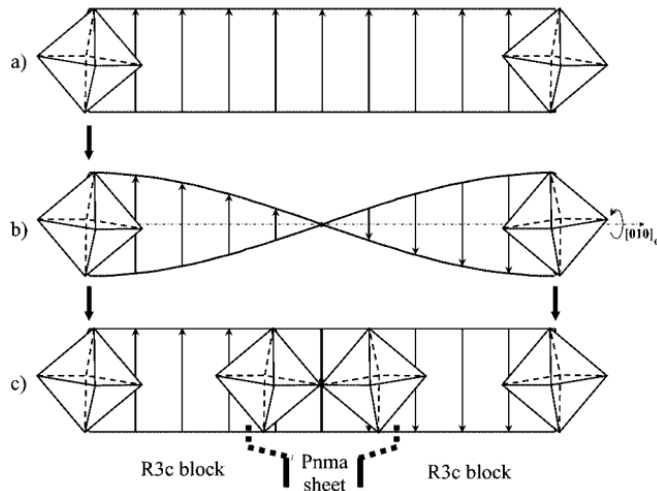n a twin plane (Fig. 5.4.2 c)). In other words, the complexity of crystallographic transformations gives rise to some interesting properties of NBT.

Fig. 5.4.2. Schematic representation showing the effect of a rotation of 180° applied to a crystal around b_O axis [G2].

Another attractive feature of NBT is that it can host various dopants and form solid solutions. Doping is done in order to reduce electrical conductivity and enhance the electromechanical properties of NBT [G4-5], or from a fundamental perspective, to gain an insight into the microscopic processes in the NBT. Strontium titanate (STO), lead titanate (PT), potassium bismuth titanate (KBT) and lanthanum magnesium titanate (LMT) [G6 – G8, G5, G9] are widely used as a secondary materials with sodium bismuth titanate. All of these additional materials influence the properties of NBT differently. It is known that strontium titanate strengthens the relaxor properties of NBT. It also diminishes the anomaly of the ferroelectric–antiferroelectric phase transition which disappears with a certain concentration of ST [G10, G7]. Relaxor properties in (1–x)NBT-xST are observable for a wide range of x. Lead titanate, on the other hand, strengthens the ferroelectric properties. This is mainly due to the huge polarizability of Pb atoms (this feature of PT is

observed in many solid solutions) [G7]. A rather low PT content ($x \geq 19$) induces a ferroelectric–paraelectric phase transition and an increase of PT content shifts the dielectric anomaly to a higher temperature region. The NBT–PT system is rhombohedral on the sodium bismuth titanate-rich side and tetragonal on the lead titanate-rich side and presents biphasic region for $0.1 < x < 0.18$ [G11].

Solid solutions that contain two components have long been the object of research interest. Recently, ternary systems have also attracted a lot of attention. The aims of such research are either to enhance the dielectric and piezoelectric properties of solid solutions, which might be suit able for various applications, or to obtain an insight into the origin of relaxor and/or dipolar glass behaviour. Furthermore, ternary systems might demonstrate interesting behaviour which might differ from those of its individual components [F1].

$0.4Na_{0.5}Bi_{0.5}TiO_3$-$(0.6-x)SrTiO_3$-$xPbTiO_3$ compositions with various concentrations of $PbTiO_3$ were prepared as ceramics by solid-state reaction from chemical-grade oxides in the Laboratory of Physics and Application of Functional Materials, Institute of Solid State Physics, University of Latvia, Latvia, by *Dunce et al.* [G12]. Two-stage calcination was applied at temperatures of 850°C and 1000°C, followed by sintering at 1200°C. Samples 1 mm thick were cut from the bulk specimens and polished. Obtained 0.4NBT–(0.6-x)ST–xPT samples were characterized by XRD (X'Pert PRO MPD, Netherlands) and SEM (Carl Zeiss EVO 50 XVP, Germany).
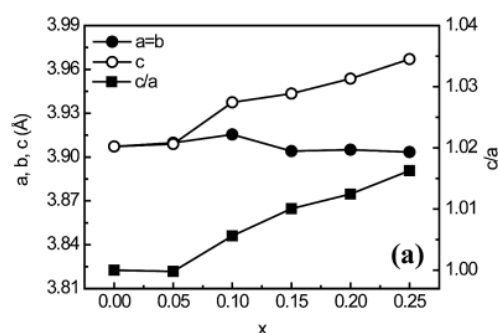

Fig. 5.4.3. Unit cell parameters a, b, c and tetragonality c/a as functions of PT concentration x at room temperature for 0.4NBT–(0.6-x)ST–xPT solid solution [G12].

Structural investigations of the NBT–ST–PT solid solutions by *Dunce et al.* revealed that all samples have single perovskite structure without secondary phases [G12].

The tetragonality factor (shown in Fig. 5.4.3) increases when the content of PT increases. $x < 0.15$ ceramics exhibit relaxor-like properties but the phase transition could only be induced for samples with $x \geq 0.1$. The ability to induce a phase transition with an external field is one of the main features of relaxors [G13-18].
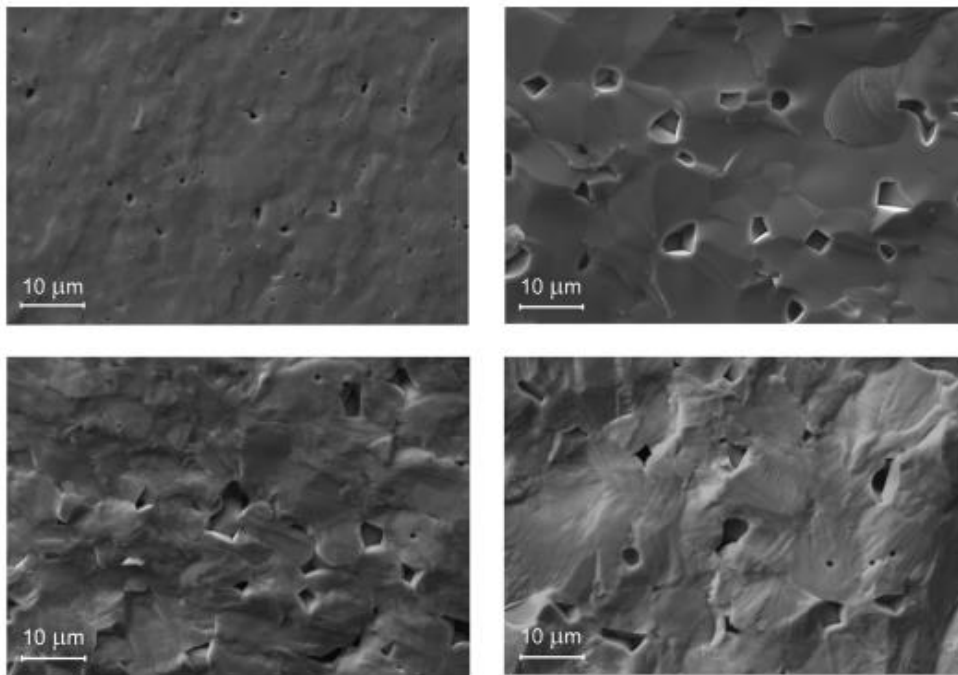

Fig. 5.4.4. SEM micrographs of 0.4NBT-(0.6-x)ST-xPT compositions with x = 0 a), x = 0.05 b), x = 0.2 c) and x = 0.25 d) [G12].

SEM images of 0.4NBT–(0.6-x)ST–xPT revealed dense microstructure with average grain size of 3-10 μm, however some amount of voids are observed. Parallel domain structure is seen at higher Pb content also.

Broadband dielectric measurements were performed for x = 0, 0.05, 0.1, 0.15 and 0.2 ceramics over the temperature range 30 - 1000 K and frequency range 10 mHz – 50 GHz. Silver paste was used as contacts for all specimens. The rate of temperature increase was 1 K/min except in the vicinity of phase transitions where it was decreased to 0.2 - 0.4 K/min. The same equipment as

in previous chapters (Chapters 5.2 and 5.3) was used for broadband dielectric spectroscopy.

Experimental dielectric spectra were fitted with the Cole–Cole (Eq. 4.21) or Havriliak–Negami (Eq. 4.24) equations. The relaxation time in Havriliak-Negami equation is neither the mean nor the most probable relaxation time. In order to obtain the mean relaxation time from this equation a recalculation must be done according to the following procedure described in [G19]. To obtain the distribution of relaxation times $f(ln\,\tau)$ from dielectric measurements, the integral of Eq. 4.18 and 4.19 must be solved. This is a problem which cannot be treated analytically in the case of experimental data, as uncertainties limit analysis to approximations. One of the possible ways to solve such an integral equation numerically is to use the Tikhonov regularization method [C12].
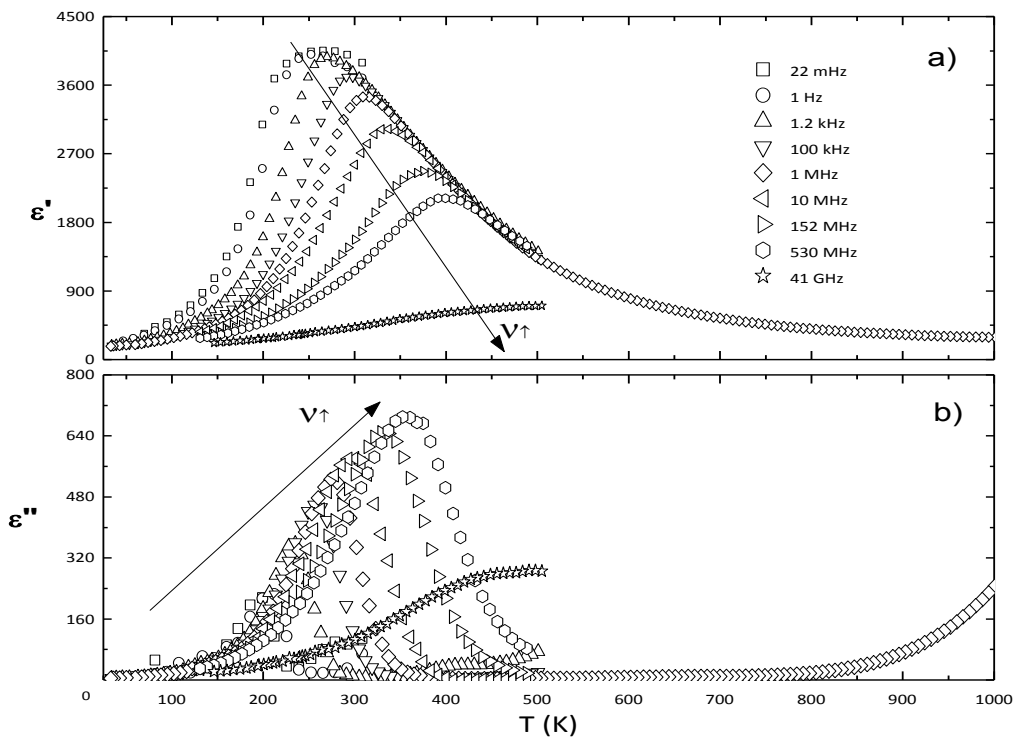

Fig. 5.4.5. Complex dielectric permittivity temperature dependences of 0.4NBT-(0.6-x)ST-xPT, with x = 0 (without lead titanate). The real part is shown in a) and the imaginary part in b).

192

The temperature dependencies of the complex dielectric permittivity (x = 0 i.e. 0.4NBT-0.6ST, without lead titanate) are shown in Fig. 5.4.5. The real part of the dielectric permittivity for x = 0 ceramics (Fig. 5.4.5 a)) shows frequency-dependent maximum and relaxor-like behaviour, but the imaginary part (Fig. 5.4.5 b)) shows some similarities with dipolar glasses. Typically, dielectric losses of relaxors are independent of frequency at low temperatures (constant loss regime). However, curves of different frequencies intersect at low temperatures and constant losses are not observed. Such behaviour is not typical for relaxors and might occur due to competing interactions (i.e. ferroelectric–antiferroelectric) or some other disorder in general. High-temperature measurements at 1 MHz show that there are no phase transitions in this temperature regime which would be visible from dielectric data. Only the impact of conductivity is observed in the imaginary part.
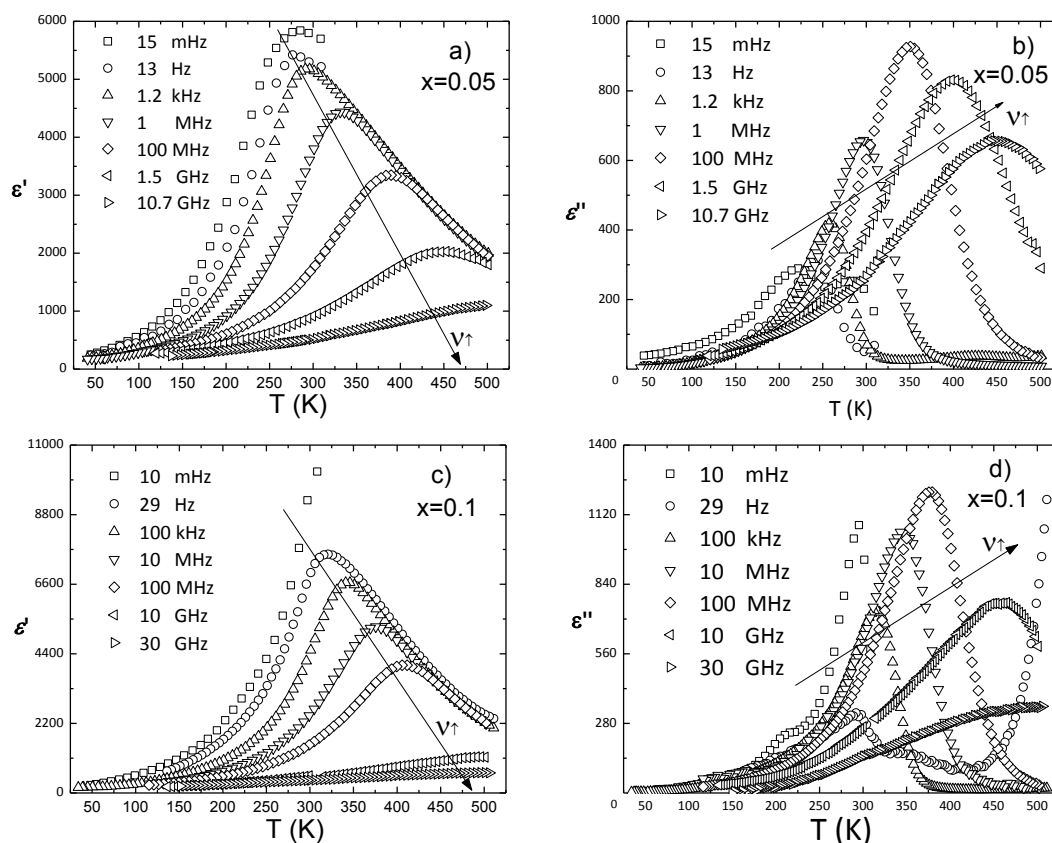

Fig. 5.4.6. Complex dielectric permittivity temperature dependences of 0.4NBT-(0.6-x)ST-xPT, with x= 0.05 and 0.1. The real part is shown in a), c), and the imaginary part in b), d).

Dielectric spectra of ceramics with x = 0.05 and 0.1 (Fig. 5.4.6) show typical relaxor behaviour. Addition of lead to the ceramics increases the dielectric anomaly and shifts it to higher temperatures. The intersection of curves in the imaginary part only occur at higher frequencies (f > 1 MHz). But it can be seen that the dielectric loss is frequency independent at low temperatures and this is one of the most important features of relaxor ferroelectrics. Furthermore, *Dunce et al.* showed that it is possible to induce phase transition in ceramics with x = 0.1 [G12]. It is possible that substitution of strontium titanate with lead titanate increases interaction and the correlation length between dipoles. The dielectric anomaly increases when the lead content increases due to the high polarizability of Pb atoms. The strengthening of relaxor properties might be associated with higher local polarization occurring when Pb atoms are introduced and the interaction between dipoles and their correlation length expands.
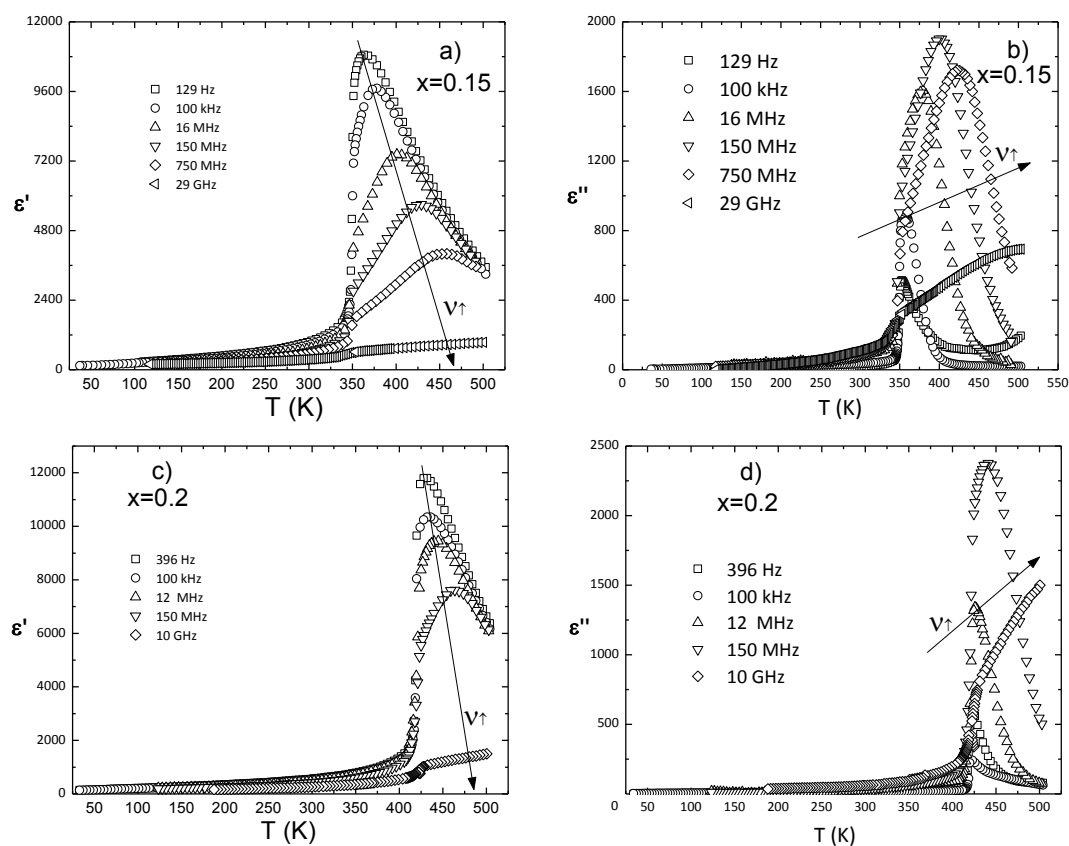

Fig. 5.4.7. Complex dielectric permittivity temperature dependences of

194

0.4NBT-(0.6-x)ST-xPT, with x = 0.15 and 0.2. The real part is shown in a), c), and the imaginary part in b), d).

A further increase in lead (x = 0.15 and 0.2) content in the solid solution induces a ferroelectric phase in the lower-temperature region (Fig. 5.4.7). Results obtained during the cooling cycle are presented here. The higher-temperature region exhibits relaxor properties which transform into a ferroelectric phase close to 350 K. The phase transition is first order, because thermal hysteresis is observed during the heating and cooling cycles. One of the possible mechanisms for this transition is that during cooling PNRs expand and at a certain temperature reach the percolation threshold, which could induce a domain-like structure. Another possible explanation is that addition of lead increases the interaction energy between PNRs. According to SRBRF, the most important quantity is the ratio of the bonding energy to the interaction energy of PNRs and random fields. If this ratio is greater than a certain value, then a phase transition occurs at a certain temperature. The larger the ratio, the higher the temperature [G20].

If we assume that the phase transition from relaxor to normal-ferroelectric occurs due to the percolation of PNRs, then PNRs must have the same local symmetry in the relaxor state as in the ferroelectric state. This means that a local breaking of symmetry must exist in the relaxor phase. Similar local symmetry breaking was also observed in the paraelectric phase of barium titanate (BTO) [G21]. It is believed that in the case of relaxors this breaking of symmetry drastically affects various properties. On the other hand, in the case of BTO the precursor of the phase transition gives only slight deviations from the Curie-Weiss law and, possibly, properties related to the noncentrosymmetric phase (piezoelectricity, etc.) [G21-23]. It is known that such local deviations in BTO appear due to the offset of Ti ions along the eight equivalent [111] directions. In our case such deviations from the ideal B-site position along with the different ions in A-site can force the formation of PNRs, which affects Curie-Weiss law

195

behaviour in the relaxor phase. In general, the properties of A-site ions also play an important role in the occurrence of relaxor behaviour, and a particular distribution of A-site cations might allow control of the offset of B-site ions.
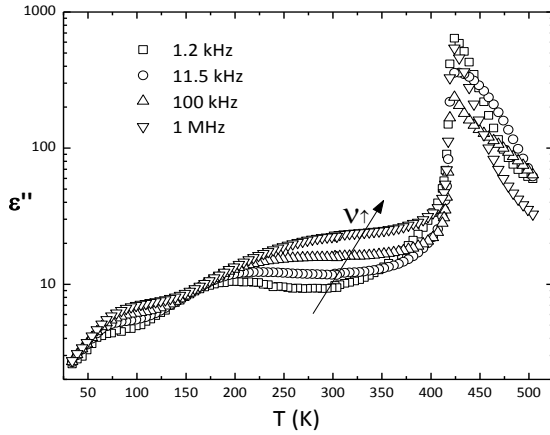

Fig. 5.4.8. Temperature dependence of the imaginary part of the dielectric permittivity for x = 0.15 in logarithmic scale.

In the low-temperature phase (ferroelectric phase), x = 0.15 ceramic has two anomalies mostly observed by the dielectric loss. This can only be seen on a logarithmic scale (Fig. 5.4.8) in the temperature intervals of 200 – 350 and 75 – 175 K. When x = 0.2 [G24] such dispersions were also visible in the ferroelectric phase. Such dispersions can be attributed to the coexistence of ferroelectric and dipolar glass phases [G25]. The appearance of a dipolar glass phase can be related to the distribution of A-site cations. If Pb atoms are distributed in such a manner that there are clusters with lead deficiency, these small clusters with strontium or bismuth and sodium surplus can give rise to dispersions in the imaginary part, while long-range ordering which includes Pb atoms caused the ferroelectric behaviour. This kind of relaxation could also be related to the domain wall motion. However, we only managed to produce minor changes in these processes under field cooling - zero field heating (FC-ZFH) protocol at 2 kV/cm DC bias.

The frequency dependence of complex dielectric permittivity and the distribution of relaxation times for a sample with x = 0 are depicted in Fig. 5.4.9. Frequency dependencies were fitted with the Havriliak–Negami (Eq. 4.24) formula. Dielectric spectra of ceramic with x = 0 (Fig 5.4.9) and 0.05 (Fig. 5.4.10 a) and b)) composition are asymmetric at low temperatures.
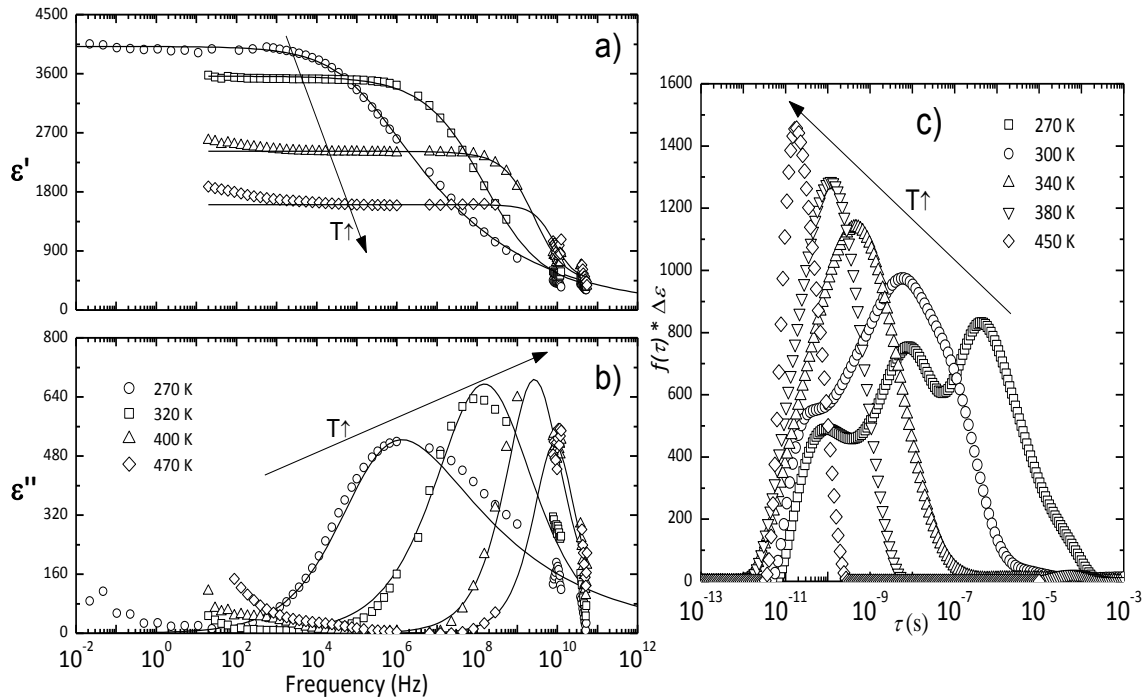
Fig. 5.4.9. Frequency dependencies of the complex dielectric permittivity for 0.4NBT-(0.6-x)ST-xPT ceramic. The real part of the dielectric permittivity a) and the imaginary part of the dielectric permittivity b), and the distribution of relaxation times c), for x = 0. Solid lines in a) and b) are Havriliak-Negami formula fits to experimental data.

The parameter γ converges to 1 and dielectric spectra become increasingly symmetric at higher temperatures (Havriliak-Negami formula with $\gamma = 1$ becomes equal to Cole-Cole formula).

The same asymmetric spectra is observed for x = 0.05 also, shown in Fig. 5.4.10 a) and b). Meanwhile the asymmetry is not observable for all fitted temperature ranges for specimens x = 0.1 to 0.2 (shown in Fig. 5.4.10 c) to f)). We see that an increase of lead concentration reduces the asymmetry of the dielectric spectra.
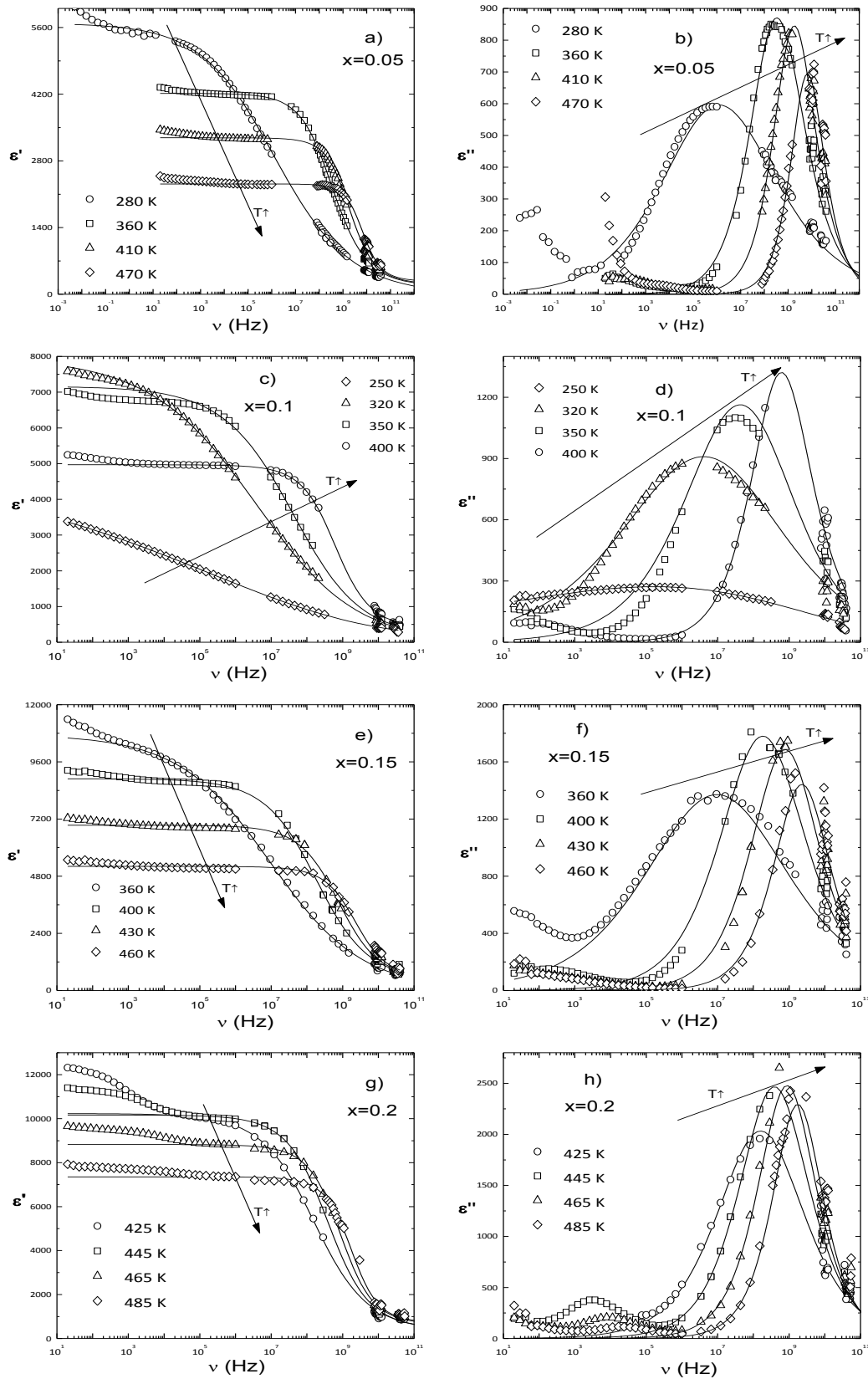
Fig. 5.4.10. Frequency dependencies of complex dielectric permittivity: the real part is shown in a), c), e), g) and the imaginary part in b), d), f), h) for

x = 0.05 to 0.2. Solid lines in a) and b) are Havriliak-Negami formula and in c) to h) are Cole-Cole formula fits to experimental data.

The distribution of relaxation times (Fig. 5.4.9 c) and Fig. 5.4.11) confirms that the dielectric spectra become more symmetric with increasing temperature.
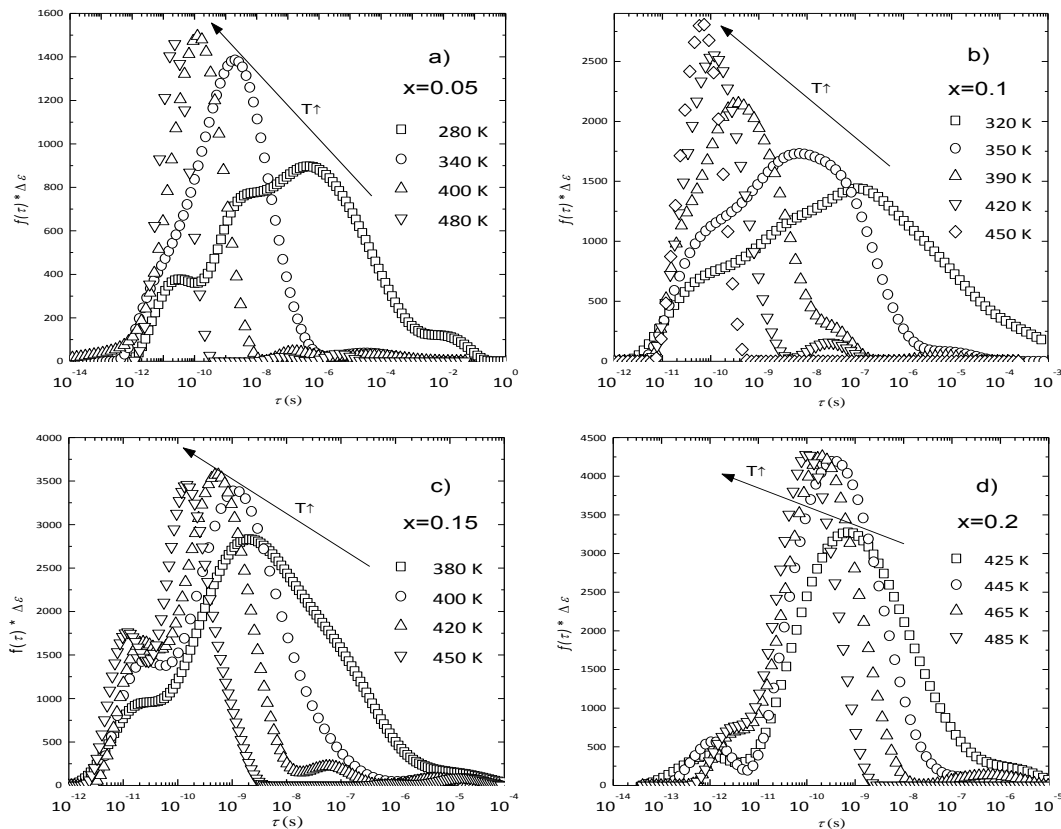

Fig. 5.4.11. Calculated relaxation time distribution function f(τ) of 0.4NBT-(0.6-x)ST-xPT ceramics for x = 0.05 to 0.2.

Also, it is seen that there is only one peak in the distribution function, which broadens when the temperature is decreased. Usually, two relaxational processes in relaxors exist that are seen in the distribution of relaxation times [E26-27, G26-27]. The existence of only one peak might indicate the glassy behaviour of the system or perhaps that one of the relaxational processes exists outside our experimentally available frequency range. In the latter case the algorithm which we use to calculate distribution function is not able to include this process. In the short-time and long-time regions few small peaks are

199

observed which occur due to the finite accuracy of our experiment. The few humps in the curves are due to the incompatibility of measured permittivity in different frequency ranges (i.e. coaxial measurements and waveguide measurements do not lay on exactly the same curve).

Mean relaxation time was obtained from the Cole–Cole equation (Eq. 4.21) in the high-temperature region, whereas in the low-temperature region the Havriliak–Negami formula (Eq.4.24) was used, and the mean relaxation time was calculated using [G19] described method. Ceramics x= 0.1 to 0.2 were fitted with the Cole–Cole equation for the entire temperature range measured. Fitting parameters are presented in Table 5.4.1.

Table 5.4.1. Parameters obtained from the Vogel–Fulcher law (Eq. 2.15) for all investigated ceramics.

x	E_A (eV)	T_{VF} (K)	τ_0 (s)
0	0.106	143	$4.97 \cdot 10^{-13}$
0.05	0.126	170	$1.63 \cdot 10^{-13}$
0.1	0.142	191	$1.09 \cdot 10^{-13}$
0.15	0.164	217	$2.72 \cdot 10^{-14}$
0.2	0.179	223	$3.39 \cdot 10^{-14}$

The activation energy and freezing temperature obtained from the Vogel–Fulcher law increase when the lead content in the ceramics increases while the attempt time decreases. These parameters obtained from the mean relaxation time do not match those obtained from the maxima of the real part of the dielectric permittivity by *Dunce et al.* [G18]. The freezing temperature obtained from the maxima of the real part of the dielectric permittivity is higher for all ceramics. At those freezing temperatures obtained by *Dunce et al.* we see nearly complete dispersion in our measured frequency range. The unanswered questions are what kind of freezing is obtained with the other approach and whether such freezing is associated with the PNRs. It is obvious from the dielectric spectra that the imaginary part is constant for all available frequency ranges at the freezing temperature obtained from the mean

relaxation time. This means that the dynamics of PNRs are critically slow in the vicinity of T_{VF}. Similar discrepancies were also observed with other materials ([G28] and references therein).
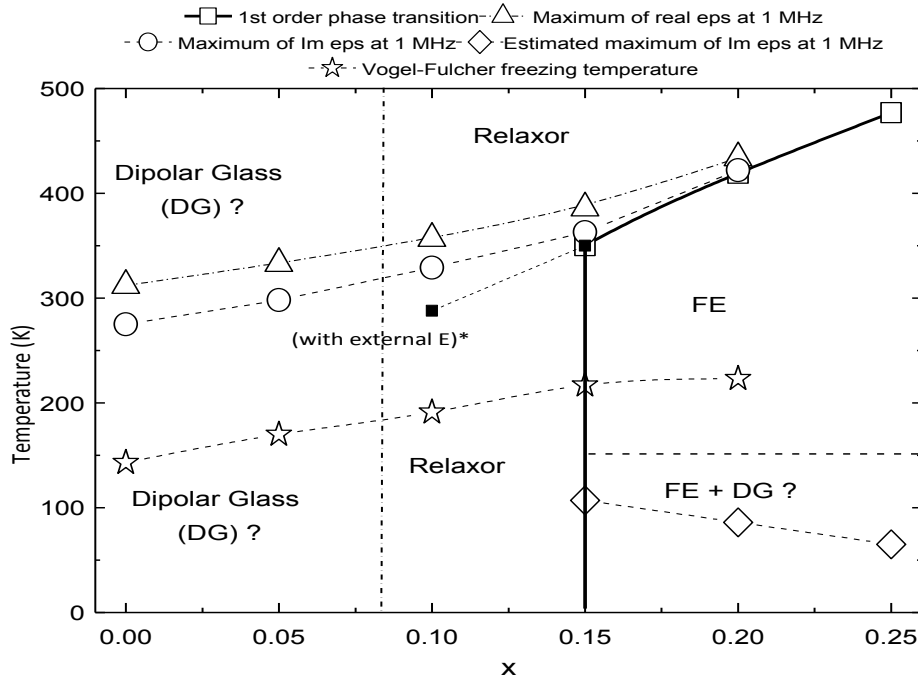

Fig. 5.4.12. Phase diagram of the $0.4Na_{0.5}Bi_{0.5}TiO_3$-$(0.6\text{-}x)SrTiO_3$-$xPbTiO_3$ system.

Fig. 5.4.12 summarizes the results of the measured ceramics. It is seen from the graph that the properties of NBT–ST–PT are strongly modified by lead titanate and cannot be unambiguously associated with relaxors. There is evidence that low-lead NBT–ST–PT specimens present dipolar glass-like behaviour which can be attributed to the low polarizabilities of the ions occupying A-sites in the perovskite lattice. In case of ferroelectric ceramics, a larger amount of lead results in a higher transition temperature. This might be related to the high polarizability of lead, which could possibly lead to stronger interactions between PNRs, thus making a spontaneous ferroelectric phase transition possible at certain lead concentrations. The larger the concentration, the higher the transition temperature.

In summary, dielectric spectroscopy results revealed that substitution of strontium ions with lead significantly changes the dielectric response of NBT–

ST–PT solid solutions. The increase in lead content strengthens the relaxor behaviour, and at a certain concentration, when the percolation threshold of PNRs is reached, a first-order phase transition occurs in the system. A more glassy state in 0.4NBT–0.6ST solid solutions might occur due to disorder of A-site ions which does not distort the perovskite structure.

When lead is introduced, greater strain occurs in the perovskite lattice which increases distortions, and the offset of ions in A-sites (particularly Pb ions) gives rise to increased relaxor behaviour. A further increase in lead concentration leads to the long-range order which is responsible for the occurrence of the phase transition. The phase transition is from relaxor to ferroelectric state: this means that the higher temperature phase is not properly paraelectric. This is the consequence of remaining local distortions. PNRs strongly influence the dielectric properties of materials at frequencies below phonon modes. This could be linked to similar phenomena in BTO, which are related to the dynamics of local polar clusters, although no obvious relaxor state is observed in the latter case.

The role of Na, Bi and Sr ions in the A-site remains quite unclear. If these ions form some disordered matrix, it might also contribute to the transformation from ferroelectric to relaxor phase. The low-temperature region has dispersions visible
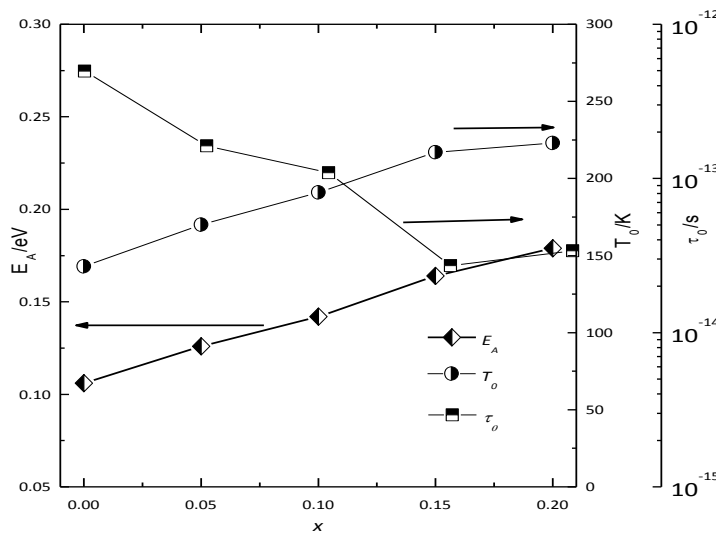
Fig. 5.4.13. Parameters of Vogel-Fulcher law for 0.4NBT-(0.6-x)ST-xPT ceramics for x=0 to 0.2.

in the imaginary part, which might be associated with such disorder. These dispersions might also be caused by domain wall motion.

Analysis of the dielectric spectra shows that mean relaxation time follows the Vogel–Fulcher law for all compositions. The activation energy and freezing temperature increase when lead content increases, while the attempt time decreases (Fig. 5.4.12). The freezing temperature might be considered as a temperature at which the dynamics of dipolar entities critically slow down and the distribution of relaxation times becomes infinitely broad. The calculated distribution of relaxation times shows that the decrease in temperature broadens the distribution. However, the freezing temperatures are lower than those obtained with the usual treatment of temperature of dielectric permittivity maxima vs. frequency. Moreover, at the latter temperatures, the dielectric permittivity is still quite "dynamic" and exhibits obvious relaxation.

The same tendency as in $Sr_{1-1.5x}Bi_xTiO_3$ ceramic was observed in $0.4Na_{0.5}Bi_{0.5}TiO_3$-$(0.6-x)SrTiO_3$-$xPbTiO_3$ also. Increasing Pb content locally increases A-site radius and tolerance factor, thus increasing polar anomaly (relaxational dispersion) temperature and at high enough concentration (further increasing tolerance factor) induces first order ferroelectric phase transition.

References

G1 Roleder K., Franke I., Glazer A., Thomas P., Miga S., Suchanicz J. J. *Phys. Condens. Matter*, 14, 5399 (2002).

G2 Dorcet V., Trolliard G., Boullay P. *Chem. Mater.,* 20, 5061 (2008).

G3 Trolliard G., Dorcet V. *Chem. Mater.,* 20, 5074 (2008).

G4 Herabut A., Safari A. *J. Am. Ceram. Soc.*, 80 [11], 2954 (1997).

G5 Salak A., Vyshatko N., Kholkin A., Ferreira V., Olekhnovich N., Radyush Y., Pushkarev A. V. *Material Science Forum Vols. 514-516,* 250 (2006).

G6 Isupov V. *Ferroelectrics*, 315, 123 (2005).

G7 Lee J., Hong K., Kim C., Park S. *J. Appl. Phys.,* 91 [7], 4538 (2002).

G8 Rout D., Moon K. S., Kang S. J. L., Kim I. W. *J. Appl. Phys.,* 108, 084102 (2010).

G9 Suchanicz J., Glos B., Stopa G., Kruzina T., Kusz J., Zubko M., *Integr. Ferroelectr.,* 108, 98 (2009).

G10 Gomah-Pettry J., Salak A., Marchet P., Ferreira V., Mercurio J. *Phys. Stat. Sol. B,* 241 [8], 1949 (2004).

G11 Elkechai O., Marchet P., Thomas P., Manier R., Mercurio J. *J. Mater. Chem.*, 7, 91 (1997).

G12 Dunce M., Birks E., Antonova M., Kundzinsh M., Sternberg A. *Integr. Ferroelectr.,* 108, 125 (2009).

G13 Schmidt G., Arndt H., Borchhardt G., von Cieminski J., Petzsche T., Bormanis K., Sternberg A., Zirnite A., Isupov V. A. *Phys. Stat. Sol. A,* 63, 501 (1981).

G14 Xu G., Zhong Z., Bing Y., Ye Z. G., Shirane G. *Nature Mater.,* 5, 134 (2006).

G15 Cross L. E. *Ferroelectrics*, 76, 241 (1987).

G16 Dunce M., Birks E., Antonova M., Sternberg A. *Ferroelectrics*, 414, 190 (2011).

G17 Birks E., Dunce M., Antonova M., Sternberg A. *Phys. Stat. Sol. C*, 6 [12], 2737 (2009).

G18 Dunce M., Birks E., Antonova M., Kundzinsh M. *Integr. Ferroelectr.*, 123, 40 (2011).

G19 Zorn R. *J. Chem. Phys.,* 116 [8], 3204 (2002).

G20 Pirc R., Blinc R. *Phys. Rev. B,* 60 [19], 13470 (1999).

G21 Ko J. H., Kim T. H., Roleder K., Rytz D., Kojima S. *Phys. Rev. B,* 84, 094123 (2011).

G22 Pugachev A. M., Kovalevskii V. I., Surovtsev N. V., Kojima S., Prosandeev S. A., Raevski I. P., Raevskaya S. I. *Phys. Rev. Lett.,* 108, 247601 (2012).

G23 Jin Y. M., Wang Y. U., Ren Y., Ma F. D., Zhou J. E., Cheng T. L. , Wang B. L., Geng L. D., Kuyanov I. A. *ArXive-prints*, 1302.5479 (2013).

G24 Svirskas S., Ivanov M., Bagdzevicius S., Dunce M., Antonova M., Birks E., et al. Integr. Ferroelectr., 134, 81 (2012).

G25 Schmidt V. H., Trybula Z., Pinto N., Shapiro S. M. *Phase Trans.*, 67, 499 (1998).

G26 Kajokas A., Matulis A., Banys J., Mizaras R., Brilingas A., Grigas J. *Ferroelectrics*, 257, 69 (2001).

G27 Macutkevic J., Lapinskas S., Grigas J., Brilingas A., Banys J., Grigalaitis R., *J. Eur. Ceram. Soc.,* 25, 2515 (2005).

G28 Tagantsev A. K. *Phys. Rev. Lett.*, 72, 1100 (1994).

6. Conclusions

This thesis describes an experimental investigation of incipient ferroelectric strontium titanate (epitaxial thin films and doped ceramics) and related solid state systems. Following conclusions are obtained:

1. Misfit (epitaxial strain by substrate) and chemical (local lattice strain by dopant induced change of tolerance factor) strain strongly influences ferroelectric and structural phase transition temperatures as well as transition character, also induces new properties at nanometric scale – polar nano-regions, antiferrodistortive nano-regions and possible ferroelectricity in antiferrodistortive phase boundaries.

2. Epitaxially strained $SrTiO_3$ is in antiferrodistortive phase at room temperature, antiferrodistortive phase transition temperature is enhanced more than 100°C from the bulk value. Ferroelectricity was not experimentally observed by piezoelectric force microscopy in antiphase boundaries at 150 K – 370 K temperatures.

3. In $A^{2+}B^{4+}O_3$ perovskites increasing tolerance factor suppress antiferrodistortive transition and strengthens polar anomaly. Such behaviour was observed in $Sr_{1-1.5x}Bi_xTiO_3$ and $0.4Na_{0.5}Bi_{0.5}TiO_3$-(0.6-x)$SrTiO_3$-$xPbTiO_3$ ceramics. In $A^+B^{5+}O_3$ type perovskite increasing tolerance factor decrease ferroelectric phase transition temperature. This was observed in $(K_{0.5}Na_{0.5})(Nb_{1-x}Sb_x)O_3$+0.5mol.% MnO_2 solid solution.